UNSTEADY AERODYNAMICS OF PITCHING FLAT PLATE WINGS

by

Huai-Te Yu

A dissertation submitted in partial fulfillment
of the requirements for the degree of
Doctor of Philosophy
(Aerospace Engineering)
in the University of Michigan
2014

Doctoral Committee:

Professor Luis P. Bernal, Chair
Associate Professor Aline J. Cotel
Associate Professor Krzysztof Fidkowski
Michael V. Ol, Air Force Research laboratory
Professor Kenneth G. Powell

DEDICATION

This dissertation is dedicated to my family.

ACKNOWLEDGMENTS

There are no words that could truly express my gratitude to my adviser, Professor Luis P. Bernal. Without his inspiration, encouragement, and guidance, this work could not have been accomplished. Also I greatly appreciate the help of Terry Larrow for making tools used in the experiment, such as wings, sensor adapter, injection rack, and visualization background board; his delicate skills make this study possible. I appreciate Chris Chartier for making a wooden mounting rod and Chris Morrison for showing me around the water channel laboratory and introducing procedures for measurements.

I am grateful to Dr. Michael V. Ol, Profs. Aline J. Cotel, Kenneth G. Powell, Krzysztof Fidkowski for serving on my dissertation committee and giving valuable comments to enrich the contents of this work.

In addition, I would like to acknowledge National Defense University (ROC) for providing this opportunity to study abroad and Prof. Wei Shyy for introducing me into Aerospace Engineering department at University of Michigan while he was still in the department.

The work was sponsored in part by the Air Force Office of Scientific Research's Multidisciplinary University Research Initiative (MURI), contract number FA9550-07-1-0547, the Michigan/AFRL Collaborative Center in Aeronautical Sciences, and National Defense University, Taiwan.

TABLE OF CONTENTS

LIST OF TABLES

LIST OF FIGURES

LIST OF APPENDICES

NOMENCLATURE

υ = kinematic viscosity
τ = ratio of pitch time to convective time, t_p/t_c, 1
λ = taper ratio, c_t/c_r, 1
$\alpha'(t)$ = pitch rate in time
α''_m = maximum pitch acceleration
α'_m = maximum pitch rate
$\alpha(t)$ = angle of attack in time
α_m = maximum angle of attack
AR = physical aspect ratio, b^2/S, 1
AR_{eff} = effective aspect ratio, $2*AR$, 1 (for water surface as symmetry plane)
b = physical wing span
b_{eff} = effective wing span, $2b$ (for water surface as symmetry plane)
c = wing mean chord
C_D = drag coefficient, $2*D/\rho U_\infty S$, 1
C_L = lift coefficient, $2*L/\rho U_\infty S$, 1
C_M = pitching moment coefficient, $2*M_p/\rho U_\infty S$, 1
c_r = wing root chord
c_t = wing tip chord
D = drag force
e = relaxation coefficient, 1
f = flapping frequency, $f = 1/T$, Hz
F_A = axial force
f_c = convective frequency, $f_c = 1/t_c$, Hz
F_N = normal force
f_p = pitch frequency, $f_p = 1/t_p$, Hz
Fx = X component of force in sensor frame of reference, N
Fy = Y component of force in sensor frame of reference, N
h = hold parameter, 1
h^* = non-dimensional plunge amplitude, h_a/c, 1
h_a = plunge amplitude
k = reduced frequency, $k = 2\pi fc/U_\infty$, 1
K = reduced pitch rate, $K = c\alpha_m'/2U_\infty$, 1
L = lift force
M_p = pitching moment about pivot axis
Re = Reynolds number, cU_∞/υ, 1
S = physical wing area, bc
s = start parameter, 1

S_{eff} = effective wing area, $b_{eff}\, c$ (for water surface as symmetry plane)
St = Stoke's number, $\alpha'_m\, c^2/\upsilon$, 1
T = period, s
t = time, s
t^* = non-dimensional time, tc/U_∞,1
t_1 = the first transition corner in time during ideal pitch up-hold-return motion, s
t_2 = the second transition corner in time during ideal pitch up-hold-return motion, s
t_3 = the fourth transition corner in time during ideal pitch up-hold-return motion, s
t_4 = the third transition corner in time during ideal pitch up-hold-return motion, s
t_c = convective time, c/U_∞, s
t_f = flapping time, c/fh_a, s
t_p = pitch time, α_m/α'_m, s
U_∞ = free-stream velocity
x_{cp} = center of pressure
x_p = pivot axis
z(t) = stroke amplitude
$z(\mathrm{t})^*$ = non-dimensional stroke amplitude, z/c, 1

ABSTRACT

In this study, the aerodynamics of a one-degree-of-freedom wing motion, a constant speed pitch ramp, were investigated to determine unsteady flow dynamics and force generation. This kinematics has discernible regions of constant rotation speed and motion acceleration, which helps isolate several effects. This pitching maneuver is analogous to the perching maneuver by birds and insects; a review of aerodynamics of natural flyers is provided. Maneuverability of natural flyers is difficult to emulate in engineered systems; the unsteady flow field of high degree-of-freedom wing kinematics complicates the analysis of the problem and the simpler one-degree-of-freedom kinematics considered here provides valuable insight for man-made fixed wing systems.

In this study, dynamic flow field was investigated over thin finite-aspect-ratio-four wings pitching at several constant pitch rates in constant free-stream flows, giving reduced pitch rate in a range of $0 \leq K \leq \infty$, in an attempt to understand the interplay of time scale between wing motion and free-stream flow. All work was conducted in free-surface water channel in a chord Reynolds number interval of $0 < Re < 13$k by means of flow visualization, force measurement, and particle image velocimetry. A simple linear potential flow theory was implemented to elucidate experimental data; effects of reduced pitch rate, pivot axis location, and wing planform were included in the theory. Moreover, the identification of vortical flow structure was presented in correlation with force generation.

The rapid increase of aerodynamic forces is associated with the formation of starting vortex in the wake and reduced-pitch-rate effect at the onset of the wing rotation; the gentle increase of aerodynamic forces is relevant to the simultaneous occurrence of leading-edge vortex formation and trailing-edge vortex shedding during constant rotation rate. Low taper-ratio wing enhances force generation at high reduced pitch rate. The pivot-axis location determines the location of the starting vortex. The leading-edge vortex

evolution after the end of the motion is delayed; the time delay is the convection time from the leading edge to the pivot-axis location. Linear potential flow theory with rotation-rate effects gives reasonable estimation of force coefficients.

CHAPTER 1

INTRODUCTION

1.1 BACKGROUND AND MOTATIVATION

Biological flyers demonstrate remarkable agility and efficiency in flight. Birds, bats, and insects are able to generate relatively large forces very quickly in response to gust and other disturbances as well as during perching maneuvers. These flight features are of considerable interest to biologists and engineers, but remain poorly understood. They have been the subject of numerous research efforts and motivate the present research. The transient aerodynamic force and flow development during the pitch up motion of a wing is a canonical flow problem encountered in flapping wings and perching maneuvers of fixed wing vehicles. These phenomena are also relevant to development of advanced small Micro Air Vehicles, which might take advantage of the large forces generated at high pitch rates. Vortical flow features, such as leading edge vortex (LEV) and wing tip vortex (TIV), develop with characteristic time scales of the order of the convective time. On the other hand the pitch rate introduces independent time scale. One important goal of the present research is to determine the interplay between these two time scales and its impact on force and flow developments for different wing geometries and pivot axis locations. Here we review first biological flyers and highlight the main wing kinematics and maneuvers found in nature, which are the main motivation for the present research. A review of pitching wing aerodynamics follows, which is the focus of the present research. Finally the parameter space of pitching wings in a uniform stream considered in the present work is introduced and scope and objectives of the research outlined.

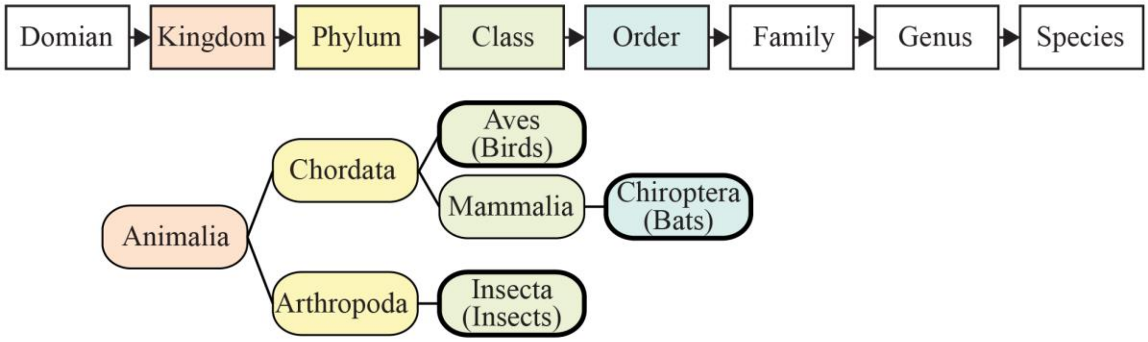

Figure 1.1 Biological classification of natural flyers.

1.1.1 Biological Flyers

In nature, animals evolve their flying skill in order to adapt to surroundings, to escape from predators, to seek food, and to migrate for better living conditions (Bishop, 1997; Feduccia, 1997). Birds, bats, and insects are common natural flyers but they are from three different Classes in biological classification, which is Aves, Mammalia, and Insecta in sequence, as shown in Figure 1.1. Interestingly, birds and bats have backbones and are considered to be the same Chordata in Phylum, one level higher than Class; however, bats do not have feathers to cover their body and wings, and are the only mammals capable of flying. Insects are invertebrates and categorized to Arthropoda in phylum. These differences reveal two facts. The first fact is that the vertebrate spine is not vital for the flying behaviors of natural flyers but accommodates their body sizes. The second fact is that natural flyers do not require feathers to stay airborne but may use them to alter maneuverability.

From an engineering point of view, Tennekes (2009) reported a log-log plot of weight as functions of cruising speed and wing load, intending to connect man-made aircrafts with natural flyers, presented as a straight line from bottom left to top right in Figure 1.2. This straight line was established using classical two-dimensional steady potential flow theory $2W/\rho U_\infty^2 S = 2\pi\alpha$ at $\alpha = 6°$ in the consideration of a long-distance cruising flight. Even though this straight line could not be truly correlated with natural flyers due to variations of wing configuration and kinematics, and the existence of three-dimensional flow field, it suggests that small aircraft may need to be wing-flapping, as birds, bats and wing-beating insects do, rather than fixed wing. The performances of present fixed-wing micro aerial vehicles (MAVs) are also presented and scattered within the shaded region in Figure 1.2; the demand of MAV is at the right upper margin of the shaded area (Pine and Bohorquez, 2006).

1.1.1.1 Birds

1.1.1.1.1Bird Wing Types

Savile (1957) observed that bird wings could be categorized into the four following primary types of function regarding their flight behavior and wing shape: (i) elliptical wing suitable for narrow space operation, (ii) high-speed wing, (iii) high-aspect-ratio wing, and (iv) high-lift wing (or slotted soaring wing) for carrying heavy loads. The representatives of these wings are illustrated in Figure 1.2. According to Savile’s calcification, some information, such as aspect-ratio and bird species, is tabulated in Table 1.1. The elliptical and high lift wings have more pronounced camber than the other two wing forms; their aspect ratio is no more than 7. For high-speed and high aspect-ratio wings, the aspect ratio could be higher than 10; most wingtips are pointed with fewer slots in appearance unlike the other two wings.

1.1.1.1.2Bird Flight Types

Kerlinger (1995) showed that behaviors of bird flight could be categorized according to their power source, which includes powered flight and unpowered flight. This classification is also considered in Table 1.1 in order to have a better idea of how birds maneuver their wings in terms of wing form.

For powered flight, birds may continuously flap their wings to stay airborne, or flap their wings in short bursts, then either extend their wings out to glide or fold their wings to speed up, and then flap their wings again. They repeat the similar maneuver until getting tired. In biology, the flap-gliding flight was regarded as undulating flight and the flap-folding flight was regarded as bounding flight. While implementing the powered flight, birds can adjust their overall flight level, such as descending, ascending, or staying in the same flight level. For unpowered flight, birds need to extend their wings out and then take advantage of either air currents to soar or earth gravity to glide. As birds ride on updrafts, they circulate upward; as birds glide from the mountain or tree top, they

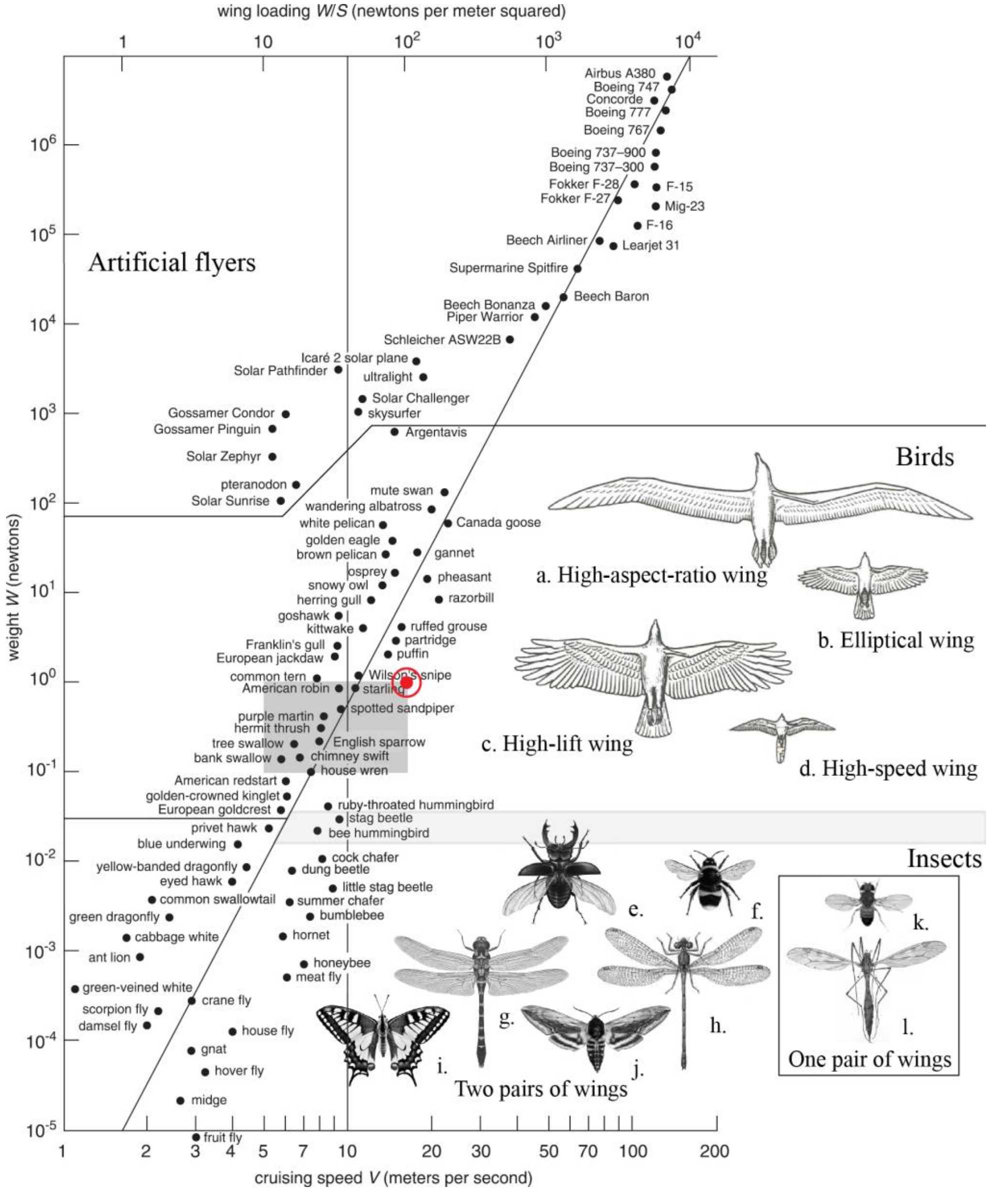

Figure 1.2 Great Flight Diagram adopted from Tennekes (2009) together with wing planform. *For birds, the representatives*[*] *are (a) albatross, (b) crow, (c) eagle, (d) falcon For insects, the representatives are (e) stage beetle*[†]*, (f) bumble bee*[‡]*, (g) dragonfly*[§]*, (h) damselfly*[**]*, (i) swallowtail butterfly*[††]*, (j) privet hawk*[‡‡]*, (k) fruit fly*[§§]*, (l) crane fly*[§]*. All images were processed using Photoshop and presented in black and white.*

descend gently toward the surface. In fact, birds applied these types of flight with regard to conditions encountered, which are not limited to perching to prey/rest, taking-off from the ground, hovering for food. Among those flight behaviors, the unpowered flights are rational approaches to save energy, especially during migration reason.

---

[*] Feduccia (1996)

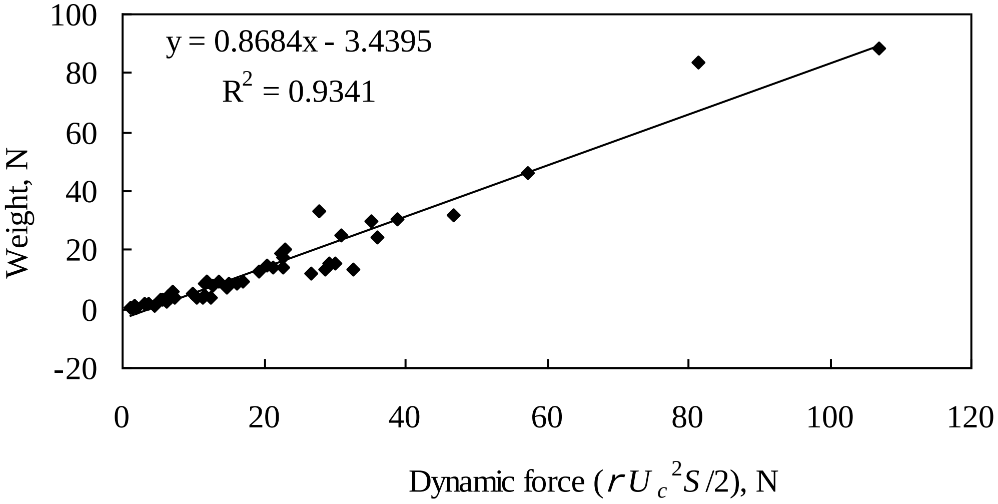

Figure 1.3 Bird weight as a function of dynamic force calibrated at sea level during cruising flight. *Data were collected from Pennycuick (1990, 1996, and 2001).*

1.1.1.1.3Birds Flight Performance

Pennycuick (1990, 1996, and 2001) tracked and reordered numerous free-flying birds in many years; he attempted to characterize bird migration behavior. Data reported in his articles included bird species, weight, wing span, wing area, air density, flight speed, and wing-beat frequency. The flight speed is the speed relative to the air, regarded as airspeed in the articles, and was obtained using ornithodolite technology (Pennycuick, 1983) and corrected to sea level condition by concepts of conservation of energy for effective comparison since different flight level was observed (Pennycuick, 2001). The wing-beat frequency was defined only within a period of continuous flapping without interruption, and determined from video recordings. We collected parts of his work and presented it in Figure 1.3 and Figure 1.4.

[†] Retrieved Aug. 4, 2013, from http://on-the-easel.blogspot.com/2011/09/wildlife-expo.html
[‡] Retrieved Aug. 4, 2013, from http://www.omlet.us/breeds/bees/bumblebee/
[§] Grimaldi and Engel (2005)
[**] Retrieved Aug. 5, 2013, from http://www.metafysica.nl/wings/wings_7.html
[††] Retrieved Aug. 4, 2013, from http://commons.wikimedia.org/wiki/File:Papilio_machaon_01_04102009.jpg
[‡‡] Retrieved Aug. 4, 2013, from http://en.wikipedia.org/wiki/Sphinx_ligustri
[§§] Retrieved Aug. 4, 2013, from http://www.news.wisc.edu/newsphotos/fruitfly.html

In Figure 1.3, bird weight was obtained from body mass multiplied by gravitational acceleration 9.81 m/s^2; dynamic force was evaluated from air density (ρ),

Table 1.1 A summary for bird wing.

Wing Type[1]	Features	Type of Flight[2]	Bird Species
Elliptical wing	• Low aspect ratio (4-5) • Pronounced camber • Wing tip slotted	Bounding, undulating	**Charadriiformes** (e.g., woodcocks), **Passeriformes** (e.g., crows, tits, sparrows, finches, wrens, dippers, thrush, starlings, warbles, jackdaw, American robin, American redstarts, kinglets, golden crests), **Piciformes** (e.g., woodpeckers, magpie), **Columbidae** (e.g., doves, pigeons), **Galliformes** (e.g., turkey, grouse, chicken, quail, ptarmigan, partridge, pheasant)
High-lift wing (or slotted soaring wing)	• Moderate aspect ratio (e.g., 5-7) • Pronounced camber • Wing tip slotted	undulating, gliding, soaring,	**Falconiformes** (e.g., buteos), **Accipitriformes** (e.g., eagles, vultures, ospreys, harriers, hawks), **Srigiformes** (e.g., owls), **Ciconiiformes** (e.g., storks)
High-speed wing	• Moderately high aspect ratio (e.g., 7-9) • Lower camber • Typically no tip slots • Tapering to elliptical tip • Leading edge Sweepback	continuous flapping, partially powered glide, gliding	**Charadriiformes** (e.g., sandpipers, plovers) **Passeriformes** (e.g., swallows, purple martins), **Falconiformes** (e.g., falcons-slotted), **Apodiformes** (e.g., swifts, humming birds)
			Charadriiformes (e.g., terns, jaegers), **Anseriformes** (e.g., ducks)
High-aspect-ratio wing	• High aspect ratio (e.g., 8-10) • Typically no tip slot	continuous flapping, partially powered glide, gliding	**Charadriiformes** (e.g., gulls, kittiwakes, puffins, razorbills), **Anseriformes** (e.g., geese-slotted, swan), **Procellariiformes** (e.g., albatrosses, shearwaters, petrels), **Phaethontiformes** (e.g., tropicbirds), **Suliformes** (e.g., gannets), **Pelecaniformes** (e.g., pelicans-slotted)

[1]Savile (1957); [2]Kerlinger (1995)

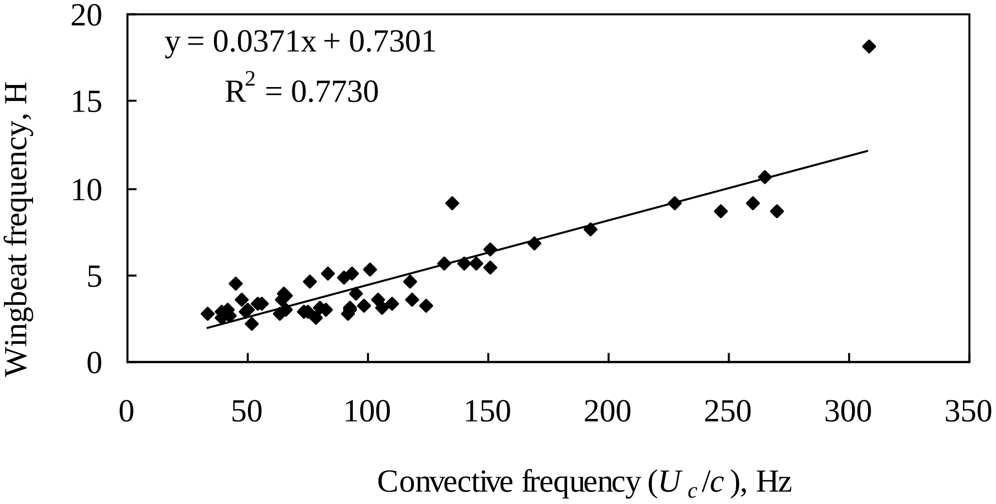

Figure 1.4 Bird wing-beat frequency as a function of convective frequency during cruising flight. *Data were collected from Pennycuick (1990, 1996, and 2001).*

flight speed (*U*), and wing area (*S*). According to force equilibrium, lift force is equal to body weight. Therefore, the slope of trend line in the figure gives lift coefficient and is equal to 0.868, which corresponds to angle of attack 7.9° assuming two-dimensional steady potential flow. This angle is higher than the one found by Tennekes (2009).

Figure 1.4 shows wing-beat frequency as a function of convective time; the reciprocal of convective time is defined as convective frequency hereafter. Considering the flight is featured by plunge motion, Strouhal number (*St*) would be a better parameter to describe the dynamic system (Shyy et al., 2008). The definition of the Strouhal number is given in Equation (1.1).

$$St = \frac{2h_a f}{U_\infty} = \frac{2h_a f}{c}\frac{c}{U_\infty} = \frac{t_c}{t_p} \tag{1.1}$$

where *f* is wing-beat frequency, h_a is plunge amplitude, *c* is mean chord length, and *U* is flight speed. Taylor et al. (2003) and Triantafyllou et al. (2000) revealed that Strouhal number often within the interval $0.2 < St < 0.4$ for efficient cruising in nature; on the other hand, the time required for a cyclic flapping motion (t_p) is within the interval of $2.5t_c < t_p < 5t_c$. As shown in Figure 1.4, the slope gives non-dimensionless wing-beat

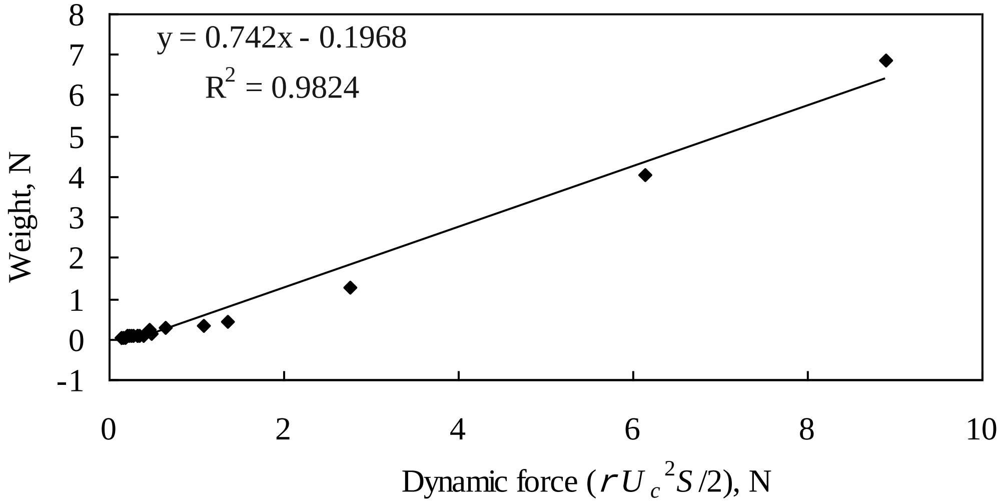

Figure 1.5 Bat weight as a function of dynamic force calibrated at sea level. *Data were collected from Bullen and Mckenzie (2002).*

frequency $fc/U_\infty = 0.0371$; Hence, the plunge amplitude normalized with chord length is suggested within the interval of $2.69 < h_a/c <. 5.39$.

1.1.1.2 Bats

Bullen and Mckenzie (2002) studied several bat species in tropical and temperate regions of Western Australia in free flight. They employed hand-held K-band radar to measure flight speed and video camera to determine wing-beat frequency. The flight speed we adapted from their work was called mode speed, which is the most probable measured speed. Since air density was not provided, we assume standard atmospheric conditions are applicable for all their data and comparable to bird data stated in preceding section. Data reported include bat species, weight, wing area, and wing span; however, their wing span was not determined from a horizontal distance from one wing tip to another but along the center of the wing through the body (Bullen and McKenzie, 2001). Since no other typical wing span was found in the literature for the bat species considered, we keep the reported data, which gives longer typical wing span and results in smaller mean chord estimates. In addition, only flying bats in open field are presented here.

Figure 1.5 and Figure 1.6 show bat weight as a function of dynamic force and wing-beat frequency as a function of convective frequency, similar to Figure 1.3 and Figure 1.4 for birds, respectively. Lift coefficient, a slope of straight line in Figure 1.5, is

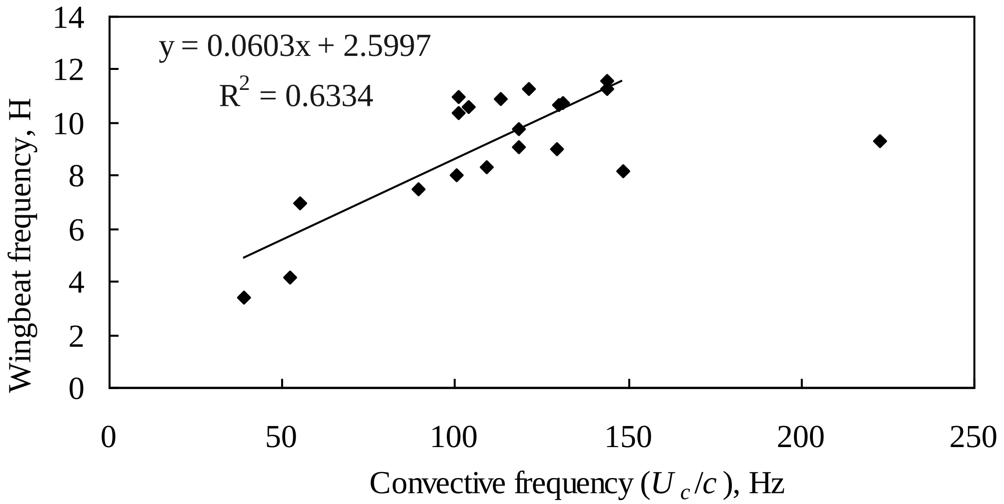

Figure 1.6 Bat wing-beat frequency as a function of convective frequency. *Data were collected from Bullen and Mckenzie (2002)*

0.74 with high coefficient of determination of 0.98. For most bat species in forward flight, the wing-beat frequency normalized with convective frequency gives $fc/U_\infty = 0.0603$, which is larger than bird flight in cruising/migration. The non-dimensional plunge amplitude (h_a/c) is suggested to be within the interval of $1.66 < h_a/c < 3.32$.

1.1.1.3 Insects

1.1.1.3.1Insects Wing Types

According to insect morphology (Dudley, 2000; Grimaldi and Engel, 2005), flying insects have one of two types of wings: one-paired wings and two-paired wings, as shown in Table 1.2. Insects with a pair of wings and a pair of halteres are categorized as one-paired wings. In general, one-paired wings are constructed by membranes and supported by branches of veins from body to wing tip. The halteres are like clubs and evolved from their old fore- or hind-wings, which are used to stabilize the insects in hover and control body rotation, just like a gyroscope (Zufferey, 2008). Insects with two-paired wings have more diverse wing morphology, which includes scale wings (e.g., butterflies), membranous wings (e.g., dragonflies), hard/leathery wings (e.g., beetles), or fringed wings (e.g., thrips). Examples of these wing forms are illustrated in Figure 1.2.

1.1.1.3.2Insect Flight Types

Similar to bird flight, there are two categories of insect flight: powered and unpowered flight, even though insect wings are more diverse in appearance and arrangement than birds, as shown in Figure 1.2. The powered flight is commonly performed by insects for either forward flight or hovering; nevertheless, both undulating and bounding flights observed for birds are not found for insects. Hovering flight is of most interest to engineering due to its singular behavior. Ellington (1984a) suggested the position of the stroke plane could be used to classify hovering flight, which includes horizontal, inclined, and vertical. The stroke plane is the plane where gives a reference of entire wing stroke and contains a pivot/hinge. During migration season, unpowered flights, such as soaring and gliding, are considerably adapted by some insects, like butterflies (Danthanarayana, 1986).

Another classification of insect flight was suggested by Grodnitsky (1999) according to wing function, which can be accompanied by wing types defined previously, as shown in Table 1.2. For insects with one-paired wings, active aerial flight is achieved by flapping a pair of forewings or hindwings since the other paired wings have been reduced to halteres. This type of flight can be found mostly for insects in the order of Diptera, whose are usually smaller than insects with two-paired wings. For insects with two-paired wings, there are four types of wing function depending on wing movement between forewings and hindwings; a short description is given as follows. (i) Coupled wings: insects operate both forewings and hindwings together as single wings. (ii) Uncoupled wings: insects keep one pair of wings open and maneuver the other pair of wings. (iii) In-phase stroke wings: insects produce a phase shift between forewing and hindwing during an entire stroke cycle; the shifted phase is short compared to entire stroke cycle. (iv) Anti-phase wings: insects perform their forewing and hindwing in a phase approximately a half of entire stroke; they are also capable of in-phase flight. The representative of each wing function is also provided in Table 1.2; apparently, two paired wings can be operated in very diverse manners.

Table 1.2 A summary for insect wing.

Wing Type	Features	Type of Flight[1]	Insect Species
One paired wing	Membranous (forewings with hind halteres)	Forewings flapping	**Diptera[1]** (e.g., midges, fruit fly, hoverflies, house fly, crane fly, meat fly, gnats, mosquitoes),
	Membranous (hind-wing s with fore halteres)	Hind-wings flapping	**Strepsiptera[1]**
Two paired wings	Scale wings	Coupled wings,	**Lepidotera** (e.g., most of Papilionidae[1])
		Uncoupled forewing flapping	**Lepidotera** (e.g., Papilionidae[1]: common birdwing, Parides neophilus, Papilio)
		In-phase forewing leading	**Lepidotera** (e.g., Micropterigoidea[1], Eriocraniidae[1])
	membranous wings	Coupled,	**Hymenoptera**[1] (e.g., wasps, bumblebees), **Hemiptera** (e.g., cimicids[1]), **Trichoptera** (e.g., Phryganeidae[1])
		In-phase forewing leading	**Neuroptera** (e.g., lacewing[1]), **Mecoptera** (e.g., scorpion flies[1]), **Plecoptera** (e.g., Perlidae[1], stoneflies[1]), **Trichoptera** (e.g., Rhyacophilidae[1])
		In-phase hind-wing leading	**Odonata** (e.g., Libellulidae[1], damselflies)
		Anti-phase wings	**Odonata** (e.g., Calopteryx Splendens[2]**)**
	Hard/leathery fore wings and membranous hind wings	Uncoupled hind-wing flapping,	**Dictyoptera** (e.g., cockroaches[1], mantis[1]), **Coleoptera** (e.g., tiger beetle[1]),
		In-phase hind-wing leading	**Orthoptera** (e.g., cricket[1], grasshopper[1]), **Mantodea** (e.g., mantis[1]), **Blattodea** (e.g., cockroach[1])
	Membranous fore wings and smaller/missing hind wings		**Ephemeroptera** (e.g., mayflies),
	All are fringed wings		**Thysanoptera** (e.g., thrips)

[1]Grodnitsky (1999); [2]Ruppell (1989)

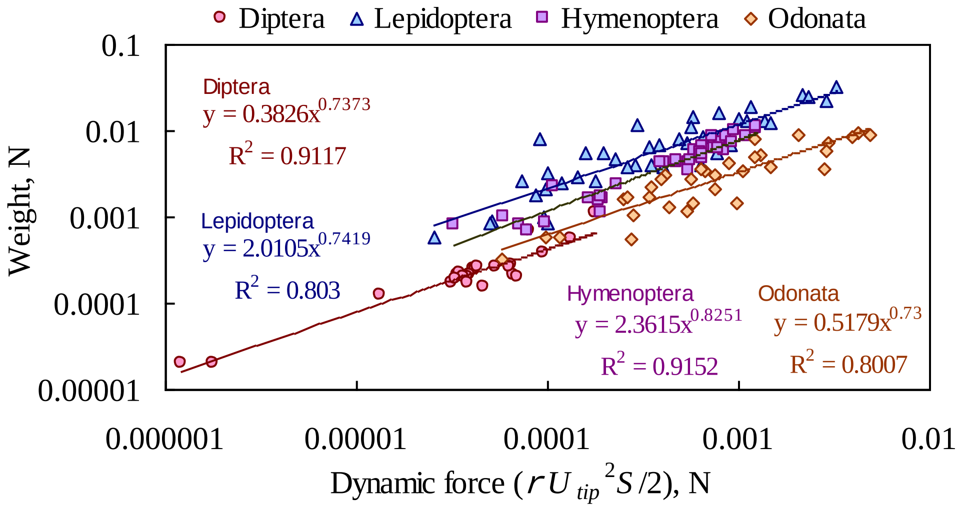

Figure 1.7 Insect weight as a function of dynamic force based on wing-beat frequency.

1.1.1.3.3Insect Flight Performance

There are numerous insects in nature, presented here are a few due to the limited information available in the literature. Data for the order of Diptera were collected from Wois-Fogh (1972 and 1973) and Vogel (1966), the order of Lepidoptera were from Bartholomew and Casey (1978), and Casey (1980 and 1981), the order of Hymenoptera were from Casey et al. (1985), and the order of Odonata were from May (1981) and Ruppell (1989).

Since hovering flight is critical and insect flight velocities were hardly detected, here we would like to focus on hovering behavior without considering the following effects: stroke angle/amplitude, stroke plane, body angle, wing trajectory, phase shift, thoracic temperature and metabolic rate. The data collected here include wing-beat frequency, body weight, wing area, and wing span, and are presented as body weight as a function of normalized force based on wing-beat frequency, shown in Figure 1.7.

The air density was obtained from ideal gas law based on mean ambient temperature given or averaged local temperature. The characteristic velocity U_{tip} is wing-beat frequency multiplied by wing length; the wing length is a distance of a single wing from the root to the tip. The weights were obtained by multipling body mass by 9.81 m/s^2.

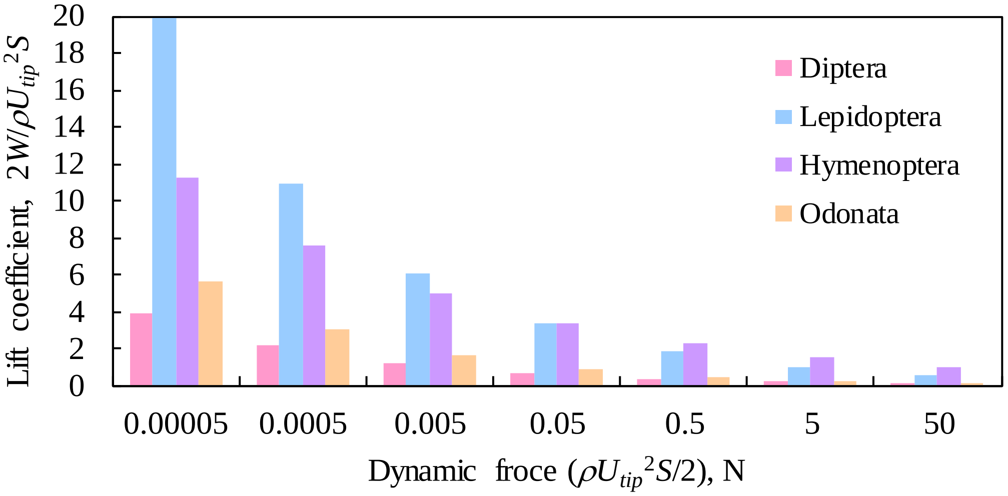

Figure 1.8 Insect lift coefficient estimation as a function of dynamic force based on wing-beat frequency.

Most wing areas were measured manually from wing outline in natural flight position on paper using planimeter or ruler, or counting square enclosed on grid paper; overlapping coupled wings was necessary for two-paired wing insects to keep natural flight position. Exclusion is the work of Ruppell (1989) who employed a digital geometric analysis computer to determine wing area.

Most of the wing-beat frequencies were determined using an oscillograph but Vogel (1966) used stroboscope and Ruppell (1989) used filming. Insects under consideration were in conditions of steady free flight. Most data were obtained while insects were flying in a confined space, whereas Ruppell (1989) and Wois Fogh (1973) obtained data from open field. In addition, the measurement of hovering insects may be coupled with slow forward flight, which may tamper with our intention.

Figure 1.7 is a log-log plot and shows dynamic pressure increases exponentially as insect weight increases. The orders of Diptera, Lepidoptera, and Odonata have similar trend-line slopes; a higher slope is given by the order of Hymenoptera. The slope of the trend line gives a coefficient analogous to typical lift coefficient. If we estimate $2W/\rho U_{tip}^2S$ over every tenfold increase of dynamic force under consideration of supporting insect weight by flapping frequency, we obtain Figure 1.8 showing that coefficient $2W/\rho U_{tip}^2S$ decreases exponentially with wing-beat frequency using the same

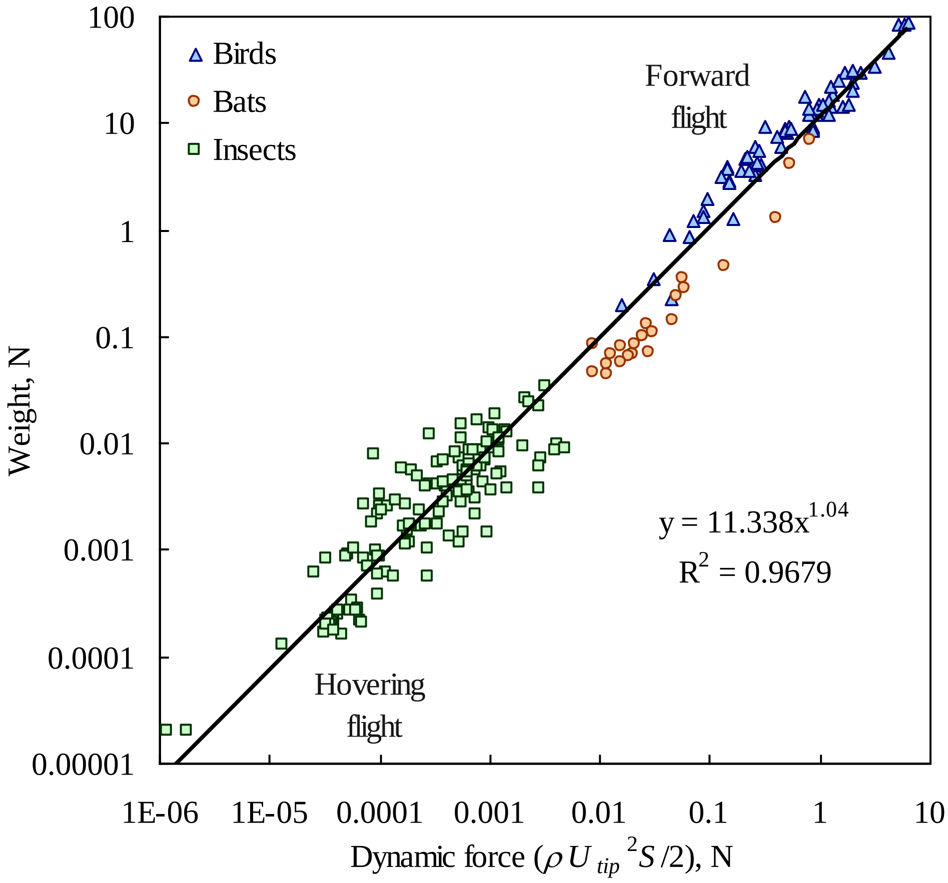

Figure 1.9 Characteristics of natural flyer in terms of weight as a function of dynamic force based on wing-beat frequency in steady flight.

wing at same level flight. If we consider the normalized force as an input and the body weight is an outcome, the coefficient $2W/\rho U_{tip}^2 S$ can be regarded as flight efficiency, especially for hovering flight in current consideration. For insects at a given body weight, two-paired wings is more efficienct than one-paired wings. Insects in the order of Lepidoptera and Hymenoptera beat their wings more efficiently than insects in the order of Odonata and Diptera.

Considering wing-beat frequency from birds and bats in steady flight together with insects in steady hover, a simple relation is observed among natural fliers in terms of body weight and wing-beat frequency normalized with air density and wing area, as shown as a trend line in Figure 1.9. The heavier the flyers the more wing-beat frequency is needed using the same wing at same level flight. This relation grows exponentially and is independent of wing form and structure. Surprisingly, Figure 1.9 also reveals the wing-beat behavior is independent of flight types since data for birds and bats were in cruising flight and insects were in hover. The way that natural flyer stay airborne should depend on other factors, for example, wing kinematics.

1.1.2 Wing Kinematics

Wing kinematics used to study unsteady aerodynamics of flapping wings includes (i) pure pitch motion, (ii) pure plunge motion (either linear or angular), (iii) combination of pitch and plunge motion, (iv) combination of plunge and elevation motion, and (v) combination of pitch, plunge, and elevation motion. The first two are one-degree-of-freedom motions; the next two are two-degree-of-freedom motions and the last is three-degree-of-freedom motion. The pitch motion changes geometric angle of attack; however, the plunge motion does not alter the geometric angle of attack. The stroke plane is formed while the plunge motion gets involved and can contain either angular strokes (i.e., sweep angle larger than 0°) or rectilinear strokes (i.e., zero sweep angle). The elevation motion is the motion deviated from the stroke plane; it could be angular or rectilinear. These motions could be implemented periodically or non-periodically; the periodic motion was mostly conducted to mimic flapping behaviors of natural flyers. The wing kinematics implemented to study flight status is briefly reviewed in the following, which is not limited to forward/cruising flight, hovering flight, and perching flight.

Hereafter, sectional wings are referred to wall-to-wall wing configuration in experiments and two-dimensional wings in modeling; finite-aspect-ratio wings are referred to the wings with free wingtips (at least one chord away from wall) in experiments and three-dimensional wings in modeling.

1.1.2.1 Forward/Cruising Flight

Platzer et al. (2008) reviewed the progress of flapping-wing aerodynamics and determined that thrust performance is the main feature in forward flight. The wing kinematics employed is shown in Equation (1.2), which is a one-degree-of-freedom pure plunging motion with rectilinear strokes.

$$\bar{h}\left(\bar{t}\right)=\bar{h}_a\sin\left(\bar{k}\bar{t}\right) \tag{1.2}$$

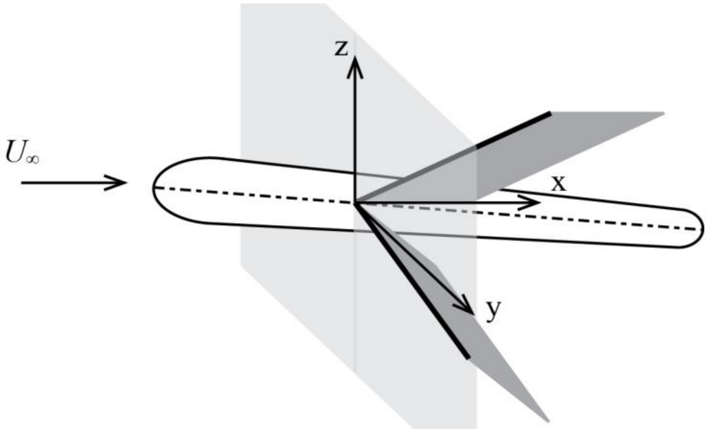

Figure 1.10 Wing kinematic coordinates.

where $\bar{h}$ is non-dimensional stroke amplitude h/c, $\bar{k}$ is twice of reduced frequency $\bar{k} = 2k = 2\pi fc/U_\infty$, $\bar{h}_a$ is non-dimensional plunge amplitude $\bar{h}_a = h_a/c$, and $\bar{t}$ is non-dimensional time tU_∞/c.

The product $\bar{k}\,\bar{h}$ was used to determine the transition from drag-producing Kármán vortex street on stationary wing to thrust-producing reverse Kármán vortex street on oscillatory wing under attached flow conditions; they are shedding of trailing edge vortices into the wake. Young and Lai (2004) showed this transition was very sensitive at chord Reynolds number within an order of 10^4 for a $\bar{k}\,\bar{h}$ value of 0.1. The product $\bar{k}\,\bar{h}$ was also used to find induced angle of attack due to plunge motion using $\alpha_i = \arctan(\bar{k}\,\bar{h})$; efficient propulsion was found approximately at $\bar{k}\,\bar{h} = 0.4$ for chord Reynolds numbers 10,000 to 30,000, which corresponds to maximum induced angle of attack of about 22° (Platzer et al., 2008). Tuncer et al. (1998) computed $\bar{k}\,\bar{h} = 0.35$ gave efficient propulsion at chord Reynolds numbers of 10^6, corresponding to 19° induced angle of attack.

Considering the product $\bar{k}\,\bar{h}$ in terms of plunge time (t_p) and convective time (t_c), as shown in Equation (1.3). A $\bar{k}\,\bar{h}$ value of 0.4 for efficient propulsion gives plunge time (t_p) equal to approximately 9 convective times. As $\bar{k}\,\bar{h}$ increases to 1.5, a shorter plunge time is obtained $t_p = 2t_c$, where vortex shedding was computed not only from the trailing edge but also from the leading edge (Platzer et al., 2008). All aforementioned results were based on two-dimensional NACA 0012 airfoil.

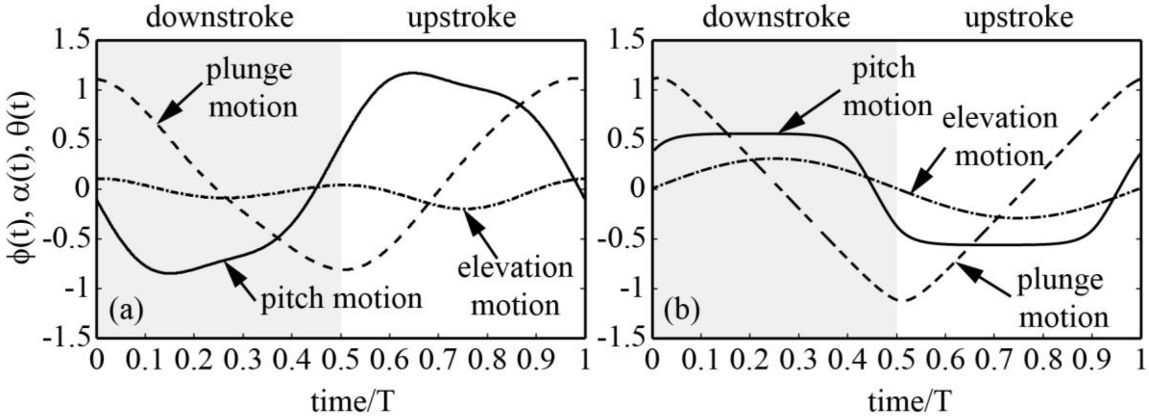

Figure 1.11 Three-degree-of-freedom wing kinematics for hovering flight in representative of (a) hawk-moth (Shyy et al., 2008) and (b) fruit fly (Sane and Dickinson, 2001)

$$\bar{h}\ \bar{k} = \pi\left(2h_a f / c\right)\left(c / U_\infty\right) = \pi\left(t_c / t_p\right) \tag{1.3}$$

1.1.2.2 Hovering Flight

Shyy et al. (2008) investigated the aerodynamics of flyers in low Reynolds number. For three-degree-of-freedom wing motion in hover, where there is no free-stream velocity, wing kinematics was defined in terms of angle change in time with respect to Cartesian coordinates, typically used for aircraft with fixed wing as shown in Figure 1.10. Considering the stroke plane was the y-z plane, the wing motion includes (i) positional angle $\phi(t)$ about roll axis (i.e., x-axis), regarded as sweep angle by Ellington (1984b); it corresponds to plunge motion in angular form, (ii) feathering angle $\alpha(t)$ about pitch axis (i.e., y-axis), also recognized as angle of attack; it corresponds to pitch motion, and (iii) elevation angle $\theta(t)$ about yaw axis (z-axis). The motion for plunge $\phi(t)$, pitch $\alpha(t)$, and elevation $\theta(t)$ were suggested in Equations (1.4)-(1.6), respectively (Liu et al., 1998; Aono and Liu, 2006; Anon et al, 2008; Aono et al., 2009).

$$\phi(t) = \sum_{n=0}^{3}\left[\phi_{cn}\cos\left(2n\pi ft\right) + \phi_{sn}\sin\left(2n\pi ft\right)\right] \tag{1.4}$$

$$\alpha(t) = \sum_{n=0}^{3}\left[\alpha_{cn}\cos\left(2n\pi ft\right) + \alpha_{sn}\sin\left(2n\pi ft\right)\right] \tag{1.5}$$

$$\theta(t) = \sum_{n=0}^{3}\left[\theta_{cn}\cos\left(2n\pi ft\right) + \theta_{sn}\sin\left(2n\pi ft\right)\right] \tag{1.6}$$

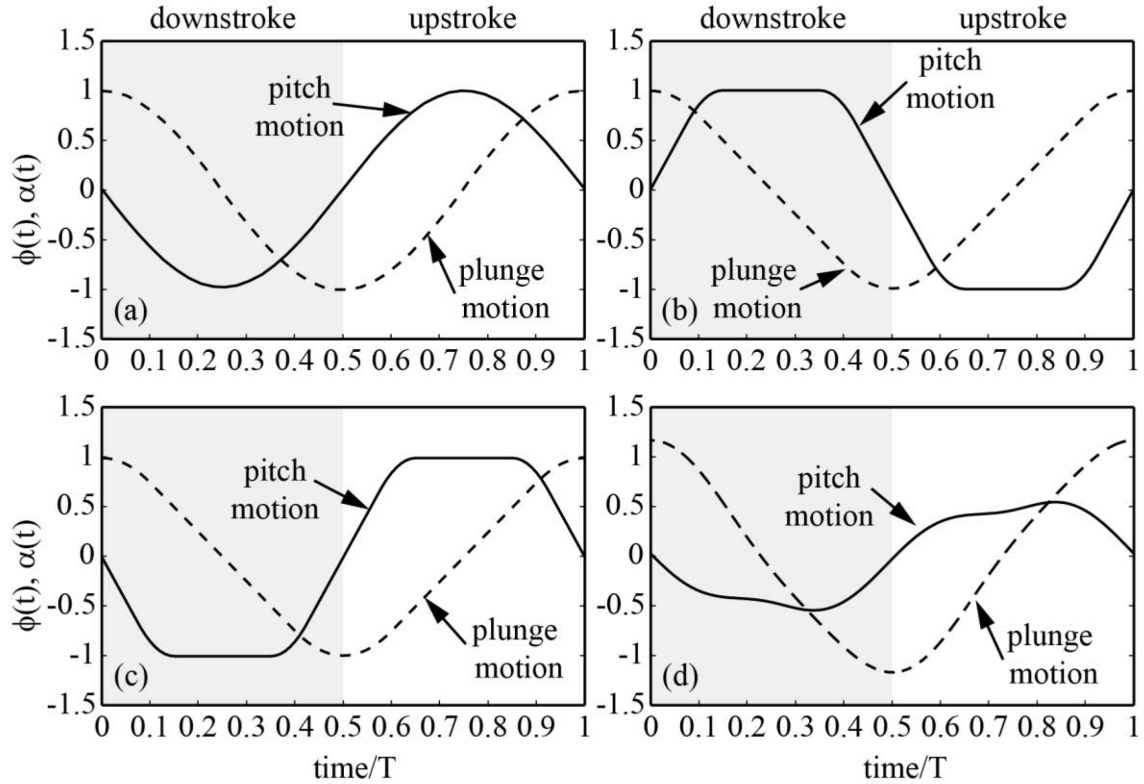

Figure 1.12 Two-degree-of-freedom wing kinematics for hovering flight in study of (a) ventral fins of fish (Freymuth, 1990), (b) fruit fly (Dickinson et al., 1999), (c) bumble bees (Nagai et al., 2009), and (d) hawk-moth (Vandenheede et al., 2012).

where ϕ_{cn}, ϕ_{sn}, α_{cn}, α_{sn}, θ_{cn}, and θ_{sn} were determined by fitting empirical data of moth species *Manduca sexta* in free flight from Willmott and Ellington (1997); the kinematics is shown in Figure 1.11(a). Similar approach was adapted by Fry et al. (2005) to study fruit fly *Drosophila melanogaster* in tethered and free flight. The kinematics shown in Figure 1.11(b) were used by Sane and Dickinson (2001) to study fruit fly species *Drosophila melanogaster*, which were approximate patterns for most of insects (Ellington, 1984c; Zanker, 1990).

For two-degree-of-freedom motion in hover, the formula most employed are represented in Equation (1.7) and (1.8) for plunge motion and pitch motion using sectional wings (Freymuth, 1990; Tuncer et al., 1998; Sunada et al., 2001; Tang et al., 2008; Ol et al., 2009; Baik et al., 2012; Rival and Tropea, 2010) and finite-aspect-ratio wings (Wang et al., 2004; Young and Lai, 2007; Trizila et al., 2011).

$$h^*(t^*) = h_a{}^* \sin\left(k^* t^* + \varphi\right) \tag{1.7}$$

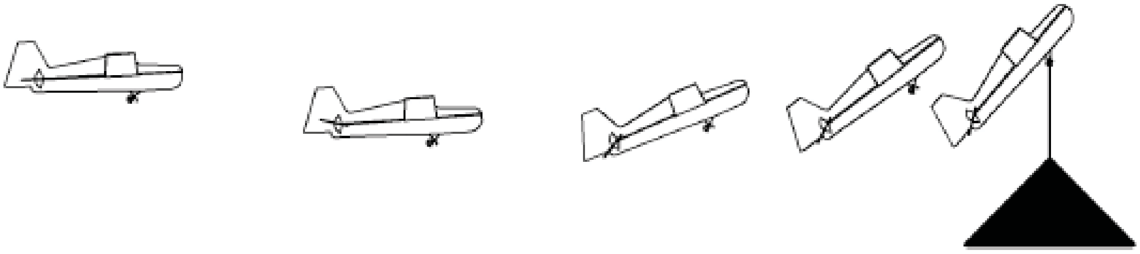

Figure 1.13 Visualization of a successful perching maneuver by Cory and Tedrake (2008).

$$\alpha(t) = \alpha_0 + \alpha_a \sin(k^* t^*) \tag{1.8}$$

where φ is phase difference between plunge and pitch motion, α_0 is initial angle of attack, and α_a is pitch amplitude; other notations are the same as Equation (1.2). An example of this wing kinematics is shown in Figure 1.12(a), which is "water threading mode" to resemble the action of the ventral fins of fishes; the parameters α_a and φ are 0° and 90°, respectively. As parameters α_a is adjusted to 90 and φ is shifted to -90, the wing kinematics is regarded as" normal hovering mode" for humming birds in hover. (Freymuth, 1990)

Figure 1.12(b)-(c) show wing kinematics employed to characterize delayed stall, rotational effects, and wake capture. Figure 1.12(b) displays patterns based on fruit fly and were introduced by Dickinson et al. (1999) to study *Drosophila* wing, and were employed by Gopalakrishnan and Tafti (2009) to study a finitely thin rectangular wing; three pitching phases in terms of plunge motion were categorized into advanced, symmetric, and delayed modes. Figure 1.12(c) shows the pitch motion has 180-degree phase difference with one in Figure 1.12(b); it was employed by Sane and Dickinson (2002) to study *Drosophila* wing and Nagai et al. (2009) to study bumblebee wings. Figure 1.12(d) was derived from hawk-moth kinematics by Vandenheeds et al. (2012), as shown in Figure 1.11(a); the Zimmerman wing was employed in their study.

1.1.2.3 Perching Flight

Another natural flight maneuver is perching, often observed when birds approach to nest or prey. Their body and wings are rotated to a high angle of attack, maybe up to 90 degrees, while their flight speed is descending to near stationary. Reich et al. (2009)

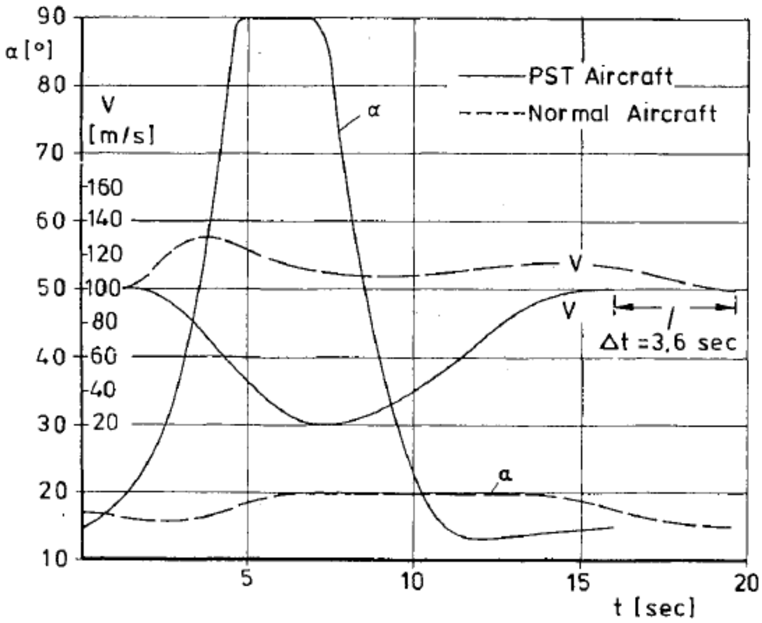

Figure 1.14 An illustration of the dynamic character for typical post stall maneuver. Adopted from Herbst (1980).

gave a definition of perching as landing with approximately zero vertical and horizontal velocity on a specific point, for designing Micro Aerial Vehicle (MAV) landing maneuver. Some valuable information of perching landing using fixed-wing glider was given in Cory and Tedrake (2008), the perching maneuver was illustrated in Figure 1.13.

The transition from attached flow to massive separation flow is the main feature of perching maneuver and remains to be fully understood. Ol et al. (2009) abstracted the perching maneuver as a classical pitch-up motion to investigate the relation between motion time history and aerodynamics, which is relevant to the interest of this study. The perching motion or pitch-up motion was also considered as an important motion to produce rotational force while using higher degree-of-freedom motions (Dickinson, 1994; Dickinson et al., 1999; Sane and Dickinson, 2002; Kim et al, 2005; Gopalakrishnan and Tafti, 2009).

1.2 REVIEW OF PITCHING WING AERODYNAMICS

Maneuverability for manned aerial vehicles required the ability to turn, to climb, and to accelerate (Herbst, 1973). The key of a successful maneuver was the capibility to sustain lift at an angle-of-attack typically higher than static-stall angle during turning and

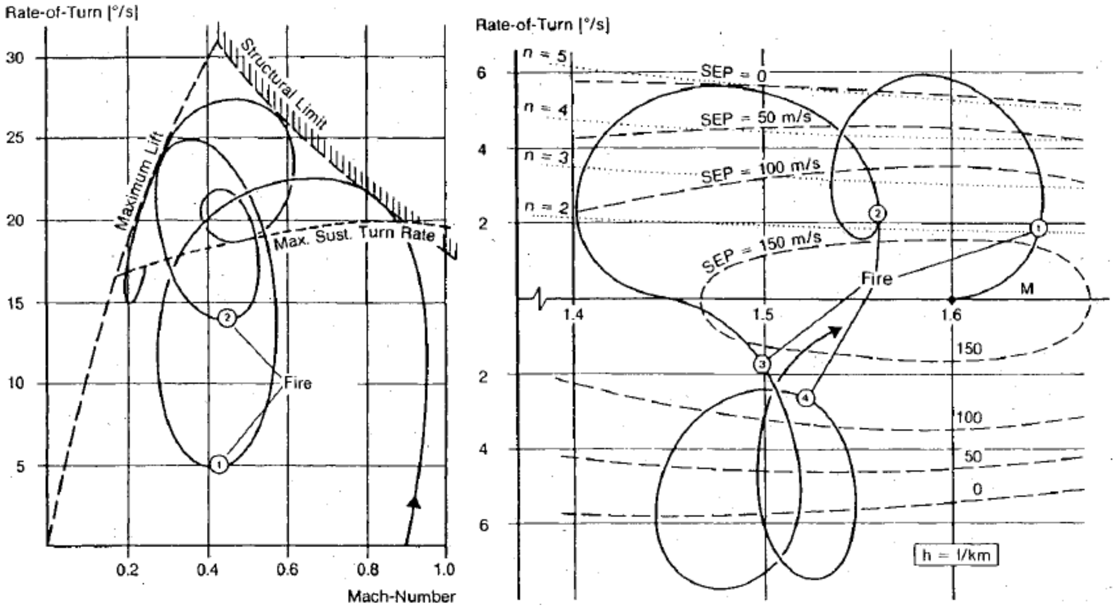

Figure 1.15 Time history maneuver conditions simulated for (left) short range combat and (right) medium range combat. SEP stands for Specific Excess Power; n denotes load factor in terms of g-level. Adopted from Herbst (1983)

was considered as post-stall (PST) maneuver (Herbst, 1980 and 1983). Herbst (1980) reported a characteristic motion of PST maneuver together with demanded airspeed (V), as shown in Figure 1.14, in comparison with normal aircraft. This dynamic character is a rapid pitch up to 90-deg, maintaining this condition for 2-3 s, followed by a fast return to normal flight. As reported the maneuvaring in 30- to 50-deg angle of attack arose most difficulties in flight and control.

Herbst (1983) simulated requirements of rate of turn in terms of flight speed for conditions of short-range combat and medium-range combat, as shown in Figure 1.15. The turn-of-rate for short-range combat in demand was significantly higher than one for medium-range combat; the maximum turn-of-rate was about 28 °/s at Mach number $M \approx 0.5$, which was limited by structure and maximum lift. Under these circumstances and considering the maximum turn-of-rate as pitch rate $\alpha_m{}'$, reduced pitch rate ($K = c\alpha_m{}'/2U_\infty$) for F-16 flighter (wing mean chord S/b = 9.146 ft)[***] is equal to 0.004 at

---

[***] F-16 flighter dimension: wing area, S = 300 ft^2 and wingspan b = 32.8 ft. Retrieved March 5, 2014, from http://www.lockheedmartin.com/us.

standard temperature and pressure (STP)[†††]. K was an important normalized parameter for separation flow due to pitching airfoils (Daley and Jumper, 1984) and is adapted to characterize the flow in present study.

Ol et al. (2010) summarized the discussion of the AIAA Fluid Dynamic Technical Committee (FDTC) Low Reynolds Number Discussion Group and introduced a similar pitch up-hold-return motion as a canonical wing kinematics in an attempt to understand unsteady problems intrigued from micro air vehicles (MAVs) maneuver and control design. This one-degree-of-freedom canonical kinematics give a constant pitch rate and is featured by maximum pitch angle $\alpha_m = 45°$, reduced pitch rate $K = \pi/16$, smoothing angle of 4.5°, and one convective time sustained at α_m.

MAVs are uninhabited air vehicles (UAVs); their sustainability at high turn-of-rate supposedly much higher than inhabited air vehicles. Fixed wing MAVs were designated to be operated within chord Reynolds number $10^4 < \mathrm{Re} < 10^5$ (Mueller, 1999) like birds and bats. Flapping wing MAVs like insects would have much smaller size and could be operated within even lower chord Reynolds number $\mathrm{Re} < 10^4$ (Ma et al., 2013). The potential wing kinematics shown by Wootton (2000) had a three-degree-of-freedom motion and exhibited pitching motion relevant to the canonical wing kinematics. During wing downstroke, the wing moves from near zero geometric angle of attack to a high geometric angle of attack and then returns to its initial position during upstroke. The progress of MAV development was reported by Pines and Bohorquez (2006); the design requirements in terms of weight, flight speed, and wing loading are highlighted in Figure 1.2. Reviews of flapping wing aerodynamics were given by Sane (2003), Platzer et al. (2008), and Shyy et al. (2010).

The intriguing problems associated with MAV flight in low Reynolds number regions include (i) circulatory vs. non-circulatory contributions to force, (ii) steady vs. unsteady flow model, (iii) two- vs. three-dimensional flow fields, (iv) vortex dynamics, (v) motion-history effects, (vi) separation effects, and (vii) laminar to turbulent transition. In this study, the complex flow problems are going to be studied using rigid wings and

---

[†††] Condition for standard temperature and pressure is dry air at temperature 20°C, pressure 101.325 kPa, density 1.205 kg/m^3, kinematic viscosity 15.127×10^{-6} m^2/s, and speed of sound 340.29 m/s.

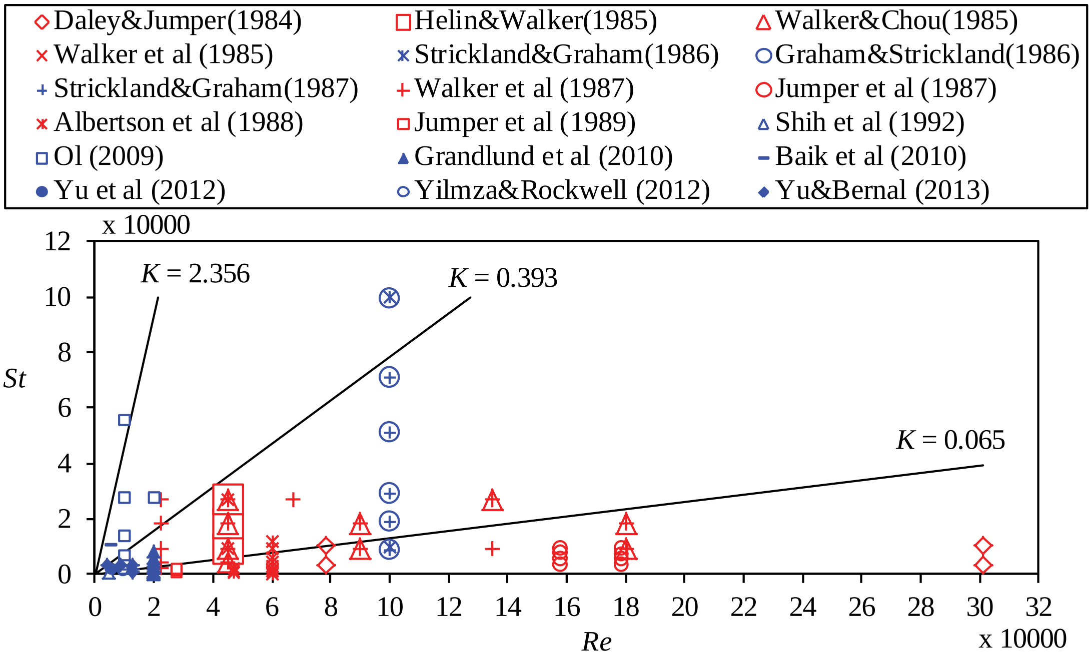

Figure 1.16 Summary of test cases considered in the literature in *Re*-*St* parameter space. *Red symbols represent experiments in wind tunnel, and blue symbols represent experiments in water channel.*

the canonical wing kinematics, which is pitch up-hold-return wing kinematics. The canonical wing kinematics is considered as a non-oscillatory motion for constant pitch rate. The studies of the sinusoidal oscillatory motion for non-constant pitch rate involved research subjects in 1970s and were typified by the works of McCroskey and Philippe (1975), McAlister and Carr (1979), McCroskey (1982), and Currier and Fung (1992).

Experimental works using constant pitch rate motion are reviewed below. The approaches and test conditions considered are summarized in Table 1.3; most works were conducted for NACA0015 airfoil in the 1980s- and 1990s. These test cases are displayed in a parameter space of Reynolds number (*Re*) and Stokes number (*St*), as shown in Figure 1.16; most test cases had reduced pitch rates *K* less than 0.39 and were conducted in wind tunnel within a Reynolds number range of 2×10^4 < Re < 3×10^5. Surprisingly, aerodynamic force data obtained from surface pressure did not reveal non-circulatory effects, in contrast with direct force measurement.

1.2.1 Quarter-Chord Separation

Daley and Jumper (1984) revealed an approach to quantify dynamic separation. They instrumented four pressure transducers at upper surface of NACA0015 airfoil pitching at mid-chord; the one at about quarter-chord was used as an indicator of occurrence of separation, where adverse pressure gradient in time ($dP/dt > 0$) was observed. The angle of quarter-chord separation was considered from a dynamic-separation angle and its difference from static-separation angle was favorable for normalizing angular rate with free-stream velocity, as shown in Equation (1.9). The normalized angular rate was valid over a range of Reynolds number from 15k to 300k, and is called reduced pitch rate in the present study. Moreover Jumper et al. (1987) pointed out that the dynamic stall was occurred at much higher angle of attack than the dynamic-separation angle using the same airfoil pitching at the same location.

1.2.2 Basic Flow Structure

The flow past a constant pitch-rate airfoil had several distinguishable features, including flow reversal, leading edge vortex or dynamic stall vortex, shear layer vortex, and starting vortex. The first three are structures on upper airfoil surface; the last one is structure in the wake.

The flow reversal occurred typically in a laminar separation bubble and indicated a propagation of laminar boundary layer to turbulent boundary layer (Leishman, 2006). McAlister and Carr (1979) evidenced that the flow reversal was uncoupled with flow separation for unsteady flow over oscillating airfoil and usually moved toward the leading edge from the trailing edge. For constant pitching airfoil, Shih et al. (1992) identified the similar flow reversal at trailing edge and expanded toward the leading edge. They also noted that the flow reversal does not imply a significant departure of the boundary layer on the rear portion of the airfoil due to finite Reynolds number effects (Sears and Telioouis, 1975; Shen, 1978).

Table 1.3 A summary of experimental work and approaches using pitching wings.

Authors	Pivot axis	*K*	Wing type	$\alpha_{m,}$	Pressure transducer	Direct force	Near surface velocity	Flow visualization	PIV
Daley & Jumper (1984)[3]	*c*/2	0.0057-0.0651	NACA 0015*		V			Smoke	
Helin & Walker (1985)[3]	*c*/4, *c*/2, 3*c*/4	0.1,0.2,0.3	NACA 0015*	60°			Hot film	Smoke wire	
Walker et al. (1985a)[3]	*c*/4	0.1, 0.3	NACA 0015*	60°			Hot wire	Smoke wire	
Walker et al. (1985b)[3]	*c*/4	0.025-0.3	NACA 0015*	60°	V				
Strickland & Graham (1986a-b,1987)[2]	*c*/4	0.088-0.99	NACA 0015*	90°	V			Bubble wire	
Walker&Chou (1987)[3]	*c*/4	0.025-0.6	NACA 0015*	60°	V		Hot film	Smoke wire	
Jumper et al. (1987)[3]	*c*/2	0.005-0.023	NACA 0015*	50°	V				
Albertson et al. (1988)[3]	*c*/4, *c*/2, 3*c*/4	0.0025-0.1	NACA 0015*	60°	V			Tungsten wire	
Jumper et al. (1989)[3]	2*c*/25, *c*/4, *c*/2	0.0089-0.064	NACA 0015*	40°	V				
Acharya et al. (1992)[3]	c/4	0.018-0.39	NACA 0012	40°	V				
Shih et al. (1992)[2]	*c*/4	0.066	NACA 0012	30°					V
Ol (2009)[1]	*c*/4	0.1-2.8	Flat plate*†, SD7003*	20°, 40°				Dyes	
Grandlund et al. (2010)[1]		0.03	SD7003*	45°		V		Dyes	
	0, *c*/4, *c*/2, 3*c*/4	0.0025-0.2	Flat plate*	90°					
Yilmaz et al. (2010)[1]	0, *c*/4, *c*/2, 3*c*/4, c	0.1-0.35	Flat plate†	40°				Dyes	
Baik et al. (2010)[1]	*c*/4	0.2, 1	Flat plate*	90°				Dyes	V
Grandlund et al. (2011a-b)[1]	0, *c*/2, c	0.1-1	Flat plates†	90°		V		Dyes	
Yu et al. (2012)[1]	0	0.2	Flat plate*	33°, 45°, 57°		V			V
Yilmaz & Rockwell (2012)[1]	*c*/4	0.098	Flat plate†	45°					V
Yu & Bernal (2013)[1]	0, *c*/2, *c*	0, 0.022, 0.065, 0.13, 0.19, 0.39, ∞	Flat plate†	45°		V			V
Yu et al. (2013)[1]	0, *c*/2, *c*	0, 0.39	Flat plates†	45°		V		Dyes	
Granlund et al. (2013)[1]	0, c/4, c/2, 3c/4, c	0.01-0.5	Flat plate*	90°		V		Dyes	

c, chord length; [1]water channel/channel; [2]tow tank; [3]wind/smoke tunnel; *sectional wing; †finite-aspect-ratio wing.

The appearances of leading edge vortex (LEV) and shear layer vortex (SLV), as interpreted by Shih et al. (1992), were due to unsteady separation by means of local thickening of the boundary layer on the upper airfoil surface. The upper part of the boundary layer forms a free shear layer and rolls up into an individual vortex in a mechanism resembling Kelvin-Helmholtz instability. The lower part of the boundary layer was known as shear layer vortex (Visbal, 1989). The shear layer vortex seemed to disappear at high Reynolds numbers, leaving only leading edge vortex (Walker et al. 1985).

The starting vortex (SV) is a counterclockwise vortex that usually rolls up at trailing edge and sheds into the wake from the lower airfoil surface, where the flow is fully attached as the pitch motion begins (Visbal and Shang, 1988; Shih et al., 1992; Pullin, 1978). The starting vortex was considered to accelerate the downstream convection process along the upper surface and some accumulation occurs near the trailing edge (Shih et al., 1992). According to Kelvin’s circulation theorem (Anderson, 2011), for inviscid and incompressible flow, the circulation around the starting vortex is equal to the circulation around the airfoil.

1.2.3 Effect of Pitch Rate

Effect of pitch rate refers to a comparison among cases whose pitch rate is changed while holding Reynolds number constant, resulting in changing reduced pitch rate K. The reduced pitch rate increase as pitch rate is increased in a constant free-stream velocity.

Most studies of effect of pitch rate were conducted using a NACA0015 airfoil pitching at quarter-chord and can be found in the work of Helin and Walker (1985) who compared $K = 0.1$, 0.2, and 0.3 in $Re = 45$k, Walker et al. (1985a) who compared $K = 0.1$ and 0.3 in $Re = 45$k, Walk et al. (1985b) who compared $K = 0.005$, 0.1, 0.2, and 0.3 in $Re = 47.5$k, $K = 0.05$ and 0.1 in $Re = 95$k, and $K = 0.025$ and 0.05 in $Re = 190$k, Strickland and Graham (1986a, 1987) who compared $K = 0.088$-0.99 in $Re = 100$k, Walker and Chou (1987) who compared $K = 0.05$ and 0.1 in both $Re = 50$k and 100k, and Albertson et al. (1988) who compared $K = 0.075$, 0.05, and 0.015 in $Re = 60$k.

The works used NACA0015 airfoil pitching at mid-chord were given by Jumper et al. (1987) who compared K = 0.009, 0.015, 0.02, and 0.026 in Re = 180k, and K = 0.01, 0.018, 0.023, and 0.03 in Re = 160k. The work using flat plate was provided by Ol (2009) who showed flow visualization for K = 0.1 0.2, 0.35, 0.7, and 1.4 in Re = 10k at quarter-chord, by Granlund et al. (2010) who provided force history for K = 0.0025, 0.005, 0.01, 0.02, 0.03, 0.05, 0.075, 0.1, 0.125, 0.15, 0.2 in Re = 20k at quarter-chord and three-quarter-chord, and by Baik et al. (2010) who attempted to determine force history from PIV data for K = 0.2 and 1 in Re = 5k at quarter-chord.

From surface pressure data, the dependence of pitch rate was less pronounced at lower free-stream velocities; maximum lift was increased while increasing pitch rate. The change of maximum lift was less pronounced as Reynolds number was increasing (Walker et al., 1985b). The lift and drag coefficients could be correlated using simple trigonometric function to a function of angle of attack and pitch rate (Strickland and Graham, 1987). The dynamic stall phenomena were reproducible; dynamic lift-curve slope prior to separation was less than static lift-curve slope in agreement with theory (Jumper et al., 1987).

From flow visualization data, several features were disclosed. (i) The initiation of the dynamic stall vortex was delayed to higher angle of attack as the pitch rate was increased; more cohesive vortices appeared. However, the delay was not a linear function of the pitch rate (Helin and Walker, 1985). (ii) The stall delay angle at leading edge determined from images was proportional to the square root of the reduced pitch rate; the delay in the onset of dynamic stall was partially due to the effective angle of attack at airfoil leading edge that decreased with increasing pitch rate (Strickland and Graham, 1986a and 1987). (iii) As pitch rate increased, leading edge vortex became more compact and a pair of vortices was formed in the near wake (Ol, 2009).

From direct force data, the stall angle was delayed as pitch rate was increased. A range of reduced pitch rate $0.005 < K < 0.02$ was determined to be quasisteady due to constant slope consistent with theory; the reduced pitch rate $0.03 < K < 0.1$ was determined to be a rate-dependent range. At higher reduced pitch rate $K > 0.15$, noncirculatory lift was present (Granlund et al., 2010).

From near-surface velocity data, the slope of velocity profile with respect to angle of attack, at a position of 6.7% chord, was relatively independent of pitch rate; maximum velocities were increased as the pitch rate was increasing, which was 140 and 210 % of the free-stream velocity (Helin and Walker, 1985; Walker et al. 1985a).

1.2.4 Effect of Reynolds Number

Effect of Reynolds number refers to a comparison among cases whose free-stream velocity is changed while holding the Strokes number constant, also resulting in the change of reduced pitch rate *K*. The reduced pitch rate decreased as the free-stream velocity increased at a constant pitch rate. The effect was studied using by NACA0015 airfoil pitching at quarter-chord by Walk et al. (1985b) for $K = 0.025$, 0.05, and 0.1 at $St = 9.5\text{k}$, $K = 0.05$, 0.1, and 0.2 at $St = 19\text{k}$, and $K = 0.1$ and 0.3 at $St = 28.5\text{k}$, and by Walker and Chou (1987) for $K = 0.05$ and 0.1 at $St = 10\text{k}$ and 20k.

The effect of varying Reynolds number contrasted effects of varying pitch rate. Maximum lift was reduced when increasing Reynolds number and was inversely dependent on Reynolds number (Walker et al., 1985b).

1.2.5 Effect at Reduced Pitch Rate

Effect of reduced pitch rate refers to a comparison among cases whose reduced pitch rate remains the same whereas pitch rate and free-stream velocity are adjusted with same ratio. The effect was studied using NACA0015 airfoil pitching at quarter-chord by Walk et al. (1985b) and Walker and Chou (1987) for $K = 0.05$ and 0.1. Granlund et al. (2010) employed both flat plate and SD7003 pitching at quarter-chord at $K = 0.03$ in $Re = 20\text{k}$ and 50k.

As a function of angle of attack, lift coefficient quantified by dynamic surface pressure on NACA0015 airfoil showed very similar tendency before stall in Reynolds number regions $47.5\text{k} < Re < 200\text{k}$ (Walker and Chou, 1987; Walk et al.,1985b). The aerodynamic forces were not generated by the dynamic stall vortex; effects of Reynolds numbers were limited to freestream velocity variations (Walker and Chou, 1987). Similar force history was also observed for flat plate in $20\text{k} < Re < 50\text{k}$ from data obtained by direct force sensor; however, SD7003 airfoil appeared to be dependent on Reynolds number (Granlund et al., 2010). The reduced pitch rate was proved to be a determining factor (Walker and Chou, 1987).

1.2.6 Effect of Pivot Location

A position where pitch or rotation shaft is located refers to a pivot point for sectional wings and pivot axis for finite-aspect-ratio wings. Experimental data considering effect of pivot location was obtained based on NACA-0015 airfoil by Helin and Walker (1985) for pivot locations of $c/4$, $c/2$, and $3c/4$ at $K = 0.2$ in $Re = 45$k, Albertson et al. (1988) for pivot locations of c/4, c/2, and 3c/4 at $K = 0$-0.2 in $Re = 60$k, and Jumper et al. (1989) for pivot locations of 0.08c, c/4, and c/2 at K up to 0.04. Some work considering flat plate were given by Ol et al. (2009) for pivot locations of 0, $c/4$, $c/2$, $3c/4$, and c at $K = 0.7$ in $Re = 10$k, Granlund et al. (2010) for pivot locations of 0, $c/4$, $c/2$, and $3c/4$ at both $K = 0.05$ and 0.2 in $Re = 20$k, and Granlund et al. (2011a) for pivot locations of 0, c/2, and c at $K = 0.2$ in $Re = 10$k. These works were for sectional wings. Granlund et al. (2011b) considered a finite-aspect-ratio rectangular flat plate for pivot locations of 0, c/4, c/2, 3c/4, and c at $K = 1$ in $Re = 5$k.

From surface pressure data, lift-to-drag ratios were found to depend on pivot location (Albertson et al., 1988); effects of pitch-location dynamic-stall could be inferred from the theoretical prediction based on quarter-chord separation approach (Jumper et al., 1989).

From near surface velocity data, the velocity profile with respect to angle of attack at 6.7% chord had decrease in slope as pitch-axis distance from leading edge was increased; the peak velocity was also decreased (Helin and Walker, 1985).

From flow visualization data, as pitch-location was moved to three-quarter chord the onset of dynamic stall was delayed, similar to effects by increasing pitch rate (Helin and Walker, 1985). The vertical extent of the wake becomes smaller with pivot point further aft (Ol. 2009). The leading edge vortex was delayed as the pivot point was taken downstream; the LEV first formed on the plate pressure side before switching to suction side (Granlund et al., 2011a-b).

From direct force measurement, both effect of pitch rate and acceleration depended on pivot location; force coefficients were generally higher as pivot location was upstream (Granlund et al., 2010). Non-circulatory effects were present for pivot locations other than mid-chord, where acceleration occurred. The unaccelerated portion of pitch motion had constant offset between pivot locations; all curve evolved to zero lift at 90° incidence (Granlund et al., 2011b).

1.2.7 Effect of Wing Section

The effect of wing section was studied using SD7003 airfoil and flat plate pitching at quarter-chord by Ol (2009) who obtained flow visualization data at $K = 0.7$ in $Re = 10$k and Granlund et al (2010) who obtained the force data at $K = 0.03$ in both $Re =$ 20k and 50k.

The flow around SD7003 airfoil was observed to have much stronger dye concentration in trailing edge vortex and tighter leading edge vortex (Ol, 2009). SD7003 airfoil exhibited the dependency of Reynolds number on force history and more pronounced flow separation in a range $8° < \alpha < 20°$ (Granlund, 2010).

1.2.8 Effect of Wing Planform

The effect of wing platform was studied using aspect-ratio-of-two flat plates pitching at quarter-chord by Granlund et al. (2011a-b) who compared Zimmerman and rectangular plates for $K = 0.03$, 0.2, 0.3, and 0.5 in $Re = 20$k, and $K = 1$ in $Re = 5$k, Yilmaz and Rockwell (2012) who compared elliptical ($K = 0.098$) and rectangular plate ($K = 0.084$) in $Re = 10$k.

Zimmerman and rectangular plates showed very similarities in force history, higher reduced pitch rate gave lower lift and drag (Granlund et al., 2011a-b). Stereoscopic particle image velocimetry data showed three-dimensional leading edge vortex formed at high angle of attack for both elliptical and rectangular plates (Yilmaz and Rockwell, 2012). The leading edge vortex was lifted up the elliptical plate surface at a higher angle of attack (45° at 4 convectime times) than the rectangular plate, where the leading edge vortex was lifted up at a lower angle of attack (27° at 2.4 convective times).

1.2.9 Sectional Wing vs. Finite-Aspect-Ratio Wing

The effect of 2D and 3D wings were inspected using flat plates pitching at quarter-chord by Ol (2009) who obtained flow visualization data for K = 0.1 and 0.2 in Re = 10k, and Granlund et al. (2011a) who obtained force history for K = 0.03 and 0.2 in Re = 20k. Finite-aspect ratio model had a tighter leading edge vortex (Ol, 2009), and stalled at higher angle of attack and smaller maximum lift (Granlund et al., 2011a).

1.3 PITCHING WING AERODYNSMIC PARAMETER SPACE

For fixed wing geometry (i.e., aspect-ratio-of-four flat-plate wings), maximum pitch angle, pivot location, there are two independent parameters that define the flow: free stream velocity and wing pitch rate. Normalizing both parameters with relevant combination of wing chord and fluid kinematic viscosity gives Reynolds number ($U_\infty c/v$) and Stokes number ($\alpha'_m c^2/v$), shown as coordinates in Figure 1.17. The abscissa is Reynolds number, which is a ratio of flow advection time to viscous diffusion time; the ordinate is Stokes number, which is a ratio of pitch rate characteristic time to viscous diffusion time.

$$K = \frac{c\alpha'_m}{2U_\infty} = \frac{St}{2\,\mathrm{Re}} = \frac{\alpha_m t_c}{2t_p} = \frac{\alpha_m}{2\tau} \tag{1.9}$$

An important parameter for flow dynamics is reduced pitch rate K, which is a straight line in Figure 1.17 through the origin with increased slope as reduced pitch rate increases. As given in Equation (1.9), the reduced pitch rate gives the relationship between Stokes number and Reynolds number, but also characteristic times for a given maximum angle of attack. The characteristic times are pitch time $t_p = \alpha_m/\alpha_m'$ and convective time $t_c = c/U_\infty$; the ratio of t_p to t_c is denoted by τ.

Figure 1.17 shows test cases in the study. There were conducted in four free-stream velocities (U_∞): 0 cm/s (Re = 0k), 8.6 cm/s (Re ~ 4.3k), 17.5 cm/s (Re ~ 8.9k), and 25.6 cm/s (Re ~ 13k), and five pitch rates: 12.5°/s (St ~ 0.5k), 25.6°/s (St ~ 1.1k), 37.5°/s (St ~ 1.7k), 76.4°/s (St ~ 3.4k), and 155°/s (St ~ 7.0k). In Figure 1.17, square symbols represent the use of only rectangular wing; triangle symbols represent the use of several wing planforms. The wings were pitched at three pivot locations from 0° to 45°, which

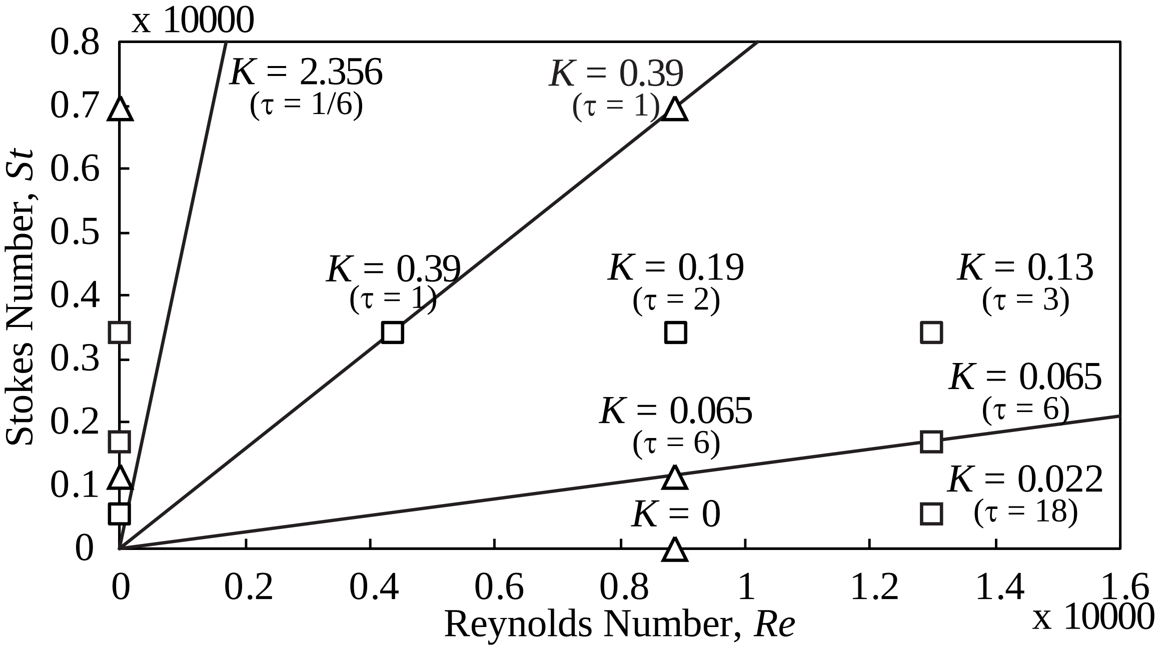

Figure 1.17 Test cases of interest in *St*-*Re* parameter space.

are leading edge, mid-chord, and trailing edge. The ratio of pitch time to convective time is also presented in parenthesis in Figure 1.17; they are from τ = 1, 2, 3, 6, to 18. Those are representatives for unsteady flow $K > 0$. Steady flow measurements $K = 0$ were also considered to quantify steady flow around fixed wings at fixed angle of attack; they are represented by the horizontal axis.

1.4 SCOPE AND OBJECTIVE

The scope of this study is to experimentally investigate unsteady flow field over pitching flat-plate wings with a mean finite-aspect-ratio in a water channel, covering Reynolds number $0 \leq Re < 1.3\times10^4$. The wings had rectangular-shaped planforms, two trapezoids, and two triangles; they had two-inch mean chord and four-effective-aspect ratio. Three approaches were conducted, including flow visualization, force measurement, and particle image velocimetry (PIV). The primary objectives of the study are listed below.

1. To determine the relation between wing kinematics and two- and three-dimensional flow structure, as well as lift generation mechanism.
2. To identify scaling properties of these flow processes.

3. To explore simple theoretical models suitable for these flows.

In addition, several effects are going to be presented, including effects of pivot location, wing planform, and reduced pitch rate. The case of zero free-stream velocity will also be considered to investigate the contribution to force and flow dynamics of non-circulatory effects.

CHAPTER 2

FLOW FACILITY AND INSTRUMENTATION

The study of unsteady flow over pitching wings was conducted by three experimental approaches: direct force measurement, PIV measurement, and flow visualization. In this chapter, facilities and procedures for these approaches are described, including water channel for constant free-stream velocity in Section 2.1. The geometry of wing planform is described in Section 2.2. All methods need stepper motors to carry out wing kinematics of interest, which is discussed in Section 2.3. Figure 2.1 shows road map for each approach. For dye injection, the evolution of streaklines is recorded by camera; it is considered as direct flow visualization and discussed in Section 2.4. Force

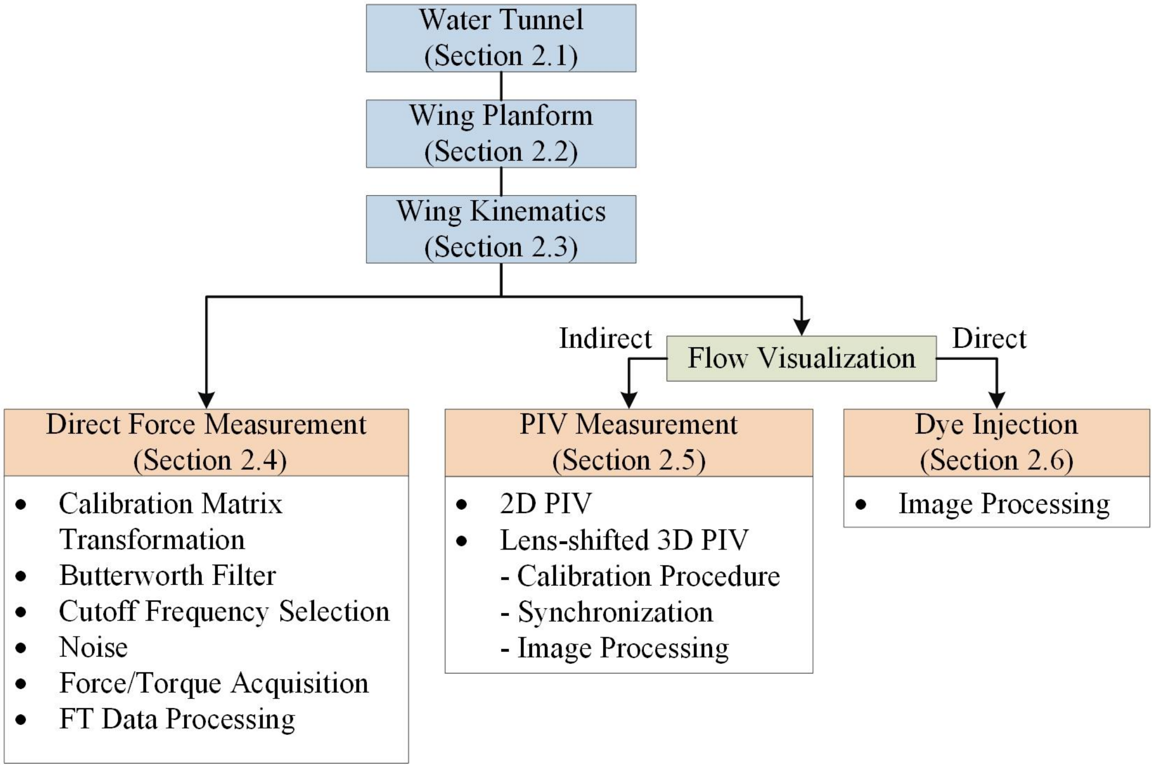

Figure 2.1 Road map for experimental approaches.

Figure 2.2 University of Michigan water channel.

measurement is discussed in Section 2.5, which includes transformation of calibration matrix about any reference coordinate of interest, determination of filter and cutoff frequency, and post-processing. For flow visualization, since PIV measurement presents flow topology quantitatively using mathematical algorism, it is regarded as indirect flow visualization and discussed in Section 2.6.

2.1 WATER CHANNEL

The free surface water channel at University of Michigan was employed to conduct experiments performed in this study, as shown in Figure 2.2; free-stream velocity was produced by a propeller controlled through AC motor controller within a region of 6 cm/s $< U_\infty <$ 60 cm/s. The AC motor controller applied pulse-width modulation (PWM) technique to modulate line-power and to adjust the rotation rate of a motor for the propeller; the motor is an AC induction motor EM3665T by BLADOR. As a result, the free-stream velocity is changed and in turn the corresponding motor frequency (*MF*) is revealed on LED display. If the power-line or motor controller is not grounded perfectly, the sensor used for force measurement would detect signals at a phase of motor frequency, which is identified in Figure 2.25. The room temperature of the water channel was kept at 72 °F.

2.1.1 Free-Stream Velocity

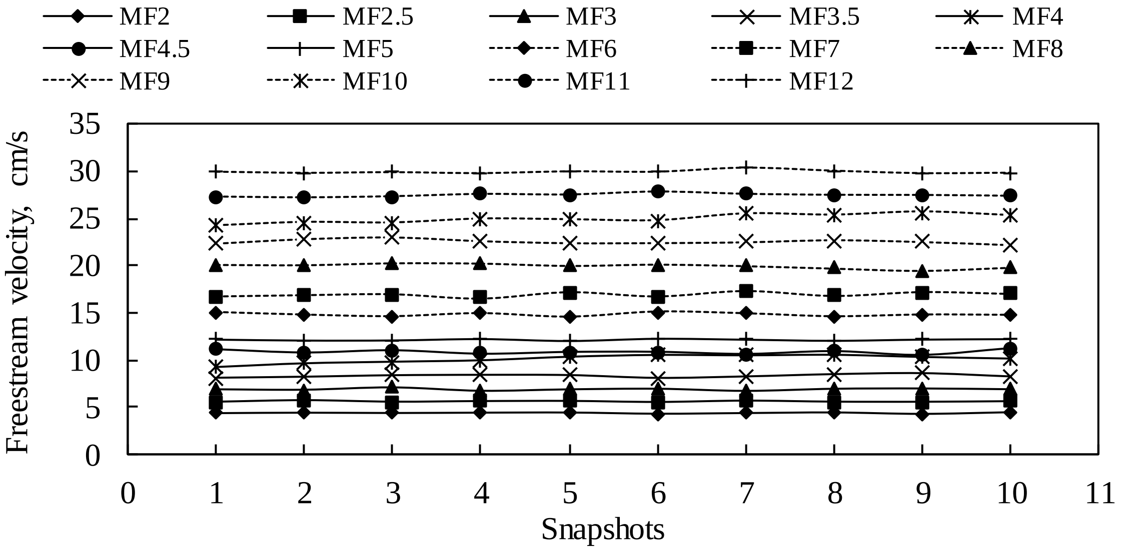

Figure 2.3 Free-stream velocity at constant motor frequency by the water channel in use.

To assure steady performance of a propeller is vital for producing constant free-stream velocity, which is evidenced in Figure 2.3. The free-stream velocity was measured using 2D particle image velocimetry in a test section with 7” wide and 22 11/16” height. The laser sheet with thickness of about 2 mm was positioned horizontally at the middle ofwater height. Each snapshot was taken by every 0.3 seconds for 10 snapshots. The average of the snapshots at each motor frequency is shown in Figure 2.4. At the given water height, free-stream velocity is related to motor frequency by Equation (2.1). For

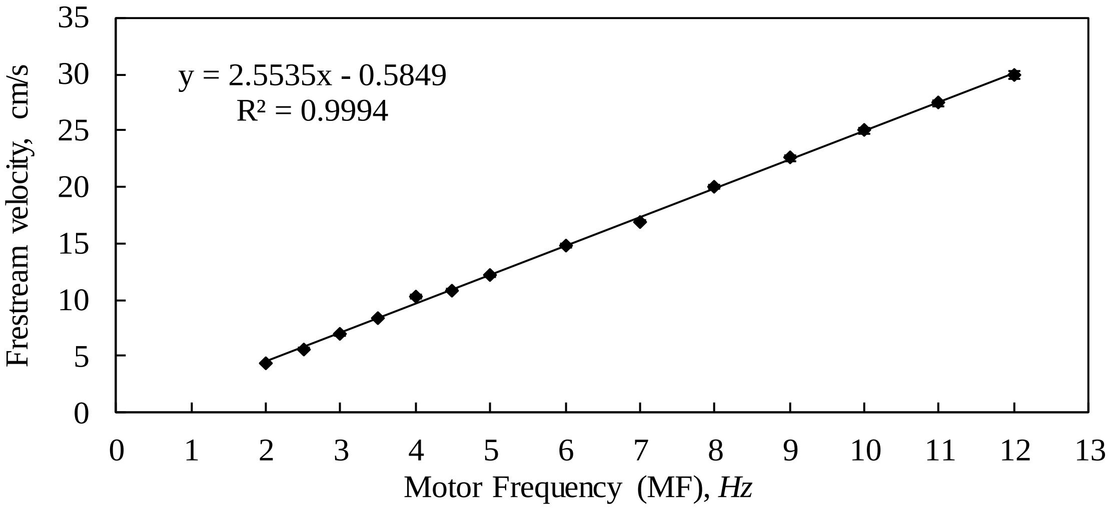

Figure 2.4 Freestream velocity as function of motor frequency.

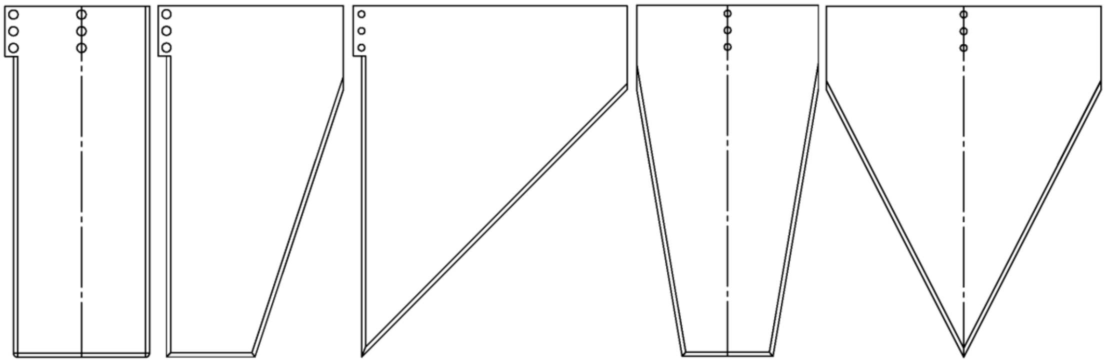

Figure 2.5 Illustrations of wing planforms *(from left to right) rectangular wing, two trapezoidal wings (isosceles and right), two triangular wings (isosceles and right) (draw water-line).*

detail PIV configuration, see Section 2.6.

$$U_{\infty} = 2.55MF - 0.58 \tag{2.1}$$

Two parameters are important to control free-stream velocity, which are water height and motor frequency. Keeping one parameter constant, three linear relations could be employed to facilitate experiment progress, as given in Equations (2.2)-(2.4).

$$U_{\infty,1} / U_{\infty,2} = MF_1 / MF_2 \text{ at } H = \text{constant} \tag{2.2}$$

$$U_{\infty,1} / U_{\infty,2} = H_2 / H_1 \text{ at } MF = \text{constant} \tag{2.3}$$

$$H_1 / H_2 = MF_1 / MF_2 \text{ at } U_{\infty} = \text{constant} \tag{2.4}$$

2.2 WING PLANFORM

The impact of flow structure on wing dynamics was studied using various wing shapes: one rectangular wing, two trapezoidal wings, and two triangular wings, as shown in Figure 2.5. All wings have 2” mean chord and 4” span immersed in the water, which give a constant effective aspect ratio of 4. These wings were made of Acrylic with wetted round edges and thickness of 1/8”; the ratio of thickness to mean chord is 6.25%. Small holes are used to fasten the wings to sensor adapter and align with pitch axis. There are three pivot-axis locations, which are leading edge (LE), mid-chord (MC), and trailing edge (TE). In addition, the wing geometry is given in Table 2.1. The taper ratio for rectangular, trapezoidal, and triangular wings is 1, 0.5, and 0, respectively. Leading-edge-sweep angle depends on both wing planform and pivot axis location; the minimum edge angle is 0° for the rectangular wing and the maximum edge angle is 45° for triangular wing at trailing-edge pivot. The total mass contributed to sensor is less than 19 grams, including wing itself, sensor adapter, and screws.

2.3 WING KINEMATICS AND IMPLEMENTATION

Pitch up-hold-return motion is a pure pitching wing motion and applied to investigate development of unsteady flow field throughout this study. Wings were pitched up linearly from a zero-degree angle of attack to a maximum angle of attack with a constant pitch rate, held for certain convective times for transient behaviors, then returned with the same constant pitch rate to initial position. In position-time space, wing motion has a trapezoidal shape, as shown in Figure 2.6. There are five phases defined (Yu and Bernal, 2013): start phase, pitch-up phase, hold phase, pitch-return phase, and relaxation phase. Additionally, this motion is considered a non-periodic motion due to the existence of start phase, hold phase, and relaxation phase. However, the wing motion was repeated several times in force measurement and PIV measurement; associated realizations are reported after phase averaging in order to obtain reasonable experimental uncertainty. The data presented in the study were averaged over 60 samples in phase.

As instantaneously starting or stopping with a constant pitch rate, the wing moves with infinite amount of acceleration, contributing infinite inertia to force sensor and making measurements impossible. This problem also challenges the field in computational fluid dynamics. In order to prevent such singular behavior at transition corners, shown as t_i with i = 1 to 4 in Figure 2.6, the smooth maneuvering was conducted and controlled using smoothing function, which yields finite acceleration regions.

Table 2.1 Wing geometry.

Properties	Rectangular wing		Trapezoidal wing			Triangular wing			Sensor adaptor & screws
	LE/TE	MC	LE	TE	MC	LE	TE	MC	
Mass (g)	22.9		24.2		24.1	27.9		27.7	18.3
Leading-edge sweep angle (degrees)	0		0	18.43	9.46	0	45	26.57	
Taper ratio (c_t/c_r)	1		0.5			0			

LE = leading edge pivot axis; MC = mid-chord pivot axis; TE = trailing-edge pivot axis

Therefore, during the pitch-up phase, the wing gradually moves to a constant pitch rate and then gently stops at a maximum angle of attack. During the pitch-return phase, the wing is maneuvered in the same manner.

In principle, the smoothing function gives wing angular position in time, and we proposed this smoothing function as a function of pitch time. The pitch time, $t_p = \alpha_m/\alpha'_m$, is defined as the time required to move the wing from zero incidence to a maximum angle of attack α_m, or vice versa with constant pitch rate α'_m. Consequently, unsteady flow field induced by wing motion acceleration and constant pitch rate under a constant free-stream velocity can be studied distinctly.

2.3.1 Smoothing Function

The first smoothing function was proposed by Visbal (1986), as indicated by the reviewed articles, for two-dimensional pitching NACA-0015 airfoil to prevent unrealistic acceleration introduced by instantaneous startup. The focus of his work was on testing the Beam-Warming scheme coupled with a developed two-dimensional Navier-Stokes solver on separated flow during the pitch-up phase from 0° to 60° angle of attack.

$$\Omega^+(t) = \Omega_0^{\ +}\left(1 - e^{-4.6t/t_0}\right)$$

where Ω^+ is non-dimensional pitch rate parameter ($\alpha' c/U_\infty$), and t_0 denotes the time required to reach 99% of the nominal pitch rate Ω_0^+.

For practical convenience, Eldredge et al. (2009) proposed a smoothing function giving homologous trapezoidal trajectory in position-time space, being able to not only pitch the wing during the pitch-up phase but also return the wing from a high angle of attack to initial zero-degree angle of attack with same constant pitch rate. The corrected expression (Eldredge and Wang, 2010) is shown below, which is a function of convective time.

$$\alpha(t) = \alpha_0 \frac{G(t)}{\max\left(G(t)\right)}$$

$$G(t) = \ln\left\{\frac{\cosh\left[aU_\infty\left(t - t_1\right)/c\right]\cosh\left[aU_\infty\left(t - t_3\right)/c\right]}{\cosh\left[aU_\infty\left(t - t_2\right)/c\right]\cosh\left[aU_\infty\left(t - t_4\right)/c\right]}\right\}$$

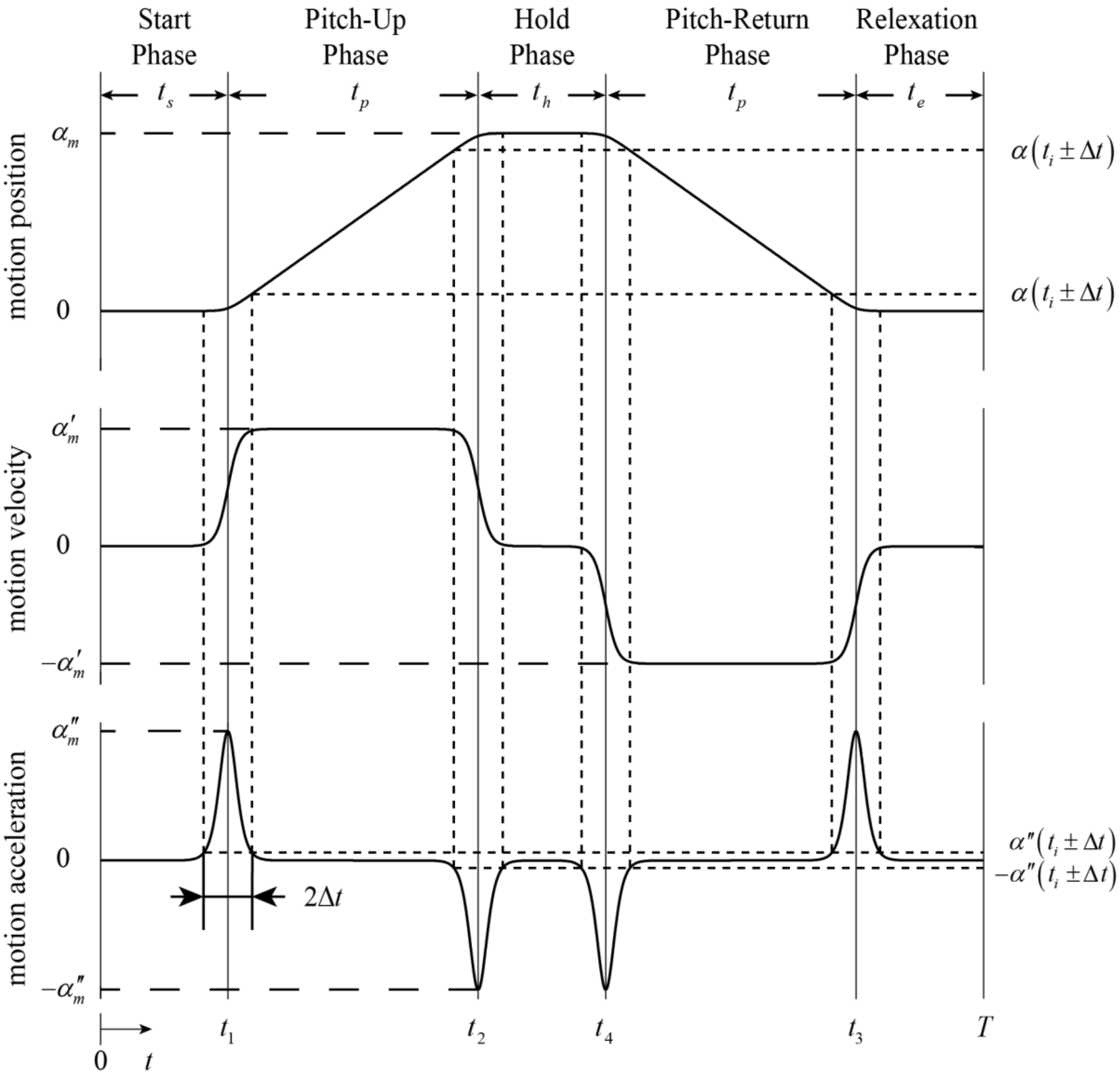

Figure 2.6 An illustration of linear pitch up-hold-return kinematics.

where α_0 is maximum angle of attack and a is a parameter defined to control the speed of the transitions around t_i. The maximum value of $G(t)$ is equal to $a\alpha_0/k$, as formulated in Yu et al. (2012).

The utilization of this function yields two questions. The first question is how wing kinematics would be in the still water since free-stream velocity is zero (i.e., $U_\infty = 0$). One possible answer is to consider the free-stream velocity in smoothing function is specified to be independent of actual flow condition, which supports the argument that pitch rate and free-stream velocity are independent. However, this causes the second question of how reasonable free-stream velocity should be specified.

To avoid confusion, a smoothing function as a function of pitch time is proposed, as shown in Equation (2.5). The first and second derivative of the smoothing function give motion speed and motion acceleration in Equation (2.6) and Equation (2.7), respectively, which in turn determines smoothing regions by parameter B ($B = t_p/t_a$). The definition of parameter B will be discussed in the following section. All angles presented in the equations are in radians. Figure 2.6 also gives profiles of motion speed and motion acceleration.

$$\alpha(t) = \frac{\alpha_m}{2B}\sum_{i=1}^{4}(-1)^{i+1}\ln\left\{\cosh\left[B(t-t_i)/t_p\right]\right\} \tag{2.5}$$

$$\alpha'(t) = \frac{d\alpha}{dt} = \frac{\alpha'_m}{2}\sum_{i=1}^{4}(-1)^{i+1}\tanh\left[B(t-t_i)/t_p\right] \tag{2.6}$$

$$\alpha''(t) = \frac{d^2\alpha}{dt^2} = \frac{B\alpha_m}{2t_p^{\ 2}}\sum_{i=1}^{4}(-1)^{i}\tanh^2\left[B(t-t_i)/t_p\right] \tag{2.7}$$

2.3.2 Behavior around Corner

To better design smooth maneuvering around corners, denoted by $t_i \pm \Delta t$ in Figure 2.6, Equations (2.5)-(2.7) are rearranged into exponential forms shown in Equations (2.8)-(2.10), respectively. The duration of the smoothing is regarded as smooth region, acceleration region, or transition region.

$$\alpha(t) = \frac{\alpha'_m}{2}\sum_{i=1}^{4}(-1)^{i+1}\left|t-t_i\right| + \frac{\alpha_m}{2B}\sum_{i=1}^{4}(-1)^{i+1}\ln\left[1+G_i(t)\right],\ 0 \le t \le T \tag{2.8}$$

$$\alpha'(t) = \frac{\alpha'_m}{2}\sum_{i=1}^{4}(-1)^{i+1}\frac{d\left|t-t_i\right|}{dt} + \alpha'_m\sum_{i=1}^{4}(-1)^{i}\frac{G_i(t)}{1+G_i(t)},\ 0 \le t \le T \tag{2.9}$$

$$\alpha''(t) = \frac{2B\alpha_m}{t_p^{\ 2}}\sum_{i=1}^{4}(-1)^{i+1}\frac{G_i(t)}{\left[1+G_i(t)\right]^2},\ 0 \le t \le T \tag{2.10}$$

where

$$G_i(t) = \exp\left[-2B\left|t-t_i\right|/t_p\right]$$

2.3.2.1 Position Kinematics

Equation (2.8) represents the motion angular position in time. The first term at right hand side is the motion without smoothing. It can be expanded as shown in Equation (2.11) for each phase. The second term contributes to smooth maneuvering, which is negligible as the parameter *B* is significantly large. For instance, assuming the angle change during smoothing region is the smallest angle Rotary Table B4836TS can be implemented, which is the resolution 0.025°; hence, the parameter *B* is found to be 5400. Rotary Table is the positioning device for wing kinematics. As the parameter *B* is larger than 5400, there is no smoothing region in effect using Rotary Table B4836TS. Moreover, the angle change during the smoothing region cannot be larger than $\alpha_m/2$ in order to maintain maximum angle of attack α_m, which indicates parameter *B* has to be equal to or higher than 6. As a result, the parameter *B* is nontrivial if $6 \le B \le 5400$ is satisfied, particularly for Rotary Table B4836TS.

$$\begin{aligned}\alpha_1(t) &= \frac{\alpha'_m}{2}\sum_{i=1}^{4}(-1)^{i+1}\left|t-t_i\right| \\ &= \begin{cases} 0 & 0 \le t \le t_1 \\ \alpha'_m(t-t_1) & t_1 < t < t_2 \\ \alpha'_m & t_2 \le t \le t_4 \\ \alpha_m - \alpha'_m(t-t_4) & t_4 < t < t_3 \\ 0 & t_3 \le t \le T \end{cases}\end{aligned} \tag{2.11}$$

Now consider smoothing region being confined within times $t_i \pm \Delta t$, where maximum acceleration occurs at t_i with a bell-like profile. The corresponding angle change can be evaluated using Equation (2.12), which is derived from Equation (2.11).

$$\Delta\alpha = \left|\alpha(t_i+\Delta t) - \alpha(t_i)\right| = \alpha'_m \Delta t \tag{2.12}$$

Introducing pitch time t_p, the ratio of angle change to maximum angle of attack, denoted by β, is obtained using Equation (2.13). This is the first important parameter to define smooth maneuvering

$$\boxed{\beta = \frac{\Delta\alpha}{\alpha_m} = \frac{\Delta t}{t_p}} \tag{2.13}$$

For Rotary Table B4836TS and 45° maximum angle of attack, β is bounded by resolution of the Rotary Table and by maximum allowable smoothing range (i.e., $\alpha_m/2$), which give $1/180 \leq \beta \leq 2$.

2.3.2.2 Angular Speed Kinematics

Equation (2.9) represents motion angular speed in time. The first term at the right hand side is the first derivative of the first term of Equation (2.11) and can be expressed in Equation (2.14).

$$\alpha'(t) = \begin{cases} 0 & 0 \leq t \leq t_1 \\ \alpha'_m & t_1 < t < t_2 \\ 0 & t_2 \leq t \leq t_4 \\ -\alpha'_m & t_4 < t < t_3 \\ 0 & t_3 \leq t \leq T \end{cases} \tag{2.14}$$

The second term is determined from smooth maneuvering, the amplitude at corner t_i is found to be half of maximum pitch rate, shown in Equation (2.15), the speed is positive during pitch-up phase, and negative during pitch-return phase.

$$\left|\alpha'(t_i)\right| = \alpha'_m / 2 \tag{2.15}$$

2.3.2.3 Angular Acceleration Kinematics

Equation (2.10) represents motion angular acceleration in time around corners. To find the existence of maximum value of motion acceleration, the third derivative of smooth function would be equal to zero, as shown in Equation (2.16).

$$\alpha'''(t) = -\frac{4B^2\alpha_m}{t_p{}^3}\sum_{i=1}^{4}(-1)^{i+1}\frac{G_i(t)\left[1-G_i(t)\right]}{\left[1+G_i(t)\right]^3} = 0 \tag{2.16}$$

Non-trivial solution could be found only if following condition is satisfied.

$$1 - G_i(t) = 0 \text{ or } -2B\left|t-t_i\right|/t_p = 0$$

which shows the occurrence of maximum acceleration is at transition corners t_i and the corresponding magnitude is given in Equation (2.17).

$$\left|\alpha''(t_i)\right| = \alpha''_m = \frac{B\alpha_m}{2t_p{}^2} \tag{2.17}$$

The corresponding acceleration at $t_i + \Delta t$ or $t_i - \Delta t$ is approximated by Equation (2.18).

$$\left|\alpha''\left(t_i \pm \Delta t\right)\right| \approx 4\alpha''_m \left\{ \frac{G_i\left(\Delta t\right)}{\left[1+G_i\left(\Delta t\right)\right]^2} \right\} = \frac{\alpha''_m}{\cosh^2\left(B\Delta t / t_p\right)} \tag{2.18}$$

The ratio of acceleration to maximum acceleration, denoted by γ, could be defined using Equation (2.19), which is obtained by substituting Equation (2.13) into Equation (2.18); this is the second important parameter to define smooth maneuvering.

$$\boxed{\gamma = \frac{\left|\alpha''\left(t_i \pm \Delta t\right)\right|}{\alpha''_m} = \frac{1}{\cosh^2\left(B\beta\right)}} \tag{2.19}$$

Consider Rotary Table B4836TS and 45° maximum angle of attack, γ is nontrivial if $0 \le \gamma \le 1$ is satisfied. As γ equal to 0, smooth maneuvering is over region of $\alpha_m/2$. As γ is close to one, smooth maneuvering will be operated within one step of stepper motor.

2.3.2.4 Role of Parameter B

In previous sections, β and γ are discovered to be beneficial in determining smoothing region and controlling stepper motor, as defined in Equations (2.13) and (2.19), respectively. And parameter B would be obtained once β and γ are given; for example, as $\beta = 5/45$ and $\gamma = 0.01$, parameter B is found to be 26.939. However, the role of parameter B is not well described and will be discussed as follows.

Consider Equation (2.17) where maximum pitch acceleration is defined. After proper arrangement, the parameter B could be formulated into Equation (2.20).

$$\frac{B}{2} = \frac{\alpha''_m}{\alpha_m} {t_p}^2 = \frac{\alpha''_m}{\alpha_m} \frac{{\alpha_m}^2}{{\alpha'_m}^2} = \frac{\alpha''_m}{\alpha'_m} \frac{\alpha_m}{\alpha'_m} = \frac{t_p}{t_a} \tag{2.20}$$

which gives the ratio of pitch time to pitch acceleration time. The pitch acceleration time is defined as $t_a = \alpha'_m/\alpha''_m$. The factor of two in Equation (2.20) indicates numbers of occurrence of motion acceleration during pitch-up/pitch-return phase. Larger the parameter B gives narrower acceleration/smoothing region. As discussed previously, the maximum parameter B is limited by the resolution of the stepper motor and $\alpha_m/2$. In

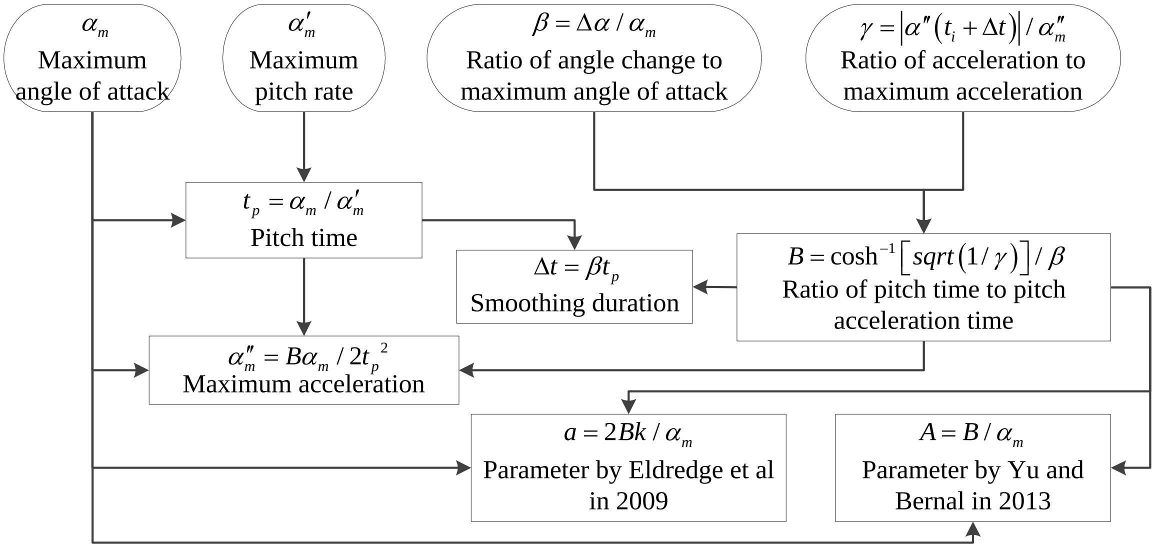

Figure 2.7 Equation flowchart in designing kinematics of interest.

addition, the parameter B is analogous to $A\alpha_m$ and $a\alpha_m/2K$ defined in Yu and Bernal (2013) and Eldredge et al. (2009), respectively.

2.3.3 Wing Kinematics of Interest

Figure 2.7 gives guidance to design and generate wing kinematics. There are two types of input parameters. The first one defines ideal linear pitching ramp motion, which includes maximum angle of attack (α_m) and maximum pitch rate (α'_m). The second type defines smooth maneuvering around transition corners, which are the ratio of angle change to maximum angle of attack (β) and the ratio of acceleration to maximum acceleration (γ). The time required for smooth maneuvering is two times that smoothing duration (Δt), defined in Equation (2.12), but not two times t_a due to γ. We may consider γ to be another type of smoothing transition parameter for ideal ramp-type acceleration.

There were two Velmex Rotary Tables employed to carry out the kinematics of interest, which are B4836TS and B4818TS, depending on maximum pitch rate. For B4836TS Rotary Table, maximum capable pitch rate is 100 degrees per second with resolution of 40 steps per degree. For B4818TS Rotary Table, maximum capable pitch rate is 200 degrees per second and resolution of 20 steps per degree. Both Rotary Tables are driven by same stepper motor model RK266-03 and controlled through COSMOS software.

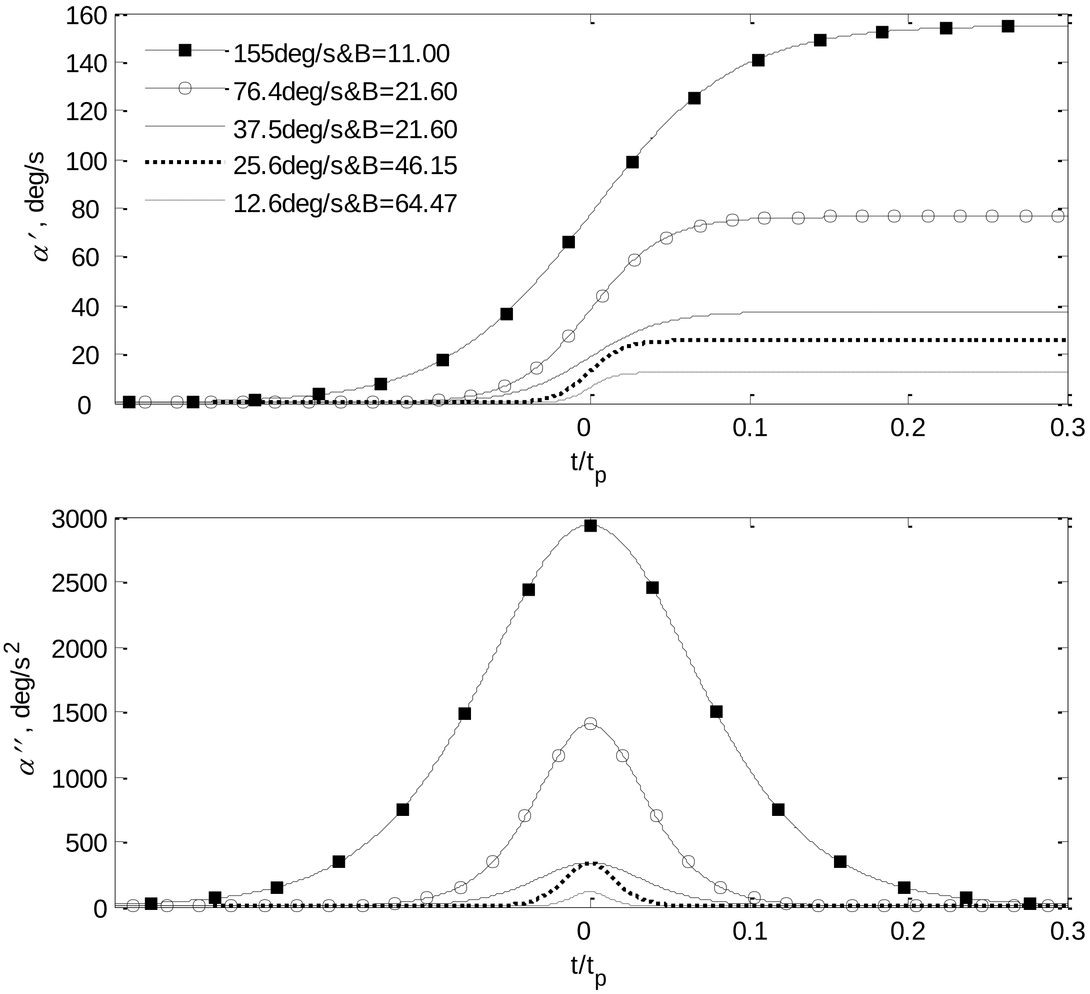

Figure 2.8 Kinematics of interest as a function of pitch time during smoothing maneuvering: (top) motion speed; (bottom) motion acceleration.

As shown in Table 2.2, there are five wing kinematics of interest being tested in this study with the same α_m = 45° and γ = 0.01. Since α_m and γ are unchanged, the duration of the smoothing was adjusted according to α''_m and α'_m. The parameters A (Yu and Bernal, 2013) and a (Eldredge et al., 2009) are also provided for comparison.

Figure 2.8 shows the comparison among wing kinematics as a function of pitch time. Since pitch-return phase has similar profile and there is no wing position change during hold phase, only motion-time trajectory during pitch up phase. Typically, lower pitch rate results in narrower smoothing regions and lower acceleration magnitude. The wing kinematics with pitch rate 155 °/s and B = 11 gives widest smoothing regions, smooth angle is 12.2° (β = 27.2). The wing kinematics with pitch rate 12.6 °/s and B =

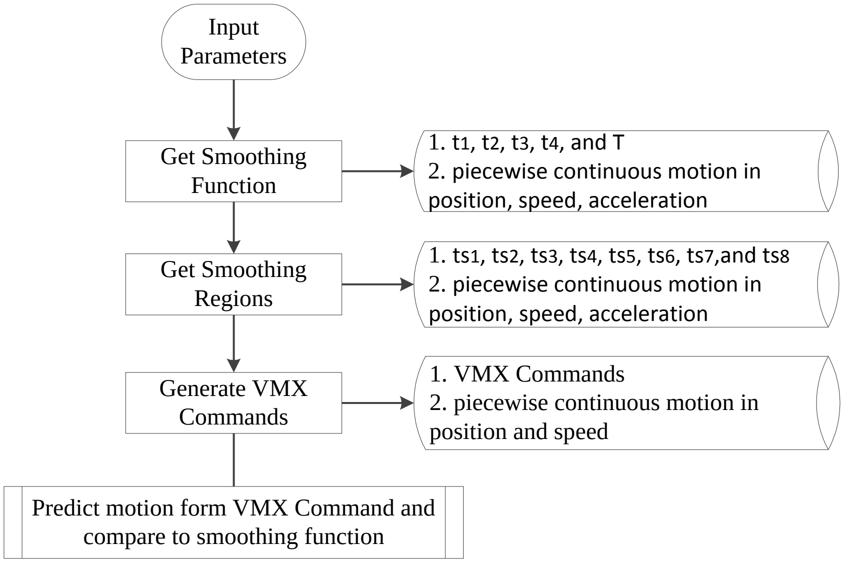

Figure 2.9 Motion command generation procedure

64.47 gives narrowest smoothing region, smooth angle is 2° (β = 4.64). Additionally, the wing kinematics with pitch rate of 155 °/s is designed for using Rotary Table B4818TS; the others require the use of Rotary Table B4836TS since their pitch rate are less than 100 °/s.

Furthermore, to study effects of motion acceleration, two pitch rates with the same B = 21.60 were generated, which are 76.4°/s, and 37.5°/s, respectively. For 37.5°/s, lower α''_m was generated and operated in flow condition to produce K = 0.065. Wing kinematics with smaller pitch rate 25.7 °/s were generated to yield the same K = 0.065 with the same α''_m but smaller smooth angle.

Table 2.2 Parameters to generate wing kinematics of interest.

#	α'_m	β, %	γ, %	α_m	c	t_p, s	α''_m	B	Yu & Bernal (2013)	Eldredge et al. (2009)		
									A	a	U_∞	K
1	155	27.2	1	45	2	0.290	2937	11.00	14.00	11	17.500	π/8
2	76.4	13.9	1			0.588	1402	21.60	27.50	11	16.944	0.2
3	37.5	13.9	1			1.199	338	21.60	27.50	11	8.314	0.2
4	25.6	6.49	1			1.754	338	46.15	58.76	11	12.153	0.0936
5	12.6	4.64	1			3.581	113	64.47	82.09	11	8.314	0.067

Unit of α'_m is degrees per second, α_m is degrees, c is inch, α''_m is degrees per second squared.

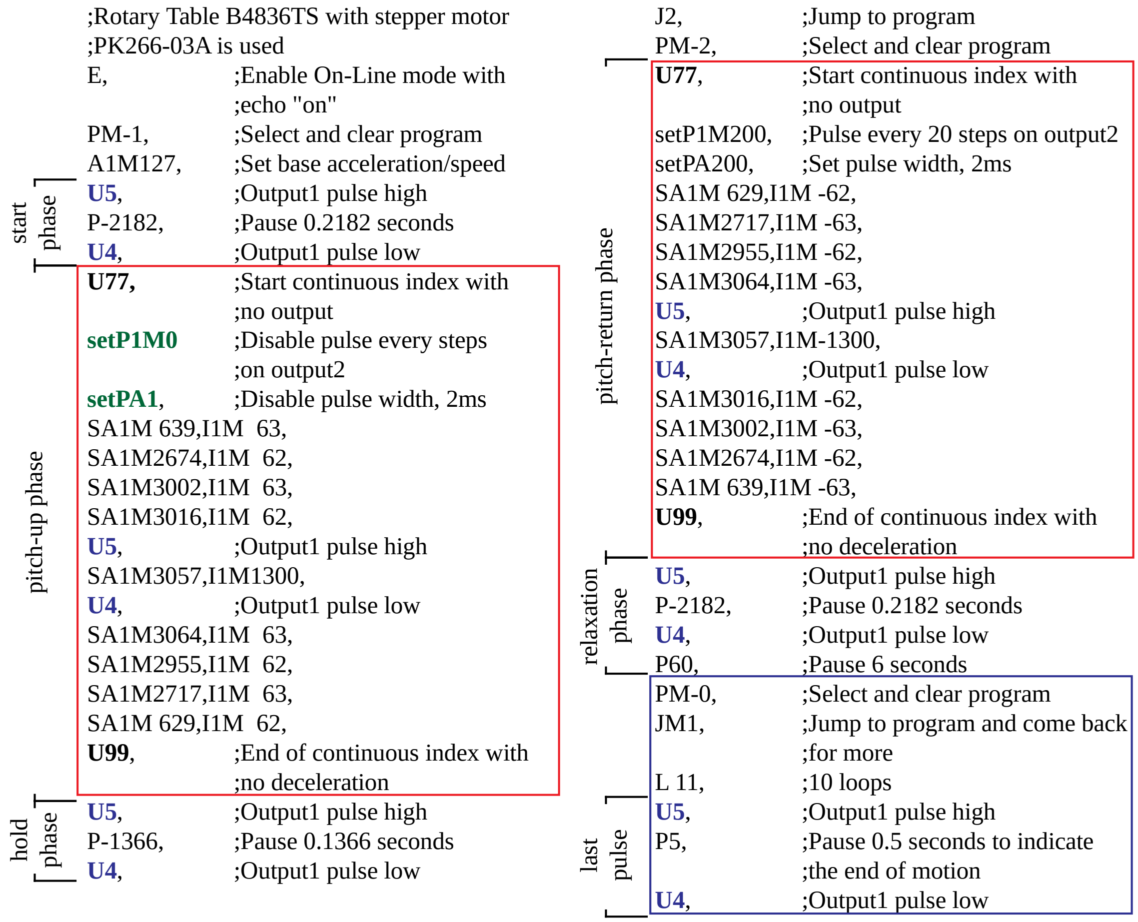

```
;Rotary Table B4836TS with stepper motor
;PK266-03A is used
E,                 ;Enable On-Line mode with
                   ;echo "on"
PM-1,              ;Select and clear program
A1M127,            ;Set base acceleration/speed
U5,                ;Output1 pulse high
P-2182,            ;Pause 0.2182 seconds
U4,                ;Output1 pulse low
U77,               ;Start continuous index with
                   ;no output
setP1M0            ;Disable pulse every steps
                   ;on output2
setPA1,            ;Disable pulse width, 2ms
SA1M 639,I1M  63,
SA1M2674,I1M  62,
SA1M3002,I1M  63,
SA1M3016,I1M  62,
U5,                ;Output1 pulse high
SA1M3057,I1M1300,
U4,                ;Output1 pulse low
SA1M3064,I1M  63,
SA1M2955,I1M  62,
SA1M2717,I1M  63,
SA1M 629,I1M  62,
U99,               ;End of continuous index with
                   ;no deceleration
U5,                ;Output1 pulse high
P-1366,            ;Pause 0.1366 seconds
U4,                ;Output1 pulse low
```

```
J2,                ;Jump to program
PM-2,              ;Select and clear program
U77,               ;Start continuous index with
                   ;no output
setP1M200,         ;Pulse every 20 steps on output2
setPA200,          ;Set pulse width, 2ms
SA1M 629,I1M -62,
SA1M2717,I1M -63,
SA1M2955,I1M -62,
SA1M3064,I1M -63,
U5,                ;Output1 pulse high
SA1M3057,I1M-1300,
U4,                ;Output1 pulse low
SA1M3016,I1M -62,
SA1M3002,I1M -63,
SA1M2674,I1M -62,
SA1M 639,I1M -63,
U99,               ;End of continuous index with
                   ;no deceleration
U5,                ;Output1 pulse high
P-2182,            ;Pause 0.2182 seconds
U4,                ;Output1 pulse low
P60,               ;Pause 6 seconds
PM-0,              ;Select and clear program
JM1,               ;Jump to program and come back
                   ;for more
L 11,              ;10 loops
U5,                ;Output1 pulse high
P5,                ;Pause 0.5 seconds to indicate
                   ;the end of motion
U4,                ;Output1 pulse low
```

Figure 2.10 An example of motion commands to VMX controller.

2.3.4 Motion Generation

Motion commands to control stepper motor are in ASCII characters; they were programmed according to wing kinematics of interest and then uploaded to the VMX controller from the Velmex COSMOS software through the RS-232 interface. Results presented in later chapters were using stepper motor PK266-03, which was embedded with Rotary Table by Velmex, Inc. This type of stepper motor has a two-phase unipolar motor, and a rotor with 50 teeth and 8 poles on its stator, resulting in 200 steps per revolution and 1.8° step-angle. Using gear ratio of 36 to 1, for instance, Rotary Table B4836TS can be operated in half-step mode at an even smaller step angle of 0.025°; this step resolution is utilized to program motion commands at 40 steps per degree.

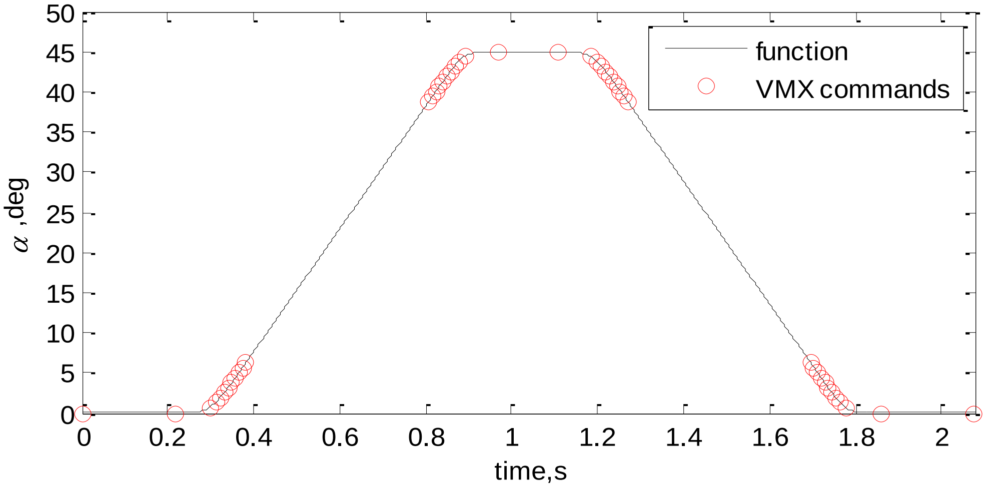

Figure 2.11 Comparison of VMX commands and smoothing function in angle of attack

In addition, operation frequency of stepper motor corresponds to half of step-speeds given in motion commands, which is “x” in “SmMx” and “SAmMx”. For instance, when the step-speed of Rotary Table is set to x = 40 steps per second, the operation frequency of stepper motor is 20 Hz, which is also considered as 20 pulses/steps per second. If the stepper motor is not well shielded, these electrical pulses/frequency will be detected by force transducer and interfere with true measurements. To ensure quality of force measurements, operation frequency of stepper motor is suggested to be higher than frequency region of interest and less than half of the sampling rate if an anti-aliasing filter is not in use. The frequency region of interest is associated with motion acceleration and is discussed in Section 2.5.

Figure 2.9 shows the workflow used to generate the motion commands for wing kinematics of interest. The continuous smoothing function was first discretized using the timestep of 1/10000 seconds, giving a piecewise continuous motion for succeeding interpolation. After defining α_m, α'_m, β, and γ, smoothing regions were obtained and all angles were rounded, consistent with stepper motor resolution. These regions were then divided into numbers of segments in turns of steps and linearly interpolated to obtain corresponding timing. As absolute positions in step and timing were obtained, the Rotary Table is commanded by specifying step speeds and indices, representative of rigid wing

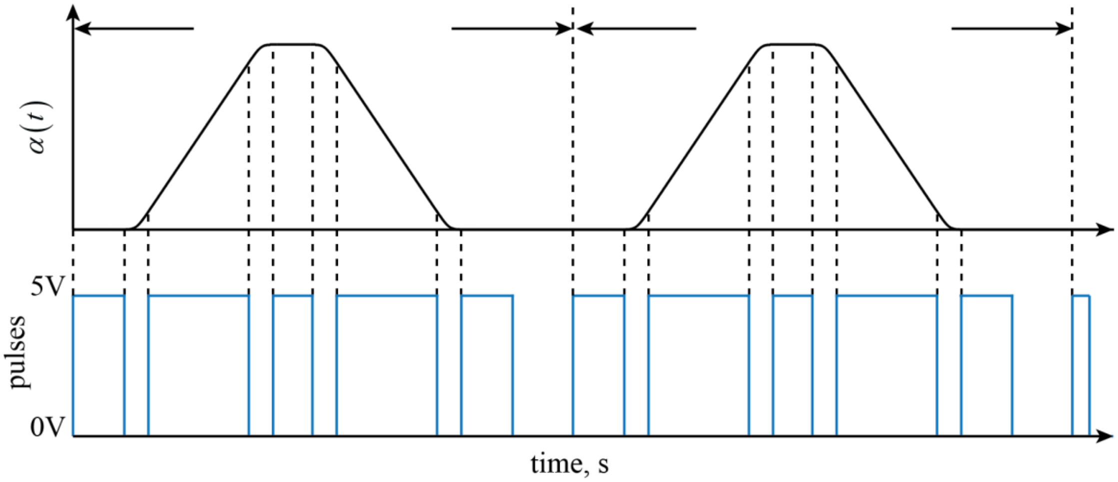

Figure 2.12 Correlation of pulses and kinematics.

motion. An example of motion commands is given in Figure 2.10; large angle increment during smoothing regions is displayed as an example.

First of all, the continuous index command (i.e., U77 or U99) is employed to prevent stepper motor from slowing down or stopping between motor indexes. Secondly, the higher timing accuracy for pausing is achieved by introducing the command “P-x” for phases, such as the start phase, the hold phase, and the relaxation phase. The time resolution is tenth milliseconds. If a longer pause is requested, the command “Px” would be used to account for additional pausing time.

To ensure the correctness of wing motion implementation, the position course of Rotary Table is predicted using motion commands and compared with the ones from smooth function. Figure 2.11 gives an example of comparison. Circle open symbols represent selected points for motion command and solid curve represents expected curve from smooth function. Our points used to generate motion commands are in good agreement with smooth function as expected for all kinematics of interest.

The corresponding angular speed is shown as the red curve in Figure 2.13, which is stair-like. Look closely to the beginning and the end of the pitch-up/return phase the difference in speed is significantly larger than the others. In conjunction with motor index, this difference may trigger structure vibrations of wings and tarnish force measurement. Therefore, it is suggested to have smaller motor index at the beginning and the end of smooth maneuvering together with higher operation frequency of stepper motor. The

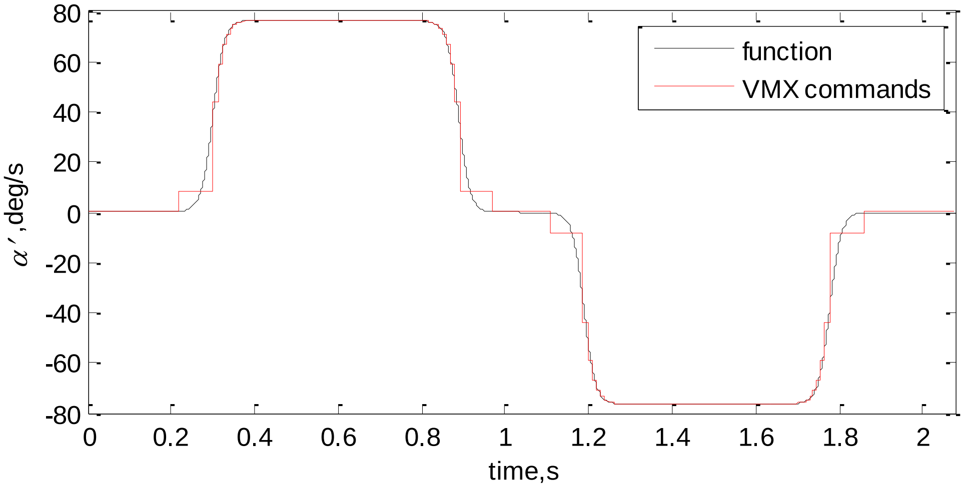

Figure 2.13 Comparison of VMX commands and smoothing function in angular speed

operation frequency should be higher than frequency region of interest of kinematics. The MATLAB program to generate commands for wing kinematics is given in Appendix A.

To distinguish samples within motion phases, auxiliary pulses were generated from Velmex controller, as commanded using U5 and U4 in motion commands in Figure 2.10, and saved to a computer through DAQ board. Figure 2.12 illustrates pulse pattern, for example, regions of acceleration, deceleration, constant pitch rate, and other pause phases are defined, which advantages post-processing of force measurements in transforming signals from sensor frame of reference to laboratory frame of reference, and displaying results for corresponding motion phase.

2.4 FLOW VISUALIZATION

Figure 2.14 Instruments for dye injection

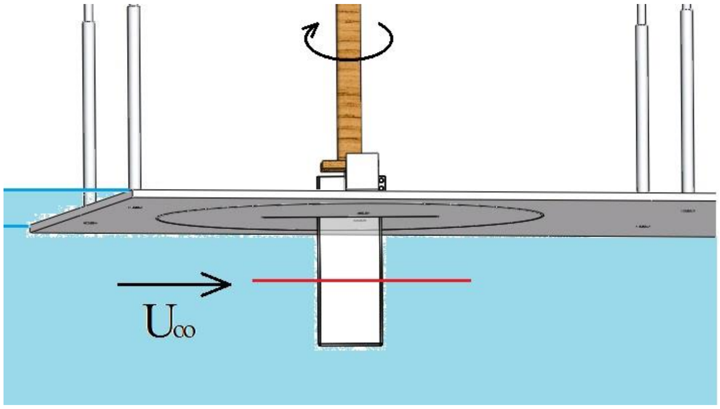

Figure 2.15 An illustration of wing configuration for flow visualization.

Flow visualization by injecting dyes over wings was conducted using a camera, syringe pumps, food dyes, and dye rake, as shown in Figure 2.14. The flow visualization data were recorded using Nikon D3100 camera. The perspective of flow was observed by two aspects, which are side view and top view. The side view provides field of view of flow about wing chord; the top view gives field of view of flow about wing span. Two colored dyes were used, which were blue dyes and red dyes by ESCO Foods with density of 1012 kg/m^3. They were mixed with 70% isopropyl alcohol (density of 685 kg/m^3) to match the water density, 998 kg/m^3.

Figure 2.15 is an illustration of wing configuration used for dye injection, the background board with thickness of 0.24" was employed to exclude distracting background features and reflection from water surface. The injection rake was placed at 50 % of wing span for all wing planforms, as shown as red line, and about three-mean-chord upstream of leading edge.

2.4.1 Dye Injection Post-Processing

All images were recorded by Nikon D3100 camera with a constant frame rate of 30 Hz and saved to a personal computer for post-processing. The data was stored in a format of MOV using 854 × 480 pixel images. Two-step procedures were conducted in the post-processing.

The first step was to abstract sequent images of interest using Windows Movie Maker. We selected the first image at the phase where the wing starts to move and the

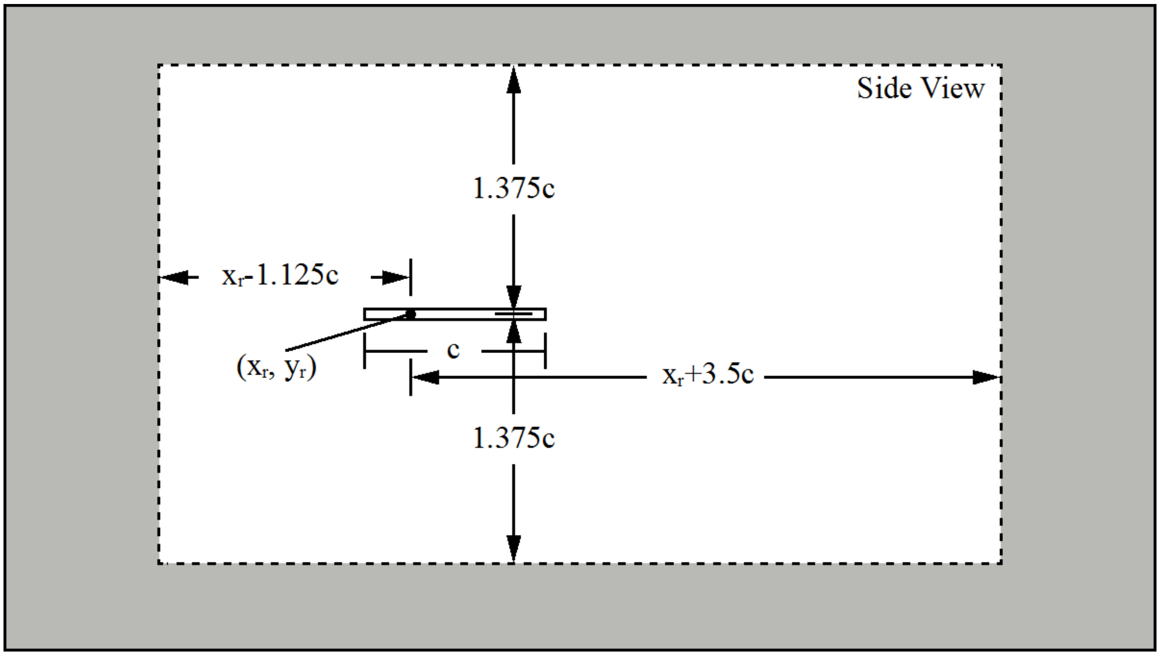

Figure 2.16 Schematics of field of view for dye-injection in side view.

last image at the phase where the flow reaches the steady state during the hold-phase at maximum angle of attack, which is about 27 convective times.

The second step was to edit image field of view using MATLAB for closer view

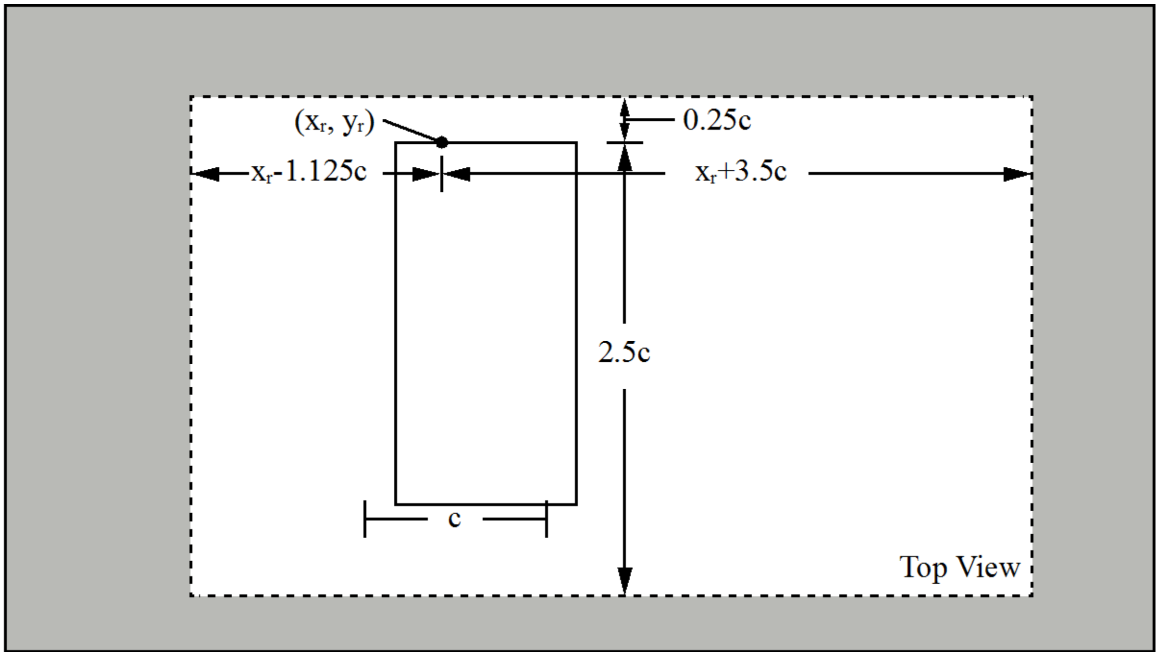

Figure 2.17 Schematics of field of view for dye-injection in top view.

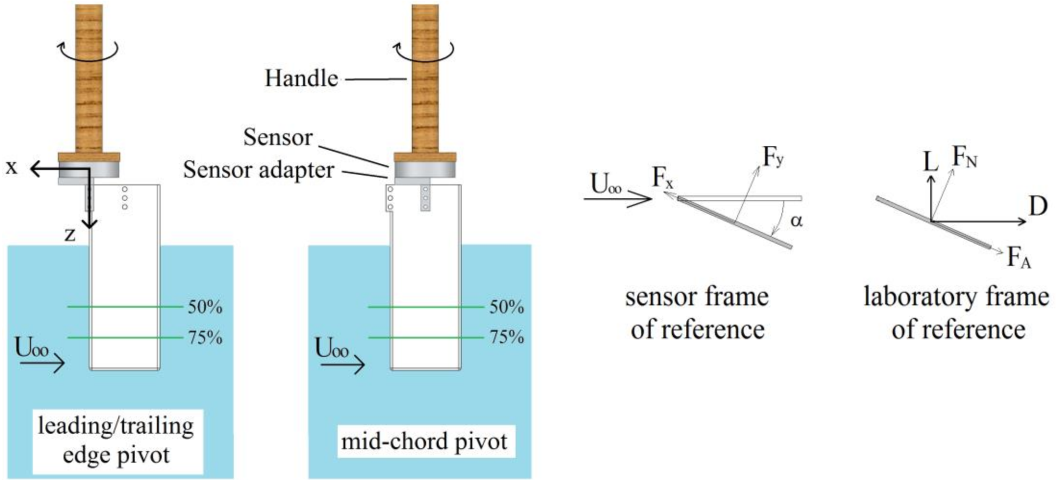

(a) (b)

Figure 2.18 An illustration of wing configuration for force measurement at different pivot-axis locations.

of flow around wings and produce a constant image size for all cases. Several actions were taken to process images, which included flipping, rotating, cropping, resizing, annotating, and merging. Figure 2.16 and Figure 2.17 illustrate image region of interest for side view and top view, respectively. The outer edges present original image size; the shadow areas represent the areas to be trimmed. The region of interest, shown as inner white region, was determined using reference point (x_r, y_r) at pivot location. The magnification factor was found using geometry of wing or passive plate; all resultant images were scaled to 320 × 190 pixels.

2.5 FORCE MEASUREMENT

Force and torque were measured using force transducer, Nano43 (series number FT12311) by ATI industrial automation. Resolutions for force and torque are 1/256 N and 1/20 Nmm, respectively; maximum capability for force is 18N and 250 Nmm for torque. The sensor mounting side is attached to a handle clamped to Rotary Table and the tool side is mounted to sensor adapter, see Figure 2.18 for illustration. All forces and torques are measured with respect to center surface of tool side, which is also defined as factory point of origin and aligned with pitching axis to facilitate data analysis.

Wing configuration at the LE and the MC is illustrated at the right and the left of Figure 2.18 (a), respectively; the TE uses the same wing configuration as the LE, but wing is rotated by 180° to position pitching axis at downstream edge. In the sensor frame of reference of the LE/MC configuration, positive x-direction is toward leading edge and positive y direction is in the direction of positive lift force. For the TE pivot, positive directions of the x- and y-axes are in opposite direction because of 180-degree rotation; normal force (denoted by F_N) and axial force (denoted by F_A) are obtained by simply sign change, shown in Figure 2.18 (b).

Force/torque measured by the sensor (i.e., Fx and Fy) are first converted to the axial and normal forces and then to laboratory frame of reference components using Equations (2.21)-(2.24) for lift (L), drag (D), and their corresponding force coefficients.

$$L = -A\sin\alpha + N\cos\alpha \tag{2.21}$$

$$D = A\cos\alpha + N\sin\alpha \tag{2.22}$$

$$C_L = L/\left(\rho U_\infty^2 S/2\right) \tag{2.23}$$

$$C_D = D/\left(\rho U_\infty^2 S/2\right) \tag{2.24}$$

Moreover, estimation of moment inertia, torque, and center of are given in Appendix G. Using maximum angular acceleration, the torque is estimated within tolerance of force transducer Nano43 for all wing planform geometries.

2.5.1 Transformation of Calibration Matrix

Force transducer provides six-channel signals for three forces (Fx, Fy, Fz) and three torques (Tx, Ty, and Tz). Inside the force transducer are strain gages attached to three beams, which are deformed due to applied loads and results in changing resistance of strain gages. By recording changes in resistance, the forces and torques can be evaluated using Equation (2.25) in reference coordinates at the center of beams.

$$\{FT\} = \begin{Bmatrix} F_x \\ F_y \\ F_z \\ T_x \\ T_y \\ T_z \end{Bmatrix} = \begin{bmatrix} C_{11} & C_{12} & C_{13} & C_{14} & C_{15} & C_{16} \\ C_{21} & C_{22} & C_{23} & C_{24} & C_{25} & C_{26} \\ C_{31} & C_{32} & C_{33} & C_{34} & C_{35} & C_{36} \\ C_{41} & C_{42} & C_{43} & C_{44} & C_{45} & C_{46} \\ C_{51} & C_{52} & C_{53} & C_{54} & C_{55} & C_{56} \\ C_{61} & C_{62} & C_{63} & C_{64} & C_{65} & C_{66} \end{bmatrix} \begin{Bmatrix} SG0 \\ SG1 \\ SG2 \\ SG3 \\ SG4 \\ SG5 \end{Bmatrix} = [C]\{SG\} \tag{2.25}$$

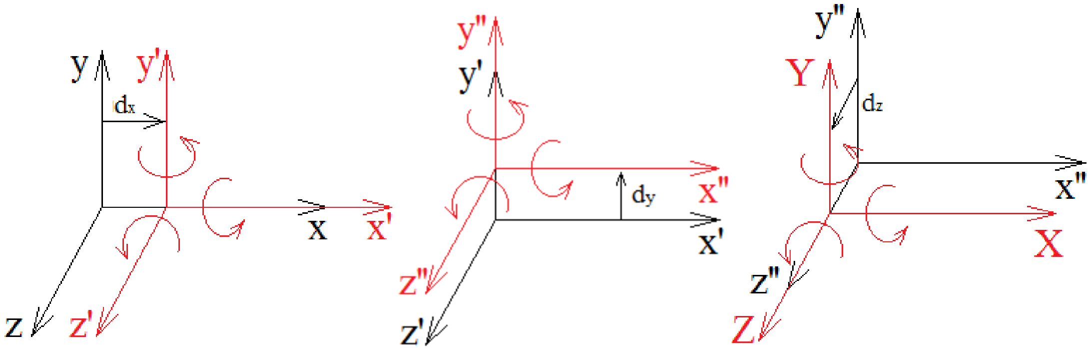

Figure 2.19 Coordinate transformation according to translational displacements.

where $\{SG\}$ are strain gage vectors in voltages, and C matrix is calibration matrix at the center of beams.

According to ATI manuals, all sensing ranges and resolutions of the forces and torques are measured at a point, which is sketched at center surface of tool adapter plate. This point is defined as factory point of origin and aligned with pitching axis of wings for all cases considered. Therefore, C matrix needs to be transformed from center of beams to factory point of origin by either translation or rotation or both, which will be discussed in detail. If point of origin is different than factory point of origin, the same approach to transform C matrix is applicable; sensing ranges of force transducer have to be adjusted to avoid strain gauge saturation.

2.5.1.1 Calibration matrix subject to coordinate translation

First, consider point of origin in Cartesian coordinates is translated to positions where distances of *dx*, *dy*, and *dz* are displaced in order, as shown in Figure 2.19 from the left to the right.

The coordinates in black color at the left of Figure 2.19 represent the coordinates at center of beams. After moving distance of *dx*, new coordinates are defined and marked with apostrophe in red color. Forces with respect to new coordinates stay the same; however, torques with respect to y-axis and z-axis are changed. New forces and torques are given in Equation (2.26). Similar consideration is also applied to the other two axis-translations.

$$F_x' = F_x,\; F_y' = F_y,\; F_z' = F_z, \tag{2.26}$$

$$T_x' = T_x,\ T_y' = T_y + \left(F_z d_x\right),\ T_z' = T_z - \left(F_y d_x\right)$$

New coordinates after displacement of *dy* are obtained and denoted by double apostrophes in red color, as shown at the middle of Figure 2.19, which results in new forces and torques, as given in Equation (2.27).

$$\begin{gathered} F_x'' = F_x',\ F_y'' = F_y',\ F_z'' = F_z' \\ T_x'' = T_x' - F_z' d_y,\ T_y'' = T_y',\ T_z'' = T_z' + \left(F_x' d_y\right) \end{gathered} \tag{2.27}$$

The last coordinate translation is accomplished by moving coordinates along z-axis with distance of *dz* and denoted using capital letters, as shown in red color at the right of Figure 2.19. The corresponding new forces and torques are given in Equation (2.28).

$$\begin{gathered} F_X = F_x'',\ F_Y = F_y'',\ F_Z = F_z'' \\ T_X = T_x'' + \left(F_y'' d_z\right),\ T_Y = T_y'' - \left(F_x'' d_z\right),\ T_Z = T_z'' \end{gathered} \tag{2.28}$$

Combining Equations (2.26)-(2.28) gives forces and torques in turns of matrix, shown in Equation (2.29). This matrix is denoted by [C_T]; the force and torques before coordinate translation are represented by {*FT*}.

$$\left\{FT\right\}_T = \begin{Bmatrix} F_X \\ F_Y \\ F_Z \\ T_X \\ T_Y \\ T_Z \end{Bmatrix} = \begin{bmatrix} 1 & 0 & 0 & 0 & 0 & 0 \\ 0 & 1 & 0 & 0 & 0 & 0 \\ 0 & 0 & 1 & 0 & 0 & 0 \\ 0 & d_z & -d_y & 1 & 0 & 0 \\ -d_z & 0 & d_x & 0 & 1 & 0 \\ d_y & -d_x & 0 & 0 & 0 & 1 \end{bmatrix} \begin{Bmatrix} F_x \\ F_y \\ F_z \\ T_x \\ T_y \\ T_z \end{Bmatrix} = \left[C_T\right]\left\{FT\right\} \tag{2.29}$$

Substituting Equation (2.25) to Equation (2.29), calibration matrix about new point of origin is obtained in Equation (2.30), and related to the voltage measured at center of beams.

$$\left\{FT\right\}_T = \left[C_T\right]\left[C\right]\left\{SG\right\} = \left[C_T\right]_{new}\left\{SG\right\} \tag{2.30}$$

2.5.1.2 Calibration matrix subject to coordinate rotation

Now consider point of origin in Cartesian coordinate is rotated. As shown in Figure 2.20, coordinates in black color indicate coordinates before rotating; coordinates in red color are results after rotating. The angle of rotation is positive in counterclockwise direction and denoted using its rotation axis. For example, θx is a rotation angle around x-

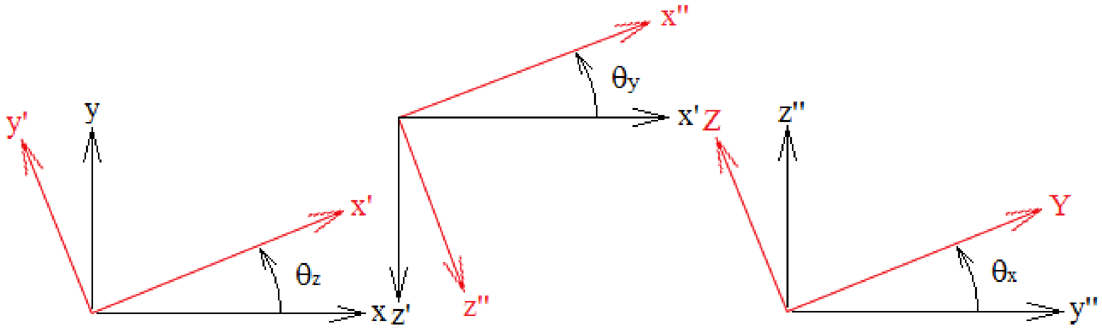

Figure 2.20 Coordinates transformation according to rotational displacements.

axis in x-y plane. Moreover, coordinates are first rotated by angle θz along z-axis, which is shown at the left of Figure 2.20, and denoted with an apostrophe. Following by the rotation angle of θy along y-axis, as shown at the middle of Figure 2.20, new coordinates are obtained with double apostrophes. Finally, coordinates are rotated by angle of θx along x-axis, which is shown with upper case in the right of Figure 2.20. The consequence due to rotations in θz, θy, and θx are formulated in Equations (2.31)-(2.33), respectively.

$$\{p'\}=\begin{Bmatrix} x' \\ y' \\ z' \end{Bmatrix}=\begin{bmatrix} \cos\theta_z & \sin\theta_z & 0 \\ -\sin\theta_z & \cos\theta_z & 0 \\ 0 & 0 & 1 \end{bmatrix}\begin{Bmatrix} x \\ y \\ z \end{Bmatrix}=\left[C_{rz}\right]\{p\}, \tag{2.31}$$

$$\{p''\}=\begin{Bmatrix} x'' \\ y'' \\ z'' \end{Bmatrix}=\begin{bmatrix} \cos\theta_y & 0 & -\sin\theta_y \\ 0 & 1 & 0 \\ \sin\theta_y & 0 & \cos\theta_y \end{bmatrix}\begin{Bmatrix} x' \\ y' \\ z' \end{Bmatrix}=\left[C_{ry}\right]\{p'\}, \tag{2.32}$$

$$\{P\}=\begin{Bmatrix} X \\ Y \\ Z \end{Bmatrix}=\begin{bmatrix} 1 & 0 & 0 \\ 0 & \cos\theta_x & \sin\theta_x \\ 0 & -\sin\theta_x & \cos\theta_x \end{bmatrix}\begin{Bmatrix} x'' \\ y'' \\ z'' \end{Bmatrix}=\left[C_{rx}\right]\{p''\}, \tag{2.33}$$

where [C_{rz}], [C_{ry}], and [C_{rx}] are defined as rotation matrix due to rotation axis at z-axis, y-axis, and x-axis, respectively. Since each torque is evaluated from 6 channels of strain gauges and not from three measured forces, {p} vectors can represent both force and torque in three individual directions.

Consider the coordinate rotation is conducted in a sequence of θz, θy, and θx, from the beginning of rotation to the end of rotation the resultant forces or torques can be expressed in Equation (2.34) by multiplying Equation (2.33), (2.32), and (2.31) in sequence.

$$\begin{aligned}\{P\} &= [C_{rx}][C_{ry}][C_{rz}]\{p\} \\ &= \begin{bmatrix} \cos\theta_y \cos\theta_z & \cos\theta_y \sin\theta_z & -\sin\theta_y \\ \sin\theta_x \sin\theta_y \cos\theta_z - \cos\theta_x \sin\theta_z & \sin\theta_x \sin\theta_y \sin\theta_z + \cos\theta_x \cos\theta_z & \sin\theta_x \cos\theta_y \\ \cos\theta_x \sin\theta_y \cos\theta_z + \sin\theta_x \sin\theta_z & \cos\theta_x \sin\theta_y \sin\theta_z - \sin\theta_x \cos\theta_z & \cos\theta_x \cos\theta_y \end{bmatrix} \begin{Bmatrix} x \\ y \\ z \end{Bmatrix} \\ &= [C_r]\{p\} \end{aligned} \tag{2.34}$$

Consider both force and torque, the rotational calibration matrix [C_R] is obtained in Equation (2.35), which is different from the translational calibration matrix [C_T] in Equation (2.29).

$$\{FT\}_R = \begin{Bmatrix} F_X \\ F_Y \\ F_Z \\ T_X \\ T_Y \\ T_Z \end{Bmatrix} = \begin{bmatrix} [Cr] & 0 \\ 0 & [Cr] \end{bmatrix} \begin{Bmatrix} F_x \\ F_y \\ F_z \\ T_x \\ T_y \\ T_z \end{Bmatrix} = [C_R]\{FT\} \tag{2.35}$$

Substituting Equation (2.25) into Equation (2.35) the corrected calibration matrix due to coordinate rotation is obtained in Equation (2.36).

$$\{FT\}_R = [C_R][C]\{SG\} = [C_R]_{new}\{SG\} \tag{2.36}$$

2.5.1.3 Calibration matrix due to both translation and rotation

We have considered the corrected calibration matrix due to coordinate translation and coordinate rotation individually in preceding sections. Now we are looking for a general form of calibration matrix with respect to an arbitrary point of origin, which is transformed from the center of beams. The procedure is simply combining results discussed before, first by coordinate translation and then by coordinate rotation, the consequence is shown in Equation (2.37). It is assumed that the coordinate translation and coordinate rotation are independent to each other, and the influences on forces and torques are linear.

$$\{FT\}_{new} = \begin{Bmatrix} F_X \\ F_Y \\ F_Z \\ T_X \\ T_Y \\ T_Z \end{Bmatrix} = [C_T][C_R] \begin{Bmatrix} F_x \\ F_y \\ F_z \\ T_x \\ T_y \\ T_z \end{Bmatrix} = [C_T][C_R][C]\{SG\} = [C]_{new}\{SG\} \qquad (2.37)$$

2.5.1.4 Verification of calibration matrix transformation

The approach of calibration matrix transformation was established and discussed previously, now we are going to verify this approach. The example demonstrated here is based on the data stored on CD, packed with force transducer Nano43, from ATI Company. The calibration matrix at center of beams, shown in Equation (2.38), was scaled and given in the text file named with sensor series number, for instance FT12311.cal. Converted with scaling factors found in the same CD, the calibration matrix before being scaled can be found and saved into MAT-file for MATLAB user.

$$[C] = \begin{bmatrix} -0.34399/S1 & -0.19774/S1 & -0.19564/S1 & 36.23983/S1 & 1.30320/S1 & -36.36261/S1 \\ -0.02564/S2 & -42.11838\ /S2 & -0.27911/S2 & 20.99353/S2 & -0.68996/S2 & 21.13467/S2 \\ 21.16568/S3 & 0.50868/S3 & 21.04355\ /S3 & -0.04462/S3 & 21.40718/S3 & -0.59299/S3 \\ -0.17765/S4 & -0.27939/S4 & 36.97439/S4 & 0.18729/S4 & -37.27381/S4 & 0.93695/S4 \\ -41.65443/S5 & -1.22311/S5 & 21.04006/S5 & -0.27136\ \ /S5 & 21.13962/S5 & -0.13057/S5 \\ 0.13396/S6 & -21.41515/S6 & 0.23018/S6 & -21.22951\ /S6 & 0.66187\ /S6 & -21.29024/S6 \end{bmatrix} \qquad (2.38)$$

where *Si* are scaling factors for channel *i*,

$$\begin{Bmatrix} S1 \\ S2 \\ S3 \\ S4 \\ S5 \\ S6 \end{Bmatrix} = \begin{Bmatrix} 16.3268754027456 \\ 16.3268754027456 \\ 13.8694114323035 \\ 1.65167278491634 \\ 1.65167278491634 \\ 1.14951433321416 \end{Bmatrix}$$

Equation (2.39) gives the translational and rotational displacements in three axes, which is found in the same text file. The *D* and *R*, represent displacement in coordinate translation and rotation, respectively, following the corresponding axis.

$$\begin{bmatrix} Dx & Dy & Dz & Rx & Ry & Rz \end{bmatrix} = \begin{bmatrix} 0 & 0 & 4.3434 & 0 & 0 & 0 \end{bmatrix} \qquad (2.39)$$

After translating and rotating coordinates from center of beams to the factory point of origin, the calibration matrix with respect to this new location is then evaluated, as shown in Equation (2.40). It is then compared to the estimation from ATIDAQFT.NET software by ATI under Tools\Calibration Info, out precision is found to be at least five digits, which indicates our approach is applicable. The consistent values are underlined.

$$[C]_{new} =$$

$$\begin{bmatrix} \underline{-0.02106894}2 & \underline{-0.012111319} & \underline{-0.011982696} & \underline{2.219642}7 & \underline{0.079819314} & \underline{-2.2271628} \\ \underline{-0.001570416}8 & \underline{-2.579696}2 & \underline{-0.017095126} & \underline{1.2858265} & \underline{-0.04225915}7 & \underline{1.294471}2 \\ \underline{1.5260690} & \underline{0.03667639}4 & \underline{1.517263}3 & \underline{-0.0032171516} & \underline{1.5434815} & \underline{-0.042755238} \\ \underline{-0.11437857} & \underline{-11.37380}8 & \underline{22.31177}5 & \underline{5.698253}2 & \underline{-22.75085}7 & \underline{6.189679}5 \\ \underline{-25.128030} & \underline{-0.6879237}2 & \underline{12.790682} & \underline{-9.8050}901 & \underline{12.45222}8 & \underline{9.59440}58 \\ \underline{0.11653617} & \underline{-18.629737} & \underline{0.20024108} & \underline{-18.468242} & \underline{0.57578229} & \underline{-18.52107}3 \end{bmatrix} \quad (2.40)$$

2.5.2 Butterworth Filter

Butterworth filter is a type of infinite impulse response (IIR) filter. Unlike the Chebyshev and Elliptic filters, the flat pass-band of the Butterworth filter ensures information is passed without distortion. Being aware of Butterworth filter is phase lag. For instance, first order filter produces phase lag of 45° at cutoff frequency, the magnitude is attenuated by 3 dB. Second order filter produces twice larger phase lag than first order filter (i.e., 90°, and so on). Hence, to prevent phase distortion, zero-phase Butterworth filter is considered.

Higher order Butterworth filter typically has transfer function composed of first order, or second order, or both, whose transition band is much shorter in order to retain frequency of interest precisely. Moreover, lower order filter yields slower roll-off (i.e., wider transition band), resulting in less noise attenuation than higher order filter. The selection of order of filter in this study depends on the ability of removing noises without introducing any digital interference.

To have better idea in determining the order of the filter, we inspect the response of motion acceleration. As shown in Figure 2.21 is the motion acceleration with pitch rate 76.4 deg/s, for example, higher order filter generates stronger overshoots oscillating around the startup and the end of motion acceleration, and is capable of maintaining its magnitude. These overshoots would be confusing with physical vibration and noises, therefore, utilization of first order filter is recommended. By the way, all filtered profiles

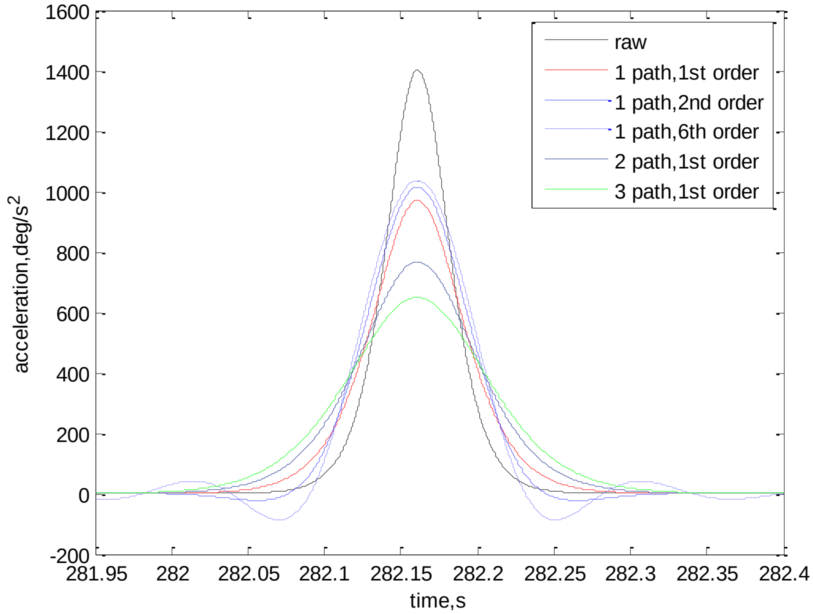

Figure 2.21 Motion acceleration response to a zero-phase low-pass Butterworth filter.

in Figure 2.21 are presented using low-pass filter with a cutoff frequency to retain 90% of frequency content of motion acceleration.

Due to slower roll-off, the first-order filter may not be able to sufficiently remove structural vibration/noise at phases higher than the cutoff frequency, which gives demands in multi-path filtering. Figure 2.21 also shows multi-path effects. Increasing number of path enlarges the width of profile and reduces the magnitude. Force data presented in the study are obtained using two-path filter.

2.5.3 Cutoff Frequency

The conclusion of the preceding discussion is the use of low-pass zero-phase first-order two-path Butterworth filter. Now curiosity in finding cutoff frequency is arisen, which intuitionally depends on frequency region of interest, and noise frequency and its strength. However, at current stage, frequency region of interest and noise source are unknown, and how noise interferes with force measurement is uncertain.

Practically, we are going to assume that there is no noise and frequency region of interest is found from driven source, such as wing kinematics. The cutoff frequency is determined by capability of preserving wing kinematics. We particularly inspect motion

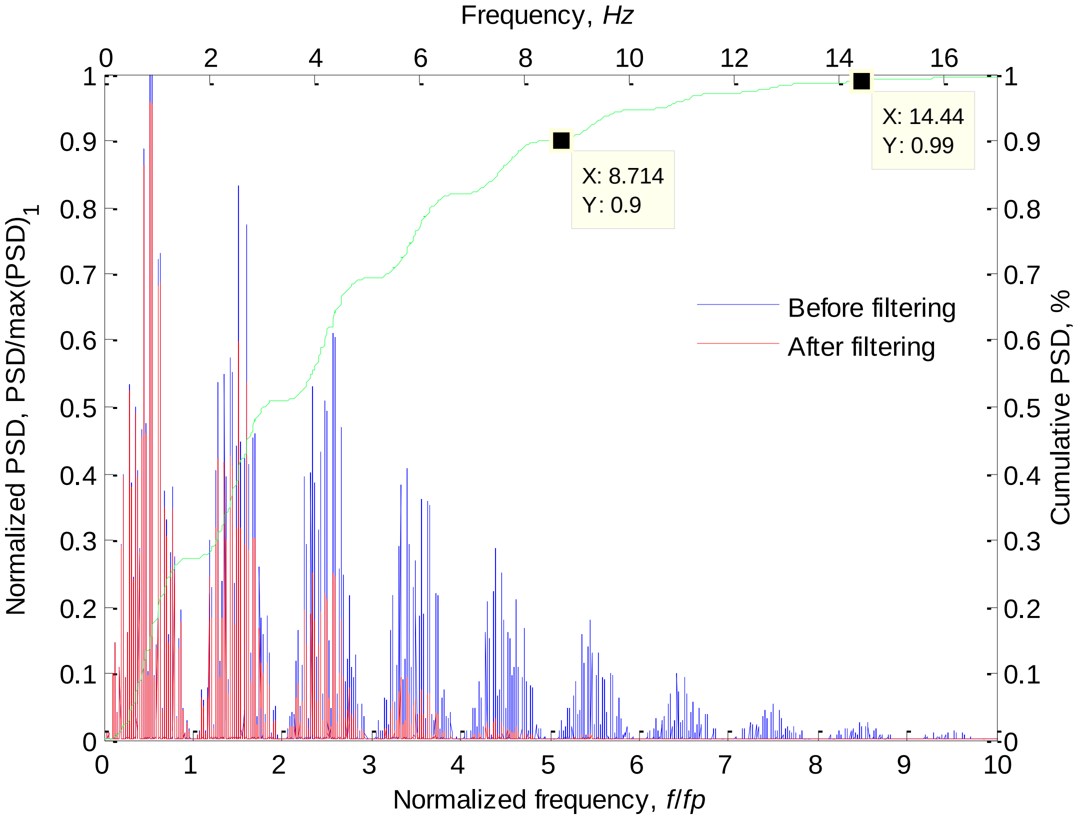

Figure 2.22 Filtering effect on frequency response of motion acceleration from wing kinematics with pitch rate 76.4 °/s.

acceleration due to two reasons. The first reason is that motion acceleration contains considerable frequency region compared to lower-order derivatives of wing kinematics. As possibly as most motion acceleration is maintained; motion position and velocity would be less influenced by filtering. The second reason is that motion acceleration is theoretically associated with non-circulatory force, playing as a critical role of generating significant aerodynamics.

Figure 2.22 shows spectrum distribution of motion acceleration by the pitch rate of 76.4 °/s. A non-dimensional frequency ($f_P = f/f_p = \alpha'_m/\alpha_m t$), is used for abscissa, which is equivalent to the time normalized with pitch time. Ordinate on the left is power spectral density (PSD) and on the right shows the accumulation of PSD. The former is normalized with the maximum magnitude of the first frequency envelope; the latter would indicate energy content at specific phase. As shown in Figure 2.22, frequency envelopes are coupled with pitch frequency; the magnitude decaies with increasing frequency. In

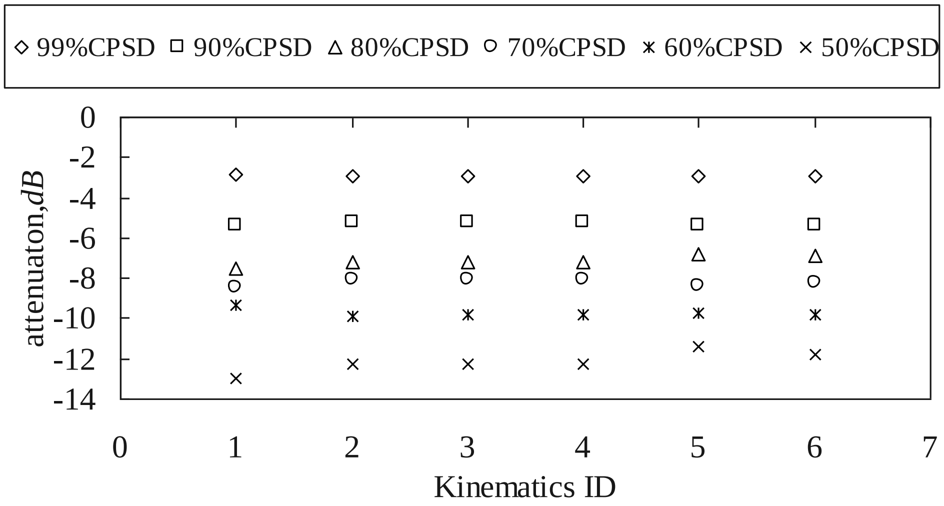

Figure 2.23 Effect of filtering on signal magnitude.

addition, data cursor shown in the figure reveals 99-percent energy/information of kinematics is contained within frequency of 14.4 Hz, which would be selected as cutoff frequency if determinative noise is removable after applying digital filter. An effect of filtering is also presented by using zero-phase first-order two-path Butterworth filter to retain 90% of kinematics. Without changing the coupling behaviors of frequency envelope, the information with frequency higher than cutoff frequency is attenuated; most information is retained at frequency lower than cutoff frequency. For detail spectrum analysis in use, see Appendix D.

Since the determination cutoff frequency is presumably unnecessary to include all information from kinematics, effects of filtering becomes important, especially for the investigation of non-circulatory effect. Figure 2.23 and Figure 2.24 show effects of filtering on magnitude and width of motion acceleration, respectively. All kinematics of interest have the same effect when the cutoff frequency is chosen to maintain at the same level of energy/information. In this study, the cutoff frequency for all force data was selected to retain 90 % of motion acceleration. See Appendix E for more information on cutoff frequency.

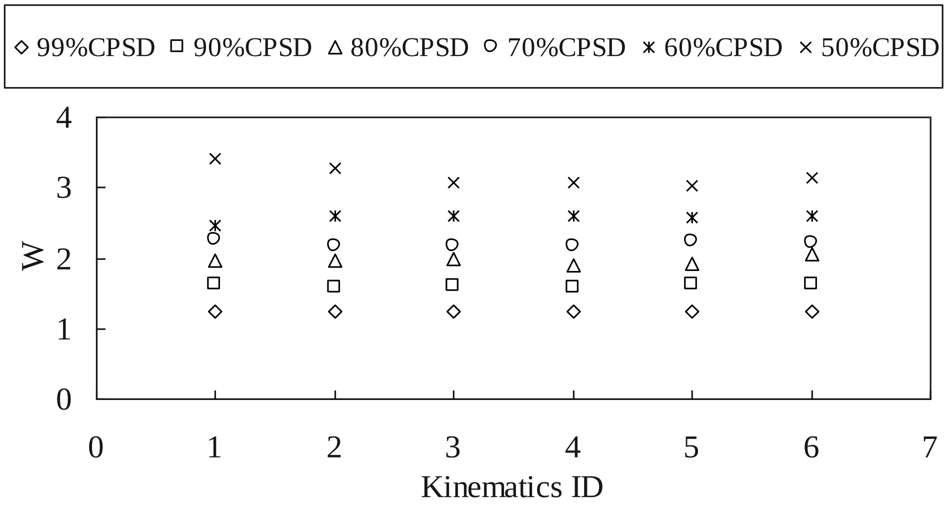

Figure 2.24 Effect of filtering on signal width.

2.5.4 Noise

The selection of cutoff frequency depends not only on preservation of energy according to wing kinematics, but also on the capability of removing noises. The former was discussed in a previous section; the latter can only be achieved after identifying noise sources. There are two types of noises contributed to force transducer. One is electronic magnet interference resulting from imperfect grounded devices; this type of noises could be contributed from power-line, AC motor controller, and stepper motor controller. The other is mechanical vibration, which may be induced from the transmission mechanism of Rotary Table and wing resonance while interacting with dynamic fluid.

Figure 2.25 shows an example of force signal in terms of power spectrum density after Fourier transform; the signals are the measured force data of rectangular wing pitching at leading edge in running water and air. The wing kinematics was programmed for the pitch rate of 76.4 °/s and repeated 20 times. As shown in Figure 2.25, most noises are detected from the vibration by transmission mechanism of Roraty Table in a frequency region higher than 50 Hz. Since the frequency region of interest for the present kinematics is 15 Hz, in order to retain 99% of information, the vibration from the Roraty Table has less influence on the frequency region of interest. In addition, there are two resonant frequencies of the clamped wing. One is 15 Hz for the wing partially immersed

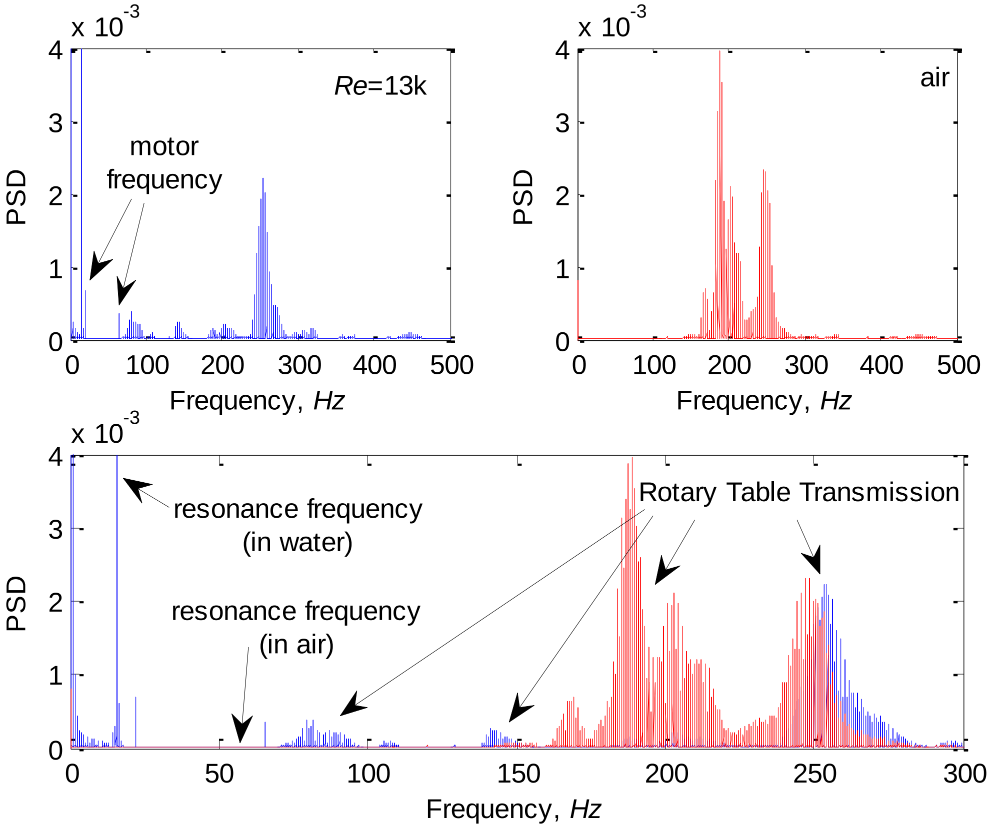

Figure 2.25 An example of noise distribution. *Based on a leading-edge-pivot rectangular wing, the input signal is the measured Fy in transducer frame of reference.*

in the water, which overlaps with the frequency region of interest and enforces the cutoff frequency to be lower within the frequency region of interest. The other is 50 Hz for the wing in the air, as expected to be higher than the one in the water. The motor frequency is harmonically distributed and may interfere with the measured force, which comes from AC motor controller.

Figure 2.26 shows the force data in response to the filter with cutoff frequency of 8.7 Hz for 90% preservation of information; the force data contains 20 kinematic samples and were obtained using wing kinematics with pitch rate 76.4 °/s in the still water. The distribution profile is very similar to Figure 2.22 where only mass acceleration was considered, indicating the importance of non-circulatory effect under this circumstance. The noises with frequencies higher than cutoff frequency are removed to an acceptable level. The structural resonance was detected at frequency higher than 15Hz, which is discussed below.

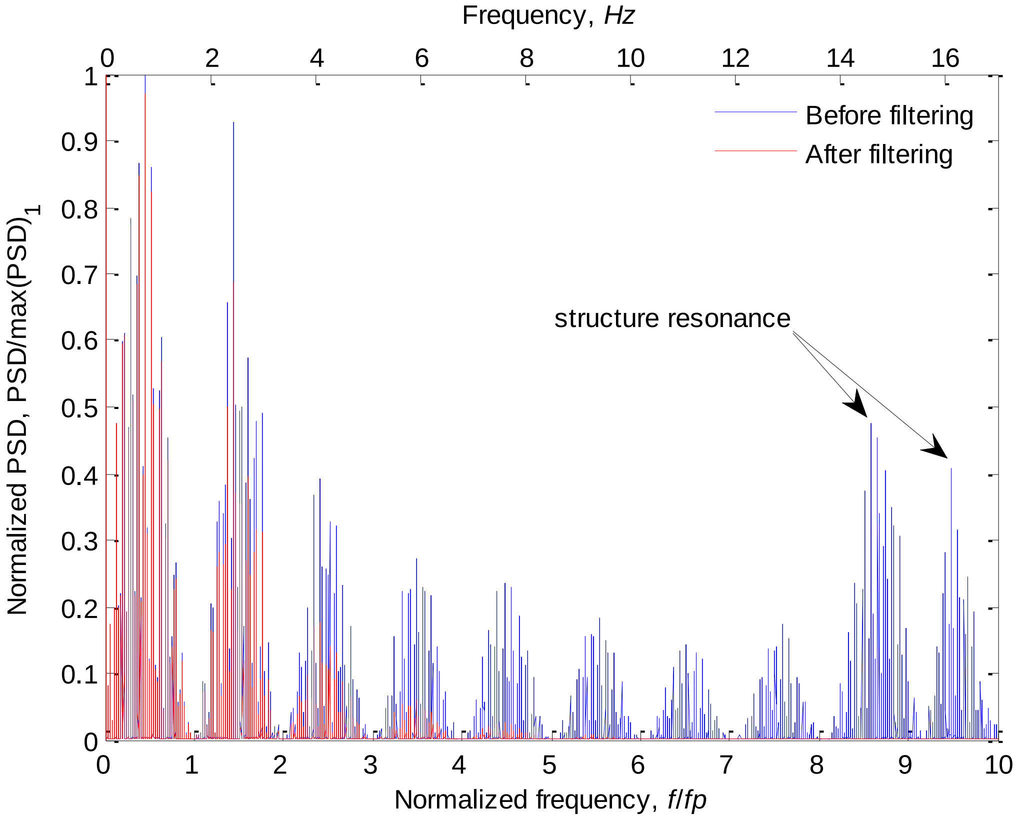

Figure 2.26 Filtering effects on frequency response of normal force in transducer frame of reference. *The input signal is the measured Fy from a leading-edge-pivot rectangular wing in still water.*

2.5.4.1 Structure Resonance

The resonant frequencies (also called fundamental frequencies or natural frequencies) of wings in water and air were determined by comparing the spectra of unsteady force data F_y with wing and without wing; the force data contained 20 wing-kinematic samples. The structural resonance of wing depends on surrounding fluid properties (e.g. density and temperature); the resonant frequency should be independent of flow condition (e.g. still water and running water) and wing kinematics. The spectrum analysis is given in Appendix D.

Table 2.3 shows resonant frequency depends on pivot-axis location and wing geometry, as well as surrounding fluid, which were determined and averaged from different flow conditions and wing kinematics. The wings at both leading-edge and trailing-edge pivot axes give lower resonant frequeny than the wings at mid-chord pivot axis; the wings in the water have lower resonant frequency than the wings in the air. Additionally, the resonant frequencies of triangular wing are higher than trapezoidal wing and rectangular wing. These resonant frequencies are higher than 15 Hz, which would justify the cutoff frequency.

2.5.4.2 Sensor Drift

Drift in force transducer is mainly caused by the heat transported from two media. One is a metal handle rod, which was attached with Rotary Table and conducted the heat to the sensor by the Rotary Table after intensive operation. The other is our hand-temperature. While being affixed to sensor adapter and handle rod, the force transducer increases its temperature. The former was prevented using the handle rod made of wood, which has poor thermal conductivity and electrical conductivity. The wooden rod also improves electromagnetic interference. The latter could not be avoided; therefore, we had to wait for the force transducer to dissipate the heat naturally before experiments could be conducted.

Figure 2.27 suggests force measurement to be conducted at least one hour after the assembly while Nano43 with series number FT12311 is in use. The averaged values and standard deviations were obtained every 60 seconds. Data were recorded while force transducer was at rest on a table after being held for a couple minutes by hands; no other

Table 2.3 Wing resonant frequency in water and air.

pivot axis	Rectangular wing		trapezoidal wing		Triangular wing	
	water	air	Water	air	water	air
LE	15.5(0.5)	51.4(1.8)	16.4(0.6)	53.2(0.2)	21.4(0.2)	57.1(0.5)
MC	19.4(0.1)	59.2(1.0)	22.0(0.5)	66.3(0.8)	29.2(0.6)	85.1(0.6)
TE	15.4(0.6)	51.4(1.5)	16.5(0.5)	53.2(0.2)	21.3(0.3)	56.9(0.2)

Unit is Hz; LE = leading edge; MC = mid-chord; TE = trailing edge; standard deviation is given in parentheses

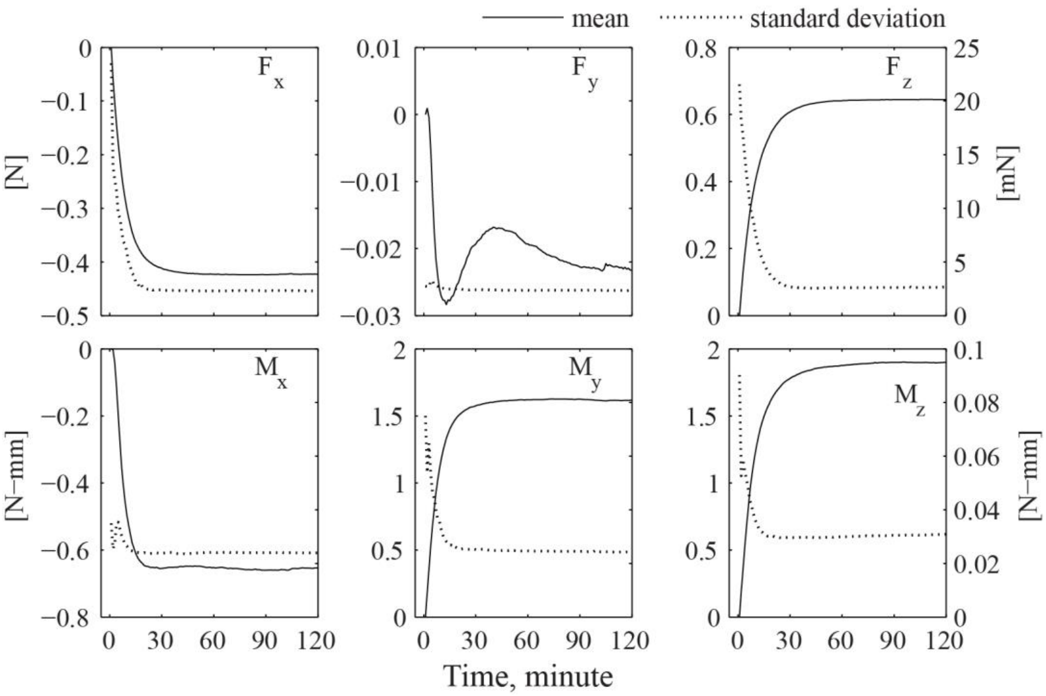

Figure 2.27 Thermal drift in force transducer on each sensor channel.

devices were attached to the force transducer. Moreover, all forces and torques except F_y and M_x are sensitive to temperature.

Figure 2.27 also reveals continuous variation of averaged F_y even though the variation of the corresponding standard deviations stay constant, this type of variation changes over time. However, the changes for the forces over one minute are within 1 mN and 0.4 N-mm for the torques, and are within the corresponding resolutions of force transducer. This observation gives the time limit for the acquisition and the demand to bias the data for every signal wing kinematics. In this study, the time durations for all wing kinematics of interest are less or about one minute.

2.5.5 Force and Torque Acquisition

Table 2.4 Types of force measurement.

Flow condition Kinematics	Running Water	Still Water	Air
Dynamic	Unsteady	Unsteady	Dynamic Tare
Static	Steady	Static Tare	Static Tare

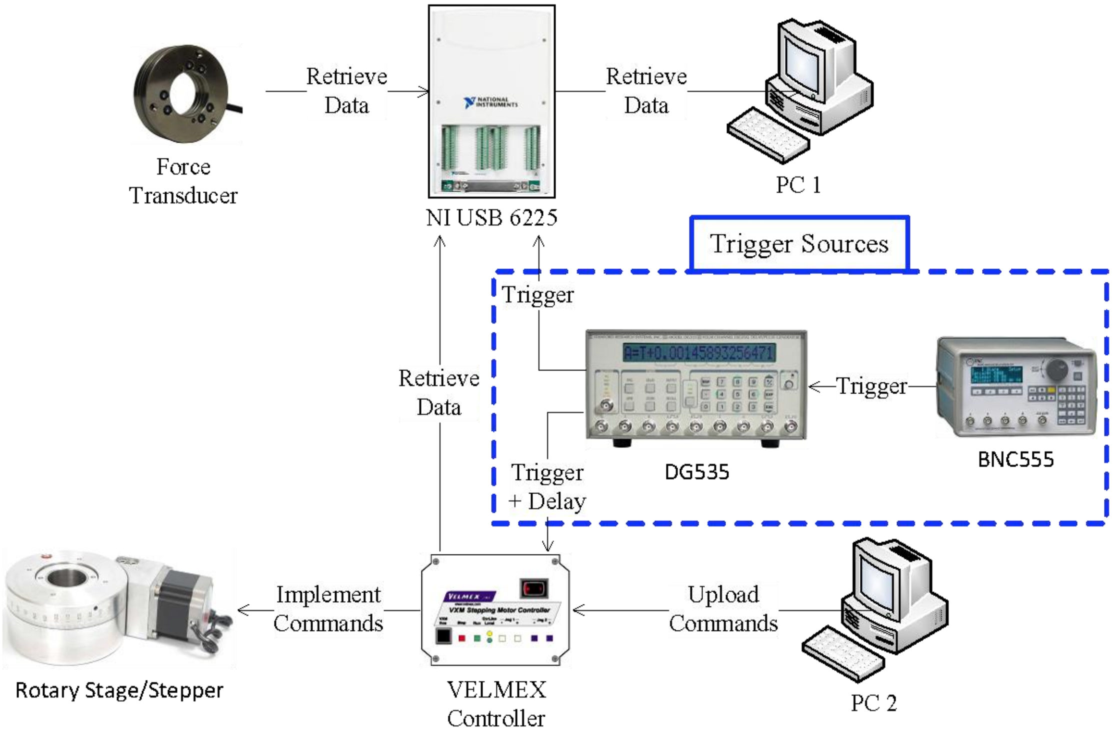

Figure 2.28 Direct force measurement control flow chart.

According to test flow condition and wing kinematics, direct force measurement is divided into four types: unsteady, steady, static tare, and dynamic tare. As shown in Table 2.4, dynamic measurement is the measurement wings move with kinematics of interest, and static measurement is the measurement wings move to fixed angle of attack without specified pitch rate. With different flow conditions, the measured data give unsteady and steady results after applying tare procedure as described in Yu.et al. (2012).

2.5.5.1 Hardware Connection

Hardware configuration for direct force measurement is shown in Figure 2.28. Two external delay/pulse generators are used as external triggers, which is BNC555 and DG535; the timing for data acquisition and wing kinematic activation is controlled through DG535. First of all, BNC555 triggers DG535 with a pulse signal of 5 VDC from Channel A. While DG535 receives the trigger signal, a pulse signal with 1.4 VDC is sent from Channel A to data acquisition board USB NI 6225 on pin PFI0 to start data acquisition. After 5 second delay DG535 delivers an active low signal from Channel CD to active the stepper motor through pin 4 on auxiliary I/O connections from VELMEX

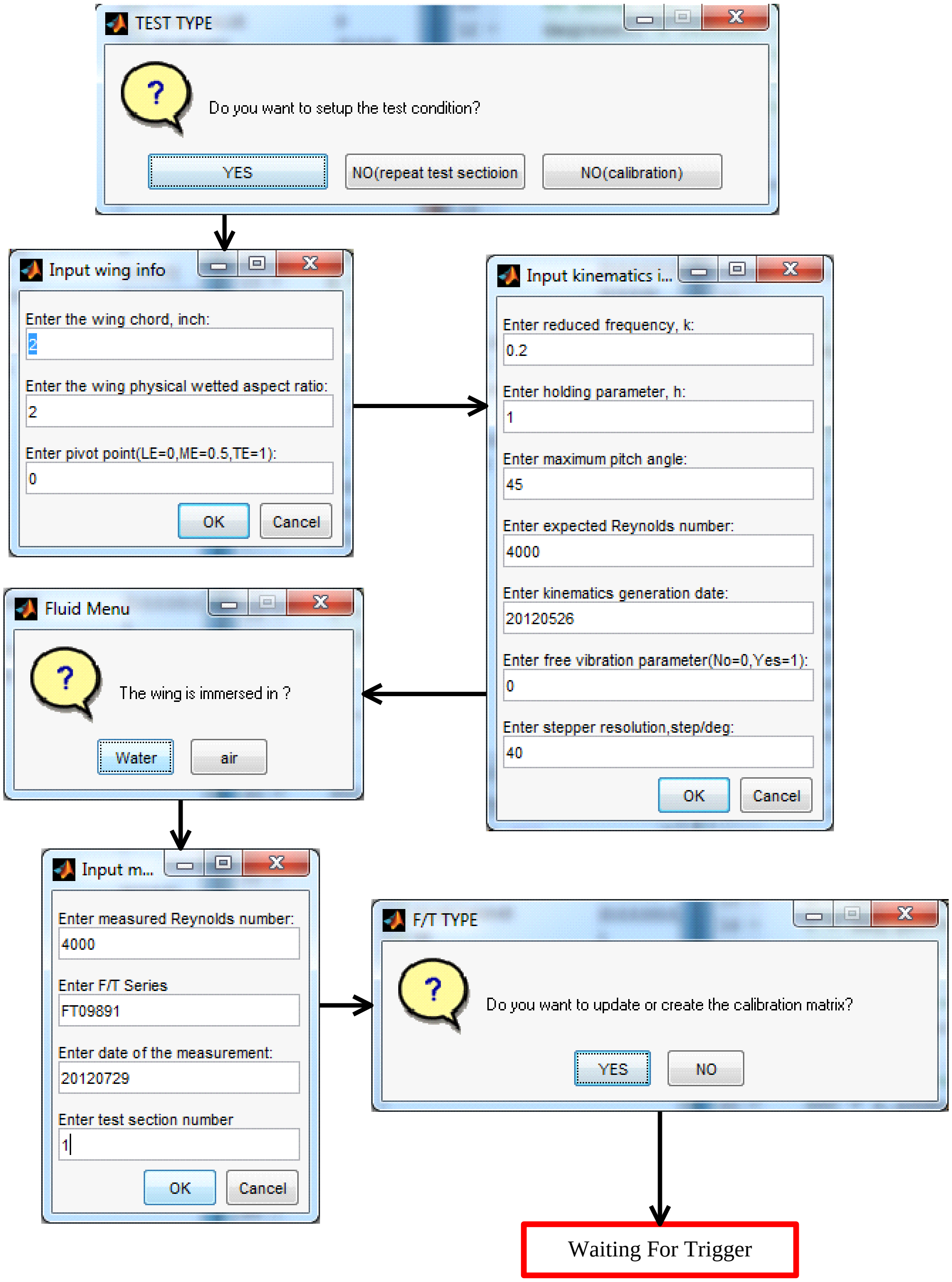

Do you want to setup the test condition?

Enter the wing chord, inch: 2

Enter the wing physical wetted aspect ratio: 2

Enter pivot point(LE=0,ME=0.5,TE=1): 0

Enter reduced frequency, k: 0.2

Enter holding parameter, h: 1

Enter maximum pitch angle: 45

Enter expected Reynolds number: 4000

Enter kinematics generation date: 20120526

Enter free vibration parameter(No=0,Yes=1): 0

Enter stepper resolution,step/deg: 40

The wing is immersed in ?

Enter measured Reynolds number: 4000

Enter F/T Series FT09891

Enter date of the measurement: 20120729

Enter test section number 1

Do you want to update or create the calibration matrix?

Figure 2.29 Input panels for force/torque acquisition.

controller. Once the stepper motor starts to run, it indexes Rotary Table following motion command stored in VELMEX controller. Positions of Rotary Table are confirmed by auxiliary pulses from VELMEX controller and recorded to USB NI 6225.

For non-triggered configuration, the delay/pulse generators are not used; signals from VELMEX controller may be recorded to USB NI 6225 as needed. This

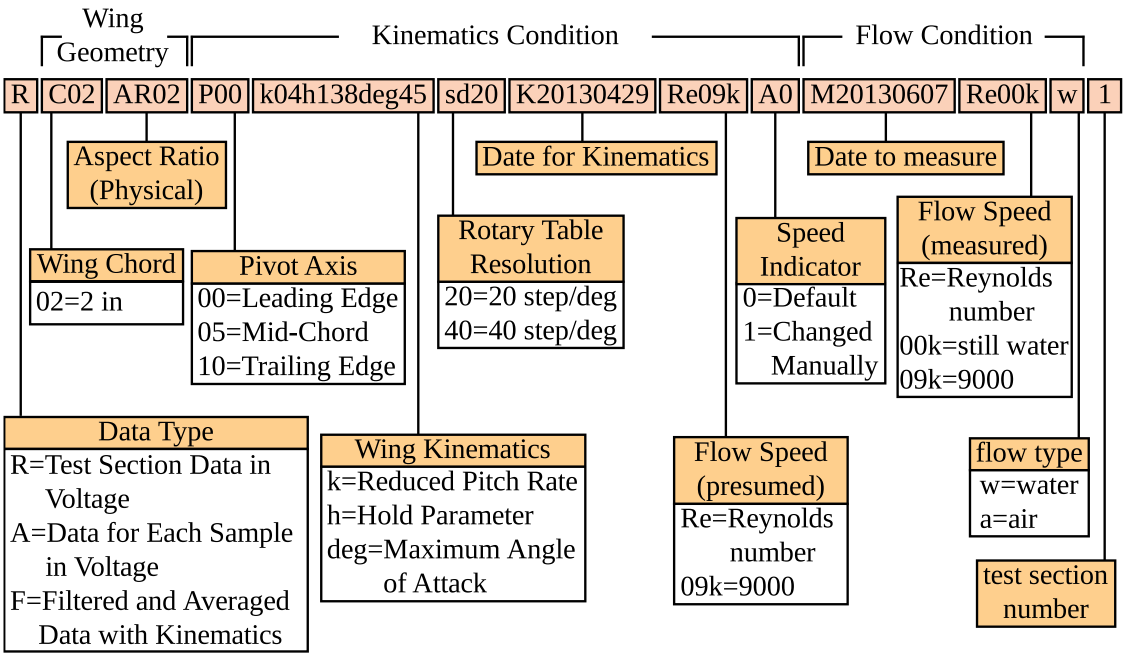

Figure 2.30 Filename notation for F/T data for unsteady measurement.

configuration is applied mostly to investigate sensor properties (such as drifting) or to calibrate hardware connection.

2.5.5.2 Data Acquisition Software Control

Acquisition software was programmed in MATLAB using section based interface in 64-bits operation system. The input dialogs shown in Figure 2.29 are for unsteady measurement, which request information of wing geometry, kinematics of interest, flow condition, and F/T series. The first three inputs give filename for raw data; the composition of filename is illustrated in Figure 2.30. The latter updates the corresponding sensor calibration matrix, which is generated using criteria demonstrated in Section 2.5.1. For steady and static-tare type measurement, only notation “Wing Kinematics” is changed with regard to type of measurement. For instance, steady measurement is notated by “Steady”. Moreover, one test section includes samples from repeated wing kinematics, and several test sections were conducted to ensure sensor drifting under measurement uncertainty within one wing kinematics.

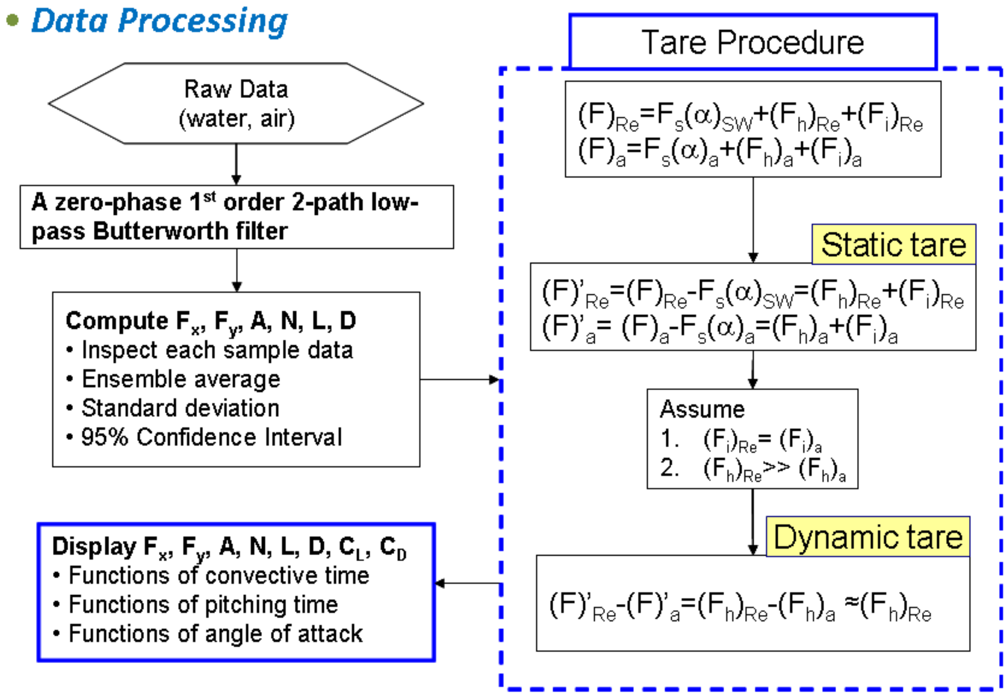

Figure 2.31 Force/torque acquisition data processing and tare procedure.

2.5.5.3 F/T Post-Processing

The post-processing includes data filtering and tare procedure, the work flow of data processing is shown in Figure 2.31. As discussed in 2.5.2, a digital filter, low pass zero-phase first-order two-path Butterworth filter, was employed, which is to avoid phase distortion, to reduce spurious oscillations introduced by the filter, and to provide sufficient attenuation of noise. The cutoff frequency was determined using criteria demonstrated in Section 2.5.3. For most kinematics of interest, cutoff frequency is to retain 90% of energy level of kinematics if not specifically stated, which gives the same level of filtering effects.

A tare procedure was employed to remove model inertia and weight contributions due to wing position and acceleration, which includes static tare and dynamic tare. The static tare is the measurement in air and still water at fixed angle of attack from 0° to 45°. The dynamic tare is the measurement in air with same kinematics in the flow experiments. The same filter and cutoff frequency as in the flow experiment were used.

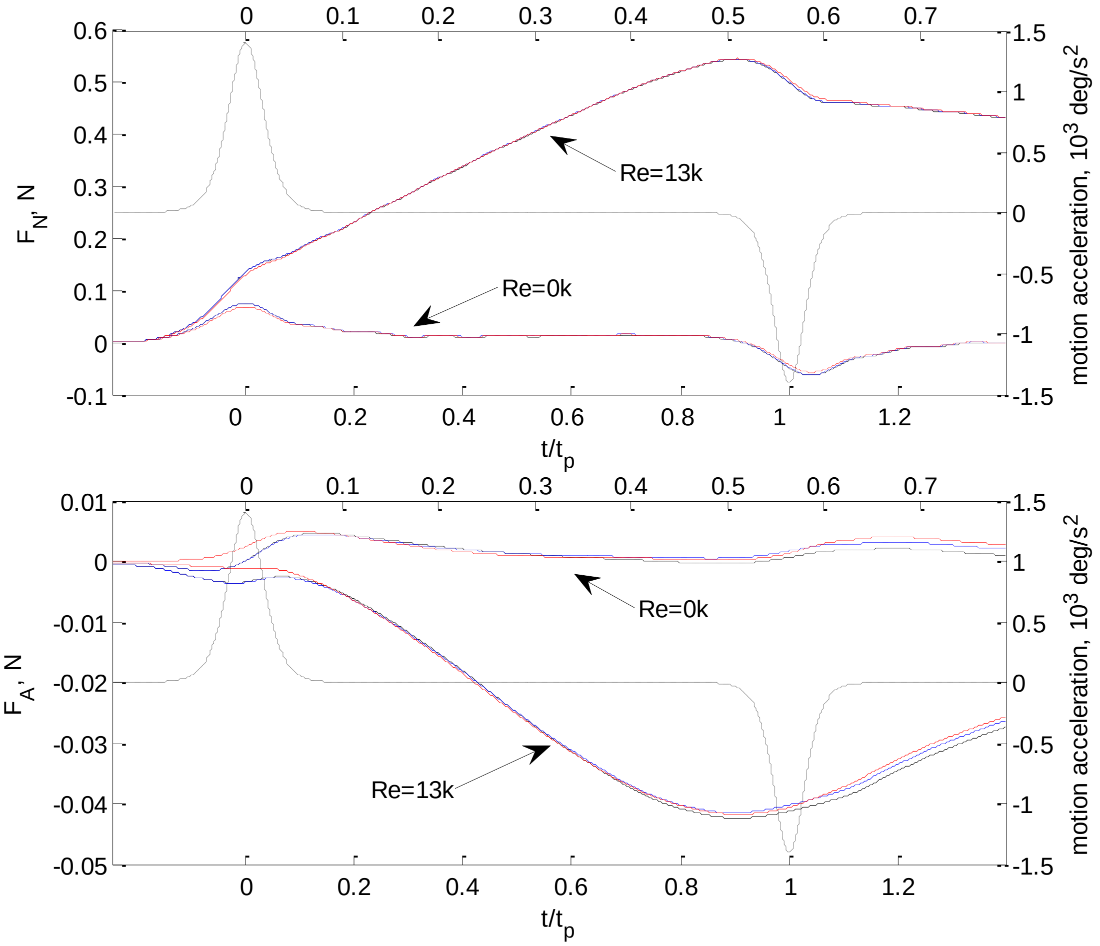

Figure 2.32 An example of force-data tare procedure. *The black curves are for initial force data after filter; the blue curves are for force data after static tare; the red curves are for force data after dynamic tare. The solid curves are for Re = 13k; the dashed curves are for Re = 0k; the dotted cures are the motion acceleration.*

Figure 2.32 shows axial and normal forces as a function of time normalized with pitch time before and after tare procedure. The force data were obtained in still water and *Re* = 13k, using rectangular wing at leading-edge axis and wing kinematics with 76.4 °/s. The force data were filtered and the average of 60 kinematic samples. As shown in Figure 2.32, the force curves are very similar before and after static tare, which is due to very small mass of the wing and mounting hardware (less than 46.2 g). There is a little difference at the phases where undergo motion acceleration after dynamic tare; the difference is less than 10 mN. See CHAPTER 5 for detail discussion of force data.

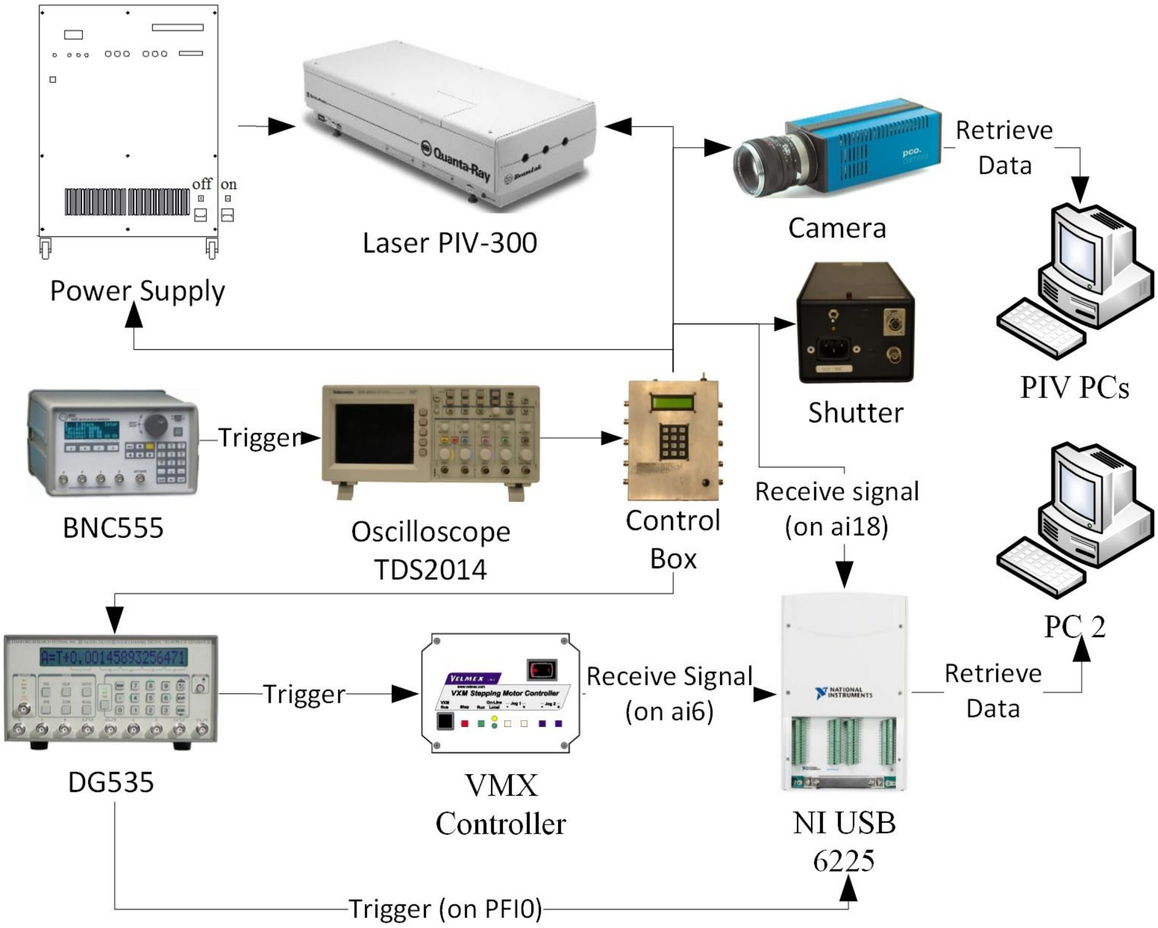

Figure 2.33 PIV system control flow chart.

2.6 PIV MEASUREMENT

Particle Image Velocimetry (PIV) applies optical technology to quantify flow field. Two aspects are considered in the study; the first is conventional PIV for two-dimensional flow field using single camera, and the second is lens-shifted stereoscopic PIV for three-dimensional flow field using two cameras.

2.6.1 Conventional PIV

Conventional PIV system includes a double-pulsed Nd-YAG laser (Spectra Physics PIV 300), light sheet optics, a dual frame digital camera (Cooke Corp. PCO.4000), computer image acquisition system and control electronics.

Figure 2.33 illustrates connections among components in PIV system. The onset of PIV acquisition was triggered by pushing run button on front panel of BNC555 pulse generator, which controls signals synchronizing with laser pulses. The frequency of laser pulse is 10Hz. These signals go through Control Box to laser chamber and power supply, and to Shutter and Camera for synchronization with wing kinematics. Numbers of images (N_i) and laser pulses within one pitch up-hold-return motion (N_p) were specified to Control Box. The phase where images were taken was controlled through DG535 pulse generator, which was also used to trigger NI USB 6225 data acquisition board and VMX controller for wing kinematics. Data from either NI USB 6225 or Camera were saved to personal computers for post-processing.

In addition, PCO.4000 camera was installed underneath the test section of water channel and equipped with either Nikon 105-mm or PC-E 85 mm Micro-Nikkor lens. The camera had 14 bits dynamics at 4008 × 2672 pixels. In order to minimize particle loss due to spanwise flow, the exposure time was specified to have particle displacement of 3 pixels in free stream.

The seedings for PIV data were titanium dioxide particles (Sigma-Aldrich) with a diameter of less than 5μm. To produce a uniform distribution of particles, a small amount (~1 cc) of dispersant (DARVAN CN, Vanderbilt) was added to a one-gram-particle solution. The dispersant also helped particles suspend in the water for a much longer period. We also used Sonicator to break down huddled particles and improve mixing quality.

2.6.1.1 Synchronization

There were two parts of synchronizations considered in the study: one was wing kinematics synchronized with laser pulses and the other one was phase of interest synchronized with camera/shutter. The phase of interest was the timing where images were taken and usually within wing kinematics.

To synchronize wing kinematics with laser pulses, firstly we needed to measure a period of wing kinematics (T_{VMX}) and then multiply by pulse frequency, which is 10Hz; the resultant value (N_p) was rounded and becomes one of inputs to Control Box. N_p

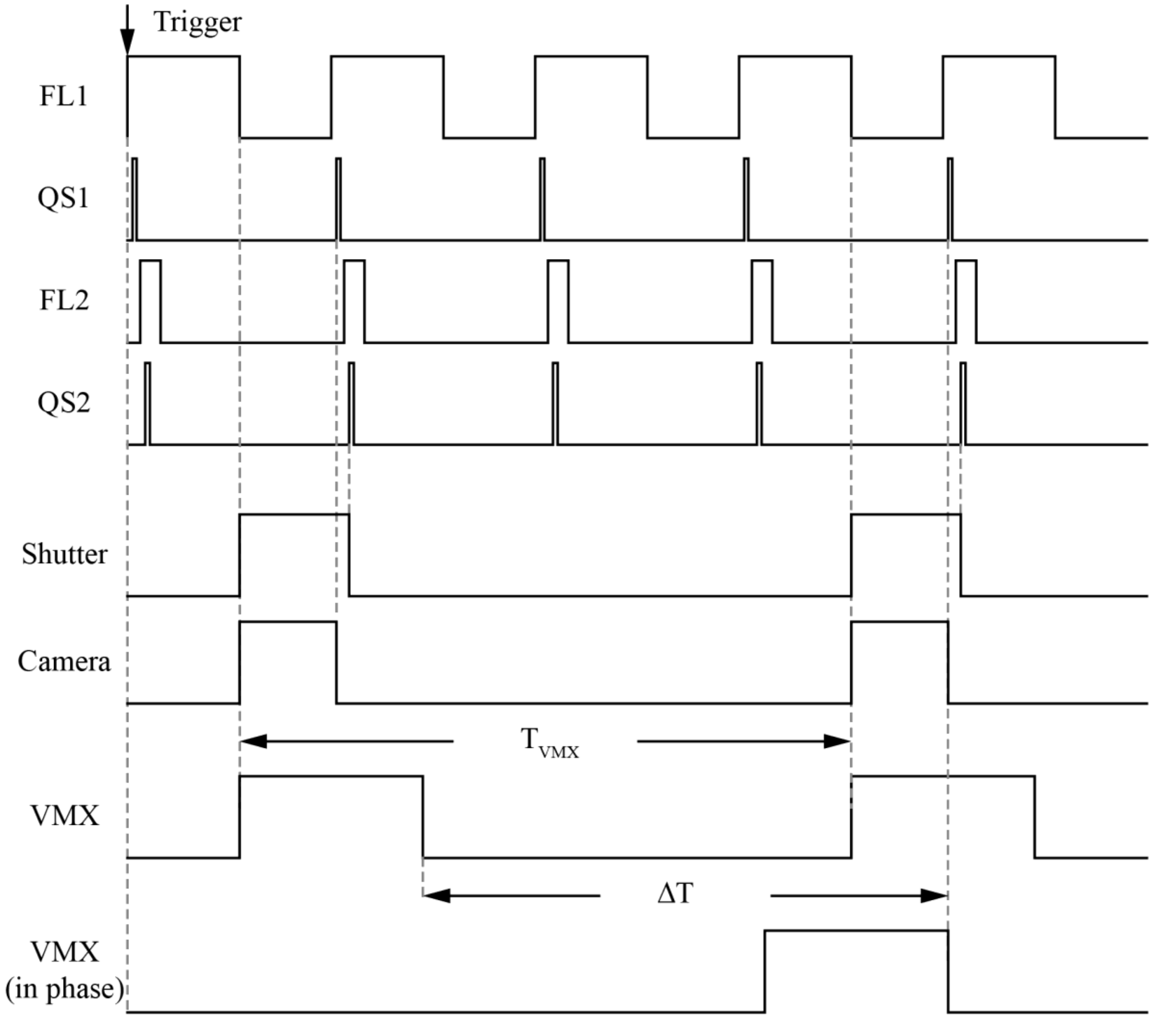

Figure 2.34 Illustration of synchronization signals among laser pulses, wing kinematics, and camera.

indicated number of laser pulses occur within wing kinematics. Dividing T_{VMX} by N_p gave a period of signals for BNC pulse generator (T_0), which had to be greater than 1/10. The parameters T_{VMX}, N_p, and T_0 were the resultant of the first part of synchronizations. Figure 2.34 shows an example of signal distribution among laser pulses and wing kinematics. Once the first part of synchronization was complete, camera and shutter were designed to work together with wing kinematics.

To synchronize the phase of interest with camera/shutter, we aligned a falling edge of signal from VMX with a falling edge of signal from Camera. The difference in time (ΔT) became a delay input for DG535 pulse generator, which delivered a signal to activate VMX controller. It is noted that the signal from VMX controller was much simpler than the ones shown in Figure 2.12 for force measurement; here, raising edge was at the start of wing kinematics and falling edge was at the phase where images were taken.

2.6.1.2 Post-Processing

An in-house developed MATALB-based PIV software was employed to analyze the PIV images. The particle displacement was determined using cross-correlation analysis between displaced interrogation windows. Particle displacement measurements were validated using two criteria: the correlation peak value must be large compared to the noise level in the cross-correlation function, and a region of interest criterion. A two-pass procedure was used to increase the spatial resolution of the measurement. The first pass used a 64 by 64 pixels non-displaced interrogation window, and the second high-resolution pass used a 32 by 32 pixels displaced interrogation window, the displacement was measured in the first pass. The flow velocity was measured in a uniform grid with 16 pixel spacing. A median filter is used to remove outliers and to interpolate points where the validation criteria failed. The time between exposures was selected to minimize the number of failed validation points due to spanwise flow. Based on these PIV parameters the spatial resolution of the PIV measurements was approximately 1 mm. A total of 60 PIV image pairs were recorded for each flow condition and wing angle. Results presented here are phase-averaged over 60-image samples.

2.6.2 Lens Shifted Stereoscopic PIV

Typically, Stereoscopic PIV has two configurations: lens-tilted configuration and lens shifted configuration (Prasad, 2000).

The lens-tilted configuration uses the Scheimpflug principle to capture the out-of-plane particle displacement; since lens plane is not parallel to image plane, images perceived by camera are distorted, a.k.a. perspective distortion, and need to be compensated (Soloff et al, 1997). This configuration was used by Sakakibara et al. (2004) on goldfish, and Suryadi et al. (2010) and Suryadi and Obi (2011) on flapping rigid plate in the condition where liquid-air interface is present.

The lens-shifted configuration is much simpler. The perspective distortion is avoided since object plane, lens plane, and image plane are parallel to each other, which

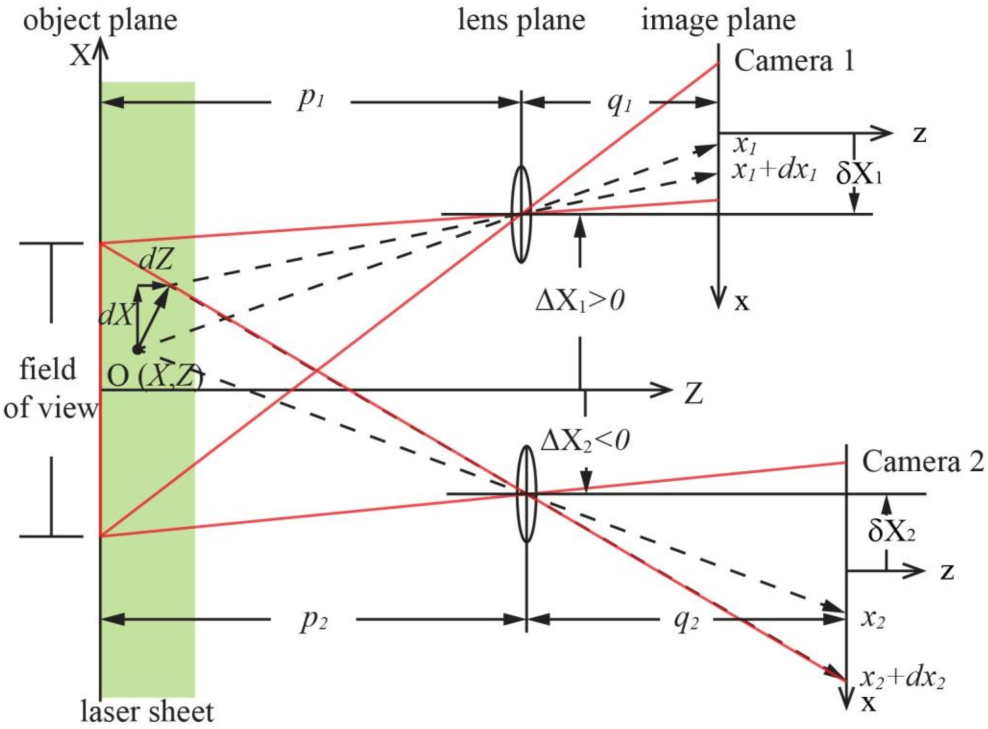

Figure 2.35 Schematics of a lens shifted Stereo PIV geometry in the x-z plane.

also results in the same magnification factor over the images when refractive index is the same among planes. In this study, we applied lens-shifted Stereo PIV system to quantify unsteady flow field in the water channel. The object plane was in the water, and the lens plane and image plane were in the air. According to the observation of Prasad and Adrian (1993), the liquid-air interface would cause astigmatic aberration, which is resulted by the curved surface of least confusion. Slightly different magnification was detected in an area close to the edge of field of view; the difference is considered as the part of measurement uncertainty.

2.6.2.1 Lens-Shifted Stereo PIV configuration

The configurations of lens shifted Stereo PIV are shown in Figure 2.35 and Figure 2.36 for coordinates on X-Z plane and Y-Z plane, respectively. The distance from object plane to lens plane is denoted by *p*, and the distance from image plane to lens plane is denoted by *q*. The subscripts, such as 1 and 2, represent Camera 1 and Camera 2, respectively.

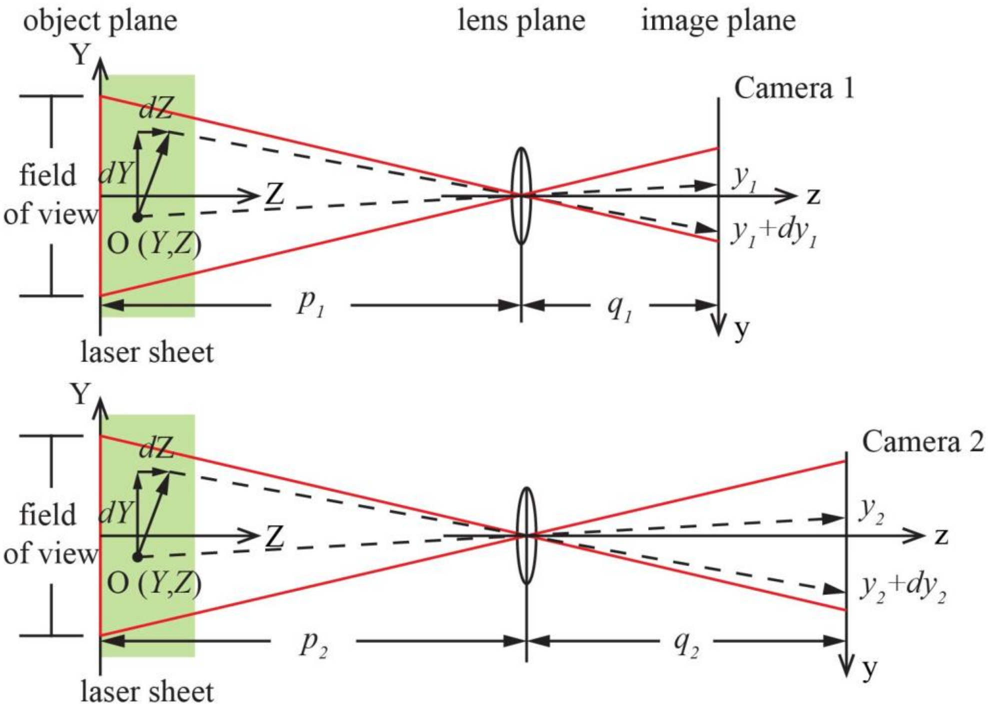

Figure 2.36 Schematics of a lens shifted Stereo PIV geometry in the y-z plane.

Coordinates on object plane are defined at the center of field of view. As shown on the left in Figure 2.35, the positive X-axis is in the upward direction on the object plane, the positive Z-axis is normal to the object plane and positive toward lens; the Y-axis is out of the paper. Figure 2.36 shows the positive Y-axis is in the upward direction, the positive Z-axis is normal to the object plane and positive toward the lens; the X-axis is toward the paper. Coordinates on image planes are shown on the right of Figure 2.35 and Figure 2.36 for positive x- and y-axis downward, respectively. The z-axes on image planes are not necessary; however, the particle displacements in Z-axis are determined by planar images acquired simultaneously from two individual cameras. The positions of the cameras follow the coordinates on object plane. In current configuration, camera lenses are shifted along the x-axis. In the object-plane coordinates, the lens of Camera 1 is shifted upward by ΔX_1, which is positive; the lens of Camera 2 is shifted downward by ΔX_2, which is negative.

2.6.2.2 Particle displacement on image plane

Since the configurations for both cameras are similar, the following derivation is based on one camera, saying only Camera 1, except magnification factor. If the distance from lens toward object (*p*) or the distance from lens toward camera (*q*) is not the same, the magnification factors are different, as determined using Equations (2.41) and (2.42).

$$M_1 = q_1 / p_1 \tag{2.41}$$

$$M_2 = q_2 / p_2 \tag{2.42}$$

Considering a particle initially at location *O* (X, Y, Z) within the thickness of laser sheet (green shaded area in the figures), the corresponding position captured on Camera 1 is (x_1, y_1). The relations between the particle on object plane and image plane are given in Equations (2.43) and (2.44).

$$(\delta X_1 - x_1)/(\Delta X_1 - X) = q_1/(p_1 - Z) \tag{2.43}$$

$$y_1 / Y = q_1/(p_1 - Z) \tag{2.44}$$

After the time interval *dt*, this particle moves to a new location ($X + dX$, $Y + dY$, $Z + dZ$), resulting in the new position ($x_1 + dx_1$, $y_1 + dy_1$) on image plane. The relations for particle position on object plane and image plane are given in Equations (2.45) and (2.46).

$$\left[\delta X_1 - (x_1 + dx_1)\right] / \left[\Delta X_1 - (X + dX)\right] = q_1 / \left[p_1 - (Z + dZ)\right] \tag{2.45}$$

$$(y_1 + dy_1)/(Y + dY) = q_1 / \left[p_1 - (Z + dZ)\right] \tag{2.46}$$

Rearranging Equations (2.45) and (2.46), the particle displacements on image plane in x and y directions are obtained and given in Equations (2.47) and (2.48).

$$dx_1 = (\delta X_1 - x_1) - \frac{q_1}{p_1 - (Z + dZ)}\left[\Delta X_1 - (X + dX)\right] \tag{2.47}$$

$$dy_1 = \frac{q_1}{p_1 - (Z + dZ)}(Y + dY) - y_1 \tag{2.48}$$

Substituting Equations (2.43) and (2.44) into Equations (2.47) and (2.48), respectively, we obtain displacements on image plane (dx_1, dy_1) in terms of displacement on object plane (dx, dy), as shown in Equations (2.49) and (2.50). It is noted that the distances lens shifted for two cameras, δX_1 and δX_2, are not important.

$$dx_1 = \frac{q_1}{p_1 - Z}(\Delta X_1 - X) - \frac{q_1}{p_1 - (Z + dZ)}\left[\Delta X_1 - (X + dX)\right] \tag{2.49}$$

$$dy_1 = \frac{q_1}{p_1 - (Z + dZ)}(Y + dY) - \frac{q_1}{p_1 - Z}Y \tag{2.50}$$

In practice, $p_1 \square Z$, the Equation (2.49) and (2.50) can be arranged into Equations (2.51) and (2.52) after substituting Equations (2.41) and (2.42) for x- and y-displacements, respectively.

$$\begin{aligned} dx_1 &= \frac{dZ}{p_1}\left[\frac{q_1}{p_1}\left(X-\Delta X_1\right)+dx_1\right]+\frac{q_1}{p_1}dX \\ &= \frac{dZ}{p_1}\left[M_1\left(X-\Delta X_1\right)+dx_1\right]+M_1 dX \end{aligned} \tag{2.51}$$

$$\begin{aligned} dy_1 &= \frac{dZ}{p_1}\left[\frac{q_1}{p_1}Y+dy_1\right]+\frac{q_1}{p_1}dY \\ &= \frac{dZ}{p_1}\left[M_1 Y+dy_1\right]+M_1 dY \end{aligned} \tag{2.52}$$

2.6.2.3 Particle displacement and velocity on object plane

Now we know in-plane particle displacements captured by cameras through Equations (2.51) and (2.52) in a time interval of *dt*, which are evaluated using the in-house MATLAB-based PIV software similar to the two-dimensional PIV. Two different flow images of the same flow field are expected since both cameras are placed at a distance apart with lens shifted. To determine the displacements of particle in the flow field (*dX*, *dY*, *dZ*), firstly we look at the particle displacement in X direction.

Consider x-displacements in Camera 1 and Camera 2, since both cameras have similar behavior, we simply change notation of Equation (2.51) from 1 to 2 for Camera 2. After proper rearrangement, we obtain Equation (2.53).

$$\frac{dx_1}{M_1}-\frac{dZ}{p_1}\left(X-\Delta X_1\right)=\frac{dx_2}{M_2}-\frac{dZ}{p_2}\left(X-\Delta X_2\right) \tag{2.53}$$

where dx_1 and dx_2 are evaluated using cross-correlation technology, and M_1, M_2, p_1, p_2, Δx_1, and Δx_2 are going to be determined during calibration process and will be discussed later. The unknown quantity *dZ* is, therefore, determined using Equation (2.54).

$$\boxed{dZ=\left(\frac{dx_2}{M_2}-\frac{dx_1}{M_1}\right)\Bigg/\left[\frac{X-\Delta X_2}{p_2}-\frac{X-\Delta X_1}{p_1}+\frac{dx_2}{M_2 p_2}-\frac{dx_1}{M_1 p_1}\right]} \tag{2.54}$$

Substituting Equation (2.54) into Equation (2.51), the particle displacement in X-direction is obtained and given in Equation (2.55).

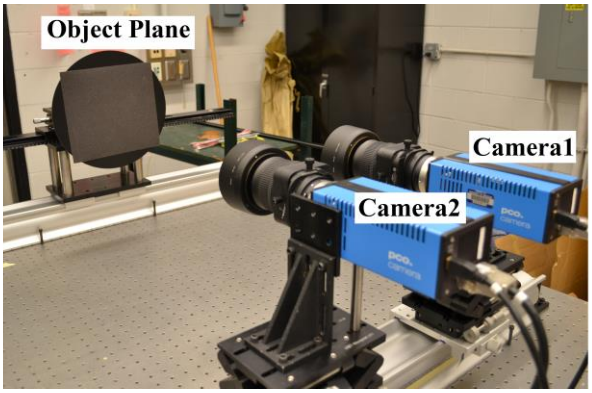

Figure 2.37 Lens-shifted SPIV for air-air interface configuration.

$$\boxed{dX = dx_1 \frac{p_1 - dZ}{p_1 M_1} - dZ \frac{X - \Delta X_1}{p_1}} \tag{2.55}$$

Similarly, substituting Equation (2.54) into Equation (2.52), the particle displacement in Y-direction is obtained and given in (2.56).

$$\boxed{dY = dy_1 \frac{p_1 - dZ}{p_1 M_1} - dZ \frac{Y}{p_1}} \tag{2.56}$$

Finally, the velocity of the particle is obtained using Equation (2.57).

$$\vec{V} = \left(d\vec{x} + d\vec{y} + d\vec{z}\right) / dt \tag{2.57}$$

where *dt* is the time between camera exposures. It is noted that two cameras have to acquire images at the same time.

The particle displacement in Z-direction can also be determined using equations of y-displacement, such as Equation (2.52), on Camera 1 and Camera 2. However, singular behavior is observed as p_1 and p_2 are the same, it is not considered to determine Z-displacement on object plane.

2.6.2.4 Calibration procedure

The calibration process helps us to ensure the same field of view for two cameras, to determine parameters such as magnifications factors (M_1 and M_2), lens-shifted distances (ΔX_1 and ΔX_2), and distances from object plane to lens plane (p_1 and p_2) for two cameras, and understand individual camera behavior. The determination of exposure time is unnecessary.

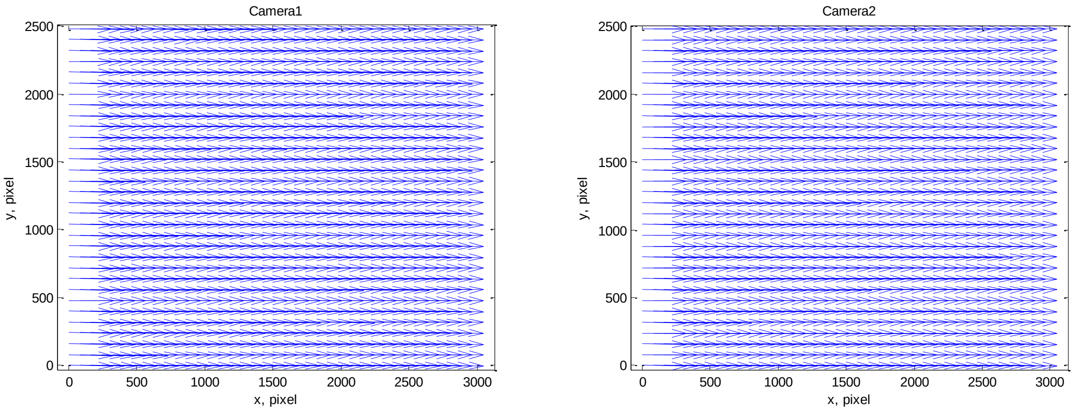

Figure 2.38 Vector field example for determining magnification factor using calibration procedure with air-air interface. *The magnification factor is 13.1 px/mm, grid size is 16 pixels.*

The first calibration is to ensure both cameras having the same field of view. We employed a Cartesian-grid board to represent the object plane, which is 18 cm wide and 24 cm height, the grid size is 1 cm by 1 cm. The grid helps in detecting the presence of image distortion and roughly estimate magnification factor over selected index points on images. The center of the Cartesian-grid board has to be oriented at the center of the image for both cameras. Once the same field of view is perceived by two cameras, the sandpaper is employed for the next calibration procedure and proper illumination may be used as needed.

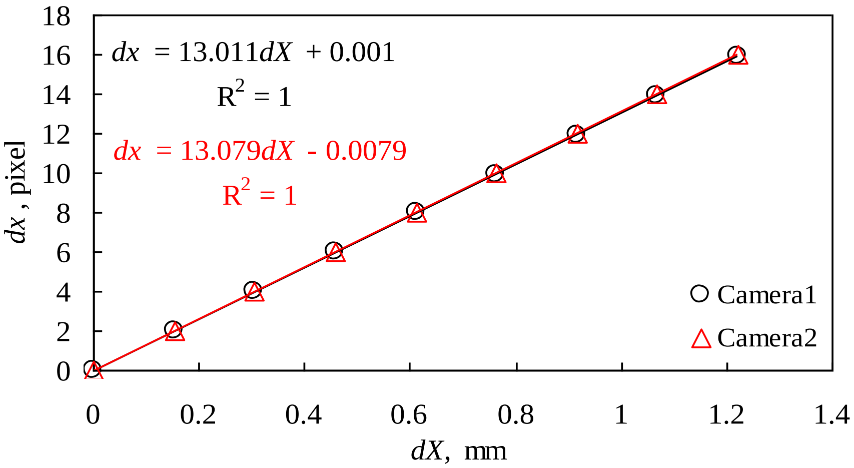

Figure 2.39 Magnification factor determined using calibration procedure with air-air interface.

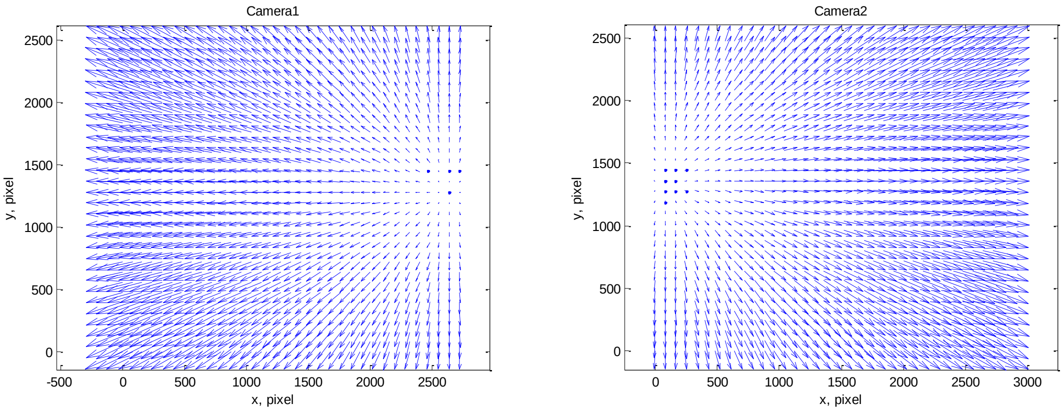

Figure 2.40 Vector field example for dZ displacement only in calibration procedure with air-air interface. *The magnification factor is 13.1 px/mm, grid size is 16 pixels.*

The second calibration process is to find the magnification factor. Substituting *dZ* = 0 into Equation (2.51), Equation (2.58) is obtained to find the magnification factor.

$$M_1 = \frac{dx_1}{dX} \tag{2.58}$$

where dx_1 is the displacement evaluated using cross-correlation technology and *dX* is the displacement of object plane adjusted manually through micrometer or transversal mechanism.

The third calibration process is to find the lens-shifted distance (ΔX) and distance from object plane to lens plane (*p*) for each camera. Substituting *dX* = 0 into Equation

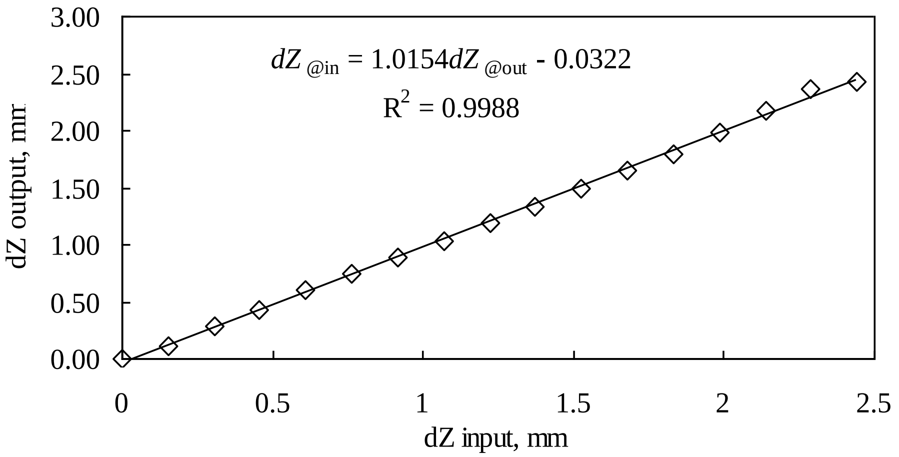

Figure 2.41 The relation of *dZ* displacement expected and evaluated with air-air interface.

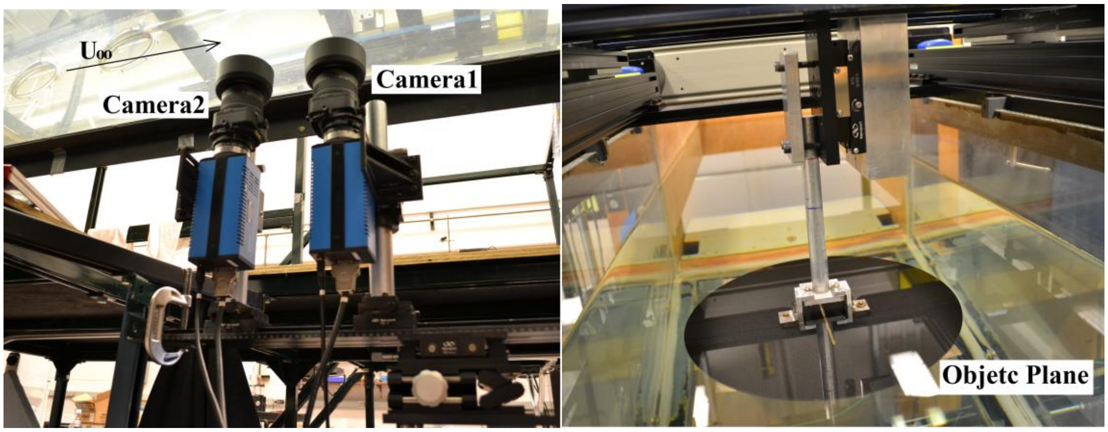

Figure 2.42 Lens-shifted SPIV for water-air interface configuration.

(2.51), we obtain Equation (2.59).

$$\frac{dx_1}{dZ} = \frac{M_1}{p_1 - dZ} X - \frac{M_1}{p_1 - dZ} \Delta X_1 \tag{2.59}$$

where X is the particle location on object plane. We can replace the particle location X with the particle position x on image using Equation (2.60).

$$X = \left(x_1 + x_0 - H/2 \right) / M_1 \tag{2.60}$$

The x_1 is particle position on the image, x_0 is the first pixel location on CCD sensor for the selected image region, and H is the horizontal pixel resolution for the CCD sensor, which is 4008 pixels. Substituting Equation (2.60) into Equation (2.59), we obtain

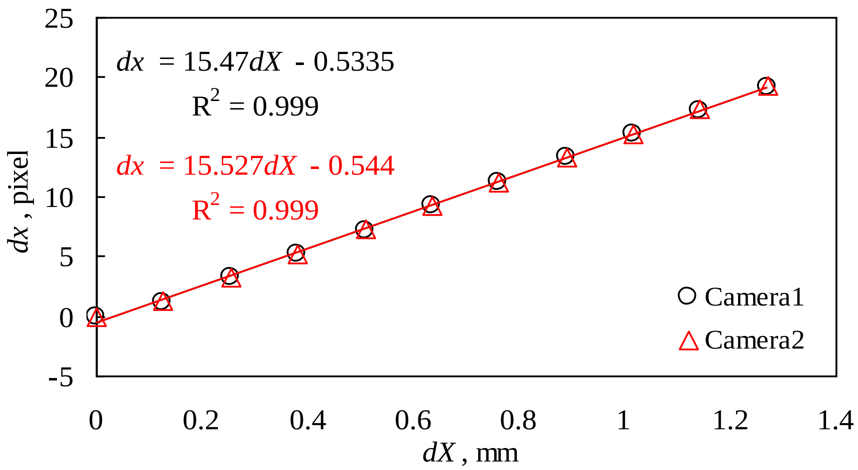

Figure 2.43 Magnification factor determined using calibration procedure with water-air interface.

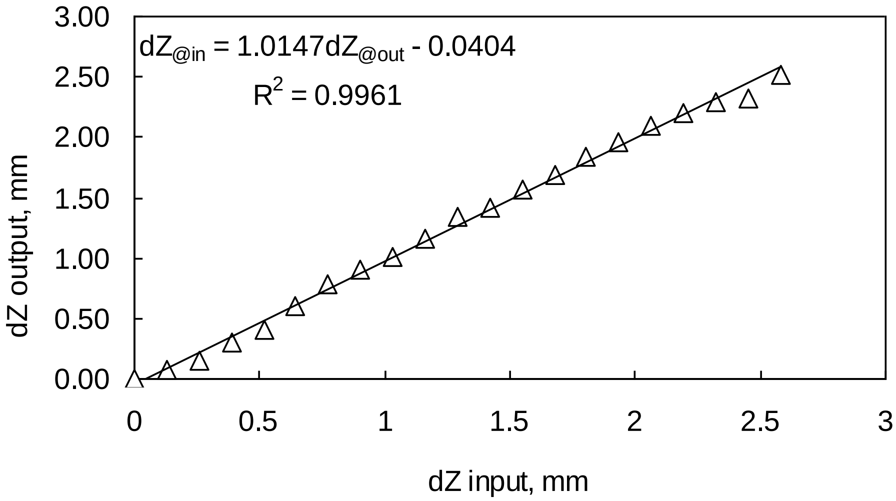

Figure 2.44 The relation of *dZ* displacement expected and evaluated with water-air interface.

a linear expression as shown in Equation (2.61).

$$\begin{aligned}\frac{dx_1}{dZ} &= \frac{1}{p_1 - dZ}x_1 + \frac{x_0 - H/2 - M_1\Delta X_1}{p_1 - dZ} = mx_1 + m\left(x_0 - H/2 - M_1\Delta X_1\right) \\ &= mx_1 + n\end{aligned} \tag{2.61}$$

where dx_1 is particle displacement on image plane with respect to the *dZ* displacement on object plane. Considering x_1 to be independent variable and dx_1/dZ is a function of x_1. The slope, *m*, can be used to find p_1. Once p_1 is found, the zero intersection, *n*, gives ΔX_1. The same procedure works for Camera2 to find p_2 and ΔX_2.

For convenience, we define the displacement on object plane has unit of millimeter and the displacement on image plane has unit of pixel. The position of camera follows the unit used on object plane. Therefore, the unit for variables *X*, *Y*, *Z*, ΔX, *p*, and *H* is in millimeter, and the unit for variables *x*, *y*, *dx*, *dy*, *q*, and x_0 is in pixel. Moreover, the calibration procedure demonstrated here uses Equation (2.51) only, which is the displacement in x-direction. We can also employ the y-displacement expression shown as Equation (2.52) to find *M* and *p*, but ΔX cannot be found. Some calibration results are provided in Figure 2.38 - Figure 2.44 to test our approaches.

CHAPTER 3

LINEAR POTENTIAL FLOW THEORY

Lifting-line theory is the simplest model to predict aerodynamic force for thin finite-aspect-ratio wings in a uniform flow field at steady state. The flow is assumed to be inviscid, irrotational and incompressible, known as potential flow. The lifting-line theory was proposed by Ludwig Prandtl and his colleagues in the early 1900s. The concept was to assume the wing itself being composed of bound vortices following Helmholtz's vortex theorems; aerodynamic loadings on the wings were evaluated by integrating the superposed steady circulations over wingspan. More description can be found in Anderson (2011), Bertin and Cummings (2009), and Kuethe and Chow (1976). In this chapter, we are going to apply the lifting-line theory for thin wings subject to a constant pitch rate in a uniform flow field, and estimate aerodynamic loadings as functions of reduced pitch rate (K) and geometric angle of attack (α); effect of pivot-axis location (x_p) are also considered. The geometric angle of attack is abbreviated to angle of attack in the following discussion.

3.1 SECTIONAL WING

Figure 3.1 presents a cross-section of a thin cambered wing. The wing is pitched about a point in clockwise direction with a pitch rate $\alpha'(t)$; this point is called pivot point for a sectional wing and pivot axis for a finite-aspect-ratio wing, shown as circle symbol in Figure 3.1. In the right of Figure 3.1, pitching motion produces normal velocity on the camber line, which is proportional to a distance r with respect to the pivot point. The direction of normal velocity due to pitching motion is consistent with pitching direction but may not be in the same direction as others due to free-stream velocity. The left panel of Figure 3.1 shows instant position of the wing at an angle of attack $\alpha(t)$ in a uniform flow U_∞; camber line z is a function of distance s from leading edge.

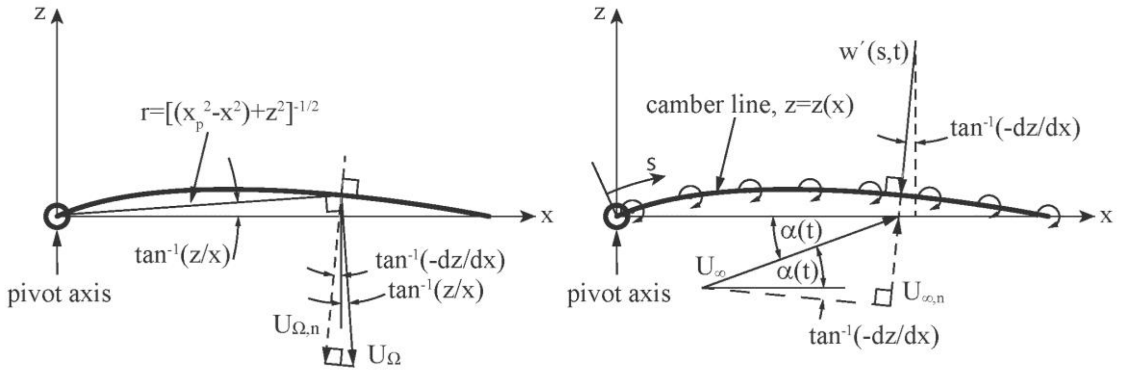

Figure 3.1 Illustration of (left) pitching wing at leading edge and (right) classical thin airfoil theory.

Following classical thin airfoil theory, a vortex sheet on camber line is placed on the chord line. The strength of the vortex sheet is a function of distance x along wing chord from leading edge, $\gamma(x)$, and satisfies the Kutta condition at trailing edge, $\gamma(c) = 0$, where there is not velocity gradient. Hence, the strength of the vortex sheet can be evaluated by considering the camber line as streamline. All velocities normal to the camber line must be zero at any point along the camber line. There are three contributions to the normal velocity, which are uniform free-stream, pitch motion, and bound vortices, as shown in Equation (3.1) for a given time. The velocity induced from the vortices in the wake is not considered since being washed far downstream.

$$U_{\infty,n}\left(x,t\right)+U_{\Omega,n}\left(x,t\right)+w'\left(s,t\right)=0 \tag{3.1}$$

3.1.1 Normal Velocity from Free-Stream

The first term in Equation (3.1) is normal velocity on the camber line from free-stream flow, $U_{\infty,n}$, and evaluated using Equation (3.2), where effect of wing position and camber line are considered. $U_{\infty,n}$ is positive as the flow is moving toward the wing from upstream, as shown on the right of Figure 3.1.

$$U_{\infty,n}\left(x,t\right)=U_\infty \sin\left[\alpha\left(t\right)+\tan^{-1}\left(-dz/dx\right)\right] \tag{3.2}$$

Assuming the wing is subject to a small angle of attack and the slope of the camber line dz/dx is also small, Equation (3.2) could be approximated to Equation (3.3) using $\sin\alpha \approx \alpha$ and $\tan^{-1}(-dz/dx) \approx -dz/dx$.

$$U_{\infty,n}\left(x,t\right)=U_\infty\left[\alpha\left(t\right)-dz/dx\right] \tag{3.3}$$

3.1.2 Normal Velocity from Pitch Motion

The second term in Equation (3.1) is normal velocity due to pitching motion, $U_{\Omega,n}$, and is evaluated using Equation (3.4).

$$\begin{aligned} &U_{\Omega,n}\left(x,t\right) \\ &=\left(x-x_p\right)\alpha'\left(t\right)\left[z^2+\left(x-x_p\right)^2\right]^{-1/2}\cos\left[\tan^{-1}\left(-dz/dx\right)+\tan^{-1}\left(z/x\right)\right] \end{aligned} \tag{3.4}$$

where x_p denotes the pivot point. The positive sense of the pitching motion is clockwise about pivot point. Consider the normal velocity on the wing; however, the positive pitching normal velocity is counterclockwise, being consistent with free-stream normal velocity. Assuming the small slope of the camber line and $z(x)/x << 1$, Equation (3.4) could be approximated to Equation (3.5).

$$U_{\Omega,n}\left(x,t\right)=\alpha'\left(t\right)\left(x-x_p\right) \tag{3.5}$$

3.1.3 Induced Velocity from Bound Vortices

The third term in Equation (3.1) is the velocity induced on the camber line by vortex sheet, $w'(s)$, and due to the presence of the wing in the flow, which is regarded as induced velocity from bound vortices. Since the wing is thin and the camber line is close to the chord line, the induced velocity on the camber line could be approximated by the velocity at the chord line $w'(x)$, as given in Equation (3.6), which is negative while vectoring downward.

$$w'\left(s,t\right)=w\left(x,t\right)=-\int_0^c\frac{\gamma\left(\xi,t\right)}{2\pi\left(x-\xi\right)}d\xi \tag{3.6}$$

Substituting the coordinate transformation in Equation (3.7) to Equation (3.6), we obtain Equation (3.8) for induced velocity from bound vortices.

$$\xi=\frac{c}{2}\left[1-\cos\left(\theta\right)\right],\ 0\le\theta\le\pi \tag{3.7}$$

$$w'\left(x,t\right)=\frac{1}{2\pi}\int_0^\pi\frac{\gamma\left(\theta,t\right)\sin\left(\theta\right)}{\cos\left(\theta\right)-\cos\left(\theta_x\right)}d\theta \tag{3.8}$$

where θ_x corresponds to any fixed point x in Equation (3.7).

3.1.4 Sectional Force Coefficient

Substituting Equations (3.3), (3.5), and (3.8) into Equation (3.1), we obtain Equation (3.9).

$$U_\infty\left[\alpha(t)-dz/dx\right]-\alpha'(t)\left(x_p-x\right)=\frac{1}{2\pi}\int_0^\pi\frac{\gamma(\theta,t)\sin(\theta)}{\cos(\theta)-\cos(\theta_x)}d\theta \tag{3.9}$$

The terms on the left-hand side of Equation (3.9) are geometric specification or control parameters we have known; the strength of vortex sheet $\gamma(\theta)$ on the right-hand side is unclear and needs to be found. A typical solution is given in Equation (3.10) using superposition principle.

$$\gamma(\theta,t)=2U_\infty\left[A_0(t)\frac{1+\cos(\theta)}{\sin(\theta)}+\sum_{n=1}^{\infty}A_n(t)\sin(n\theta)\right] \tag{3.10}$$

The first term of the square bracket in Equation (3.10) implies a singular behavior at the leading edge (i.e., $\theta = 0$) and a stagnation behavior at the trailing edge (i.e., $\theta = \pi$), effects of wing planform and pitch rate are included in the second term of the square bracket in Equation (3.10).

Substituting Equation (3.10) to the term on the right-hand side of Equation (3.9), we obtained Equation (3.11), which indicates the solution of Equation (3.9) can be found once the coefficients, A_0 and A_n are determined.

$$\begin{aligned}&\frac{1}{2\pi}\int_0^\pi\frac{\gamma(\theta,t)\sin(\theta)}{\cos(\theta)-\cos(\theta_x)}d\theta\\&=\frac{U_\infty}{\pi}\left\{\int_0^\pi A_0(t)\frac{1+\cos(\theta)}{\cos(\theta)-\cos(\theta_x)}d\theta+\sum_{n=1}^{\infty}\int_0^\pi A_n(t)\frac{\sin(\theta)\sin(n\theta)}{\cos(\theta)-\cos(\theta_x)}d\theta\right\}\\&=U_\infty\left\{A_0(t)-\sum_{n=1}^{\infty}A_n(t)\cos(n\theta_x)\right\}\end{aligned} \tag{3.11}$$

Substituting Equation (3.11) to Equation (3.9), effective camber line could be obtained using Equation (3.12); both effects of pivot point location and pitch rate are included.

$$\boxed{\left(dz/dx\right)_{eff}=dz/dx+\alpha'(t)\left(x_p-x\right)/U_\infty=\alpha(t)-A_0(t)+\sum_{n=1}^{\infty}A_n(t)\cos(n\theta_x)} \tag{3.12}$$

It is noted that Equation (3.12) is a form of a Fourier cosine series expansion; the coefficients A_0 and A_n can be found by solving Equation (3.13) and Equation (3.14), respectively.

$$\alpha(t) - A_0(t) = \frac{1}{\pi}\int_0^{\pi} (dz/dx)_{eff}\, d\theta_x \tag{3.13}$$

$$A_n(t) = \frac{2}{\pi}\int_0^{\pi} (dz/dx)_{eff} \cos(n\theta_x)\, d\theta_x \tag{3.14}$$

Substituting Equation (3.12) into Equations (3.13) and (3.14), the coefficients A_0 and A_n are obtained and given in Equations (3.15) and (3.16).

$$A_0(t) = \alpha(t) - \frac{1}{\pi}\int_0^{\pi} (dz/dx) d\theta_0 + \frac{\alpha'(t)c}{2U_\infty}\cos(\theta_p) \tag{3.15}$$

$$A_n(t) = \frac{2}{\pi}\int_0^{\pi} (dz/dx)\cos(n\theta_x)\, d\theta_x + \frac{\alpha'(t)c}{2U_\infty} \tag{3.16}$$

where θ_p corresponds to the pivot point x_p, and $x_p = c(1\text{-}cos\theta_p)/2$. As pivot point is at leading edge $\theta_p = 0$; as pivot axis is at trailing edge $\theta_p = 1$.

Finally, sectional lift coefficient $C_L{}'$ and pitching moment coefficient $C'_{M,LE}$ at leading edge could be evaluated using Equations (3.17) and (3.18), respectively, according to the Kutta-Joukowski theorem ($L' = \rho U_\infty \Gamma$). Since steady Bernouli equation is assumed, the results are valid for steady flow conditions. Also non-circulatory effects and normal velocity due to vortices generated by pitching motion in the flow are not considered.

$$C_L' = \frac{2\rho U_\infty \Gamma}{\rho U_\infty^2 S} = \pi\left[2A_0 + A_1\right] \tag{3.17}$$

$$C'_{M,LE} = -\frac{2}{\rho U_\infty^2 S c}\int_0^{c} \rho U_\infty \Gamma(\xi)\xi\, d\xi = -\frac{\pi}{2}\left[A_0 + A_1 - \frac{A_2}{2}\right] \tag{3.18}$$

where Γ is circulation around the vortex sheet on the sectional wing and evaluated using Equation (3.19).

$$\boxed{\Gamma = \int_0^{c} d\Gamma = \int_0^{c} \gamma(\xi)\, d\xi} \tag{3.19}$$

According to Kelvin circulation theorem, the circulation around the sectional wing is equal to the circulation around vortices in the wake.

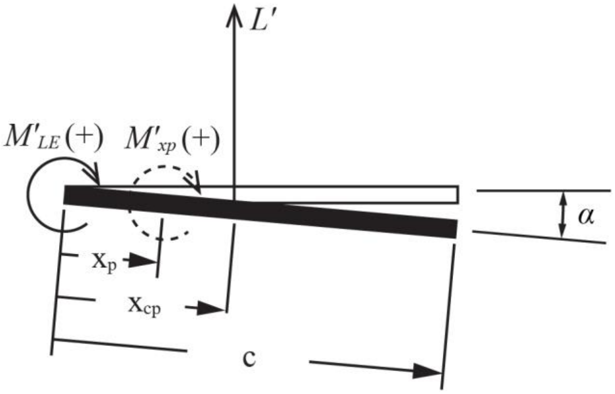

Figure 3.2 Force distribution on sectional thin flat plate.

3.1.5 Sectional Thin Flat Plate

For a sectional thin flat plate, the slope of the camber line is zero ($dz/dx = 0$); the sectional lift coefficient is evaluated using Equation (3.20) and presumably applied on center of pressure where pitching moment is absent by definition (Anderson, 2011).

$$C_L' = a_0\left(\alpha - \alpha_{L=0}\right) = a_0\alpha_{eff} = 2\pi\left\{\alpha + \left[\cos\left(\theta_p\right) + \frac{1}{2}\right]K\right\} \tag{3.20}$$

where the square bracket give effective angle of attack α_{eff}; zero-lift angle of attack $\alpha_{L=0}$ is given in the second term of square bracket and is negative. The slope of lift-coefficient-curve ($dC'_L/d\alpha$) is $a_0 = 2\pi$, which is the same as classical thin airfoil theory. This expression also shows the effect of pitch rate disappeared as the pivot point positioned at three-quarter chord.

In addition, the sectional pitching moment coefficient around leading edge is found using Equation (3.21); effect of pitch rate is attenuated as the pivot point is at the trailing edge.

$$C'_{M,LE} = -\frac{\pi}{2}\left\{\alpha + \left[\cos\left(\theta_p\right) + 1\right]K\right\} \tag{3.21}$$

By the definition of zero pitching moment production, the center of pressure x_{cp} is determined using Equation (3.22). The force distribution on sectional flat plate is illustrated in Figure 3.2.

$$x_{cp} = -cC'_{M,LE} / C'_L \tag{3.22}$$

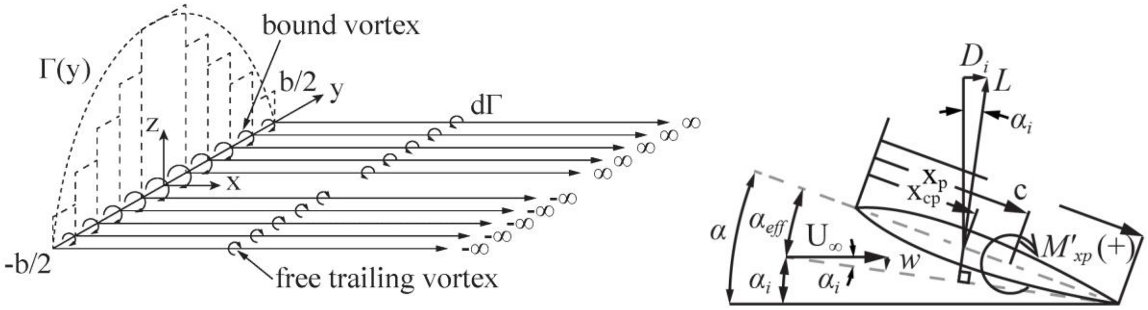

Figure 3.3 (left) Illustration of Prandtl's lifting line theory over a finite-aspect-ratio wing; (right) effect of downwash velocity illustrated on a sectional wing.

Substituting Equations (3.20) and (3.21) into Equation (3.22), we obtain the center of pressure as a function of reduced pitch rate, pivot axis location and angle of attack, as shown in Equation (3.23).

$$x_{cp} = \frac{c}{4}\left\{\frac{\alpha + \left[\cos\left(\theta_p\right) + 1\right]K}{\alpha + \left[\cos\left(\theta_p\right) + 1/2\right]K}\right\} \tag{3.23}$$

As center of pressure is at quarter-chord, effects of reduced pitch rate are unimportant, which is consistent with typical steady flow approximation.

Moreover, sectional pitch moment coefficient at pivot point $C'_{M,xp}$ can be found using Equation (3.24).

$$C'_{M,xp} = C'_{M,LE} + C'_L x_p / c \tag{3.24}$$

Substituting Equations (3.20) and (3.21) into Equation (3.24), $C'_{M,xp}$ is obtained and given in Equation (3.25).

$$C'_{M,xp} = \pi\left[1/2 - \cos\left(\theta_p\right)\right]\alpha - \left[\pi\cos^2\left(\theta_p\right)\right]K \tag{3.25}$$

As the pivot point is at leading edge, $\theta_p = 0$, Equation (3.25) and Equation (3.21) give the same $C'_{m,xp}$ as expected.

We can also evaluate a distance between pivot point and center of pressure, $x_p - x_{cp}$, using Equation (3.26), which is a function of reduced pitch rate, pivot point, and angle of attack; this relationship is going to apply for finding pitching moment coefficient at any pivot axis location for finite-aspect-ratio wings.

$$\frac{x_p - x_{cp}}{c} = \frac{C'_{M,xp}}{C'_L} = \frac{\left[1-2\cos\left(\theta_p\right)\right]\alpha - \left[2\cos^2\left(\theta_p\right)\right]K}{4\alpha + \left[4\cos\left(\theta_p\right)+2\right]K} \tag{3.26}$$

3.2 FINITE ASPECT RATIO WING

For a finite-aspect-ratio wing, Prandtl's lifting line theory assumes that uniform free-stream velocity is along chord line at rest. Even the leading edge of the wing may be swept backward or forward with respect to wing span; effect of swept angle is not considered and gives a straight vortex-filament along wing span. The vortex-filament is composed of vortices with constant strength of $d\Gamma(y)$ changing along wing span.

3.2.1 Downwash Velocity

According to Helmholtz's vortex theorem, vortex-filament is going to terminate at fluid boundaries or in a closed path. Prandtl and his colleagues proposed U-shape vortex-filament for a finite-aspect-ratio wing in steady flow. The center portion of the vortex-filament along wing span produces vortices regarded as bound vortices; portions of the vortex-filament at two ends terminate far away downstream. The vortices on wing span are unlike bound vortices from the sectional-thin wing discussed previously; these vortices do not generate velocity on the wing because wing chord is relatively small compared to filament length and is considered a point source in cross section. However, the vortices by the vortex-filament terminating downstream produce downwash velocity on wing span; these vortices are regarded as free-trailing vortices. The velocity induced by free trailing vortices is evaluated using Equation (3.27) at any fixed point y_0 along wing span, according to the Biot-Savart law.

$$dw\left(y\right) = -\frac{\left(d\Gamma / dy\right)dy}{4\pi\left(y_0 - y\right)} \tag{3.27}$$

Distributions of vortices over wing span by superposing numerous U-shape vortex-filaments are shown in the left panel of Figure 3.3. Integrating Equation (3.27) over entire wing span, total downwash velocity at y_0 is obtained and given in Equation (3.28).

$$w\left(y_0\right) = -\frac{1}{4\pi}\int_{-b/2}^{b/2} \frac{\left(d\Gamma / dy\right)dy}{y_0 - y} \tag{3.28}$$

3.2.2 Force Coefficients

Effect of downwash velocity is shown in the right panel of Figure 3.3, which indicates lift force L is smaller than one from the sectional wing at same angle of attack (α). L corresponds to a smaller angle, regarded as effective angle of attack (α_{eff}). Furthermore, a pressure-like drag, called induced drag D_i, is generated due to induced angle of attack (α_i). The relation among α, α_i, and α_{eff} is shown in Equation (3.29) at y_0.

$$\alpha(y_0) = \alpha_i(y_0) + \alpha_{eff}(y_0) \tag{3.29}$$

where α_i can be found using Equation (3.30).

$$\alpha_i(y_0) = \tan^{-1}\left(\frac{-w(y_0)}{U_\infty}\right) \tag{3.30}$$

Substituting Equation (3.28) into Equation (3.30) and assuming $w(y_0) << U_\infty$, we obtain Equation (3.31) for α_i at y_0.

$$\boxed{\alpha_i(y_0) = \frac{1}{4\pi U_\infty}\int_{-b/2}^{b/2} \frac{d\Gamma/dy}{y_0 - y}\,dy} \tag{3.31}$$

To find α_{eff}, we have to consider sectional lift coefficient C_L' as follows.

$$C_L' = a_0\left(\alpha_{eff} - \alpha_{L=0}\right), \tag{3.32}$$

where $\alpha_{L=0}$ is zero-lift angle of attack to account for effects of wing camber line and pitch rate, and a_0 is the slope of lift-coefficient-curve. Both are from the sectional wing approximation in previous section. Using Kutta-Joukowski theorem based on steady Bernoulli equation, the sectional lift coefficient is given in Equation (3.33).

$$C_L'(y_0) = \frac{2\Gamma(y_0)}{U_\infty c(y_0)} \tag{3.33}$$

Combining Equations (3.32) and (3.33), the effective angle of attack is obtained and given in Equation (3.34).

$$\boxed{\alpha_{eff}(y_0) = \frac{2\Gamma(y_0)}{a_0 U_\infty c(y_0)} + \alpha_{L=0}} \tag{3.34}$$

Substituting Equations (3.31) and (3.34) into Equation (3.29), we obtain new expression for angle of attack as shown in Equation (3.35).

$$\boxed{\alpha(y_0) = \frac{1}{4\pi U_\infty}\int_{-b/2}^{b/2} \frac{d\Gamma/dy}{y_0 - y}\,dy + \frac{2\Gamma(y_0)}{a_0 U_\infty c(y_0)} + \alpha_{L=0}} \tag{3.35}$$

To solve Equation (3.35) we still need to know strength of vortex filament, $\Gamma(y)$. The general solution is given in Equation (3.36).

$$\Gamma(\phi) = 2bU_{\infty}\sum_{1}^{N} D_n \sin(n\phi),\ y = -\frac{b}{2}\cos(\phi),\ 0 \le \phi \le \pi \tag{3.36}$$

Equation (3.35) would be well defined if coefficients D_n could be found. The approach applied to find D_n is similar to Glauert (1926) and is demonstrated in the following discussion.

Finally, lift coefficient (C_L) and induced drag coefficient (C_{Di}) are evaluated by integrating distributed forces on wing span and obtained in Equations (3.37) and (3.38), respectively, for the flow at steady-state. It is noted that both C_L and C_{Di} depend on aspect ratio (b^2/S), and not depend on wing swept angle.

$$C_L = \frac{2}{\rho U_{\infty}^2 S}\int_{-b/2}^{b/2} \rho U_{\infty}\Gamma(y)\,dy = \frac{b^2}{S}\pi D_1 \tag{3.37}$$

$$C_{D_i} = \frac{2}{\rho U_{\infty}^2 S}\int_{-b/2}^{b/2} \rho U_{\infty}\Gamma(y)\alpha_i(y)\,dy = \frac{b^2}{S}\pi\sum_{n=1}^{N} nD_n^2 \tag{3.38}$$

To obtain pitching moment coefficient about pivot axis $C_{M,xp}$, as shown on the right of Figure 3.3, the sectional pitching moment can be found using force-torque equivalence shown in Equation (3.39) in accordance with small angle approximation, for example, $\cos(\alpha_{eff}) \approx 1$ and $\sin\alpha \approx \alpha$. Both forces $L(y_0)$ and $Di(y_0)$ are assumed to act on center of pressure at a fixed point y_0 on wing span.

$$\begin{aligned} M'_{xp}(y_0) &= L'(x_p - x_{cp})\cos(\alpha_{eff}) + D'_i(x_p - x_{cp})\sin(\alpha) \\ &\approx (x_p - x_{cp})(L' + D'_i\alpha) \end{aligned} \tag{3.39}$$

Integrating the pitching moment over entire wing span and normalized with $\rho U_{\infty}^2 Sc/2$, we obtain Equation (3.40).

$$C_{M,xp} = \int_{-b/2}^{b/2} C'_{M,xp}(y)\,dy = \int_{-b/2}^{b/2}\left(\frac{x_p - x_{cp}}{c}\right)\left[\frac{L'(y) + D'_i(y)\alpha}{\rho U_{\infty}{}^2 S/2}\right]dy \tag{3.40}$$

Recall from Equation (3.36), the term (x_p - x_{cp}) is independent of span location y; therefore, we can pull this term out of the integration. After substituting Equation (3.36) into Equation (3.40), the final expression for $C_{M,xp}$ is given in Equation (3.42), which is a function of C_L and C_{Di}, K, and θ_p.

$$C_{M,xp} = \frac{\left[1-2\cos\left(\theta_p\right)\right]\alpha - \left[2\cos^2\left(\theta_p\right)\right]K}{4\alpha + \left[4\cos\left(\theta_p\right)+2\right]K}\left(C_L + C_{Di}\alpha\right) \tag{3.41}$$

3.2.3 Thin Flat Plate with Finite Aspect Ratio

To find coefficients of C_L, C_{Di}, and $C_{M,xp}$, coefficients D_n need to be determined. Equation (3.42) shows angle of attack α at a span location y from Equation (3.35) with coordinate transform y=-$b$cos(ϕ)/2 for flat plate. The number of D coefficient depends on number of span location in use; more D coefficients give more accurate estimation.

$$\alpha\left(\phi\right) = \sum_{n=1}^{N} nD_n \frac{\sin n\phi}{\sin\phi} + \frac{4b}{a_0 c\left(\phi\right)} \sum_{n=1}^{N} D_n \sin n\phi - K\left(\cos\theta_p + \frac{1}{2}\right) \tag{3.42}$$

The first term on the right-hand side of Equation (3.42) presents induced angle of attack, the last two terms presents effective angle of attack. The a_0 in the second term is the slope of lift-coefficient-angle curve, for instance, $a_0 = 2\pi$ for a flat plate. The last term presents zero-lift angle of attack ($\alpha_{L=0}$). Both two parameters a_0 and $\alpha_{L=0}$ are obtained from estimation of sectional wing as discussed previously. Equation (3.42) can be expanded in matrix form, as shown in Equation (3.43) to find coefficients D_n.

$$\begin{aligned}
&\begin{bmatrix} 1/\sin\phi_1 & 0 & \cdots & 0 \\ 0 & 1/\sin\phi_2 & \cdots & 0 \\ \vdots & \vdots & \ddots & 0 \\ 0 & 0 & \cdots & 1/\sin\phi_n \end{bmatrix}
\begin{bmatrix} \sin\phi_1 & 2\sin 2\phi_1 & \cdots & n\sin n\phi_1 \\ \sin\phi_2 & 2\sin 2\phi_2 & \cdots & n\sin n\phi_2 \\ \vdots & \vdots & \ddots & \vdots \\ \sin\phi_n & 2\sin 2\phi_n & \cdots & n\sin n\phi_n \end{bmatrix}
\begin{Bmatrix} D_1 \\ D_2 \\ \vdots \\ D_n \end{Bmatrix} + \\
&\frac{4b}{a_0}\begin{bmatrix} 1/c\left(\phi_1\right) & 0 & \cdots & 0 \\ 0 & 1/c\left(\phi_2\right) & \cdots & 0 \\ \vdots & \vdots & \ddots & 0 \\ 0 & 0 & \cdots & 1/c\left(\phi_n\right) \end{bmatrix}
\begin{bmatrix} \sin\phi_1 & \sin 2\phi_1 & \cdots & \sin n\phi_1 \\ \sin\phi_2 & \sin 2\phi_2 & \cdots & \sin n\phi_2 \\ \vdots & \vdots & \ddots & \vdots \\ \sin\phi_n & \sin 2\phi_n & \cdots & \sin n\phi_n \end{bmatrix}
\begin{Bmatrix} D_1 \\ D_2 \\ \vdots \\ D_n \end{Bmatrix} \\
&= \begin{Bmatrix} \alpha\left(\phi_1\right) + K\left(\cos\theta_p + 1/2\right) \\ \alpha\left(\phi_2\right) + K\left(\cos\theta_p + 1/2\right) \\ \vdots \\ \alpha\left(\phi_n\right) + K\left(\cos\theta_p + 1/2\right) \end{Bmatrix}
\end{aligned} \tag{3.43}$$

For simplicity, Equation (3.43) is expressed in terms of algebra, as shown in Equation (3.44).

$$\left(\left[I\right]\left[J\right] + \left[M\right]\left[N\right]\right)\left\{D\right\} = \left\{Q\right\} \tag{3.44}$$

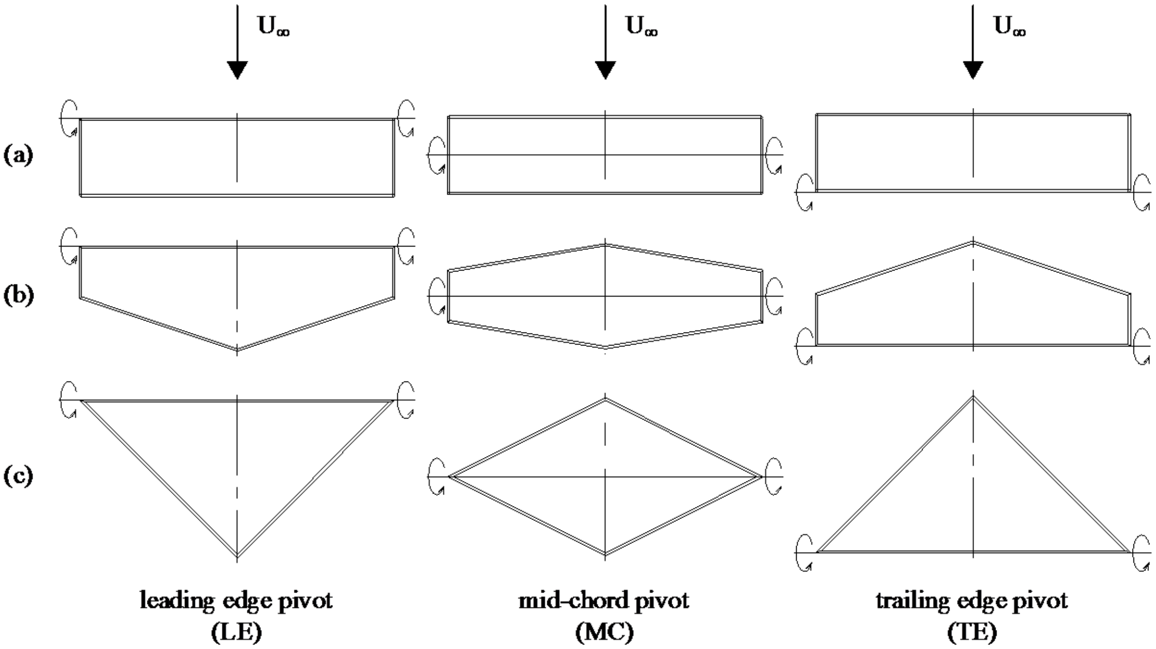

Figure 3.4 Illustrations of wing planforms and pivot axes of interest: (a) rectangular wing, (b) trapezoidal wing, and (c) triangular wing.

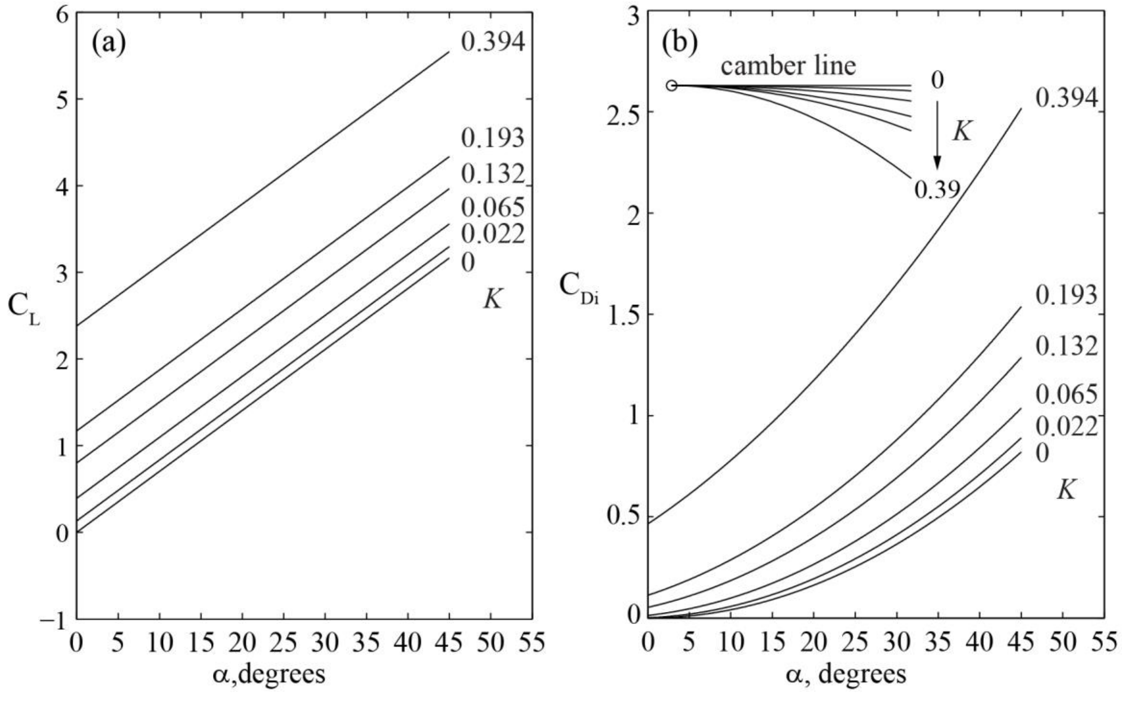

Figure 3.5 Force coefficients as a function of angle of attack using lifting-line theory by rectangular wing at leading edge pivot for (a) lift coefficient (b) induced drag coefficient.

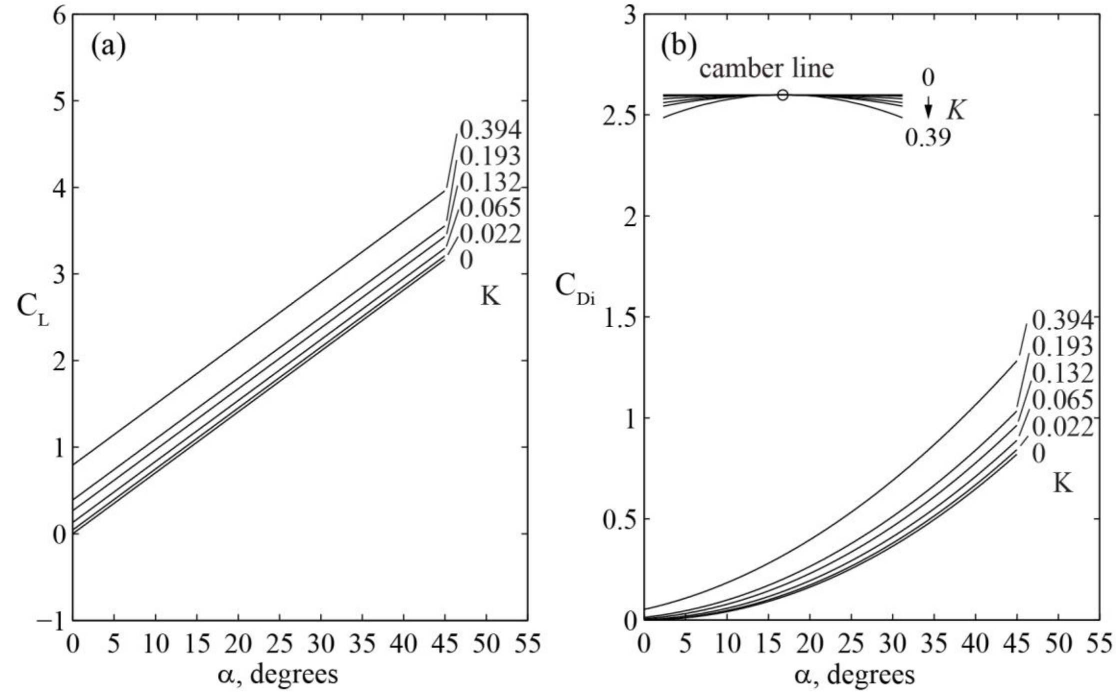

Figure 3.6 Force coefficients as a function of angle of attack using lifting-line theory by rectangular wing at mid-chord pivot for (a) lift coefficient (b) induced drag coefficient

The coefficient vector $\{D\}$ is obtained by inversing the matrices in the parentheses. Once each component of D coefficients is found, C_L and C_{Di} are obtained by substituting coefficients D_n into Equations (3.37) and (3.38), respectively; $C_{M,xp}$ can also be found by Equation (3.41). It is noted that these force coefficients are approximated by small angle assumption.

3.3 APPLICATION FOR FLAT PLATE WING

In previous discussion, the lifting line theory was developed to include effects of pivot axis location, reduced pitch rate, and taper ratio. Now we are going to apply the theory for test cases of interest in the study. There are three pivot-axis locations (i.e., leading edge pivot, mid-chord pivot, and trailing edge pivot), three wing planform geometries (i.e., rectangular, trapezoidal, and triangular wings), and six finite reduced pitch rate (i.e., K = 0, 0.022, 0.065, 0.132, 0.193, and 0.394). The wings are rigid and do not exhibit elastic deformation. In other words, there is no wash-out ($\alpha_{rot} > \alpha_{tip}$) or wash-in ($\alpha_{rot} < \alpha_{tip}$), angle of attack α is the same at any span location y.

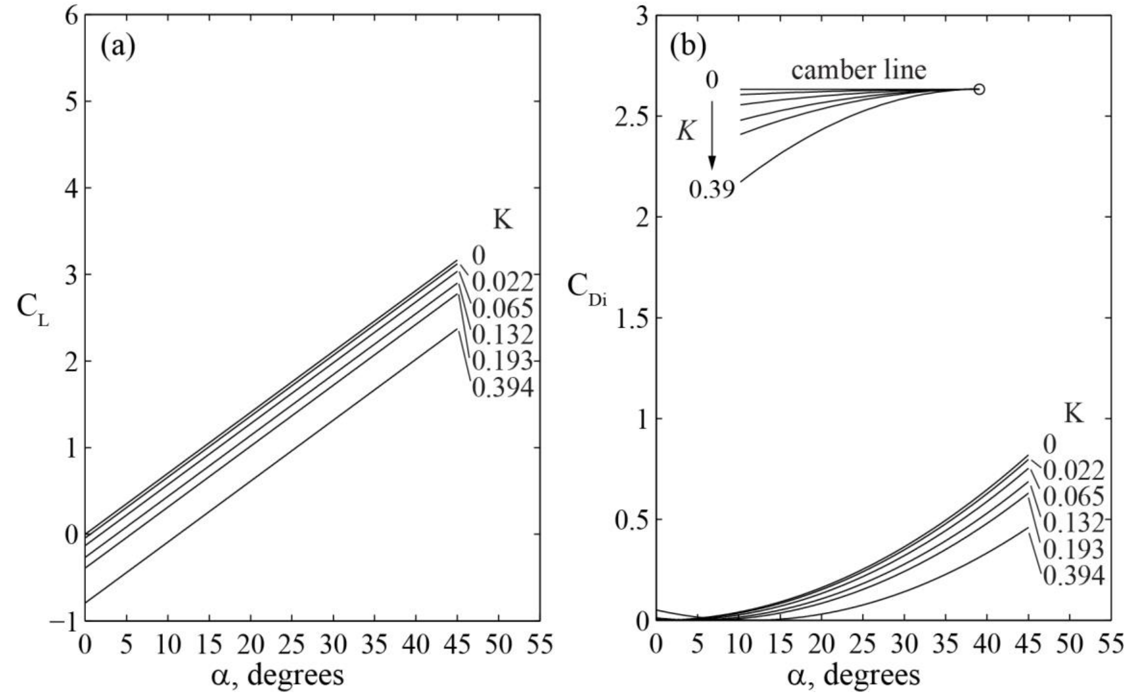

Figure 3.7 Force coefficients as a function of angle of attack using lifting-line theory by rectangular wing at trailing-edge pivot for (a) lift coefficient (b) induced drag coefficient.

Figure 3.4 illustrates various wing planforms in full span at pivot axis location under consideration. From top to bottom are rectangular, trapezoidal, and triangular wings, and from left to right are pivot axes at leading edge, mid-chord, to trailing edge. The leading/trailing edge swept angles are different for wings with taper ratio $\lambda < 1$. The wing geometries are given in Section 2.2.

Both C_L and C_{Di} were predicted using D coefficients equal to 203, which are determined from 203 locations on wing span uniformly distributed from one wingtip to another. The angle of attack is the same along the wing span since rigid wing is assumed. For taper ratio $\lambda < 1$, wing chord varies along wing span and is evaluated using Equation (3.45).

$$\begin{aligned} c(\phi) &= c_r(1+\cos\phi) - c_t\cos\phi \text{ for } \pi/2 \le \phi \le \pi \\ c(\phi) &= c_r(1-\cos\phi) + c_t\cos\phi\text{, for } 0 \le \phi \le \pi/2 \end{aligned} \tag{3.45}$$

Figure 3.5 - Figure 3.7 show predicted force coefficients as a function of angle of attack for leading edge, mid-chord, and trailing edge pivot axes using the rectangular wing. It is noted that effect of reduced pitch rate (K) is attenuated at three-quarter chord,

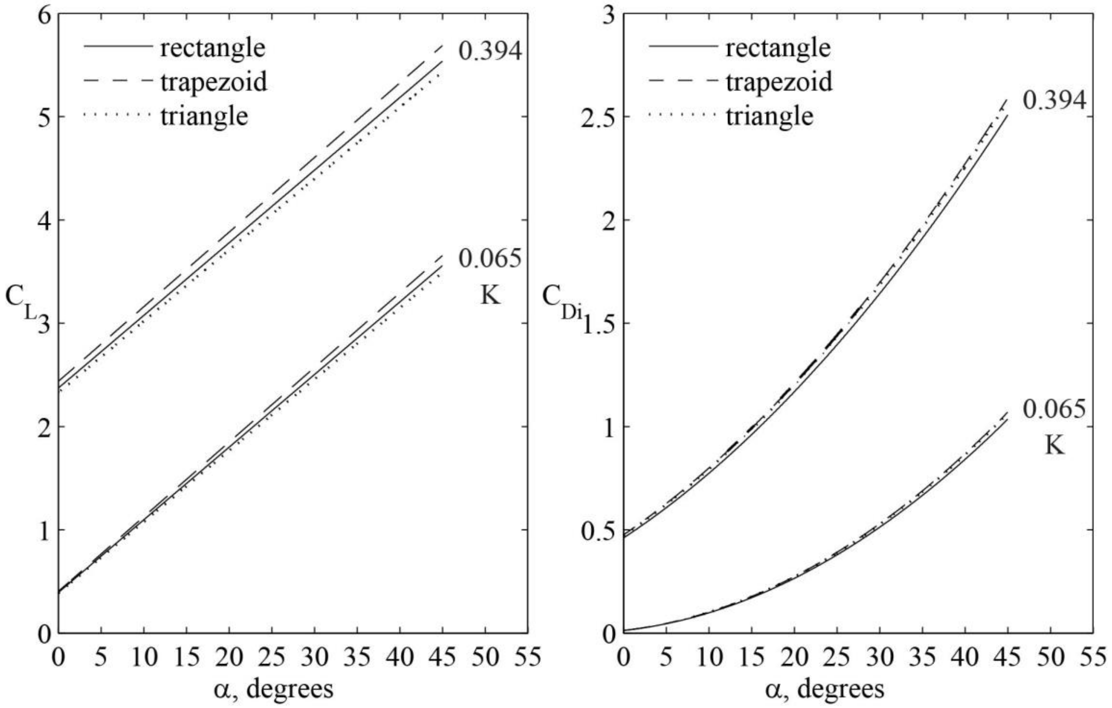

Figure 3.8 Force coefficients as function of angle of attack using lifting-line theory for selected wing planforms at leading edge pivot, (left) lift coefficient (right) induced drag coefficient.

as discovered in Equation (3.20) and (3.21). The force curves, shown in both Figure 3.5 and Figure 3.6, give similar tendency since their pivot axes are located before three-quarter chord. Both C_L and C_{Di} increase with increasing reduced pitch rate K at fixed angle of attack. Higher force coefficients are obtained at a fixed K as pivot axis location is moved toward to the leading edge. Additionally, C_L increases linearly with angle of attack; however, C_{Di} increases exponentially. For pivot axis location after three-quarter chord, shown in Figure 3.7, force coefficients have contrary behaviors with increasing K. For a given angle of attack, the force coefficients decrease with increasing reduced pitch rate. As angle of attack is increased, both C_L and C_{Di} are increased in the same manner as pivot axis location at leading edge or mid-chord. Additionally, the effective camber line at given pivot axis is also plotted in the figures using Equation (3.12) and scaled with chord length, which is stimulated by effects of reduced pitch rate and pivot axis location. The pivot axis location is denoted by circle symbol.

Figure 3.8 shows effects of wing planform at leading edge pivot. Even though a trapezoidal wing gives higher forces than the other wing planforms for a given K, the differences of force coefficients are fairly small for different taper-ratio wings. As the location of pivot axis is moved toward trailing edge, much smaller variances are predicted, which is not shown.

CHAPTER 4

FLOW VISUALIZATION

Flow visualization data by injecting dyes at 50% span of several flat-plate wings are presented. The wings were pitched at two constant pitch rates in a uniform free-stream U_∞ = 17.5 cm/s (*Re* = 9k), which are 155 °/s and 25.6 °/s. As a result, dynamic flow is incorporated to two reduced pitch rates *K* = 0.39 and 0.065 and highlighted as solid symbol in *St*-*Re* space in Figure 4.1. The wing planforms under consideration were rectangle, trapezoid, and triangle; all wings had the same effective aspect ratio of 4, thickness to mean chord ratio of 6.25%, mean chord of 2”, and rounded edges. The details of wing geometry, wing-kinematic implementation, and dye-injection procedure are given in Sections 2.2, 2.3, and 2.4, respectively.

A injection rake was placed at three-mean-chord upstream of leading edge, which

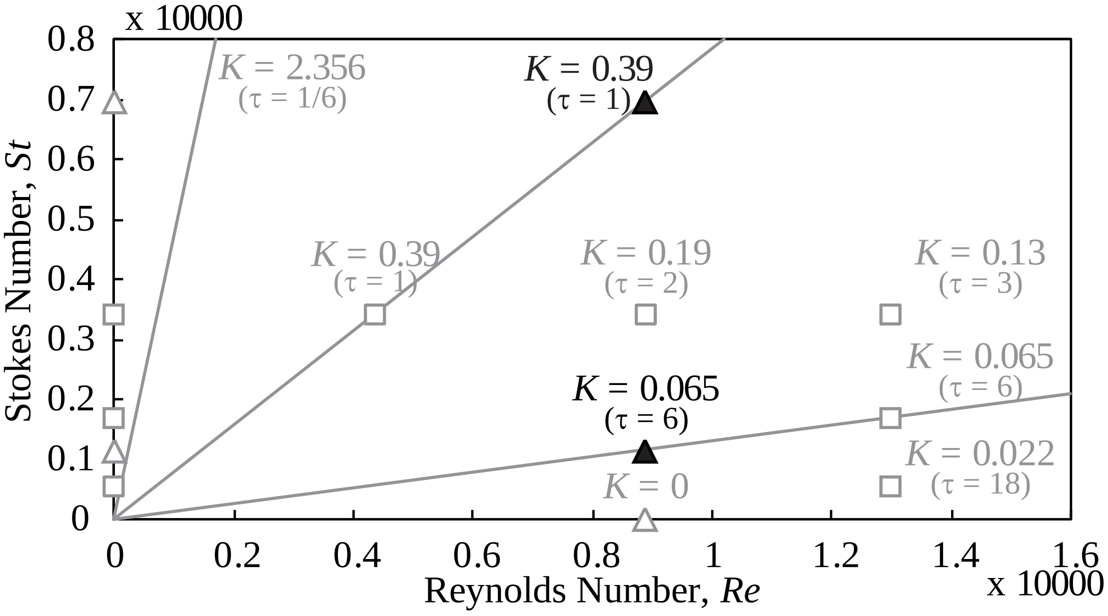

Figure 4.1 Test cases of dye injection in *St* - *Re* space.

had 7 probes with 1” spacing; there were three probes for red dyes and four probes for blue dyes. The center probe released the red dye to the leading edge of wings at initial position, which is zero angle of attack. These dyes move with the flow and are representative of streaklines in fluid mechanics. Two views were used to determine the flow characteristics, which are side view and top view. All flow visualization data were recorded using a camera with a frame rate of 30Hz; the onset of time scale was set to t_1 as shown in Figure 2.6.

4.1 EFFECT OF PITCH RATE

Figure 4.2 and Figure 4.3 show comparisons of reduced pitch rates of $K = 0.39$ and 0.065 in a constant free-stream from side view and top view, respectively; the top view would reveal the evolution of three-dimensional flow. A single event sequence of flow over a rectangular wing was recorded as it pitched up about leading edge in angle of attack from 0° to 45°; the flow visualization data at same angle of attack for $K = 0.39$ and 0.065 are presented. The pitching wings with $K = 0.065$ have pitch time equal to six convective times; whereas the pitching wings with $K = 0.39$ has pitch time equal to one convective time.

As shown in Figure 4.2, Kármán Vortex Street is observed on stationary wing at zero-degree angle of attack in the wake for both reduced pitch rate; the flow is typically two dimensional; outer streaklines are straight around the wing. As the angle of attack is increased to 16°, a starting vortex can be clearly seen in the near wake for $K = 0.39$ and causes the outer streaklines to deflect. The incoming center-streakline swirls around the leading edge, which is called leading-edge swirling and indicates the formation of leading-edge vortex. Some residual center-streakline stays on the leeward side of the wing surface. The residual dyes on the leeward surface indicate regions of lower pressure extending from the trailing edge. For $K = 0.065$ the starting vortex is weak but the deflected outer streaklines identify its presence at further downstream. The incoming center-streakline swirls around the leading edge; the residual center-streakline does not attach to the wing surface but interacts with some residual red-dyes at trailing edge. The flow development at angle of attack of 15° is two-dimensional from the top view. As the angle of attack is further increased, the starting vortex for $K = 0.39$ convects further downstream, followed by several vortices with same counter rotation from the trailing edge. The leading edge swirling becomes much larger, but does not cover the entire wing chord. A portion of residual center-streakline is pushed away from the wing surface and starts to undergo wavy-like distortion, which indicates the viscous-inviscid interface. The flow is likely two-dimensional from the top view. For $K = 0.065$, the starting vortex moves out of the sight, followed by several vortices, unlike typical Kármán vortex street. The leading-edge swirling covers entire wing chord and starts to curl upward into wing leeward surface. The streaklines in the wake deviate from their incoming plane. As the angle of attack is increased to 44°, for $K = 0.39$ the starting vortex is convected about one-chord downstream consistent with free-stream flow; the leading-edge swirling becomes much larger on the same plane with one end attached to the wing surface on the leeward side. The residual center-streakline moves a little upward from the top view; the outer streaklines seem likely to deviate from their incoming plane. For $K = 0.065$, the leading-edge swirling moves upward, then curls to the leeward surface, and then is washed down to wing tip along leading edge.

According to the evolution of dyes over the pitching wing, several features are summarized as follows:

1. At early stage of pitching flat-plate wing and higher reduced pitch rate, the flow is essentially two dimensional.
2. The strength of starting vortex is much stronger at higher reduced pitch rate and formed at lower angle of attack. The formation of the starting vortex may be associated with wing motion acceleration and is discussed in the next chapters.
3. The leading-edge swirling for lower reduced pitch rate is much larger at a lower fixed angle of attack. However, this leading-edge swirling is also demolished much earlier at high angle of attack by a three-dimensional flow developed in the wake, leading to the saturation of forces.

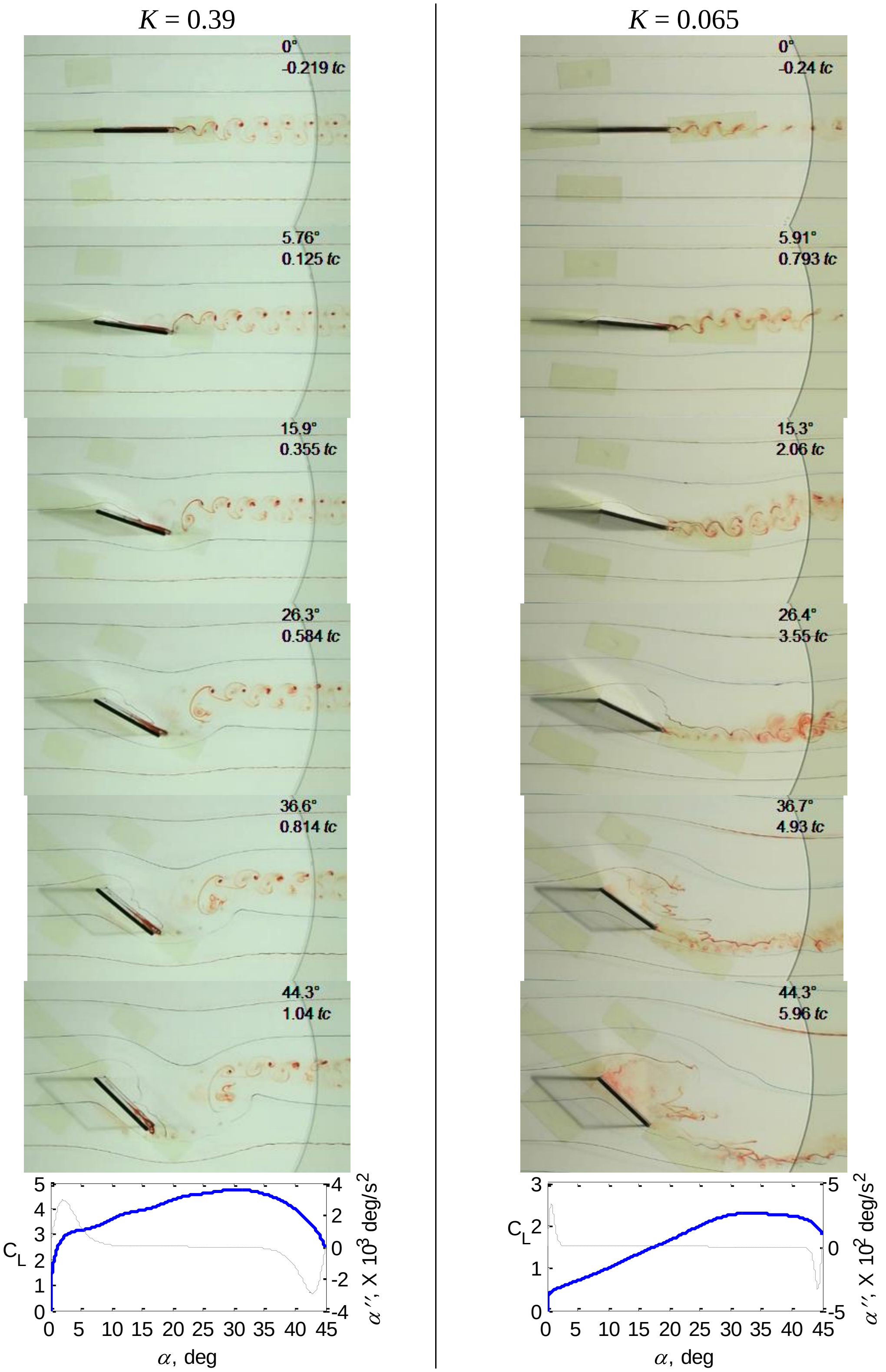

Figure 4.2 Effect of pitch rate in side view during pitch-up phase.

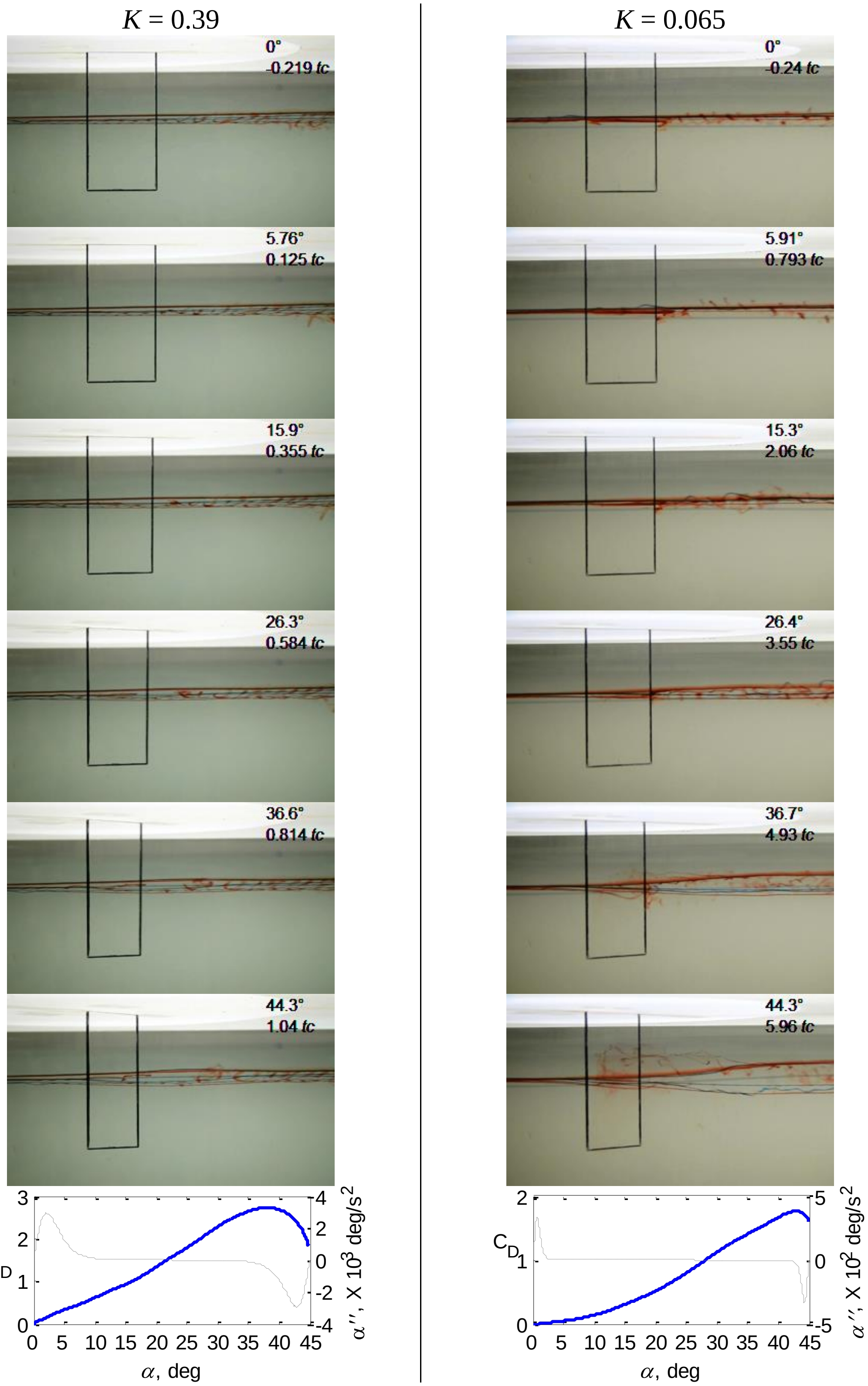

Figure 4.3 Effect of pitch rate in top view during pitch-up phase.

4.2 EFFECT OF PIVOT AXIS LOCATION

Figure 4.4 and Figure 4.5 show effect of pivot axis location of rectangular wing in side view and top view, respectively. The location of pivot axis includes leading edge, mid-chord, and trailing edge. The pitching wing at $K = 0.39$ was studied due to simply two-dimensional flow even at higher angle of attack, as observed previously. The top view was used to determine the onset of three-dimensional flow.

As shown in Figure 4.4, a center streakline reveals the attached flow over the wing and Kármán vortex street in the wake at lower angle of attack. As the angle of attack is increased to 21°, for leading-edge-pivot wing, a typical starting vortex is observed in the near wake. For trailing-edge-pivot wing, a center-streakline swirls at about quarter-chord on the windward surface and presents a formation of a starting vortex at leading edge. In the near wake, there is a vortex with clockwise rotation shed from the leeward surface at trailing edge, different from the typical starting vortex with counterclockwise rotation. The deflections of outer streaklines by leading-edge-pivot and trailing-edge-pivot wings move in the opposite direction. The deflection of outer streaklines by mid-chord-pivot wing indicates the presence of a weak starting vortex in the wake; it is unclear that there is another starting vortex formed at leading edge. Detail review of the video disclosed the typical starting vortex at trailing edge was formed at 6° (0.125 t_c) and 16° (0.355 t_c) by leading-edge-pivot wing and mid-chord-pivot wing, respectively; the "reverse" starting vortex was formed at 16° (0.355 t_c) by trailing-edge-pivot wing. This disclosure indicates there would be no vicinity of starting vortex by three-quarter-chord-pivot wing. As the angle of attack is increased to 45°, the starting vortex by leading-edge-pivot wing convects further downstream; however, the starting vortex by trailing-edge-pivot wing grows in size at the same location, determined from an increase of red-dye concentration.

Since injection rake probes were positioned at the same place while center dyes were injected to the chord line at zero-incidence; the incoming streaklines confronted the pitching wing at different places on the wing, depending on pivot axis location. The evolution of vortical structure is not captured in detail by flow visualization data. However, it was revealed that leading-edge-pivot wing produces a starting vortex at

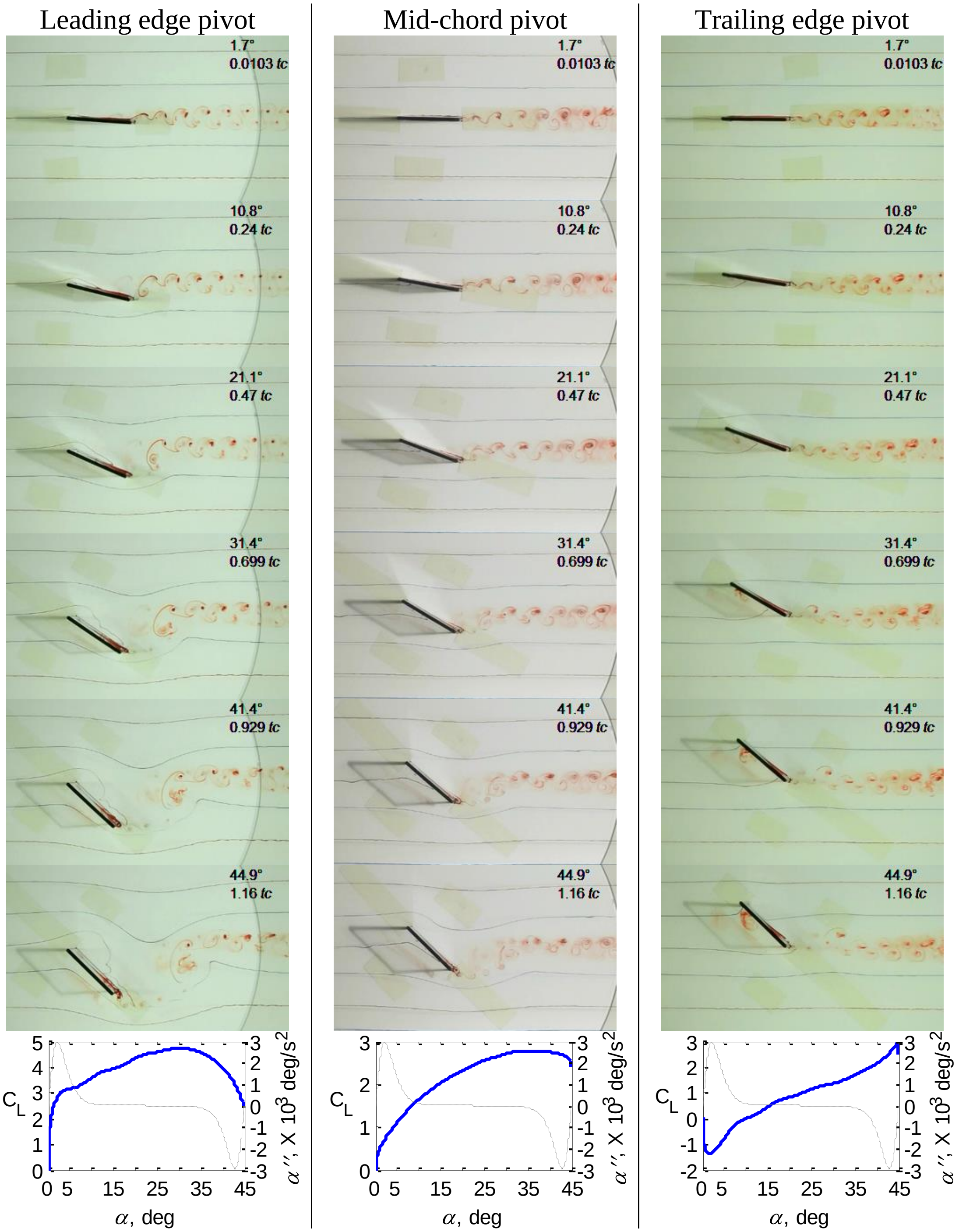

Figure 4.4 Effect of pivot axis location in side view during pitch-up phase.

trailing edge, and trailing-edge-pivot wing produces a starting vortex at leading edge on the windward surface and a reverse starting vortex at trailing edge. The streaklines stay on the same plane during the formation of starting vortex, indicating two-dimensional flow evolution.

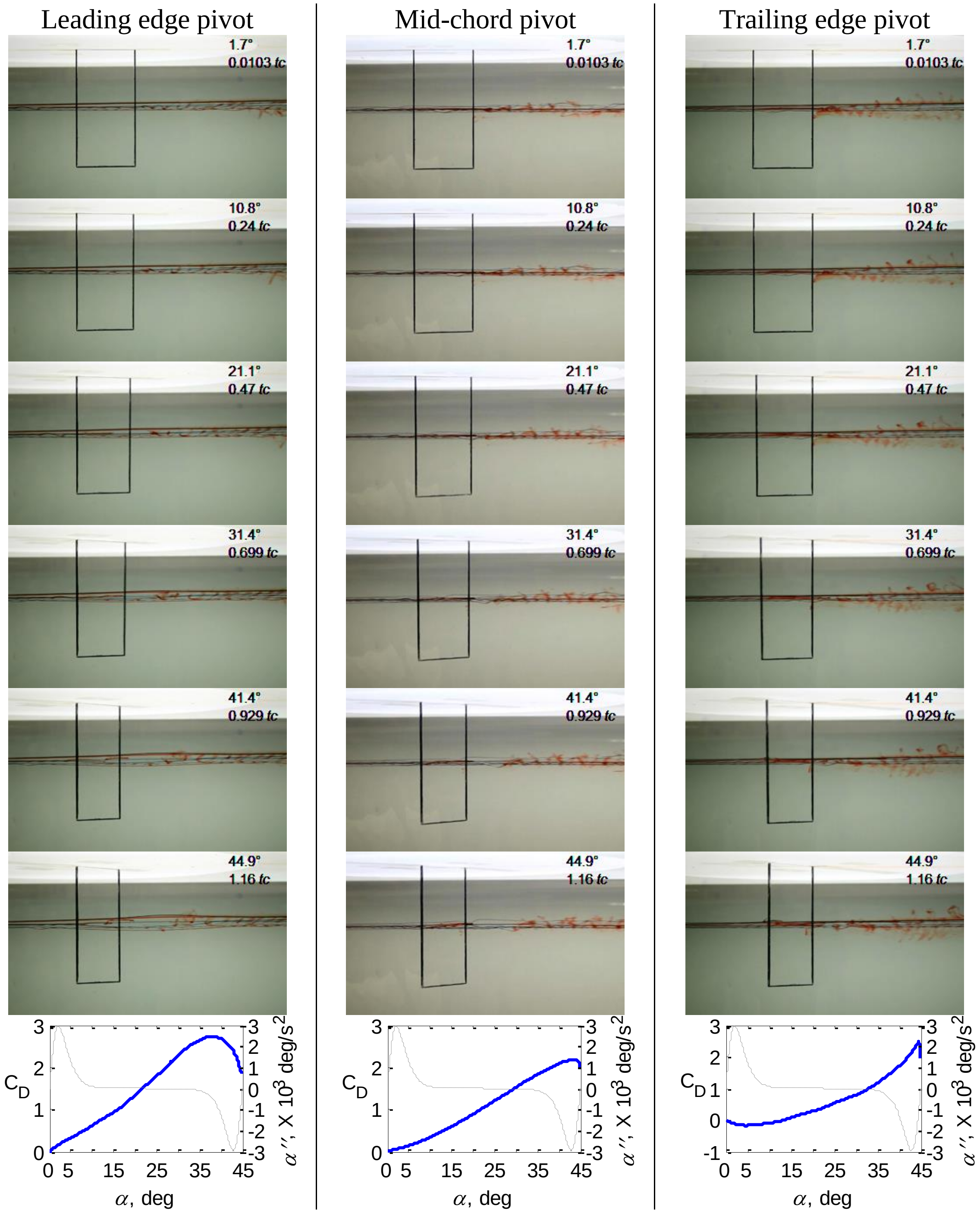

Figure 4.5 Effect of pivot axis location in top view during pitch-up phase.

4.3 EFFECT OF WINGPLANFORM

The flow visualization data have revealed two-dimensional flow field over a rectangular flat-plate wing pitching at a higher reduced pitch rate *K* = 0.39, where the pitch time is equal to one convective time. There is a starting vortex at trailing edge by leading-edge-pivot wing and a starting vortex at leading edge by trailing-edge-pivot wing. Now the impact of wing planform on dynamic flow is presented under the same circumstance, which includes rectangular, trapezoidal, and triangular wings. The flow visualization data are selected to represent the flow structure in three states: unsteady state, transient state, and steady state. For leading-edge-pivot and trailing-edge-pivot wings, the pivot axis is always at an axis with zero-degree sweep angle; the sweep angle on the other edge is 0°, 18.4°, and 45° for rectangular, trapezoidal, and triangular wings, respectively. For mid-chord-pivot wings, the leading-edge and trailing-edge sweep angles increase with decreasing taper ratio. The geometry of wing planform is given in Table 2.1.

4.3.1 Unsteady Flow

Flow structure in an unsteady state is characterized using streaklines at a phase where uniform free-stream flow was disturbed by wings for one-chord convective time and the wing position was near the maximum angle of attack (i.e., α_m = 45°). The flow visualization data shown in Figure 4.6-Figure 4.8 are for leading-edge-pivot, mid-chord-pivot, and trailing-edge-pivot wings, subsequently.

As shown in Figure 4.6, for rectangular wing in the side view, there are Kármán vortices in the far wake, which were formed as the wing was at zero-degree angle of attack. A typical starting vortex with a count clockwise rotation is observed in the wake at a distance of one-chord downstream from the trailing edge, which was formed at 6-degree angle of angle detached from the chord line. After forming the starting vortex, most of the dyes from the center streakline resided on the rear portion of the leeward surface during pitch motion. Meanwhile, the center streakline near the leading edge deflects upward and swirls over three-quarter chord of the wing, and then becomes wrinkled before merging with the residual dyes on the leeward surface. The center streakline behind the merging point moves slightly upward in a spanwise direction, as shown in the top view. The streaklines before the merging progress (i.e., at lower angle of attack) remain on the same plane, as observed in the top view, which indicates flow dynamic is two-dimensional.

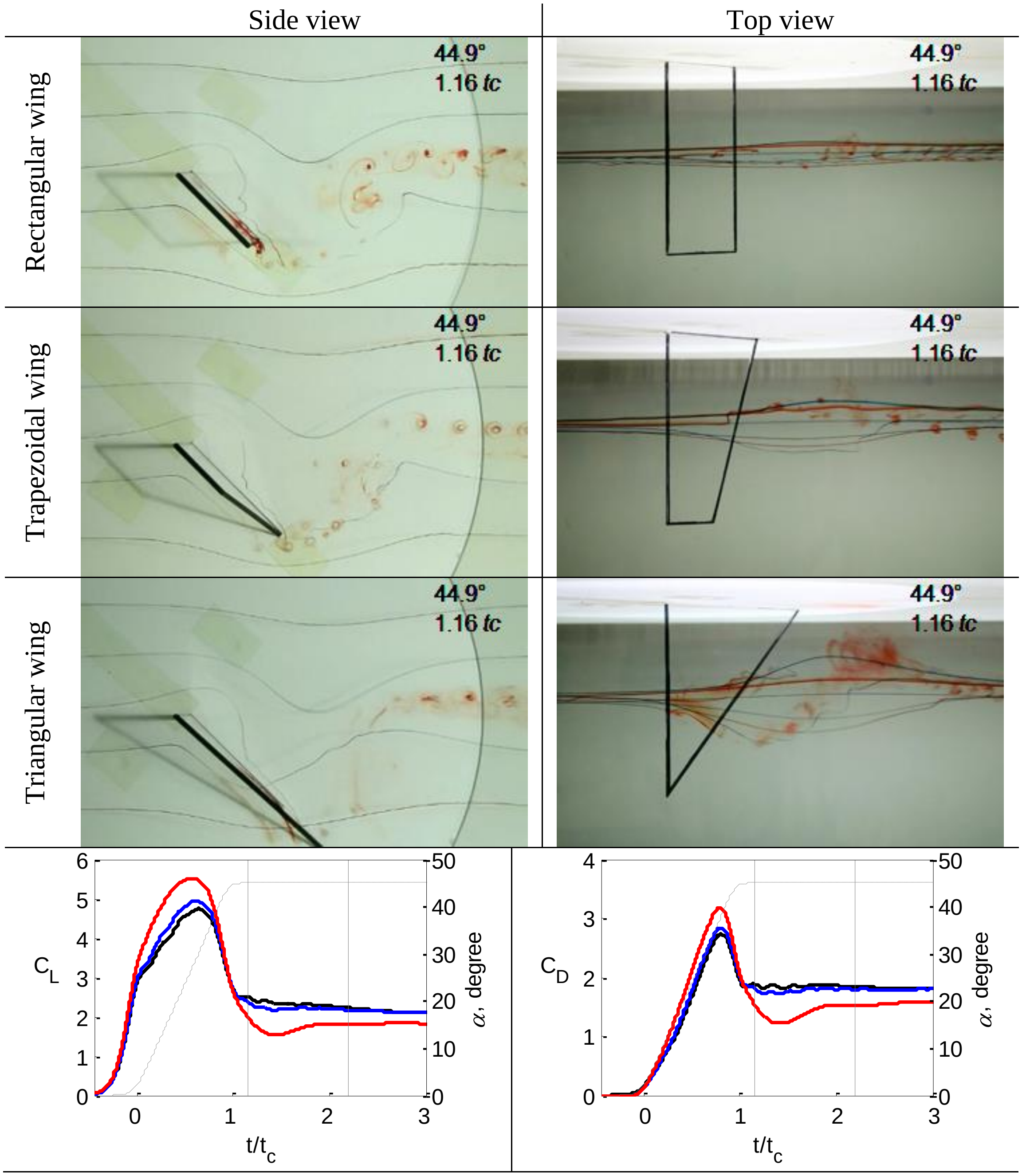

Figure 4.6 Effect of wing planform for pivot axis location at leading edge in unsteady flow.

For trapezoidal wing in the side view, there are few vortices in the far wake with more diffusion due to trailing-edge sweep angle. Unlike the rectangular wing, there were no residual dyes in the vicinity of the leeward surface; the merging process was not observed. The center streakline over leading edge has similar profile as that for the rectangular wing. Even though there is no merging progress, the center streakline near the trailing edge swirls upward in the spanwise direction, as shown in the top view, indicating an occurrence of spanwise flow. The deflection of outer streaklines indicates the existence of a weak starting vortex in the wake; from the top view, this starting vortex is stretched due to trailing-edge sweep angle. In addition, the expansion of outer streaklines in the near wake is more pronounced than that by the rectangular wing; the vortices in the far wake move downward.

For triangular wing in the side view, vortices in the far wake have more diffusion than that for the other two wing planforms. The center streakline produces similar structure over the leading edge on the same plane as that for the other wing planforms; however, there is no starting vortex observed in the wake. In the top view, the center streakline is pushed upward along the trailing edge at a distance of about one-chord downstream, which indicates an existence of axial flow. The outer streaklines on the leeward side deflects significantly upward from their original path; however, the outer streaklines on the windward side move downward. As a result, a significant streakline expansion is observed in the near wake, forming an oval profile. A dye concentration is also observed at the center of streakline expansion, where the starting vortex was observed from the other wing planforms as taper ratio is higher than 0.5. This dye concentration is attributed to an out-of-plane starting vortex and enhances the force generation. The vortices in the far wake stay on the same plane as they were at earlier stage.

Figure 4.7 shows flow visualization data for mid-chord-pivot wings; leading-edge sweep angle is same as trailing edge sweep angle, which is 0°, 9.5°, and 26.5°, respectively. For rectangular wing in the side view, the Kármán vortices are in the vicinity of the far wake, just like the leading-edge-pivot wing but with weaker circulation, which was determined from the amount of deflection of outer streaklines. There is an in-plane starting vortex located at a closer downstream distance from the trailing edge than the leading-edge-pivot wing. The incoming center streakline moves toward the quarter-chord on the windward surface, instead of swirling around the leading edge as the leading-edge-pivot wing, because the position of center-dye-probe was half-

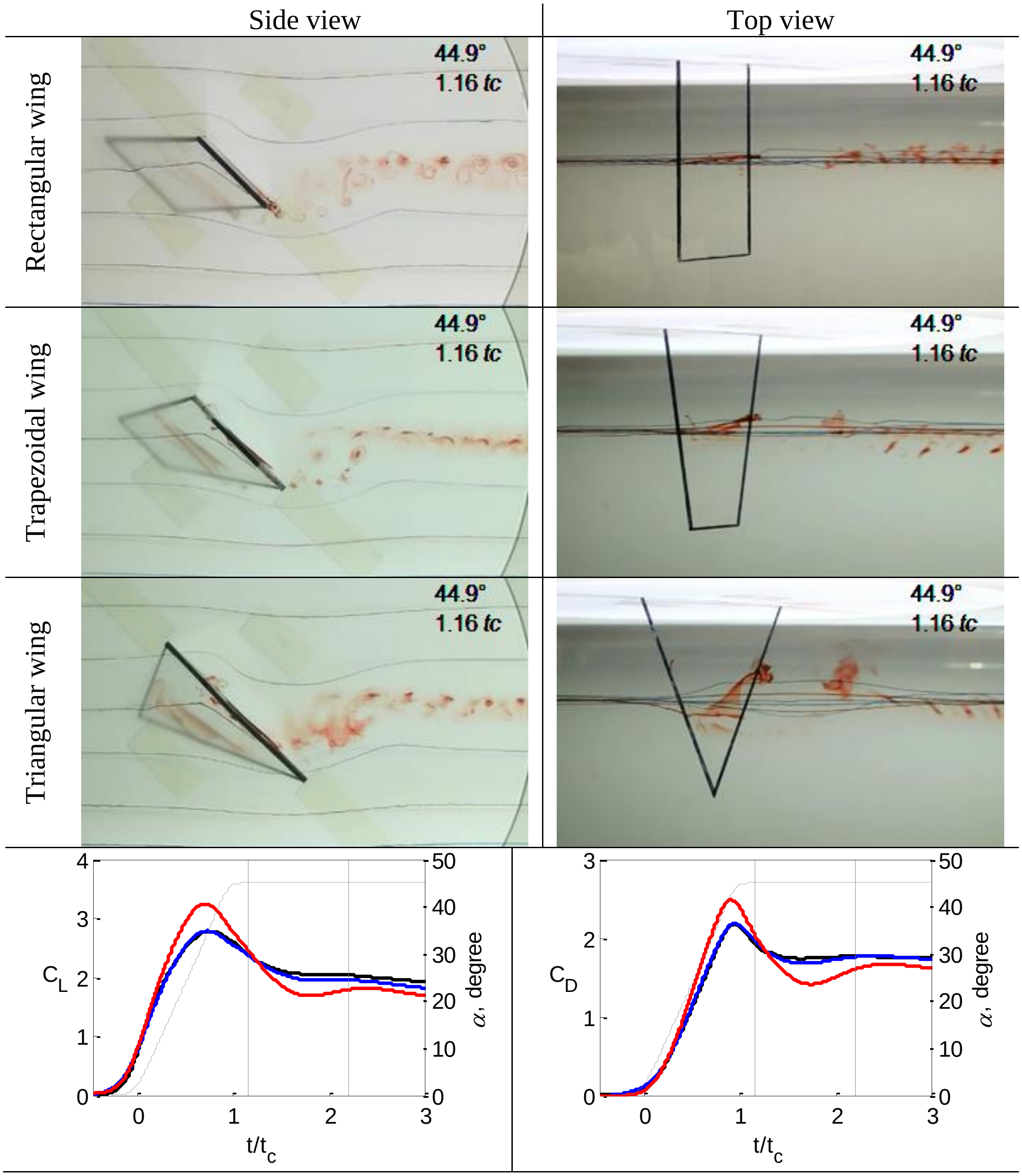

Figure 4.7 Effect of wing planform for pivot axis location at mid-chord in unsteady flow.

chord projection distance lower from the leading edge. In the top view, residual dyes on the leeward surface remained on the same plane as incoming dyes, similar to that by the leading-edge-pivot wing.

For trapezoidal wing in the side view, the structure of vortices in the far wake is different from the rectangular wing due to leading-edge and trailing edge sweep angles. A starting vortex is in the vicinity of the wake at the same location as the rectangular wing. In the top view, the center of far-wake-vortex is pulled downward and toward the wingtip. Some dye-concentration is observed at the location of starting vortex; some of residual dyes on the leeward surface are pushed upward at trailing edge but stay close to the leeward surface. Some of residual dyes on the windward surface swirl upward around leading edge, indicating a stagnation axis.

For triangular wing in the side view, the far-wake vortices have very different patterns from higher taper-ratio wings due to sweep angle at leading edge and trailing edge. A starting vortex is present in the wake at the same location as the other two wing planforms. In the top view, the centers of far-wake vortices were pulled away from the wingtip. Much more dye concentration is significantly appeared at the location of the starting vortex by the other two wing planforms, indicating the occurrence of starting-vortex re-orientation and the formation of out-of-plane starting vortex. The process of starting-vortex re-orientation promotes the force generation, similar to the observation from the leading-edge-pivot wing, and is accompanied by an expansion of outer streaklines.

Figure 4.8 shows flow visualization data for trailing-edge-pivot wings; leading-edge sweep angle for rectangular, trapezoidal, and triangular wings is 0°, 18.4°, and 45°, respectively. For rectangular wing in the side view, the Kármán vortices in the far wake were formed at zero-degree angle of attack before the onset of pitch motion, similar to that by the other axis-pivot wings. A vortex with clockwise rotation was formed at higher angle of attack of 16° and is shown at a distance of less than one chord downstream from trailing edge. This vortex is different from the typical starting vortex and regarded as a reverse-starting vortex. The outer streaklines are deflected in the opposite direction of the leading-edge-pivot wing, which could be employed to identify the occurrence of the reverse-starting vortex. During the pitch motion, some dyes from the center streakline stayed at the rear portion of the leeward surface, whereas some dyes remained on the windward surface around the quarter chord. Consequentially, a vortex structure with counterclockwise rotation is observed close to the leading edge, which is akin to the typical starting vortex, like one by leading-edge-pivot wing but being formed at different location. As the angle of attack was increasing, the upstream center streakline moved along the chord line on the windward side toward the trailing edge until 45° angle of attack. Once this center streakline meets with residual dyes on the leeward surface at trailing edge, the formation of trailing edge vortex with counterclockwise rotation is initiated. The vortical flow evolution over the wing during the pitch-up phase is two-dimensional from the top view.

For trapezoidal wing in the side view, the far-wake vortices are significantly different from the Kármán vortices shown by the rectangular wing. A reverse-starting vortex with clockwise rotation is presented at the same location in the wake as that by the rectangular wing. During pitch-up phase some dyes from center streakline remained on the rear portion of the leeward surface; at the same time, the center streakline moves toward the windward surface and travels along wing chord to trailing edge. Once this center streakline encounters the residual dyes on the leeward surface at trailing edge, the formation of trailing edge vortices is initiated. This flow evolution is similar to that by the rectangular wing. There is no indication of a starting vortex at leading edge in the side view, but a dye accumulation at the leading edge on the windward surface is observed from the top view. Also observed from the top view is the in-plane streaklines during the pitch–up phase, indicating two-dimensional flow dynamic.

For triangular wing in the side view, the dye evolution is very similar with the other wing planforms, except vortices in the far wake have much more diffusion. A reverse-starting vortex is formed in the wake at a distance of less than one chord downstream of trailing edge, which is similar to the other two wing planforms. No starting vortex at leading edge is observed from either the side view or the top view. Some dyes from center streakline resided on the leeward surface during pitch motion; meanwhile the upstream center streakline moved toward the windward surface and traveled to trailing edge along the chord-line to initiate the formation of trailing edge vortex. The in-plane streaklines from the top view reveals two-dimensional flow evolution as that for the other wing planforms.

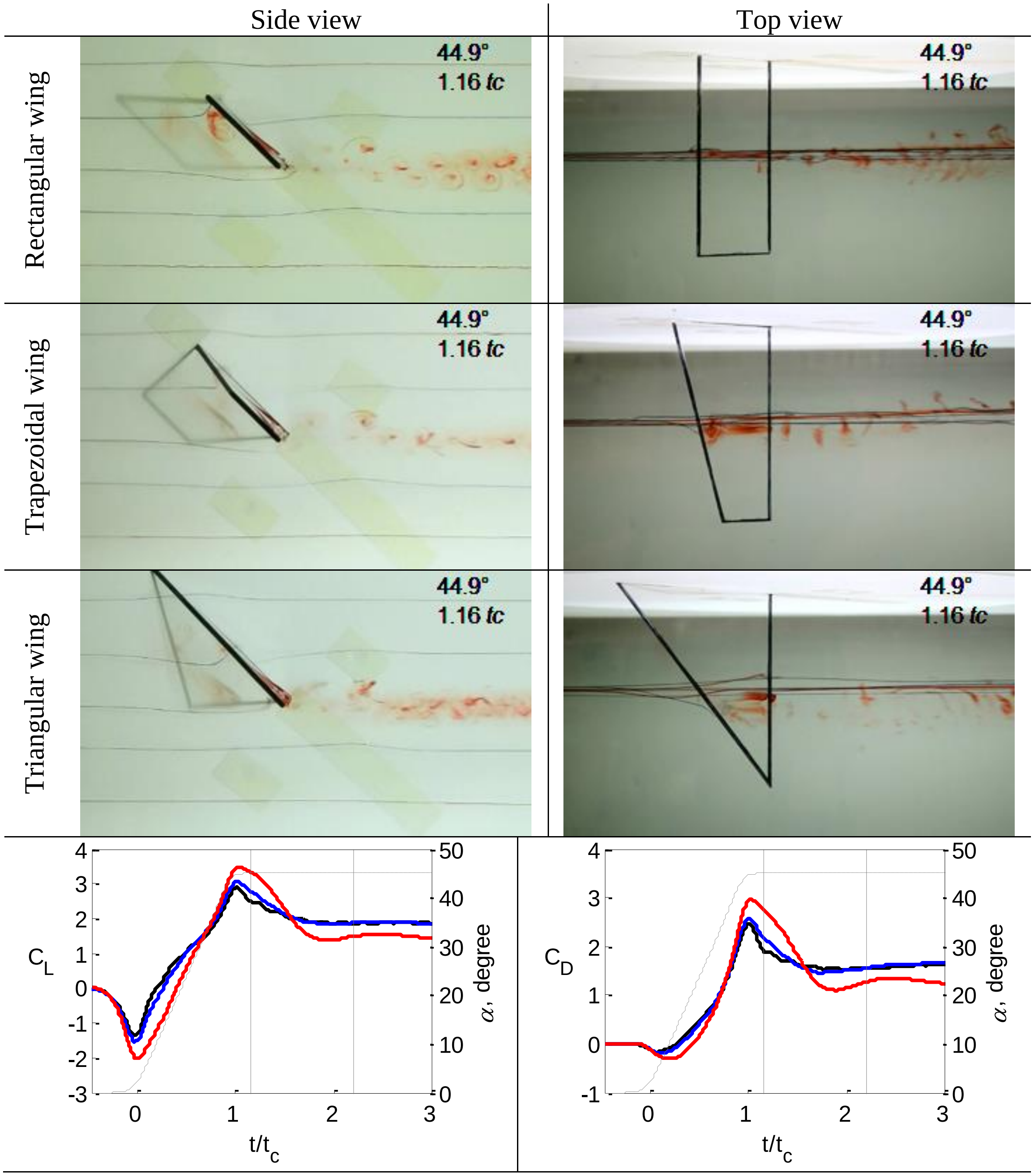

Figure 4.8 Effect of wing planform for pivot axis location at trailing edge in unsteady flow.

4.3.2 Transient Flow

Dynamic flow in transient state is characterized using streaklines at a phase where wings stayed at 45° angle of attack for one-chord convective time. Figure 4.9-Figure 4.11

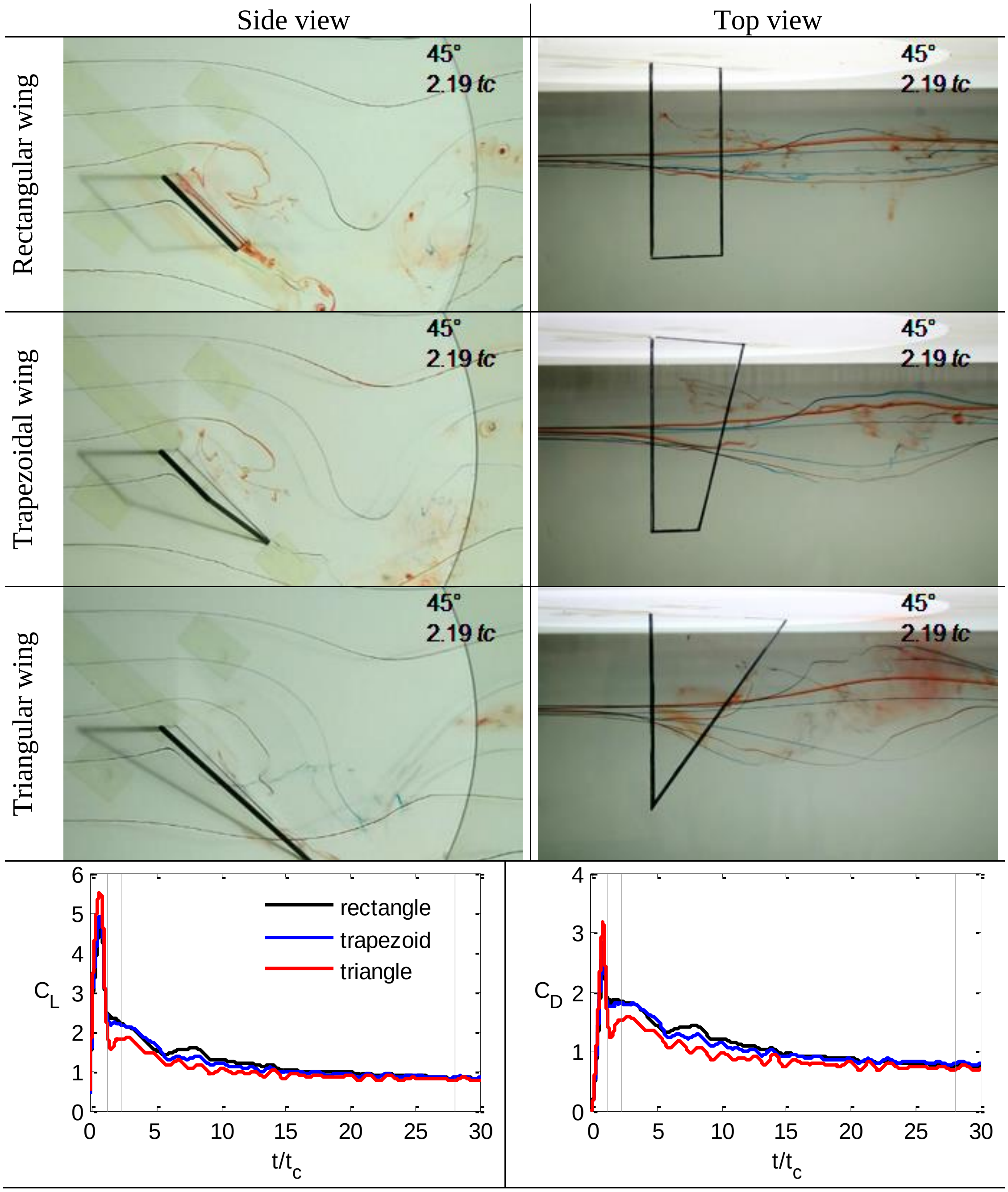

Figure 4.9 Effect of wing planform for pivot axis location at leading edge in transition flow.

show flow visualization data over wings as their pivot axis locations were at leading edge, mid-chord, and trailing edge, subsequently.

As shown in Figure 4.9, for the rectangular wing in the top view, the center streakline over the leading edge undulates and swirls upward, indicating there is a spanwise flow on the leeward side and turbulent flow in progress. And also push some residual dyes circulating toward the leading edge on the leeward surface, forming a well-known secondary vortex in the side view. The leading-edge swirling enforces outer streaklines on the leeward side to curl in the same direction and promote the deflection of outer streaklines caused by the starting vortex. The outer streaklines on the windward side curl downward. This progress expands the streaklines in the wake, as shown in the top view, and forms in-transition streaklines. The expansion of streaklines was also observed on the wings with lower taper ratio during pitching motion due to trailing-edge sweep angle. Some residual dyes meet with the center streakline from the windward surface at trailing edge and form trailing-edge vortices. A blue streakline below the center streakline moves toward the quarter chord of the windward surface and follows the surface downstream at a later time. After four convective times, this blue streakline reveals the formation of another type of trailing edge vortex, where normal force decreases and axial force increases (Yu et al., 2013). In the top view, the center of the starting vortex rotates downward and toward the wingtip, shown at a distance of two-chord downstream from the trailing edge.

For the trapezoidal wing in the side view, the evolution of center streakline over the leading edge is similar to that for the rectangular wing. After one-chord convective time at maximum angle of attack, the center streakline around the leading edge swirls upward, like the rectangular wing, and produces the same force. The leading-edge swirling evolves into the direction of normal force at a later time. This progress is quicker than that by the rectangular wing. There are no residual dyes on the leeward surface. A blue streakline below the center streakline moves toward the quarter chord on the windward surface and follows the surface downstream, which is similar to that for the rectangular wing. The development of trailing-edge vortex is also observed after four convective times, which corresponds to a decrease of normal force and an increase of axial force (Yu et al., 2013). In the top view, the in-transition streaklines in the wake are more pronounced than that for rectangular wing, but have less influence on force generation.

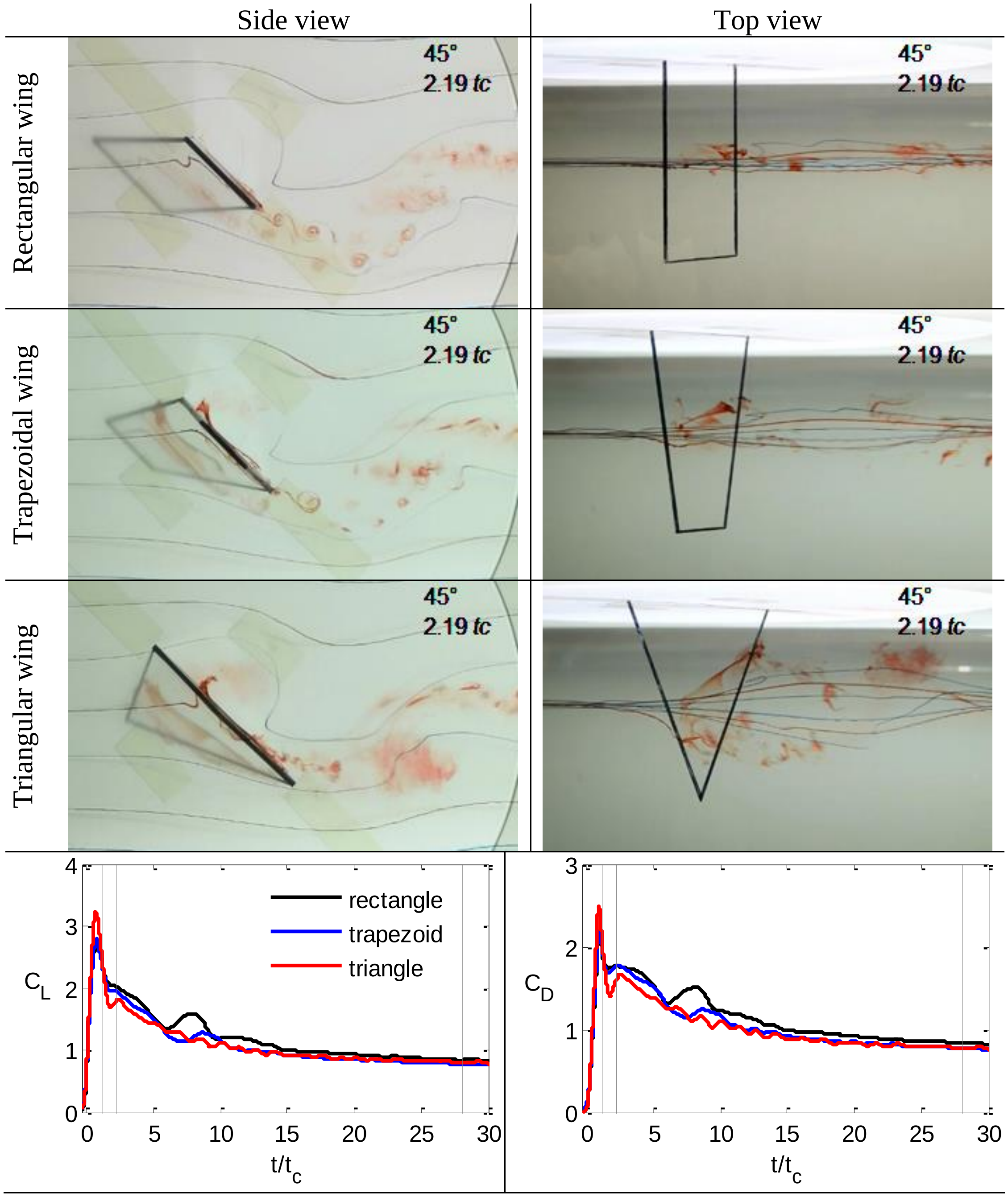

Figure 4.10 Effect of wing planform for pivot axis location at mid-chord in transition flow.

For the triangular wing in the side view, the leading edge swirling covers entire wing chord; its evolution toward normal-force direction is more pronounced and earlier than the other two wing planforms, which deteriorates the force generation. There is no evidence of residual dyes on the leeward surface. A blue streakline below the center streakline moves toward the quarter chord on the windward surface, similar to the other wing planforms, and follows the surface downstream. However, unlike the rectangular and trapezoidal wings, the development of trailing-edge vortex is imperceptible at a later time. Additionally, the in-transition streaklines are much more pronounced than the other two wing planforms.

Figure 4.10 show flow visualization data based on mid-chord-pivot wings in transient flow. For the rectangular wing in the side view, the starting vortex is convected one-chord further downstream in accordance with free-stream velocity. There are few trailing-edge vortices shed from the windward surface, following the starting vortex. Some residual dyes on the leeward surface are in attempt to travel reversely toward leading-edge and form a well-known secondary vortex, which is driven by axial flow on the leeward side and progressed in circulation, as shown in the top view. The upper streakline reveals a leading-edge swirling over entire wing chord. The expansion of in-transient streaklines is less pronounced than that by the leading-edge pivot wing.

For the trapezoidal wing in the side view, the starting vortex is convected to a location in correspondence with free-stream velocity and is pushed upward. Several trailing-edge vortices were formed in the wake and followed the starting vortex. Some residual dyes on the leeward surface close to the trailing edge move upward and travel toward the leading edge to form a secondary vortex at a later time. The dye-diffusion at the location of secondary vortex discloses a paired axial flow in progress. There is an axial flow washing toward wingtip close to the leeward surface and an axial flow toward wingroot on the outer of the leeward surface. The leading-edge swirling is revealed by a blue streakline above the center streakline, covering the entire wing chord similar to the rectangular wing. The in-transition streaklines are more pronounced than the rectangular wing and less pronounced than the leading-edge-pivot wing, which indicates the expansion of in-transition streaklines depends on the trailing-edge sweep angle.

For the triangular wing in the side view, the starting vortex in the far wake is diffused significantly in comparison with the other wing planforms. Its presence at an upper position from the top view indicates an axial flow from the wingtip toward wingroot in the wake. There are no trailing-edge vortices in the vicinity of near wake, like the other two wing planforms. Some residual dyes on the leeward surface at trailing edge were pushed upward and are convected into the wake. Simultaneously, some dyes on the windward surface traveled downward and convected downstream in the same path. The leading-edge swirling revealed by the blue streaklines has similar appearance to the other two wing planforms. The incoming center streakline is moving to a lower leading edge; portion of its dyes reveals a sharp shear layer across the leading edge and in front of the secondary vortex on the leeward surface. The in-transition streaklines are more pronounced than other two wing planforms and less pronounced than the leading-edge-pivot wing, which supports a conclusion that the expansion of in-transition streaklines is dependent of trailing-edge sweep angle.

As shown in Figure 4.11, for the rectangular wing in the side view, the reverse-starting vortex is convected in a distance of one-chord further downstream. As the center streakline on the windward surface met the residual dyes on the leeward surface at trailing edge, a trailing-edge vortex in counterclockwise rotation was formed, which is at a distance of about one-chord downstream from the trailing edge. This trailing-edge vortex is larger than following trailing edge vortices. The starting vortex at leading edge was broken into two portions, observed from video. One portion is sucked toward and turns around the leading edge to form the leading-edge vortex; the other portion moves downstream along wing chord on the windward surface to form a trailing-edge vortex. On the leeward surface, residual dyes transport reversely toward the quarter chord of the wing and form a secondary vortex at a later time, where the dyes are washed toward wingtip. Simultaneously, the leading edge swirling curls upward in spanwise direction, which is represented by a blue streakline above the center streakline and red dyes from the starting vortex at leading edge. The in-transition streaklines are indistinguishable at this phase.

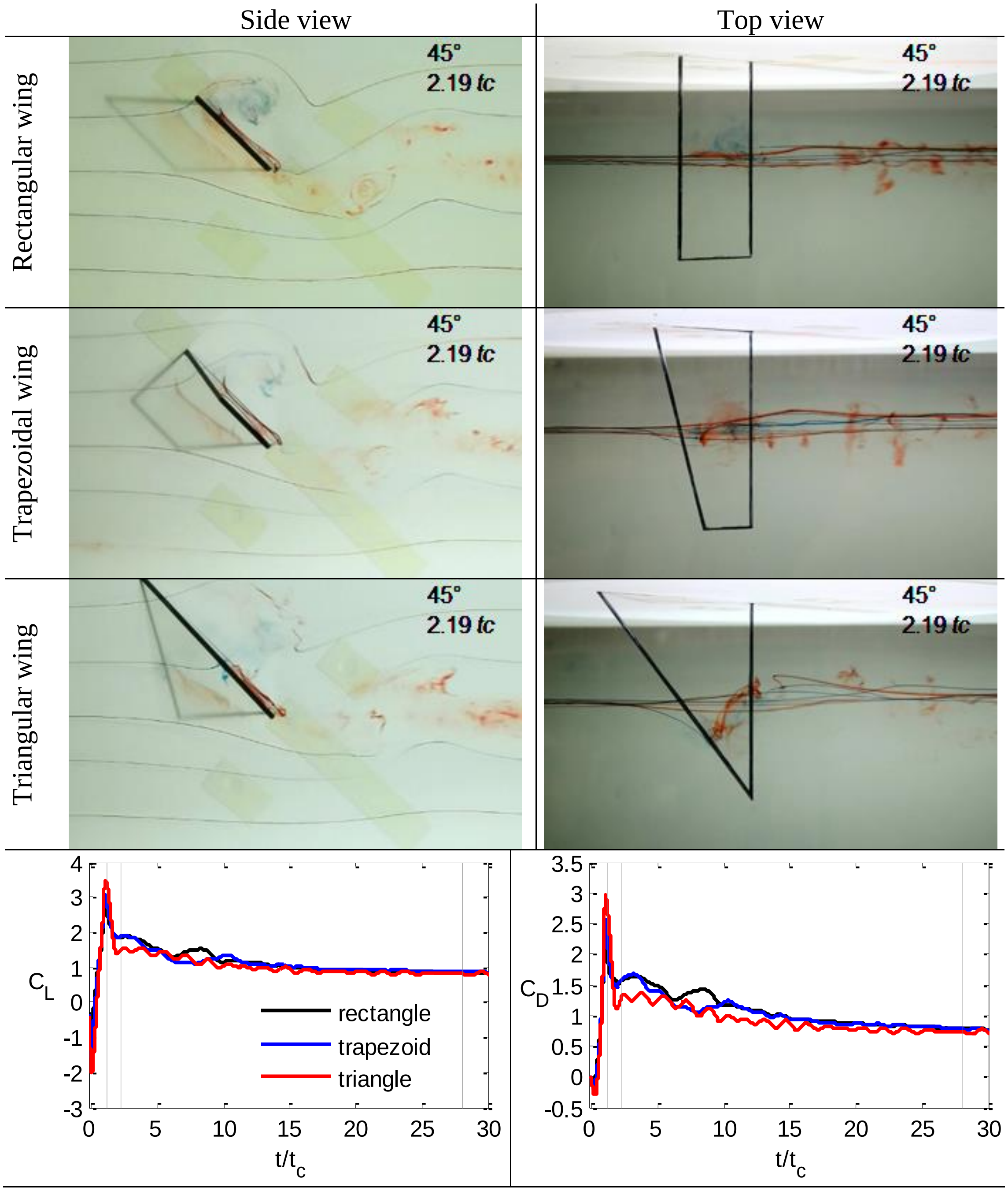

Figure 4.11 Effect of wing planform for pivot axis location at trailing edge in transition flow.

For the trapezoidal wing in the side view, the reverse-starting vortex is convected downstream in accordance with free-stream velocity, similar to that for the rectangular wing. A trailing-edge vortex was formed while the center streakline met with the residual dyes on the leeward surface, which is shown at a distance of one-chord downstream from

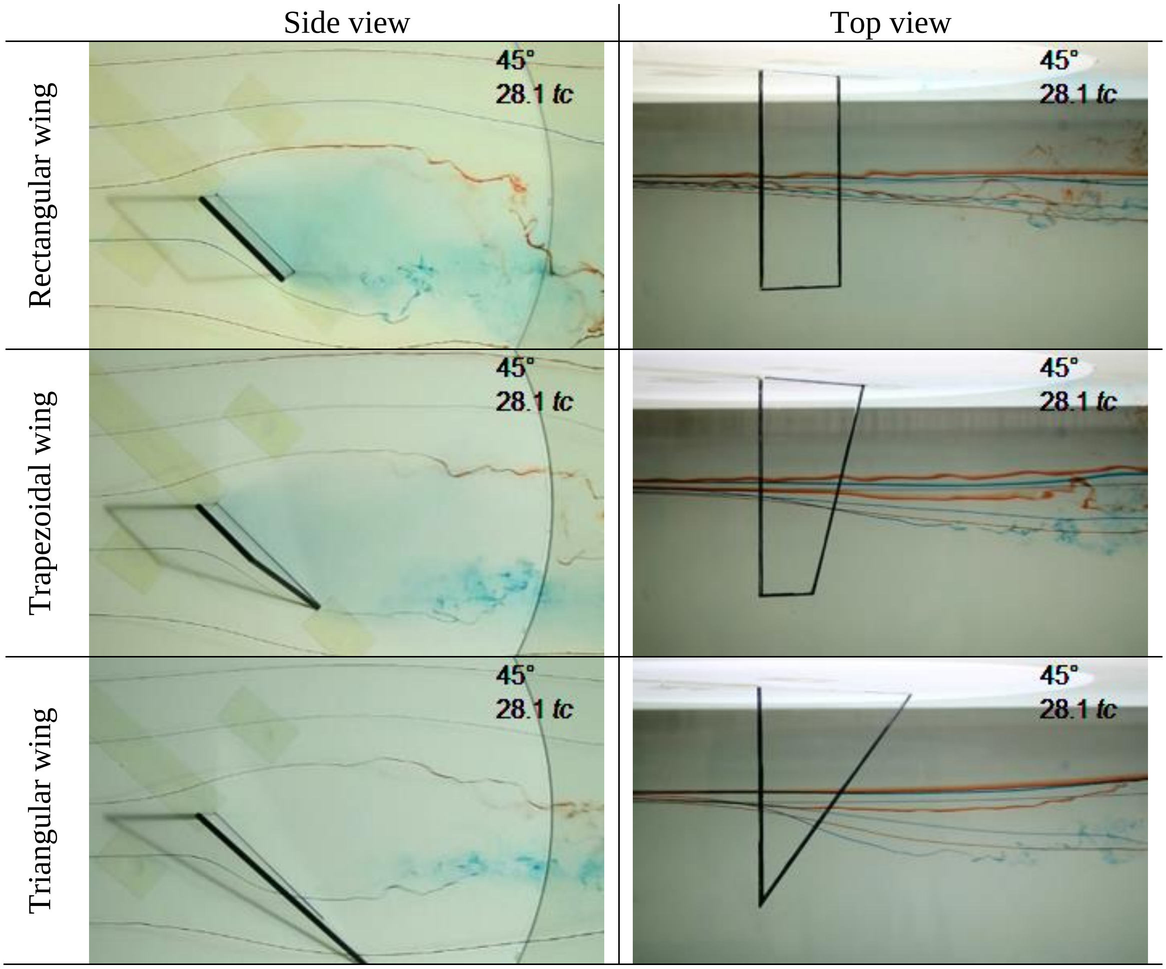

Figure 4.12 Effect of wing planform for pivot axis location at leading edge in a steady state.

the trailing edge. The breaking progress of the starting vortex as observed from the rectangular wing is imperceptible. The dye accumulation at leading edge on the windward surface, observed in Figure 4.8, is convected downstream and diffused very quickly into spanwise direction. On the leeward surface, the residual dyes near the trailing edge travel reversely toward the leading edge and form a secondary vortex, which is similar to that by the rectangular wing. These reversed dyes meet with blue dyes upstream at leading edge. A portion of these dyes is washed downward on the leeward surface and a portion of them is pushed toward wingroot, which indicates the presence of a pair of axial flow. The expansion of in-transition streaklines is less pronounced than the other pivot-axis wings. However, the occurrence of the in- transition streaklines is shifted upstream, which is influenced by leading-edge sweep angle.

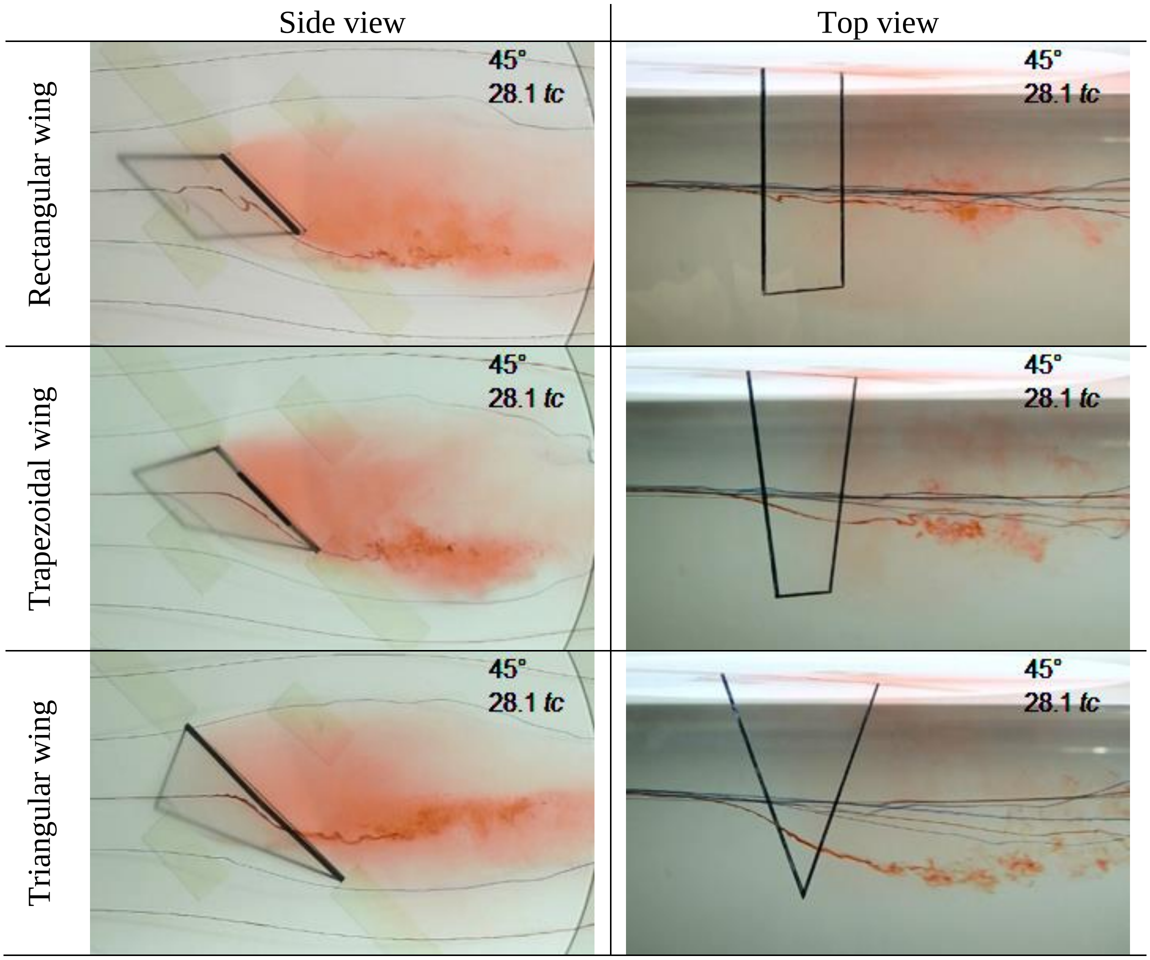

Figure 4.13 Effect of wing planform for pivot axis location at mid-chord in a steady state.

For the triangular wing in the side view, similar to the other wing planforms, a trailing edge vortex was formed as the center streakline met the residual dyes on the leeward surface at trailing edge, which is present at a distance of one-chord downstream from the trailing edge. The residual dyes on the leeward surface transport toward the leading edge, unlikely forming a secondary vortex, the reversed dyes was washed down along the leading edge and meet with upstream blue streakline at leading edge. The formation of leading edge swirling is hardly identified from the blue streakline above the center streakline, unlike the other wing planforms. The expansion of in-transition streaklines is more pronounced than that by the other two wing planforms.

4.3.3 Steady Flow

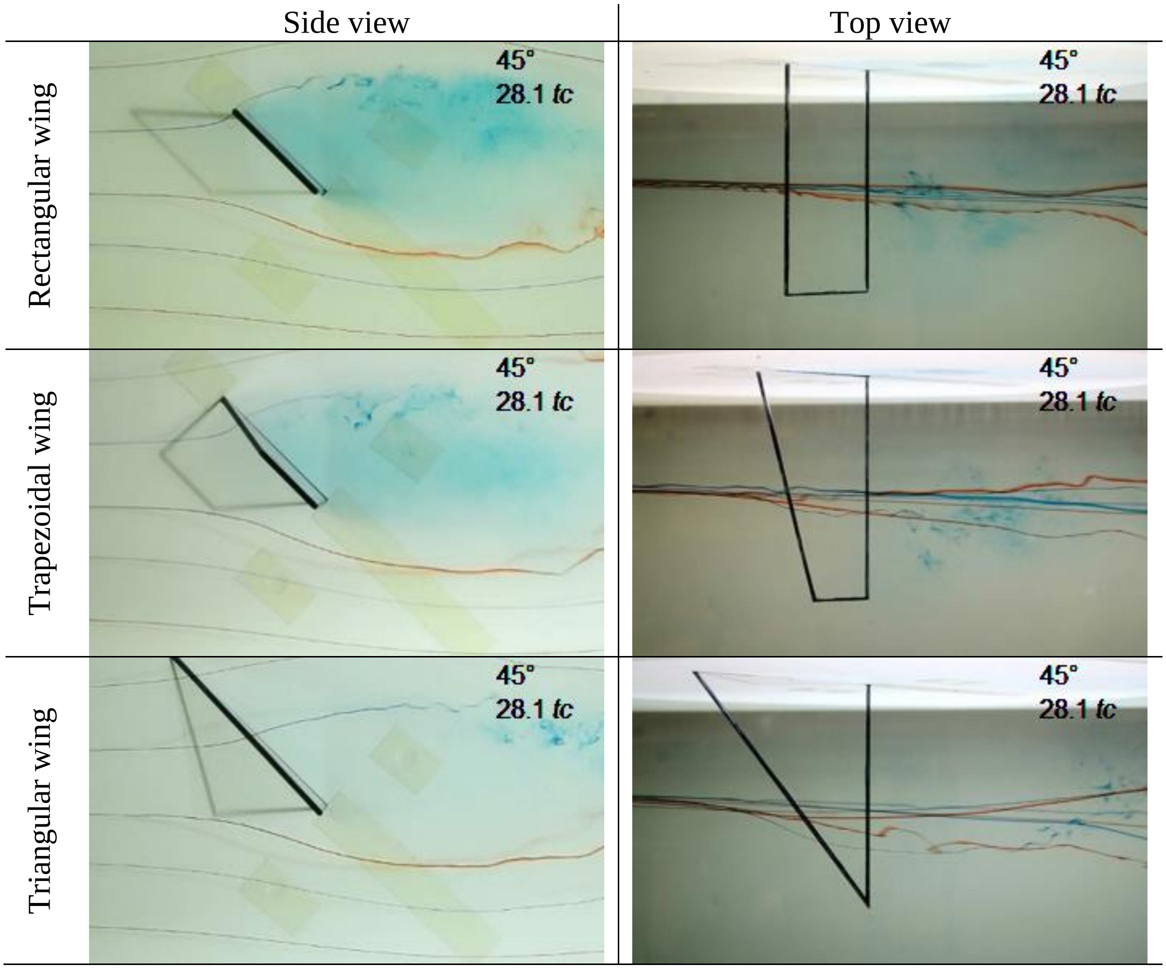

Figure 4.14 Effect of wing planform for pivot axis location at trailing edge in a steady state.

As revealed from force data by Yu and Bernal (2013), steady flow was achieved after 27 convective times, where oscillatory force behavior due to transient vortex was not in the vicinity; effects of pivot-axis location and taper ratio are less pronounced. The steady-flow force data are given in Section 5.1. Figure 4.12-Figure 4.14 show flow visualization data of wings at 28 convective times as their pivot axis locations were at leading edge, mid-chord, and trailing edge, subsequently.

The streaklines in Figure 4.12 show the flow over leading-edge-pivot wings in the steady state. For the rectangular wing, the unsteady flow structures are not observed even for trapezoidal and triangular wings, which are not limited to a starting vortex in the wake, residual dyes on the leeward surface, reversal flow on the leeward surface, a leading-edge swirling, trailing-edge-vortex shedding, and in-transition streaklines. In addition, the center streakline and the blue streakline below the center streakline flow around the wing; both streaklines stay almost on the same plane as shown in top view. For the trapezoidal wing in the side view, the streaklines around the wing have similar profiles to less dye-diffusion on wing leeward side while compared to the rectangular wing. However, as shown in the top view, the streaklines at lower position move downward across the wing downstream. For the triangular wing in the side view, both streaklines are closer together across the wing, which is because the blue streakline below the center streakline deflects more downward.

Figure 4.13 shows the steady flow over mid-chord-pivot wings. There are no unsteady flow structures in the vicinity, which are not limited to a leading-edge swirling, trailing-edge vortex shedding, residual dyes on the leeward surface, reversal flow on the leeward surface, trailing-edge-vortex shedding, a typical starting vortex in the wake, and in-transition streaklines. Instead, massive dye diffusion is present. As taper ratio is decreased, the center streakline moves across the leading edge at a lower position; however, less dye diffusion is observed from the top view.

Figure 4.14 shows the streaklines around trailing-edge-pivot wings in a steady state. Similar to leading-edge-pivot wings, the unsteady flow are inevident for all wings, also indicating minor effect of pivot-axis location. The unsteady-flow features are not limited to a leading-edge swirling, trailing-edge vortices, residual dyes on the leeward surface, reversal flow on the leeward surface, and in-transition streaklines. The characteristic features of trailing-edge-pivot wings, such as a reverse-starting vortex in the wake and a typical starting vortex at leading edge, are not in the vicinity. Moreover, the center streakline and blue streakline above the center streakline are far apart across the wing in the wake; they are closer for the rectangular and the triangular wings because streaklines deflect toward wingtip, less dye diffusion is also observed as taper ratio is decreased.

CHAPTER 5

DIRECT FORCE MEASUREMENT

5.1 STEADY FLOW

Steady flow measurements were conducted at 15 different fixed angles of attack from 3° to 45° in 3° increments under a uniform flow field U_∞ = 17.5 cm/s (i.e., *Re* = 8.9k); each fixed angle was repeated 60 times from initial zero angle of attack. Data were processed using zero-phase first-order two-path Butterworth filter with cutoff frequency of 8.76 Hz, which is same filter and cutoff frequency as cases with *K* = 0.39 in the same free-stream flow. For each fixed angle of attack, the averaged forces and standard deviation were evaluated as the flow was in a steady state; the sample duration was 50 convective times. The steady-state flow was determined to be after 80 convective times at fixed angle, where the transient force-oscillation was not in the vicinity.

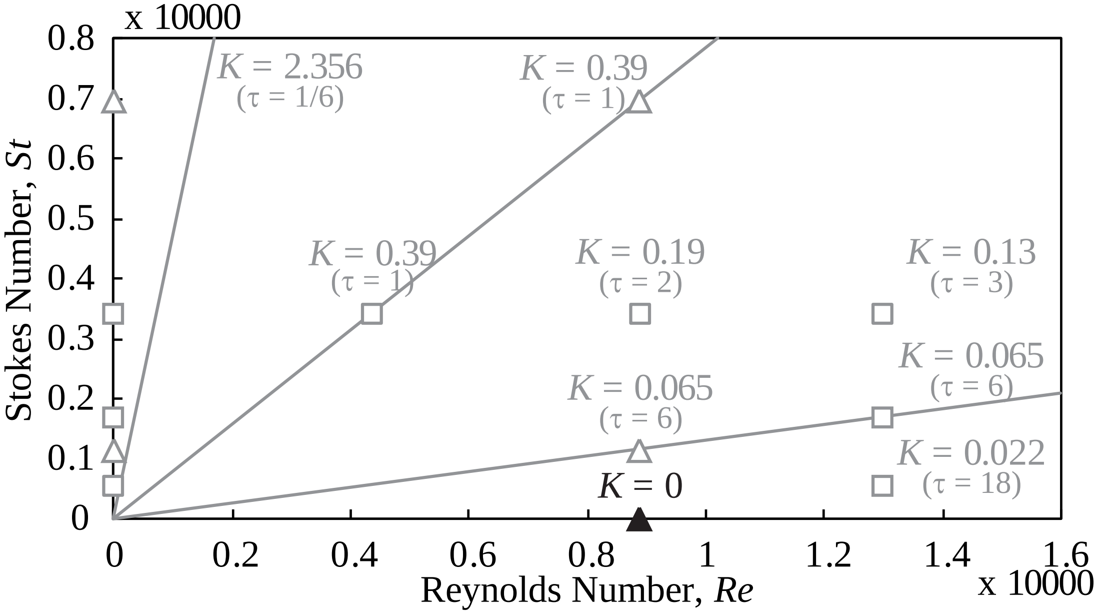

Figure 5.1 Cases for steady-flow force measuremen in *St* – *Re* space.

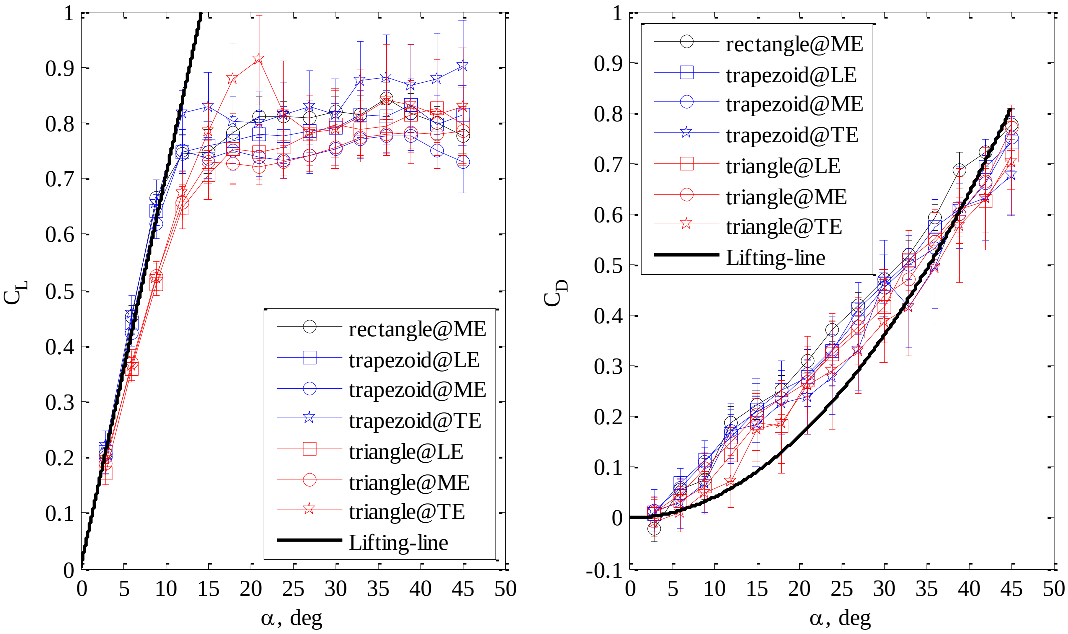

Figure 5.2 Force coefficients as a function of angle of attack for (left) lift coefficient and (right) drag coefficient.

Figure 5.2 and Figure 5.3 show effect of wing planform in the steady state; the theoretical estimation was obtained using lifting-line theory based on rectangular wing and is denoted by “lifting-line” in the figures.

Figure 5.2 shows lift coefficient and drag coefficient as a function of angle of attack. Two main features are observed for lift coefficient. The first is, for both rectangular and trapezoidal wings (i.e., taper ratio higher than 0.5) the lift coefficient follows the lifting-line theory up to 9°; effect of taper ratio is absent. Lower taper ratio wing (i.e., triangular wing) gives lower lift coefficient. The second is that trapezoidal and triangular wings at trailing edge pivot give higher stall-angle-of-attack, which is 15° and 21° respectively. For drag coefficient, effect of taper ratio is small; drag coefficient increases linearly with angle of attack, which is not estimated by lifting-line theory.

Figure 5.3 shows pitching moment coefficient about the pivot axis as a function of angle of attack. Leading edge pivot gives negative pitching moment coefficient; whereas mid-chord and trailing edge pivots produce positive pitching moment coefficient. At lower angle of attack, effect of taper ratio is small. The triangular wing at trailing edge

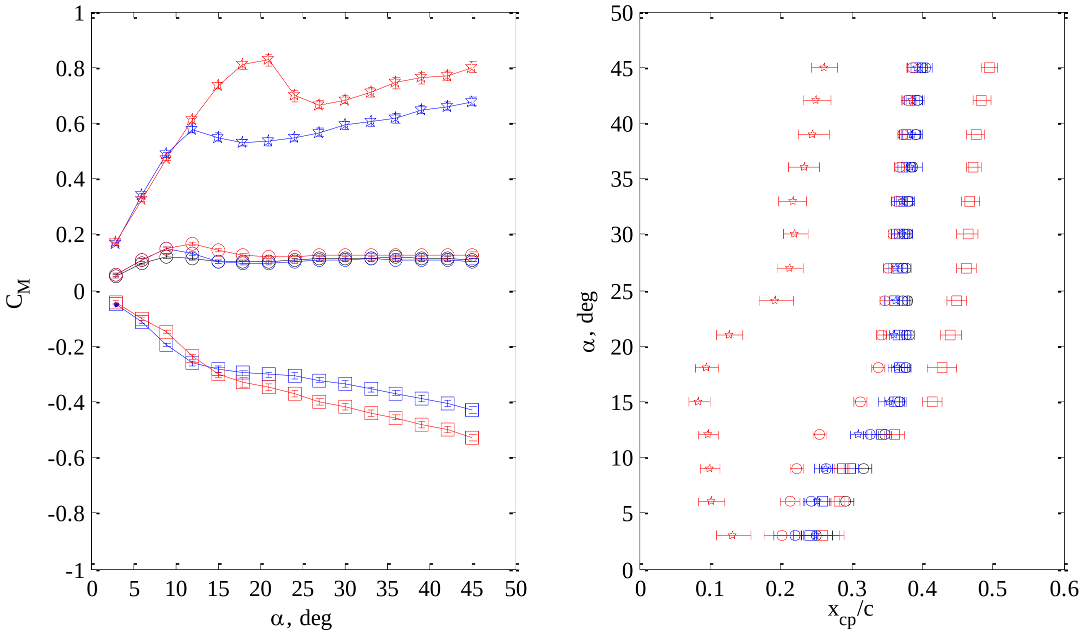

Figure 5.3 (left) Pitching moment coefficient as a function of angle of attack and (right) center of pressure as a function of angle of attack. *Square, circle, star symbols represent pivot axes at leading edge, mid-chord, and trailing edge, respectively. The black, blue, and red colors represent rectangular wing, trapezoidal wing, and triangular wing, respectively.*

pivot gives stall angle of attack at 21°, which is consistent with the observation from the lift coefficient in Figure 5.2. In addition, the fluctuation of lift coefficient at post-stall angle of attack is not observed on the pitching moment coefficient.

Figure 5.3 also shows location of center of pressure x_{cp} as a function of angle of attack, which is evaluated using Equation (5.1) and normalized with wing mean chord. For taper ratio higher than 0.5, the center of pressure fluctuates about quarter chord at lower angle of attack in accordance with wing planform and pivot axis location. They move to about 40% of wing chord for post-stall condition. For triangular wing shown as red symbols, different profiles are obtained according to pivot axis location, which is possibly due to three-dimensional effects.

$$x_{cp} = x_p - M_p / F_N \tag{5.1}$$

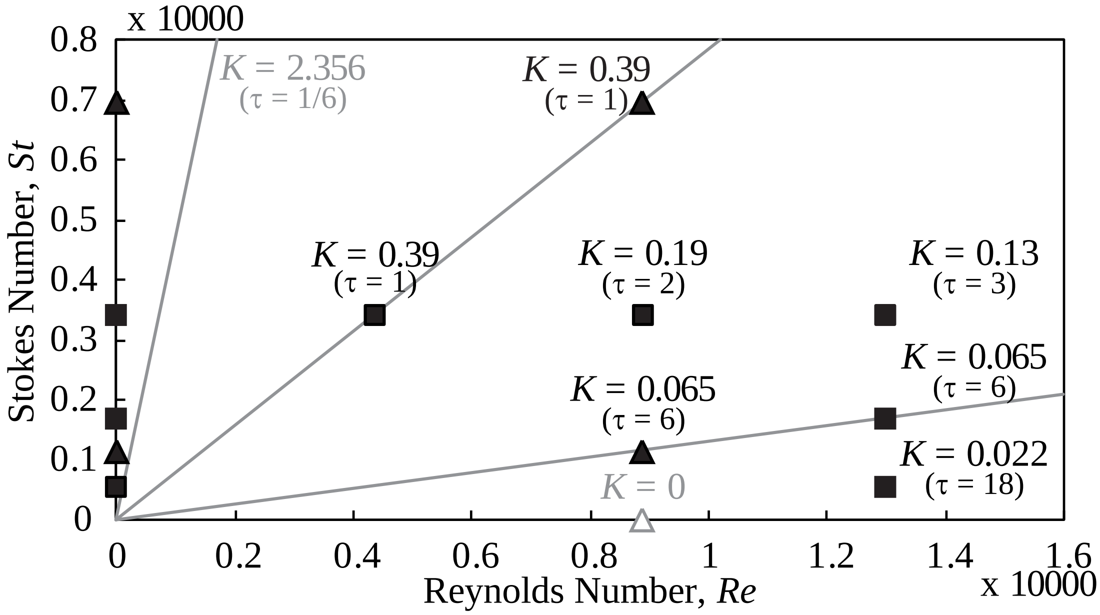

Figure 5.4 Cases for unsteady-flow force measurement in *St* - *Re* space.

where x_p is pivot axis location, M_p is pitching moment about pivot axis, and F_N is normal force.

5.2 UNSTEADY FLOW

The unsteady flow measurements were taken in conditions shown in Figure 5.4, highlighted as solid symbols; they were cases $K > 0$ in *St*- *Re* space. The triangle symbols represent cases in consideration of three wing planforms, which are rectangular, trapezoidal, and triangular wings; the square symbols represent cases in consideration of only rectangular wing. The wing property is given in Section 2.2.

5.2.1 Wall Effect

To investigate the influence of the channel side walls, force measurements were conducted using a rectangular wing at several wing initial positions across the water channel, as shown in Figure 5.5, which may have dramatic impact on our measured force dynamically or statically (Granlund et al., 2010). The wing had two-inch chord, an aspect ratio of 4, and rounded edges. Nine locations across the water channel were considered, as shown in Figure 5.5. One location was at the center of water channel, four locations were at the upper side of the center of the water channel, and four locations were at the

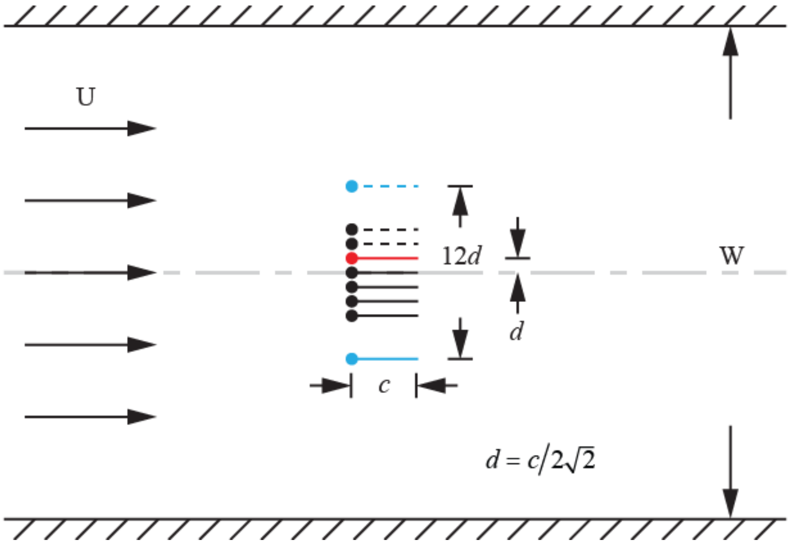

Figure 5.5 Schematics of pitching wing at initial positions to study wall effects. The wing position was drawn to scale with respect to water channel width, but wing chord was not drawn to scale. The solid circle represents pivot axis location.

lower side of the center of water channel. The first three locations on either side of water channel center were displaced by a distance *d*, which was half of projected length of wing chord. The furthest location from the center of water channel was placed by 6*d*, which gave 3.8-chord distance away from the wall. The red solid line represents the wing location where most experiments were conducted, such that the wing-chord center would be at the center of water channel at $\alpha_m = 45°$. The upper locations are presented in dotted lines, and the lower locations are presented in solid lines. The blue lines indicate the wing locations were close to the wall. The line style and color also apply for normal force and axial force shown in Figure 5.6.

Figure 5.6 shows normal and axial forces as a function of time normalized with pitch time; a comparison of wing location at water channel is displayed. The wing kinematics was maneuvered to generate a constant pitch rate of 155 °/s (*St* = 7.0k). A rectangular wing was pitched at leading edge pivot axis in two flow conditions, which are still water *Re* = 0k and running water *Re* = 9k. The incorporation of constant pitch rate and free-stream velocity gives reduced pitch rate *K* = 0.39 for *Re* = 9k and *K* = ∞ for *Re* = 0. All forces were normalized with dynamic pressure based on characteristic speed $c\alpha_m'$, instead of free-stream velocity, which results in pitch velocity pressure (q_p) being four times of finite reduced pitch rate squared of free-stream velocity pressure (q_U). As

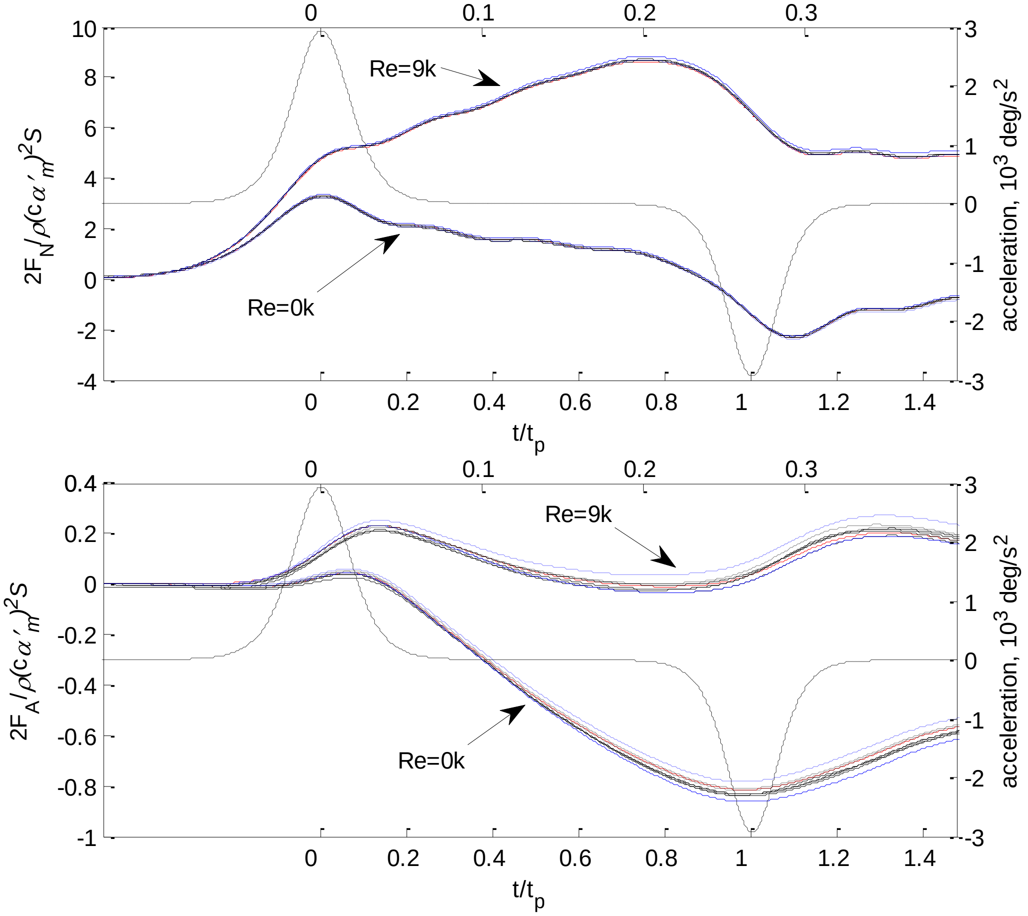

Figure 5.6 Forces as a function of time normalized with pitch time for (top) normal force (bottom) axial force. The color code and curve style represent wing positions shown in Figure 5.5; wing acceleration is plotted as dashed curve; wing kinematics was for pitch rate of 155 °/s.

observed in Figure 5.6, both normal and axial forces have same tendency at different crosswise locations; this independence does not change with flow condition. The variations of forces at crosswise locations are less pronounced than computation results by Lian and Ol (2010), who modeled two-dimensional flat plate pitching at leading edge for $K = 0.2$. Our results suggest a wide operation range for experiments using two-inch-chord pitching wing in the water channel.

5.2.2 Effect of Reduced Pitch Rate and Pivot Axis Location for Rectangular wing

Presenting here are data obtained using an aspect-ratio-four rectangular wing. The wing had two-inch chord and rounded edges; the thickness to chord ratio was 6.25%. The

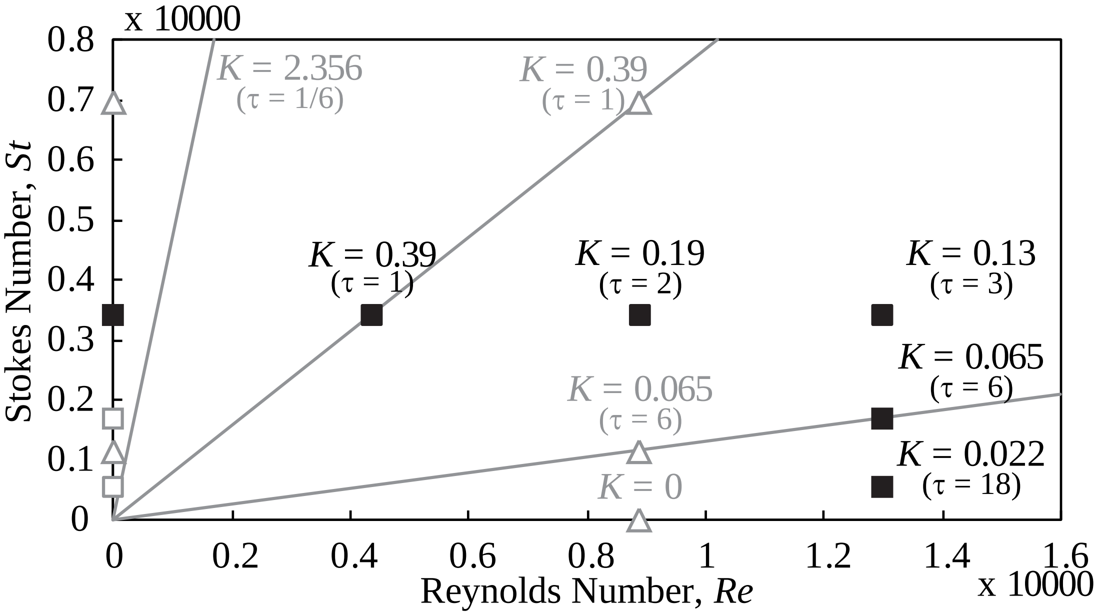

Figure 5.7 Cases in study of pivot axis location effect.

wing property is given in Section 2.2. The test cases discussed here are highlighted in Figure 5.7. There are three constant pitch rates (i.e., α_m' = 76.4 °/s, 37.5 °/s, and 12.6 °/s) implemented to maneuver the wing in a free-stream flow U_∞ = 25.6cm/s, incorporated to three reduced pitch rate K = 0.13, 0.065, and 0.022. While pitching the wing with 76.4 °/s in free-stream conditions of U_∞ = 0, 8.6, and 17.5 cm/s, we obtained yields $K = \infty$, 0.39, and 0.19. Conditions used to generate the three pitch rates are given in Table 2.2.

5.2.2.1 Axial Force and Normal Force as a Function of Convective Time

Figure 5.8 - Figure 5.10 show axial and normal forces as a function of time normalized with convective time for pivot axis location at leading edge, mid-chord and trailing edge, sequentially. The onset of normalized time is at the first sharp transition corner of ideal pitch up-hold-return motion, which is denoted by t_1 as illustrated in Figure 2.6. The blue, green and red lines represent Reynolds number from low to high; the solid, dashed, and dotted lines represent reduced pitch rate from high to low. The corresponding motion position is plotted as gray line. Error bars are representative of the 95% confidence intervals of the measurement; they are of the order of 10 mN or less for both axial and normal force. For the axial force these error bars are small but significantly compared to the measured force. For the normal force these error bars are very small and

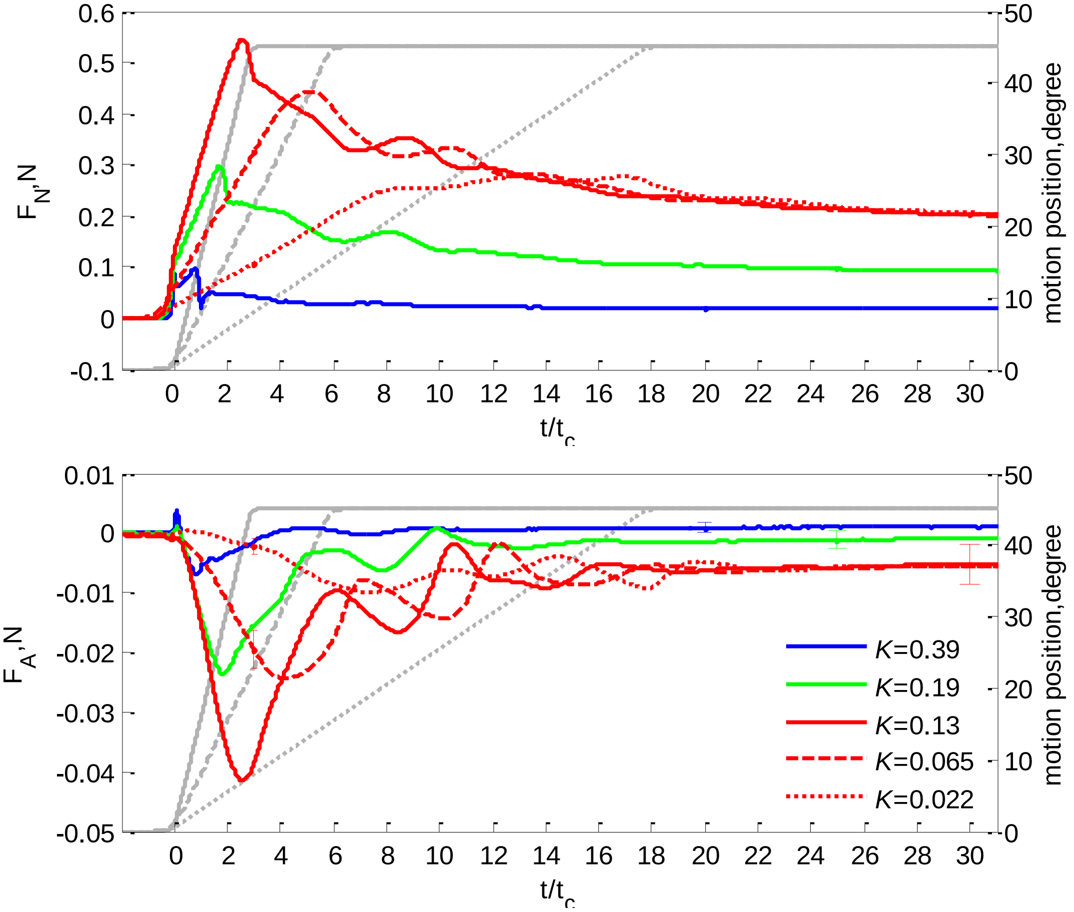

Figure 5.8 Forces as a function of time normalized with convective time for rectangular wing at leading edge pivot (top) normal force (bottom) axial force.

hardly to identify while comparing with the significant normal force. As expected the error bars are larger for measurements in higher free-stream velocity and for measurements at both leading and trailing edge pivot axis. Note also that the forces for the low Reynolds number cases are very small due to small dynamic pressure.

Figure 5.8 - Figure 5.10 show that the normal force increases rapidly during the pitch-up motion, followed by a decrease until a constant steady value is reached. The decrease in normal force reveals some oscillatory behavior at early times, which is in phase with the axial-force oscillation. An increase in normal force occurs at the same phase as a more negative axial force (i.e., increased axial force towards the leading edge). This is consistent with an increase of leading edge suction associated with a lower pressure on the leeward side of the plate. The period of these oscillations is consistent with a transient vortex shedding process. The oscillations disappear before the flow

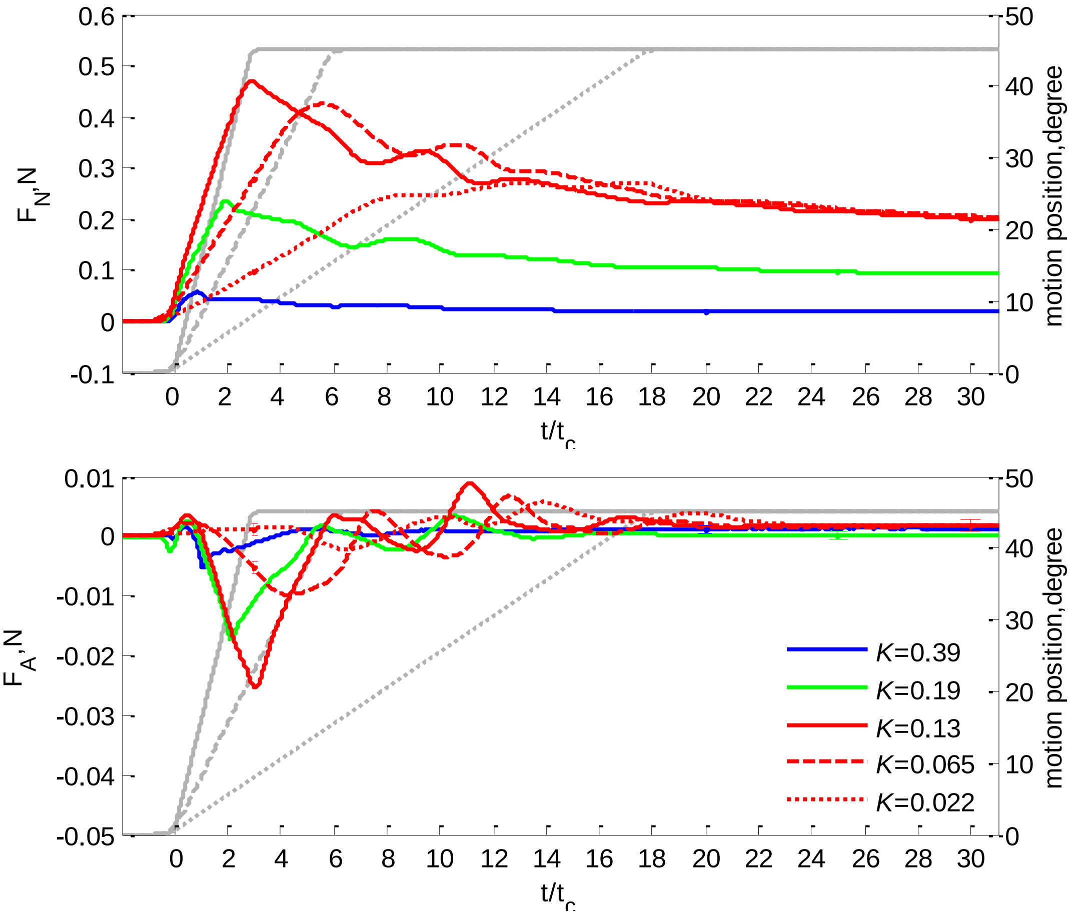

Figure 5.9 Forces as a function of time normalized with convective time for rectangular wing at mid-chord pivot (top) normal force (bottom) axial force.

reaches steady state, which suggests that there is no vortex shedding at steady state conditions. Close examinations of individual realization do not show oscillatory behavior at steady state conditions, which supports this conclusion. Maximum normal force depends on both pivot axis location and reduced frequency, which will be addressed in the following discussion by means of force coefficients.

Figure 5.8 - Figure 5.10 also show the axial force is significantly smaller than the normal force at steady sate. The axial force at steady state is negative which implies forward force and significant leading edge suction. The magnitude of the leading edge suction force is very small compared to potential flow theory estimates, as expected for separated flow at the leading edge. It is not clear at this point how this suction force depends on the geometry of the leading edge (e.g., a sharper leading edge may promote

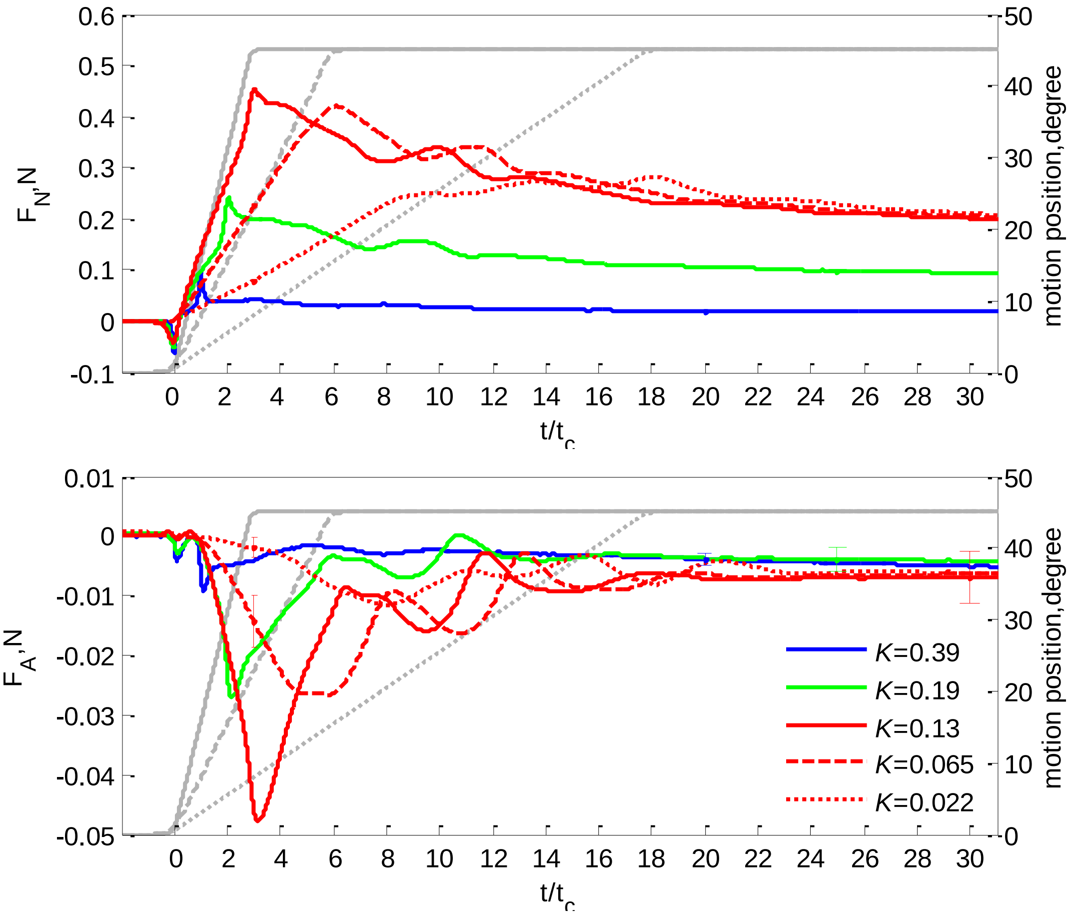

Figure 5.10 Forces as a function of time normalized with convective time for rectangular wing at trailing edge pivot (top) normal force (bottom) axial force.

leading edge suction). The axial force reaches its steady-state values at approximately the same convective time as the normal force ($t/t_c > 30$).

Figure 5.11 shows a preliminary study of effect of pivot location on normal force coefficients in a uniform free-stream flow Re = 13k. The solid, dashed, and dotted lines are for leading edge pivot, mid-chord pivot, and trailing edge pivot, respectively. The red, blue, and black lines represent pitch rate of 76.4 °/s, 37.5 °/s, and 12.6 °/s, respectively; the corresponding reduced pitch rate is K = 0.132, 0.065, and 0.022, respectively. All cases show that normal force coefficients converge to the same value of approximately C_N = 1.1 after about 30 convective times in the same free-stream flow. Leading edge pivot produces larger normal force coefficients compared to mid-chord pivot, which in turn produces larger normal force coefficients compared to trailing edge pivot. At low reduced pitch rate K = 0.022, the normal force coefficient increases rapidly until the wing

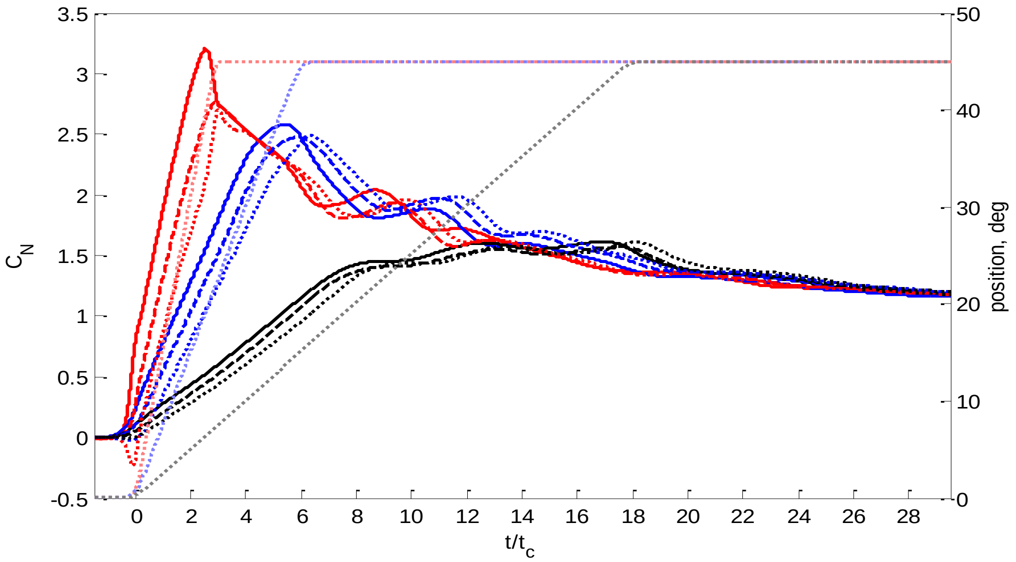

Figure 5.11 A comparison of normal forces as a function of time normalized with convective time for rectangular wing at selected pivot locations. *The solid, dashed, and dotted curves represent the leading edge pivot, the mid-chord pivot, and the trailing edge pivot, respectively. The red, blue, and black curves denote the cases for K = 0.13, K = 0.065, and K =0.022, respectively.*

reaches an angle of about 20 degrees at 8 convective times and remains slightly above this value for the remaining pitch time. For a given phase during pitch-up phase, effect of pivot location is more pronounced as reduced pitch rate is increased. For higher reduced pitch rate $K > 0.065$, the maximum normal force coefficient occurs at approximately the maximum angle of attack; the maximum normal force coefficient changes as pivot location is adjusted. Figure 5.11 also shows the oscillatory behavior discovered earlier in the range of 8-20 convective times for lower reduced pitch rate $K = 0.022$; for higher reduced pitch rate $K > 0.065$, the oscillatory behavior occurs after the end of wing pitch motion. This oscillatory behavior is attributed to transient vortex shedding.

5.2.2.2 Non-Circulatory Effect

Figure 5.12-Figure 5.14 show normal force as a function of time normalized with pitch time; the attention is focused on pitch-up phase (t_1-t_2) as labeled from 0 to 1. In this time scale, non-circulatory apparent mass effect associated with motion acceleration would be observed around phases denoted by 0 and 1; constant pitch rate effect would be displayed between these two time points. The black, blue, green and red lines represent Reynolds number from low to high; the solid, dashed, and dotted lines represent the

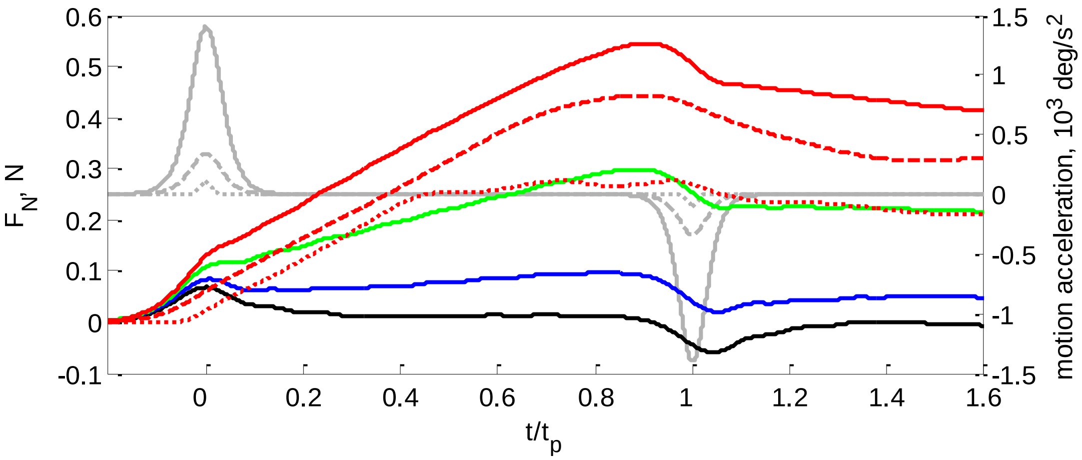

Figure 5.12 Normal force as a function of time normalized with pitch time for rectangular wing at leading edge pivot. *The black solid curve is for K = ∞, the blue solid curve is for K = 0.39, the green solid curve is for K = 0.19, the red solid curve is for K = 0.13, the red dashed curve is for K = 0.065, and the red dotted curve is for K = 0.022*.

reduced pitch rate from high to low. The corresponding motion acceleration is plotted as gray line with line style corresponding to the pitch rate; as shown in the figures, the kinematics of higher pitch rate has wider and higher acceleration.

Figure 5.12 shows normal-force course for leading edge pivot. The main feature in this plot is the non-circulatory apparent mass spikes occurring at the start and the end

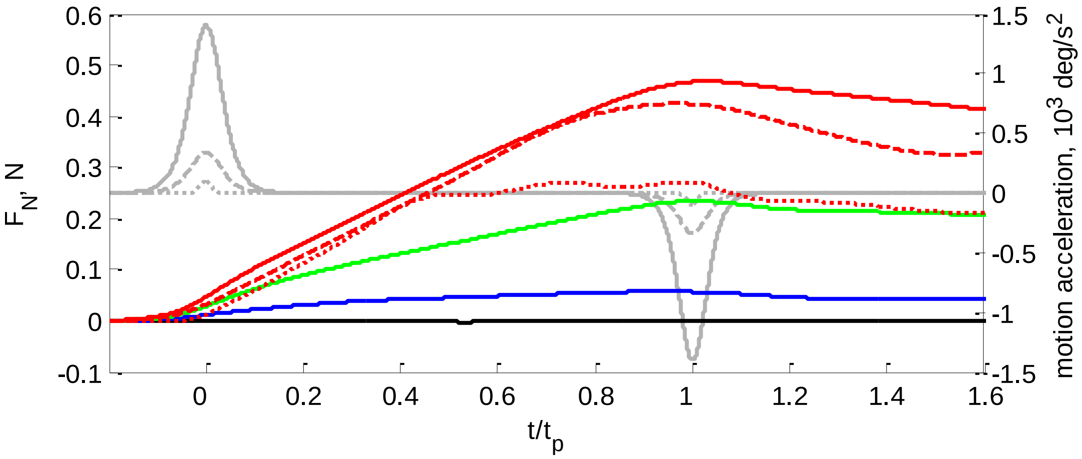

Figure 5.13 Normal force as a function of time normalized with pitch time for rectangular wing at mid-chord pivot. *The black solid curve is for K = ∞, the blue solid curve is for K = 0.39, the green solid curve is for K = 0.19, the red solid curve is for K = 0.13, the red dashed curve is for K = 0.065, and the red dotted curve is for K = 0.022*

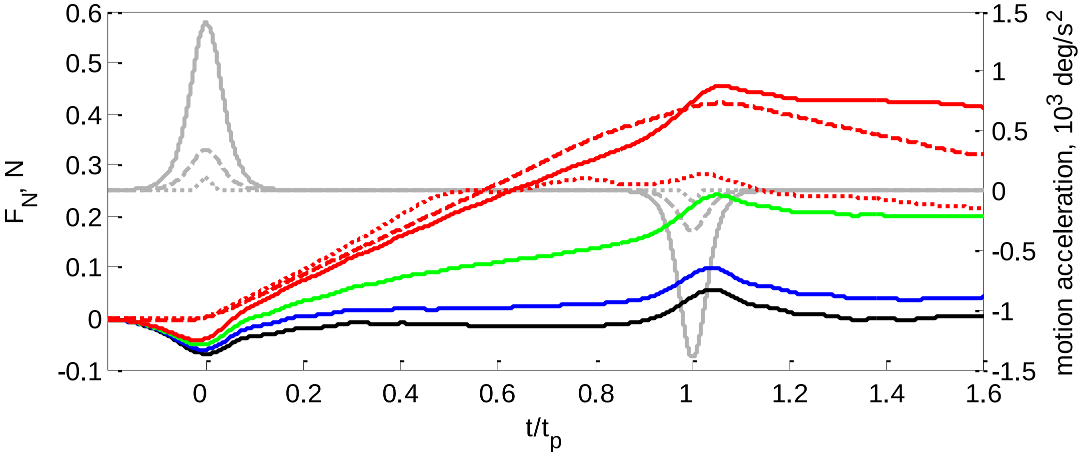

Figure 5.14 Normal force as a function of time normalized with pitch time for rectangular wing at trailing edge pivot. *The black solid curve is for* $K = \infty$, *the blue solid curve is for* $K = 0.39$, *the green solid curve is for* $K = 0.19$, *the red solid curve is for* $K = 0.13$, *the red dashed curve is for* $K = 0.065$, *and the red dotted curve is for* $K = 0.022$.

of rotation for reduced frequencies above 0.065. These spikes have been documented by many researchers (Eldredge et al., 2009; Granlund et al., 2010; Ramesh et al., in 2011). The normal force spike is positive at the start of pitching and negative at the end of pitching, as would be expected from simple consideration of mass loading due to pitching acceleration. The magnitude of the spikes increases with the free-stream velocity at the start of pitching, which suggests that non-circulatory apparent mass effects are enhanced by circulatory pitch rate effects. The constant pitch rate portion of the motion between time scale 0 and 1 shows an increase in normal force with time and angle of attack. The slope increases as reduced pitch rate decreases with increasing free stream velocity; this portion of the motion will be discussed in detail in the next section in terms of lift and drag coefficients as a function of angle of attack.

Figure 5.13 shows the normal-force course for mid-chord pivot. In this case there is no non-circulatory contribution to the normal force, as would be expected from symmetry of the pitch acceleration. It should be noted that non-circulatory apparent mass effects are not found at the end of pitch where circulatory effects must have introduced asymmetry vortex structure between the leading edge and the trailing edge.

Figure 5.14 shows normal force-course for trailing edge pivot. In this case non-circulatory effects are in the opposite direction compared to cases with leading edge pivot.

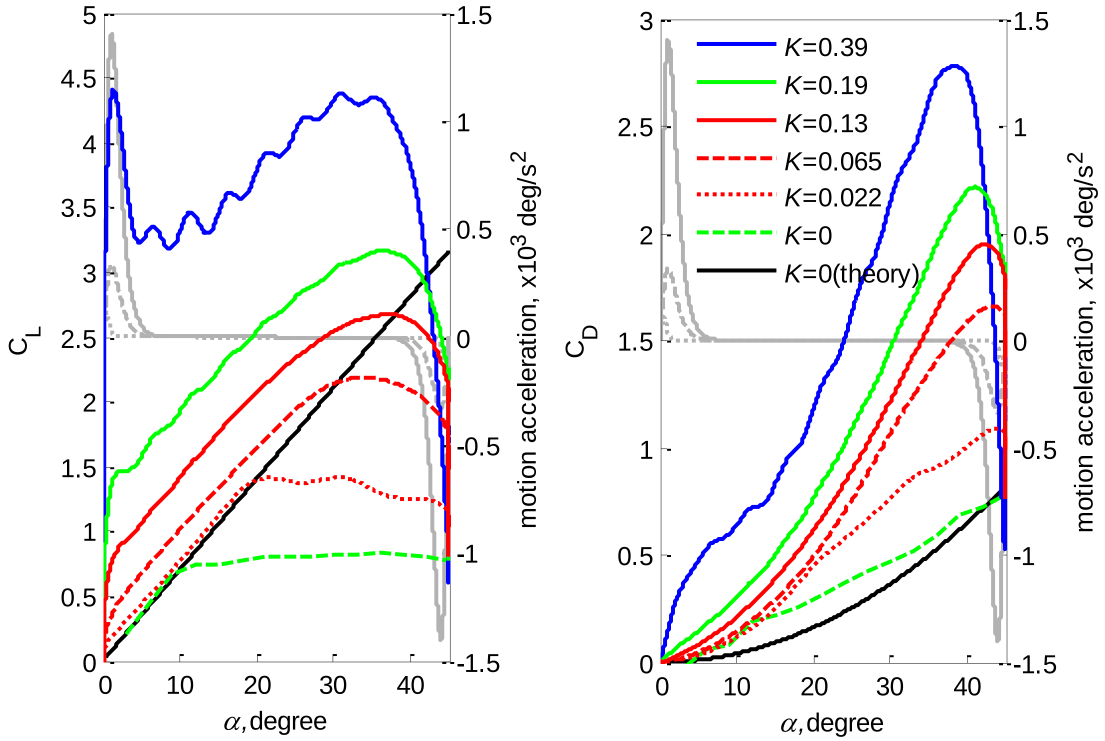

Figure 5.15 Force coefficients as a function of angle of attack using rectangular wing at leading edge pivot (left) lift coefficient (right) drag coefficient.

A negative normal force spike is produced at the start of pitching and a positive spike is produced at the end of pitching for $K > 0.065$. The magnitude of the spike decreases with the increasing free-stream velocity in contrast with the results from leading edge pivot, which suggests that non-circulatory apparent mass effect at the start of pitching are reduced by circulatory pitch rate effect. However the increase in normal force during the constant pitch rate portion of the motion shows the same trend of increasing slope with reduced pitch rate as for leading edge pivot.

5.2.2.3 Effect of Reduced Pitch Rate K

Figure 5.15 shows the lift and drag coefficients of the rectangular wing pitching at leading edge. At the lowest reduced pitch rate (i.e., $K = 0.022$) the lift coefficient follows the theoretical result closely up to an angle of attack of 20 degrees, which corresponds to the steady stall angle of attack. The slope of lift-curve is slightly depressed due to the onset of rotation; this characteristic was noticed by Jumper et al. (1987) for NACA0015 at $K < 0.01$. The drag coefficients are significantly higher than the prediction by the

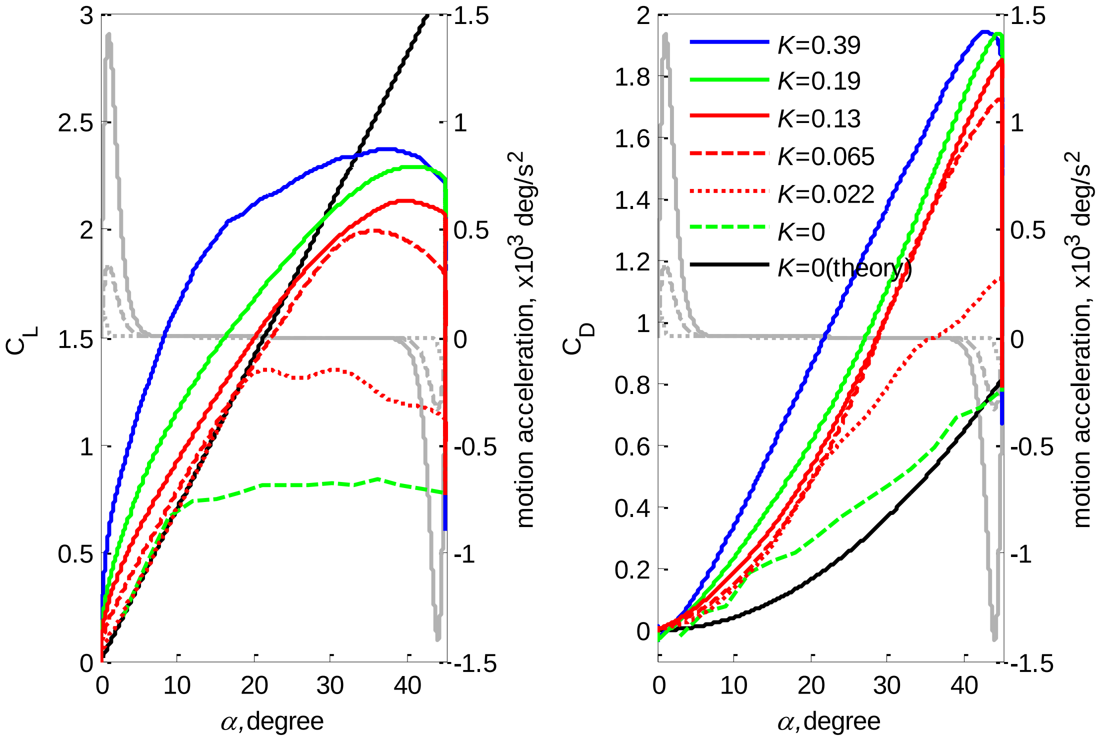

Figure 5.16 Force coefficients as a function of angle of attack using rectangular wing at mid-chord pivot (left) lift coefficient (right) drag coefficient.

lifting-line theory, a better estimate consistent with the relatively small value of the leading edge suction is assumed that the aerodynamic force is normal to the plate, which follows the dashed line in the right panel of Figure 5.15. For larger angles of attack the drag coefficient increases while the lift coefficient remains approximately constant which implies smaller L/D values. These data suggest that for $K < 0.022$ the flow is quasi-steady and the lifting-line theory provides good estimates of the lift coefficients up to the stall angle of attack. In this regime the drag coefficient is under predicted by the lifting line theory by a factor of two. Thus the lifting-line theory appears to correctly account for finite wing effects in the slope of the lift curve (i.e. a 33% reduction of the lift coefficient according to the infinite wing), but fails to account for the significant reduction in leading edge suction which results in largest drag coefficients compared to induced drag calculations.

For $K > 0.022$ unsteady effects are important; the flow visualization data revealed two-dimensional flow is more pronounced as the reduced pitch rate increases. There are two main effects for the lift coefficient: a non-circulatory peak during wing acceleration,

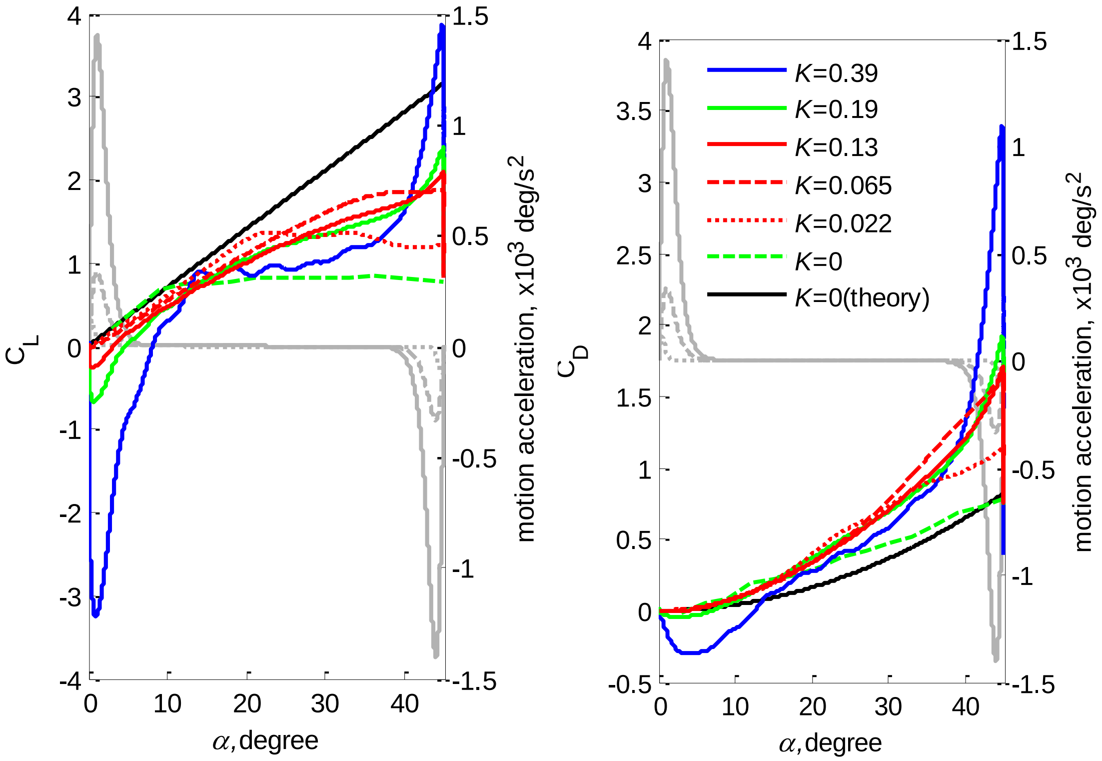

Figure 5.17 Force coefficients as a function of angle of attack using rectangular wing at trailing edge pivot (left) lift coefficient (right) drag coefficient.

and pitch rate effects within regions of constant pitch rate, the lift coefficients shift upward with same amount as reduced pitch rate increases. Similar effects were documented for 2D flow by Granlund et al. (2010). Both effects are very strong at much higher reduced pitch rate K = 0.39. As noted earlier, non-circulatory effects produce a positive spike at the start of pitch-up phase and a negative spike at the end of pitch-up phase within acceleration region. These force spikes are associated with the formation of the starting vortex and will be discussed in the next chapter. The shift in the lift coefficient curve due to pitch-rate effect is similar to mean camber effects as would be expected from linear potential flow theory. Unsteady effects result in an increase in drag coefficient. At K = 0.39 there is a significant increase of drag at small angle of attack during the acceleration portion of the pitching motion.

Figure 5.16 shows the lift and drag coefficients at mid-chord pivot axis as a function of angle of attack. At the lowest reduced pitch rate (K = 0.022) the lift coefficient follows the theoretical results closely up to an angle of attack of 20 degrees.

The drag coefficient follows similar trends as for the leading edge pivot axis. These data confirm the conclusion that for $K < 0.022$ the flow is quasi-steady and the lifting line theory provides good estimates of the lift coefficient up to the stall angle of attack.

For values of $K > 0.022$ unsteady effects are important. However the trends are different compared to leading edge pivot. In this case non-circulatory effects are very small. Pitch rate effects between the initial and final acceleration are much stronger at $K > 0.065$, which increases the lift coefficient at small angles of attack. Within the constant pitch rate region, the lift coefficient curves are likely shifting upward as reduced pitch rate increases, but not with the same amount for leading edge pivot axis. The drag coefficient shows small change in the drag coefficient for $K < 0.39$. The case $K = 0.39$ shows larger effects in both the lift and drag coefficients.

Figure 5.17 shows the lift and drag coefficients for trailing edge pivot axis. At the lowest reduced pitch rate ($K = 0.022$) the lift coefficient and drag coefficient show similar quasi steady behavior as for other pivot axes. At higher reduced pitch rate the lift coefficients are less than the estimation from the lifting line theory, and not very different compared to the results at $K = 0.022$, except for $K = 0.39$. Non-circulatory effects result in a negative lift coefficient at the beginning of pitch and a positive spike at the end of

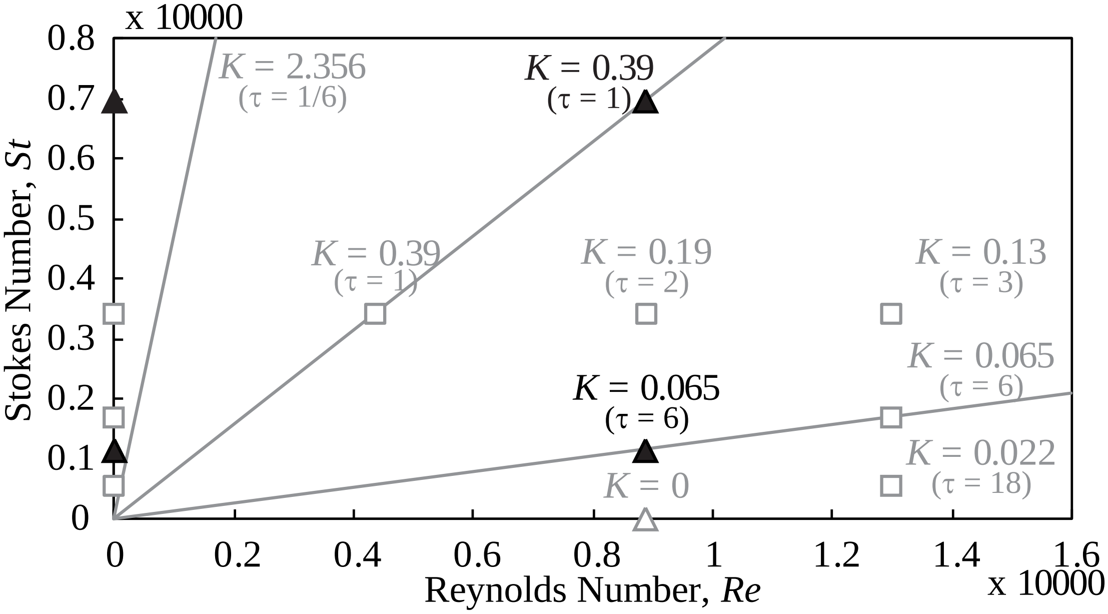

Figure 5.18 Cases in study of wing planform effect.

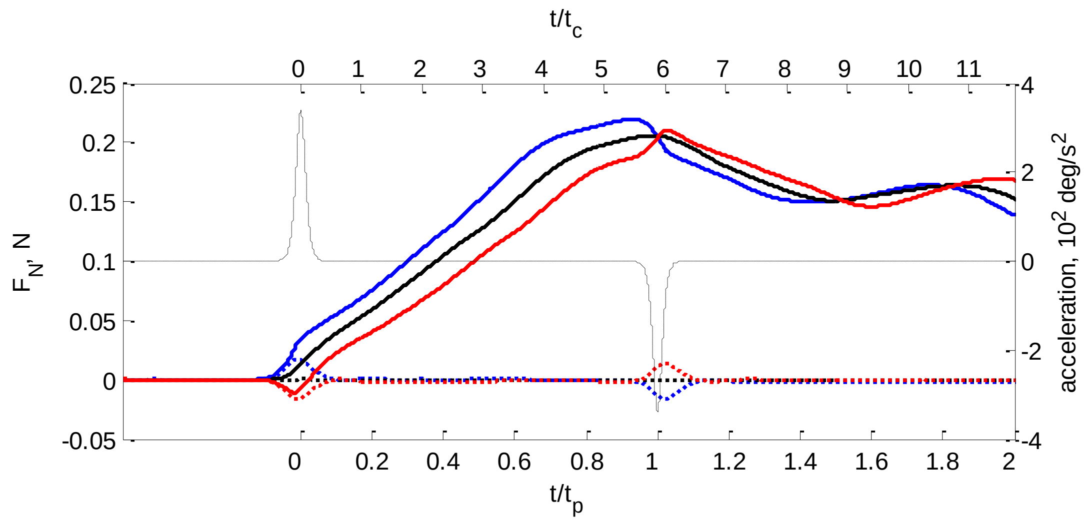

Figure 5.19 Normal force as a function of time normalized with pitch time for rectangular wing. *Blue, black, and red curves represent the pivot axis at leading edge, mid-chord, and trailing edge, respectively. The solid curves are for K = 0.065, and the dotted curves are K = ∞ (still water).*

rotation. The magnitude of the spike is moderate except for the K = 0.39 case. For K = 0.39 the initial acceleration persist well beyond the end of the acceleration period where the lift coefficient is negative. The drag coefficient is also negative in this region.

5.2.3 Wing Planform Effect and Pivot-Axis Location at *K* = 0.065

Presenting in current and next sections are force data obtained for K = 0.065 and 0.39, sequentially, using aspect-ratio-four wings. Three wing planforms were considered, which were rectangular, trapezoidal, and triangular wings. All wings had two-inch mean chord and rounded edges; the thickness to chord ratio was 6.25%. The wing property is given in Section 2.2. The wings underwent two reduced pitch rates in a uniform free-stream velocity U_∞ = 7.5 cm/s, which are K = 0.065 and 0.39; they are highlighted in Figure 5.18. Two constant pitch rates were programmed; they were α_m' = 155 °/s (St = 7k) and α_m' = 25.6 °/s (St = 1.1k). The same kinematics was also implemented in still water. Conditions used to generate the three pitch rates are given in Table 2.2.

5.2.3.1 Normal Force as a Function of Time Normalized with Pitch Time

Figure 5.19 through Figure 5.21 show normal force for K = 0.065 as a function of time normalized with pitch time for rectangular, trapezoidal, and triangular wings,

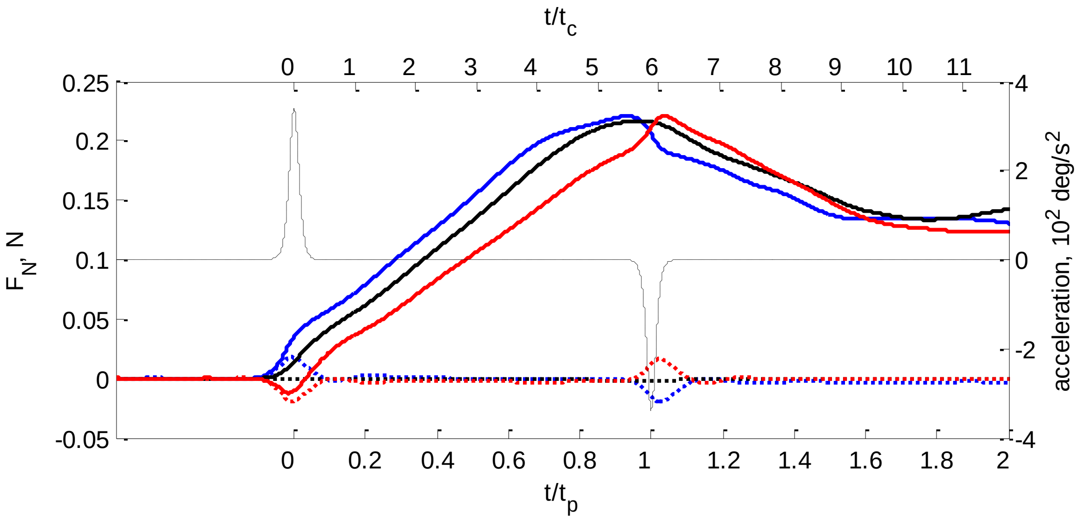

Figure 5.20 Normal force as a function of time normalized with pitch time for trapezoidal wing. *Blue, black, and red curves represent the pivot axis at leading edge, mid-chord, and trailing edge, respectively. The solid curves are for K = 0.065, and the dotted curves are K = ∞ (still water).*

respectively. The blue, black, and red curves represent pivot location at leading edge, mid-chord, and trailing edge, respectively. The solid and dotted curves represent K = 0.065 (St = 1.1k and Re = 8.9k) and $K = \infty$ (still water), respectively. The motion acceleration is given as a black dashed curve.

All wing planform shapes produce same trends in force course as higher reduced pitch rate *K* = 0.39 at a given pivot location. The positive and negative normal force spikes are consistent with motion acceleration as pivot location is at leading edge; however, they are contrary to motion acceleration as pivot location is at trailing edge. This is because the asymmetric motion acceleration is exhibited on both wing-chord ends. As pivot location is at mid-chord, normal force spikes are not observed due to symmetrical motion acceleration on both wing-chord ends. Moreover, effect of non-circulatory apparent mass is much pronounced as taper ratio decreases; similar tendency is also observed for higher reduced pitch rate *K* = 0.39.

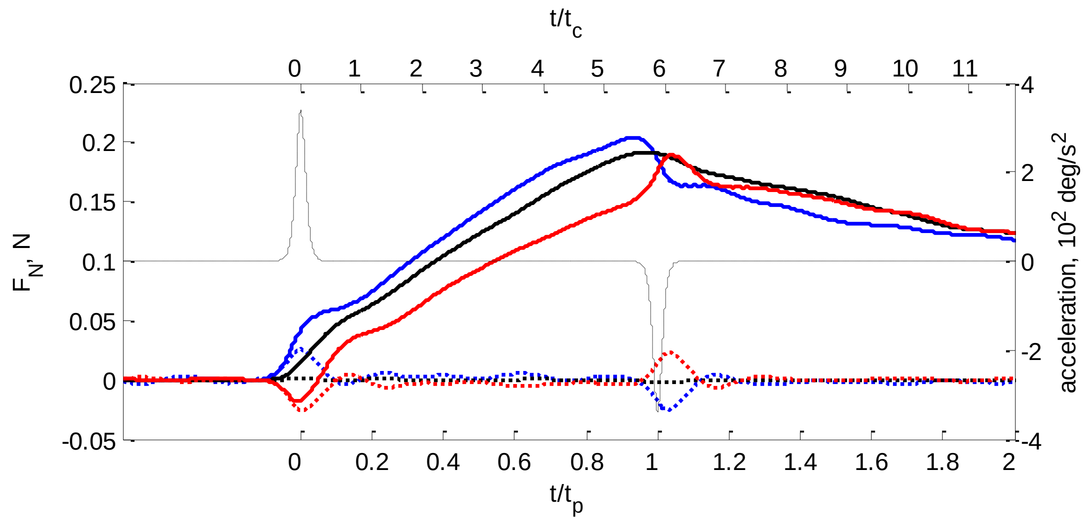

Figure 5.21 Normal force as a function of time normalized with pitch time for triangular wing. *Blue, black, and red curves represent the pivot axis at leading edge, mid-chord, and trailing edge, respectively. The solid curves are for K = 0.065, and the dotted curves are K = ∞ (still water).*

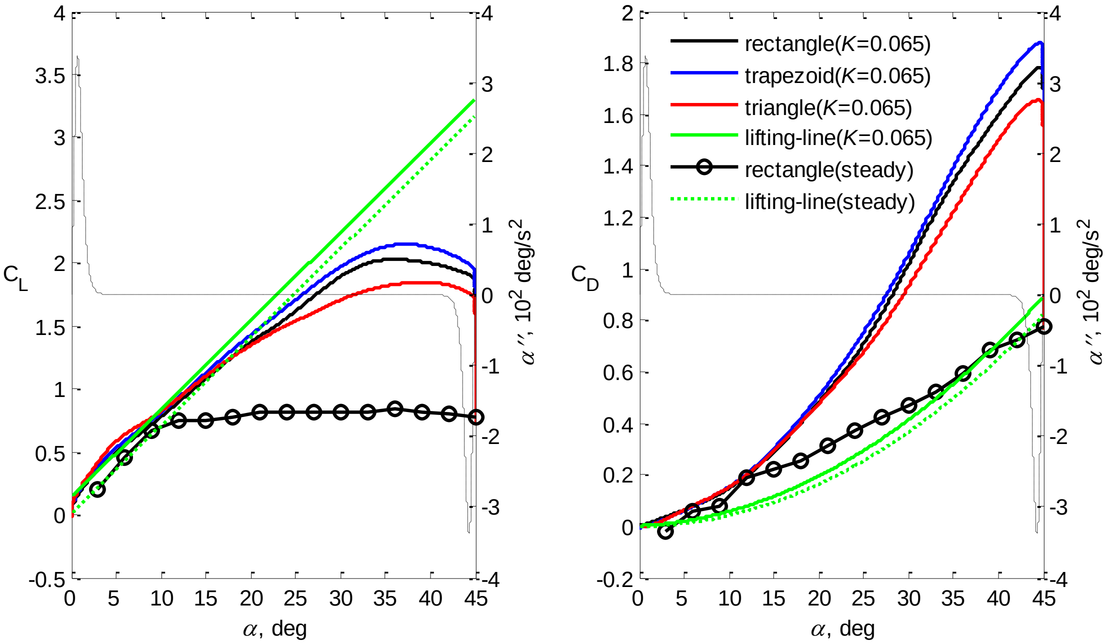

Figure 5.23 Force coefficients of K = 0.065 as a function of angle of attack for different wing planforms at mid-chord pivot: (left) lift coefficient and (right) drag coefficient.

The symmetrical force courses shown among pivot locations in still water are also observed, which indicates good data accuracy and proper wing positioning. Unlike K = 0.39, there are no significant forces measured during the portion of constant pitch rate of wing motion; the difference is partially due to pronounced vortical flow induced by motion acceleration for higher reduced pitch rate K = 0.39. Referring to Table 2.2, the kinematics of K = 0.39 has maximum acceleration (α_m'' = 2937 °/s^2) 8.7 times higher than maximum acceleration of K = 0.065 (α_m''= 338 °/s^2). The acceleration duration of K = 0.39 ($2t_a$ = $0.36t_c$) is 50% lower than the acceleration duration of K = 0.065 ($2t_a$ = $0.52t_c$); both acceleration durations are less than one convective time.

Moreover, contrary to the current data of K = 0.065 in Re = 8.9k, the data of K = 0.065 shown in Figure 5.12 - Figure 5.14 in Re = 13k exhibits no effect of non-circulatory apparent mass. Both kinematics have the same maximum acceleration but different acceleration duration. The former kinematics of K = 0.065 in Re = 13k has acceleration duration larger than one convective time ($2t_a$ = $1.1t_c$), which is twice the duration of the kinematics of K = 0.065 in Re = 8.9k ($2t_a$ = $0.52t_c$). It is obvious that existence of non-circulatory apparent mass effect depends on pivot locations and acceleration duration in terms of convective time, which is associated with rapidly increase of force.

5.2.3.2 Force Coefficients as a Function of Angle of Attack

Figure 5.22 - Figure 5.24 show force coefficient for pivot location at leading edge, mid-chord, and trailing edge, respectively. The black, blue, and red curves represent rectangular, trapezoidal, and triangular wings, respectively. The solid curves represent K = 0.065; the dotted curves represent K = 0 (denoted by "steady"), which were obtained using a rectangular wing with mid-chord pivot axis in the steady flow and same free-stream flow Re = 8.9k. The theoretical estimation by lifting-line theory for rectangular wings is given as green curve. For steady-state data over various wing planforms, see Section 5.1.

Figure 5.22 shows force coefficient as a function of angle of attack for pivot location at leading edge. Non–circulatory apparent mass effect is pronounced for lower taper-ratio wing at the beginning and the end of pitch-up phase. During constant pitch-rate phase, higher taper-ratio wing ($\lambda \geq 0.5$) gives the same lift and drag coefficients. The lift coefficients follow the estimation by lifting-line theory with a gentle slope; however, the drag coefficients are well beyond the theoretical estimation at higher angle of attack. The wing with a lower taper ratio gives lower lift and drag coefficients at a given angle of attack. Moreover, the dynamic flow (K = 0.065) produces more lift than the steady flow.

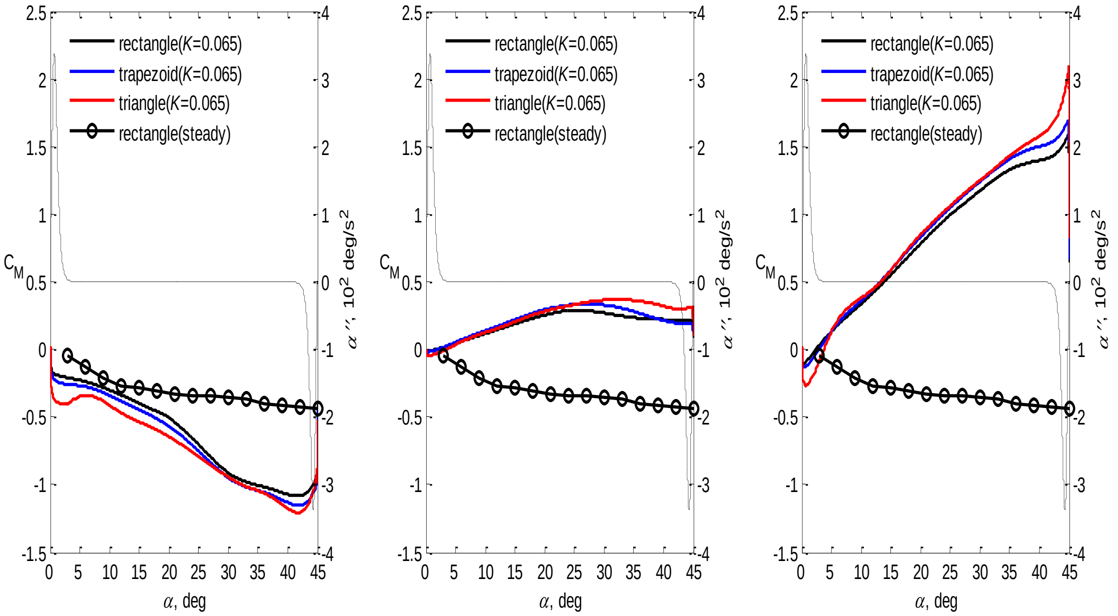

Figure 5.25 Pitching moment coefficient of K = 0.065 as a function of angle of attack for different wing planforms at (left) leading edge pivot, (middle) mid-chord pivot, and (right trailing edge pivot.

Figure 5.23 shows force coefficient as a function of angle of attack for pivot location at mid-chord. Non–circulatory apparent mass effect is absent for all wing planforms. During constant pitch-rate phase, effect of wing planform is indistinct at lower angle of attack. The lift coefficients follow the theoretical estimation up to 10 degrees; the drag coefficients are higher than theoretical estimation. Effect of wing planform becomes significant after 15 degrees.

Figure 5.24 shows force coefficient as a function of angle of attack for pivot location at trailing edge. Similar to leading edge pivot, non–circulatory apparent mass effect is pronounced for lower taper-ratio wing at the beginning and the end of pitch-up phase. Higher taper-ratio wings produce the same force coefficients during the pitching motion; lower taper-ratio wing produces lower force coefficients at a given angle of attack. During constant pitch-rate phase, the lift coefficient is below the theoretical estimation; however, the drag coefficient is higher than theory.

Figure 5.25 shows pitching moment coefficients of K = 0.065 about the pivot axis for different wing planforms, the black, blue, and red curves represent rectangular,

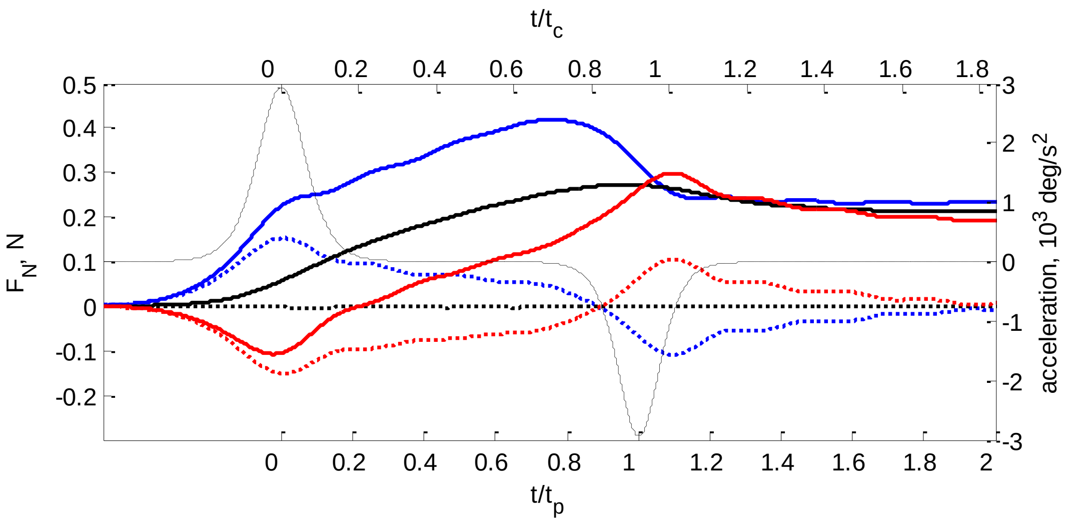

Figure 5.26 Normal force as a function of time normalized with pitch time for rectangular wing. *Blue, black, and red curves represent the pivot axis at leading edge, mid-chord, and trailing edge, respectively. The solid curves are for $K = 0.39$, and the dotted curves are $K = \infty$ (still water).*

trapezoidal, and triangular wings, respectively. The steady flow data using rectangular wing pitching at mid–chord is plotted as circle symbols, and evaluated for leading edge pivot and trailing edge pivot.

As pivot location is at leading edge, the negative pitching moment coefficient is observed over entire pitching angle. The non-circulatory apparent mass effect is pronounced for lower taper-ratio wing and appears at the beginning and the end of pitch-up phase. The magnitude of the pitching moment coefficient is larger than steady-state data, but is significantly smaller compared with higher reduced pitch rate $K = 0.39$. As pivot location is at mid-chord, positive pitching moment coefficient is present over the pitch angle, which is consistent with steady-state data. Effect of wing planform is very small at an angle of attack lower than 20 degrees. As pivot location is at trailing edge, non-circulatory apparent mass effect is pronounced at lower taper-ratio wing, giving negative pitching moment coefficient at lower angle of attack. Lower taper-ratio wings ($\lambda \leq 0.5$) give the same positive pitching moment coefficient with increasing angle of attack.

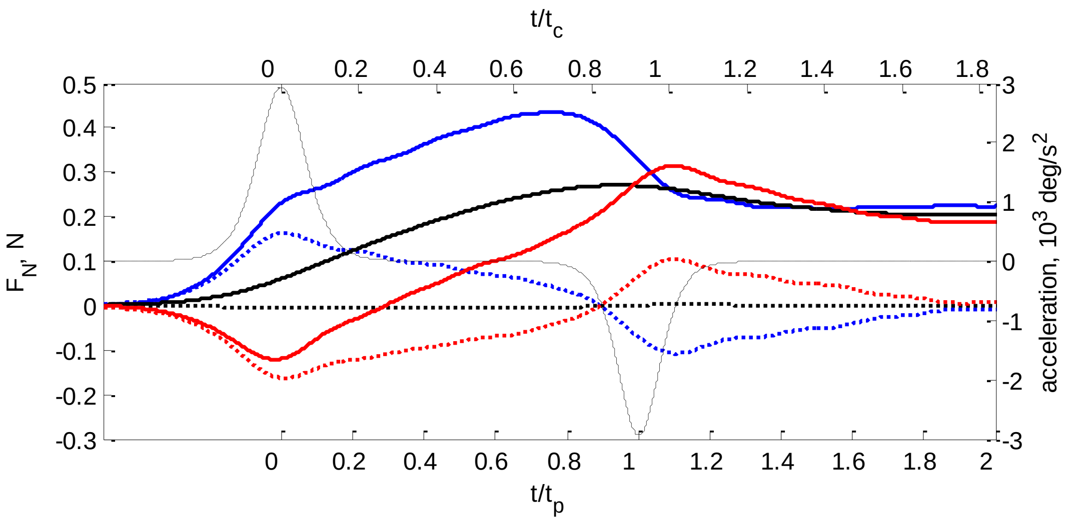

Figure 5.27 Normal force as a function of time normalized with pitch time for trapezoidal wing. *Blue, black, and red curves represent the pivot axis at leading edge, mid-chord, and trailing edge, respectively. The solid curves are for K = 0.39, and the dotted curves are $K = \infty$ (still water).*

5.2.4 Wing Planform Effect and Pivot-Axis Location at K = 0.39

The data presented here were obtained using aspect-ratio-four wings in three wing planforms for high reduced pitch rate K = 0.39, which was implemented using α_m' = 155 °/s (St = 7k) and uniform free-stream velocity U_∞ = 7.5 cm/s (Re = 8.9k). The wing property is given in Section 2.2. The steady data are also considered, which were obtained using a rectangular wing pitching at mid-chord in the same free-stream flow Re = 8.9k. For steady-state data over various wing planforms, see Section 5.1.

5.2.4.1 Normal Force as a Function of Time Normalized with Pitch Time

Figure 5.26 - Figure 5.28 show normal force for K = 0.39 as a function of time normalized with pitch time for rectangular, trapezoidal, and triangular wings, respectively. The blue, black, and red curves represent pivot location at leading edge, mid-chord, and trailing edge, respectively. The solid and dotted curves represent K = 0.39 (St = 7k and Re = 8.9k) and $K = \infty$ (still water), respectively. The motion acceleration is given as a black dashed curve.

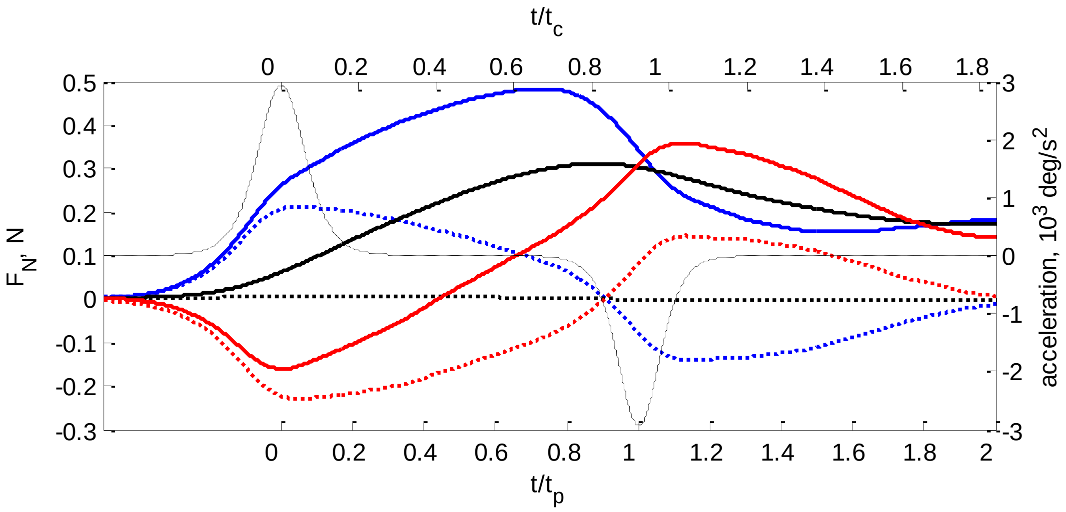

Figure 5.28 Normal force as a function of time normalized with pitch time for triangular wing. *Blue, black, and red curves represent the pivot axis at leading edge, mid-chord, and trailing edge, respectively. The solid curves are for K = 0.39, and the dotted curves are K = ∞ (still water).*

All wing planform shapes produce similar trends in force course at a given pivot axis. As pivot location is at leading edge, it is certain that the normal force spike is positive at the beginning of pitching and negative at the end of pitching, which is consistent with the direction of the motion acceleration. However, as pivot location is at trailing edge, the direction of pitching motion is in the opposite direction of the normal force, as a result, the negative normal force spike is observed at beginning of pitching and positive at the end of pitching.

As pivot location is at mid–chord, normal force spikes are not observed, which indicates non–circulatory apparent mass effects are not present due to symmetrical motion acceleration on both wing-chord ends. Additionally, as taper ratio decreases, the force course is much smoother, even in the still water measurement, which indicates stronger three-dimensional pitch rate effects. Additionally, measurements in still water give symmetrical force course for pivot location at leading edge and trailing edge, and zero-force course for mid–chord pivot as expected, which give a good indication of the accuracy of the measurements.

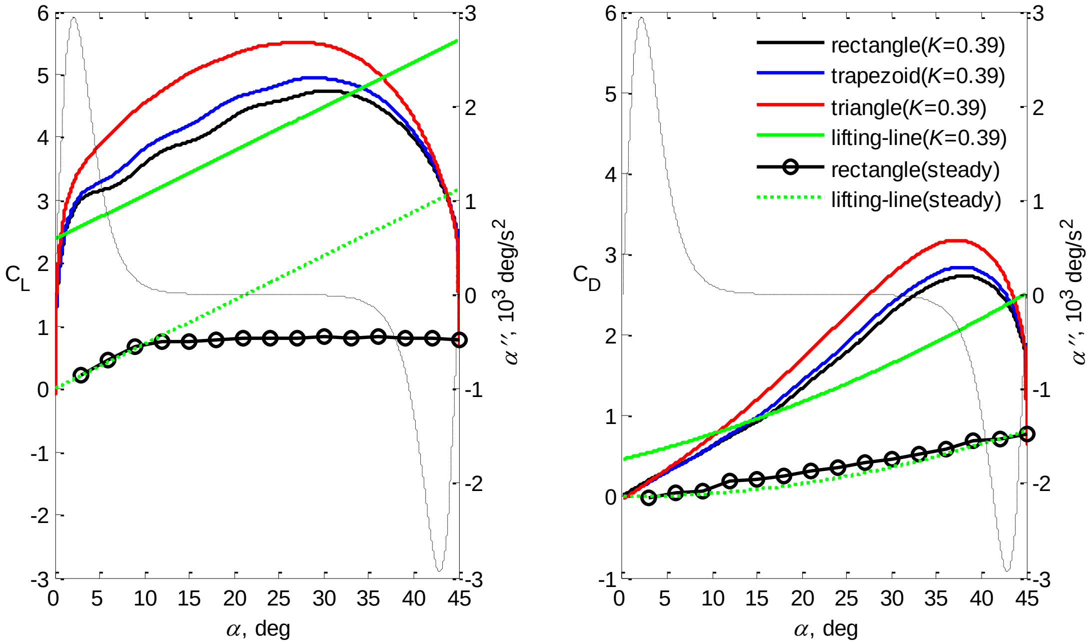

Figure 5.29 Force coefficients of K = 0.39 as a function of angle of attack for different wing planforms at leading edge pivot: (left) lift coefficient and (right) drag coefficient.

5.2.4.2 *Force Coefficients as a Function of Angle of Attack*

Figure 5.29 through Figure 5.31 show force coefficient of wings pitching at leading edge, mid-chord, and trailing edge, respectively. The black, blue, and red curves represent rectangular, trapezoidal, and triangular wings, respectively. The solid curves are for cases $K = 0.39$ and dotted curves are for cases $K = 0$ (denoted by “steady”). The theoretical estimation by lifting-line theory based on rectangular wing is given as green curve.

Figure 5.29 shows force coefficient as a function of angle of attack for pivot location at leading edge. For lift coefficient at $K = 0.39$, non–circulatory apparent mass effect is observed at the beginning and the end of pitch–up phase. During the constant pitch-rate phase, lower taper ratio wings produce lift and drag coefficients well beyond the prediction by lifting-line theory and steady-state data, which are due to three–dimensional pitch rate effects. The lift coefficient of triangular wings increases unlinearly with angle of attack, unlike other higher taper-ratio wings. For the drag coefficient, the pitch-rate effect is over-predicted by lifting–line theory at lower angle of attack and

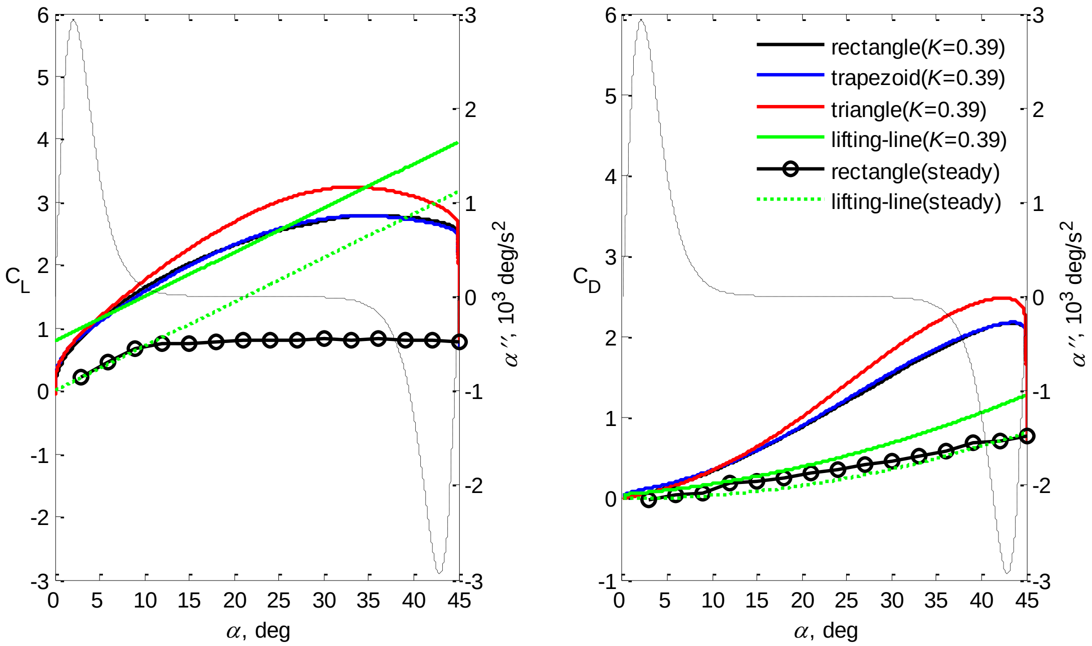

Figure 5.30 Force coefficients of K = 0.39 as a function of angle of attack for different wing planforms at mid-chord pivot: (left) lift coefficient and (right) drag coefficient.

under-estimated at higher angle of attack. The drag coefficient of dynamic flow ($K > 0$) is higher than the flow in steady-state.

Figure 5.30 shows force coefficient as a function of angle of attack for pivot location at mid-chord. Non–circulatory apparent mass effect is absent. Higher taper ratio wing ($\lambda \geq 0.5$) gives the same lift and drag coefficients, the wing with lower taper ratio gives higher lift and drag coefficients at higher angle of attack, which do not follow the theoretical result. For all wing planforms, dynamic forces are higher than forces in steady-state on a rectangular wing.

Figure 5.31 shows force coefficient as a function of angle of attack for pivot location at trailing edge. Non–circulatory apparent mass effects are found at the beginning and the end of pitch–up phase. Lift coefficient for taper ratio higher than 0.5 during a constant pitch rate region follows the theoretical estimation closely, whereas drag coefficients are not well predicted. Lift and drag coefficients are below the steady flow measurement using rectangular wing at lower angle of attack, and above steady measurement at higher angle of attack.

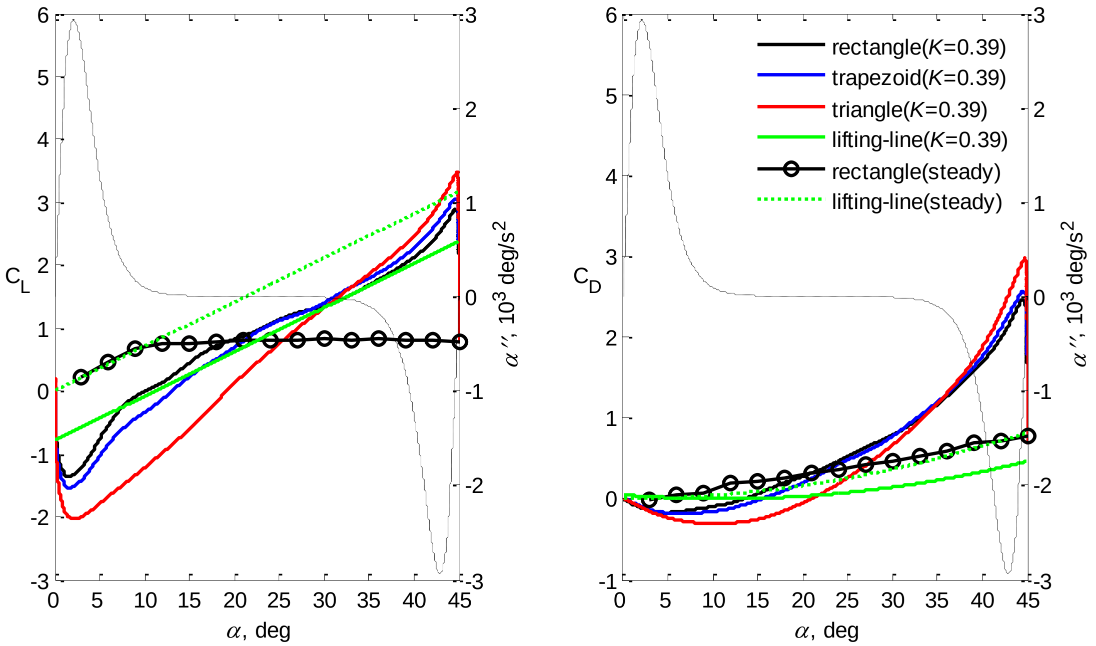

Figure 5.31 Force coefficients of K = 0.39 as a function of angle of attack for different wing planforms at trailing edge pivot: (left) lift coefficient and (right) drag coefficient.

Figure 5.32 shows pitching moment coefficients about the pivot axis for different wing planforms, the black, blue, and red curves represent rectangular, trapezoidal, and triangular wings, respectively. The steady flow data using rectangular wing pitching at mid–chord are given as circle symbols and evaluated for leading edge pivot and trailing edge pivot.

As pivot location is at leading edge, negative pitching moments are found in the range of pitch angle, which are consistent with steady flow measurements about corresponding pivot axis. Lower taper ratio gives higher pitch moment coefficient. As pivot location is at mid-chord, higher taper-ratio wings ($\lambda \geq 0.5$) give same pitching moment coefficients, lower the taper ratio gives higher pitch moment coefficients, and all of them have magnitude less than one. Moreover, negative pitch moment coefficient is observed at lower angle of attack, which is contrary to the steady flow data. As pivot location is at trailing edge, negative pitching moment coefficients are also observed at lower angle of attack with much larger amplitude than ones pitching at mid–chord.

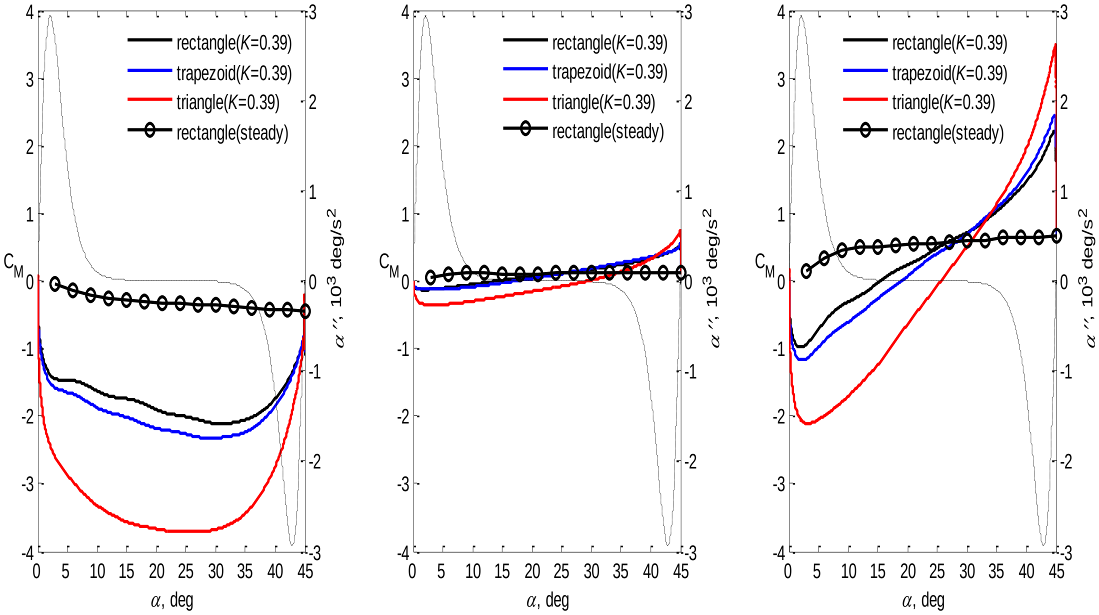

Figure 5.32 Pitching moment coefficient of $K = 0.39$ as a function of angle of attack for different wing planforms at (left) leading edge pivot, (middle) mid-chord pivot, and (right trailing edge pivot.

To sum up, there are several features observed for wing planforms subject to $K = 0.39$ and $K = 0.065$. (i) At lower reduced pitch rate, higher taper-ratio wings ($\lambda \geq 0.5$) give the same force coefficients for pivot location other than mid-chord pivot; lower taper-ratio wing gives lower force coefficients at a given angle of attack. The effect of wing planform is very similar to the wings at a steady state as discussed in Section 5.1. (ii) Lift and drag coefficients are pronounced using lower taper-ratio wings at higher reduced pitch rate $K = 0.39$. (iii) Lower taper-ratio wings produce pronounced non-circulatory apparent mass effect at higher reduced pitch rate and pivot location other than mid-chord.

5.2.5 Effect of Kinematics and Reynolds Number

In previous discussion, we have shown effects of pivot axis location and wing planforms within a Reynolds number range $0 \leq \mathrm{Re} \leq 1.3\times10^4$; reduced pitch rates were achieved either by varying pitch rate while holding Reynolds number or by varying Reynolds number while holding pitch rate. Most literature has shown the reduced pitch rate is a good normalized parameter to incorporate both pitch rate and flow velocity for Reynolds number $2\times10^4 < \mathrm{Re} < 3\times10^5$ (Daley and Jumper, 1984; Jumper et al., 1987;

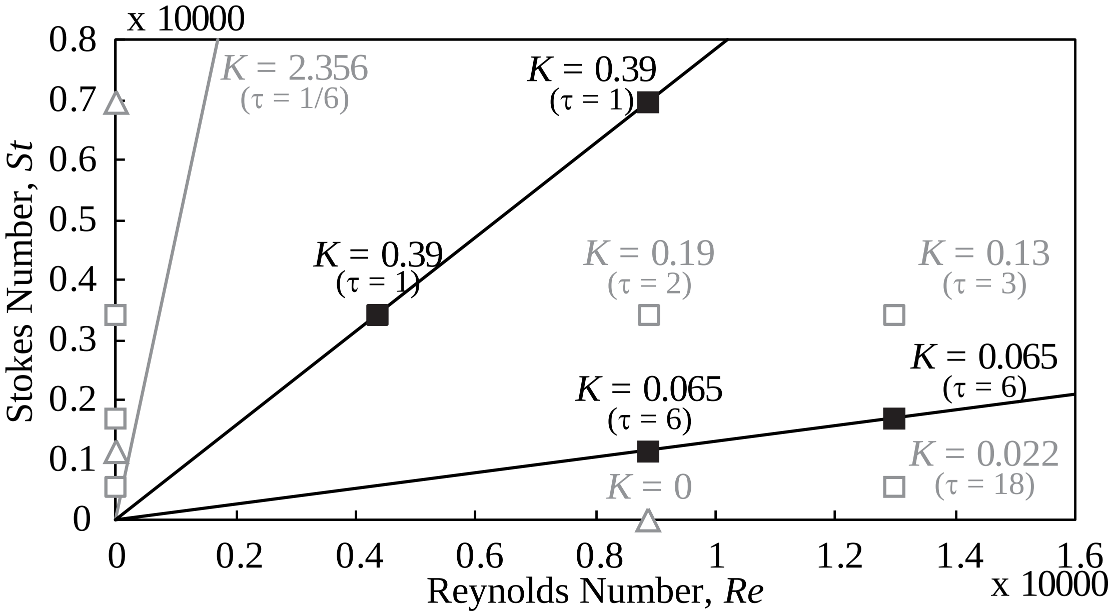

Figure 5.33 Cases in study of effect of kinematics and Reynolds number.

Walker and Chou, 1987; Walker et al., 1985b). It is unclear how both pitch rate and Reynolds number are incorporated within present Reynolds number range and its impact on both non-circulatory effect and pitch rate effetc in terms of pivot-axis location.

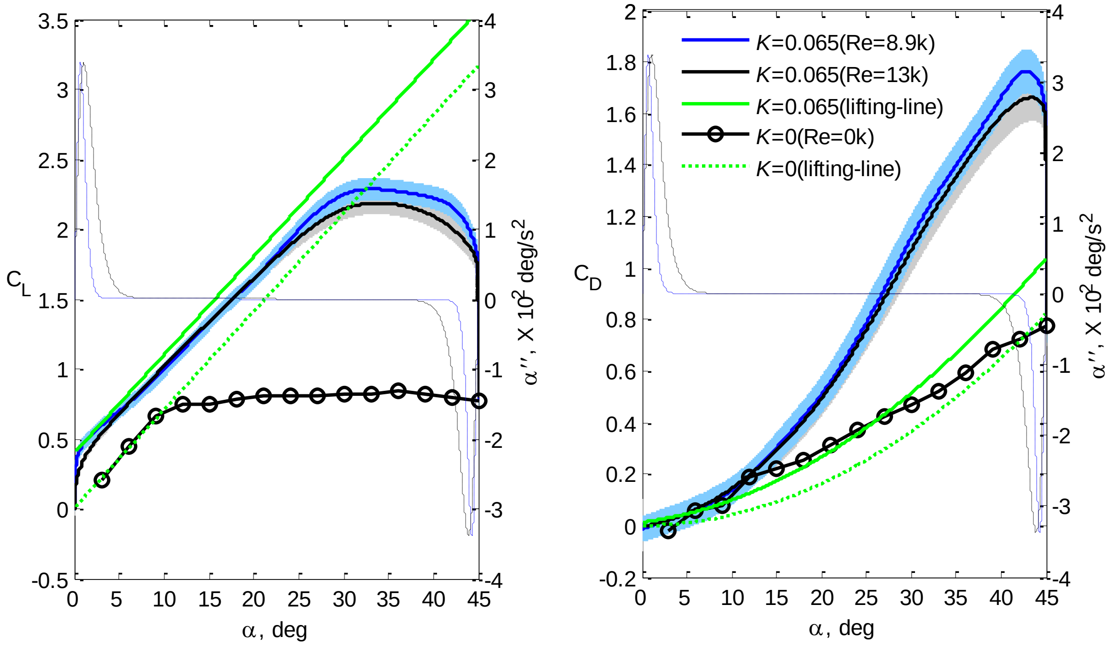

Figure 5.34 Force coefficients of K = 0.065 as a function of angle of attack at leading edge pivot (left) lift coefficient (right) drag coefficient.

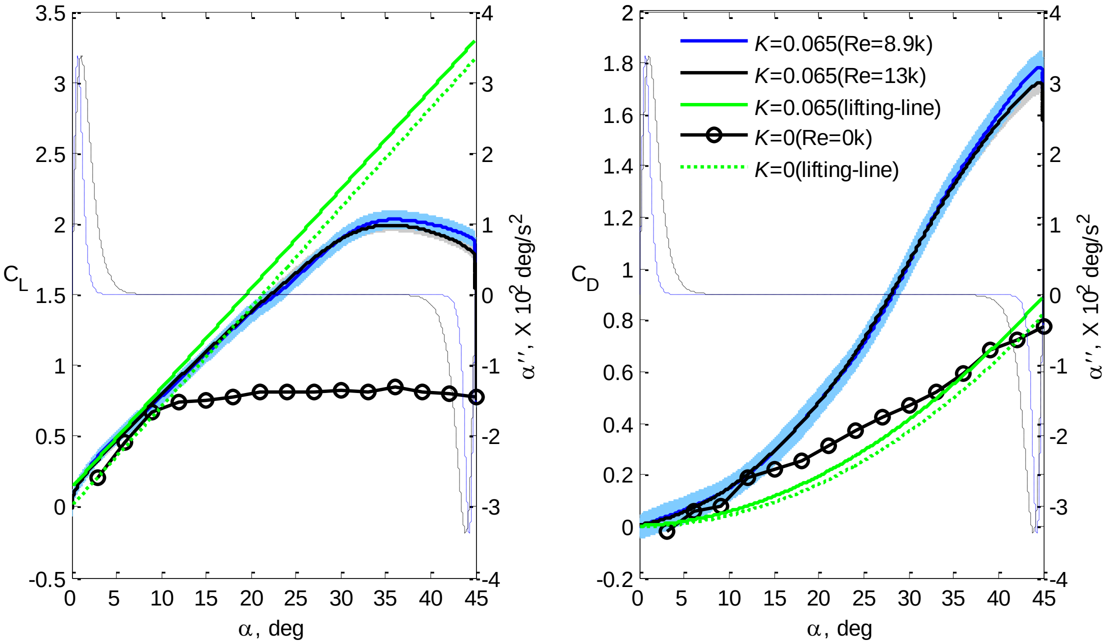

Figure 5.35 Force coefficients of $K = 0.065$ as a function of angle of attack at mid-chord pivot (left) lift coefficient (right) drag coefficient.

In this section, a rectangular wing was pitched at leading edge, mid-chord, and trailing edge pivot axes with two constant reduced pitch rate $K = 0.065$ and 0.39, as highlighted in Figure 5.33. For $K = 0.065$, the comparison was made between test cases using $St = 1.7\text{k}$ in $Re = 13\text{k}$ and $St = 1.1\text{k}$ in $Re = 8.9\text{k}$. For $K = 0.39$, the comparison was made between test case using $St = 7.0\text{k}$ in $Re = 8.9\text{k}$ and $St = 3.4\text{k}$ in $Re = 4.3\text{k}$. All kinematics has different smoothing maneuvering at beginning and the end of pitching motion. The shaded area in figures presents the standard deviation in the measurement. Conditions used to generate these two constant pitch rates are given in Table 2.2.

5.2.5.1 Constant Reduced Pitch Rate K = 0.065

Figure 5.34 - Figure 5.36 show lift and drag coefficients of $K = 0.065$ as a function of angle of attack for pivot axis location at leading edge, mid-chord, and trailing edge, sequentially. The blue and black curves represent unsteady flow data in $Re = 8.9\text{k}$ and 13k, respectively. The steady flow data based on rectangular wing is given as circle symbols; the estimation by lifting-line theory is given as green curve. The shaded area presents data standard deviation.

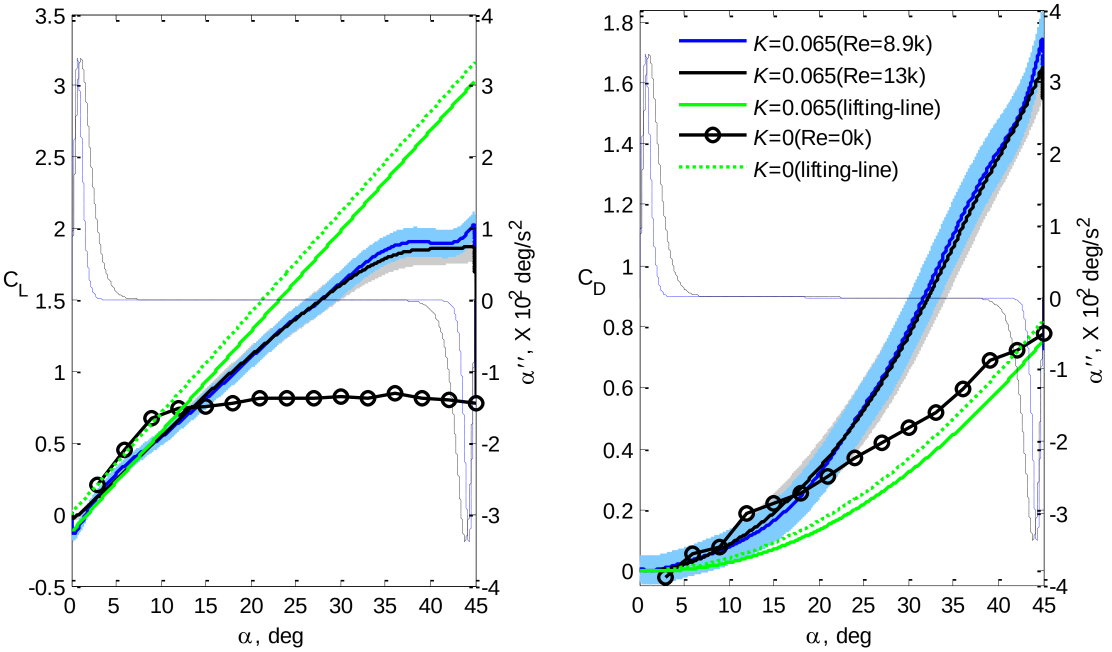

Figure 5.36 Force coefficients of K = 0.065 as a function of angle of attack at trailing edge pivot (left) lift coefficient (right) drag coefficient.

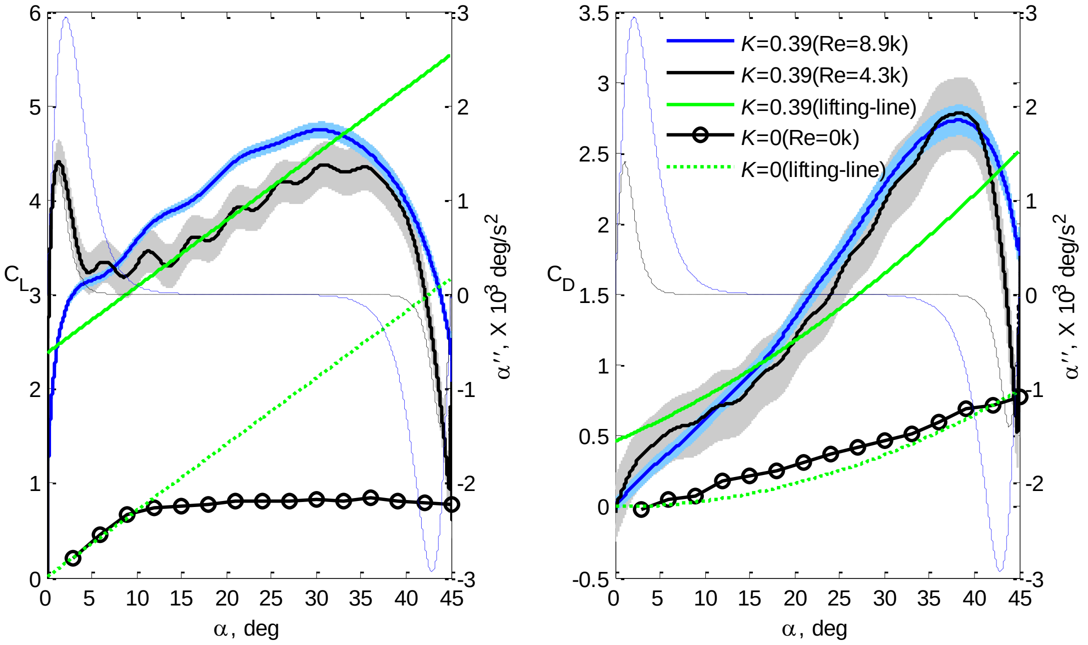

Figure 5.37 Force coefficients of K = 0.39 as a function of angle of attack at leading edge pivot (left) lift coefficient (right) drag coefficient.

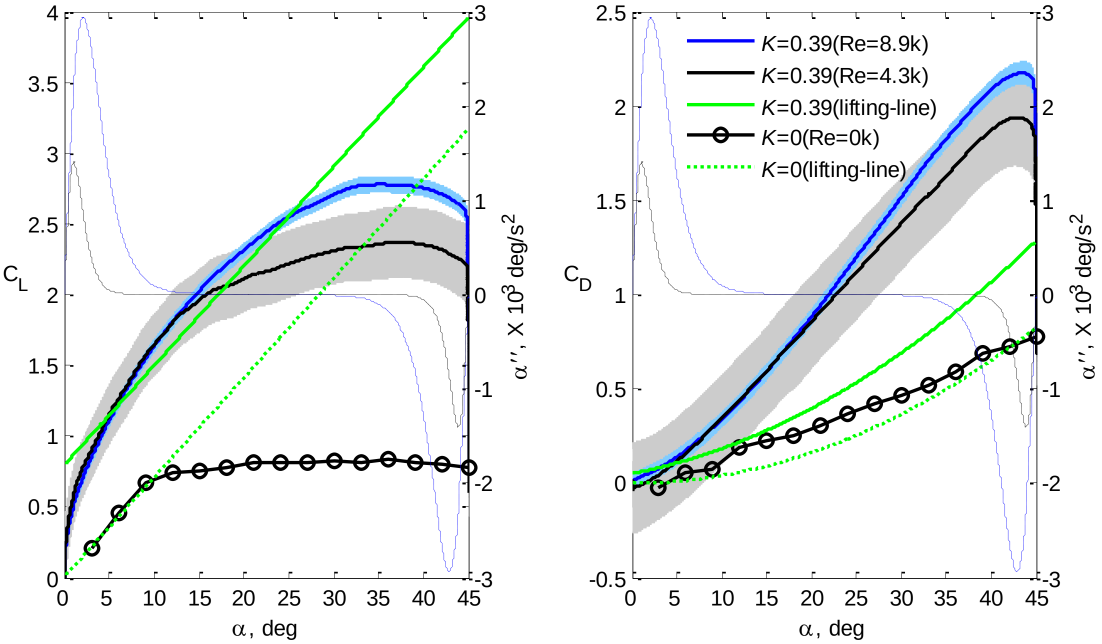

Figure 5.38 Force coefficients of K = 0.39 as a function of angle of attack at mid-chord pivot (left) lift coefficient (right) drag coefficient.

All pivot axis location show similarity of lift and drag coefficients with respect to angle of attack at given constant reduced pitch rate. Close examination of two data reveals several distinct features. First, non-circulatory apparent mass effect is much pronounced for both leading edge and trailing edge pivots in *Re* = 8.9k, caused by motion acceleration. Even both kinematics has the same maximum acceleration, acceleration duration for *Re* = 8.9k is half of one for *Re* = 13k and shorter than one convective time. Second, despite the variation of pivot axis location, the occurrence of non-circulatory effect at the beginning of the motion has little impact on rotation rate effect before saturation of forces during constant pitch-rate phase. The force curves are similiar up to 20 degree angles of attack for leading edge pivot axis, 30 degree angles of attack for other two pivot axes.

5.2.5.2 Constant Reduced Pitch Rate K = 0.39

Figure 5.37 - Figure 5.39 show lift and drag coefficients of K = 0.39 as a function of angle of attack for pivot axis location at leading edge, mid-chord, and trailing edge, sequentially. The curve legends are similar to K = 0.065. The blue and black curves

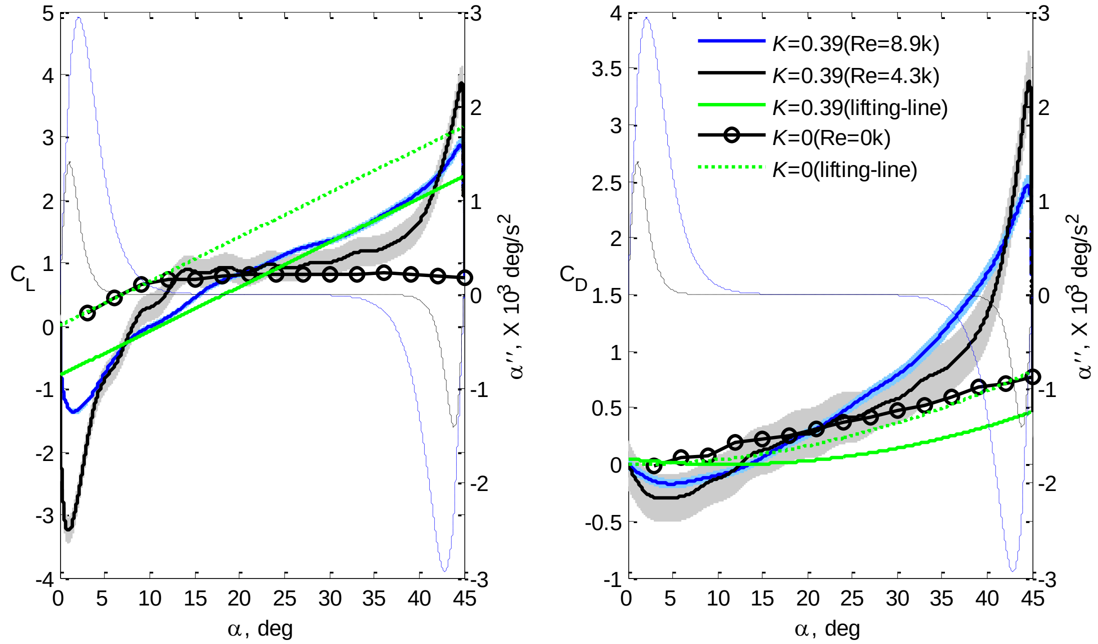

Figure 5.39 Force coefficients of *K* = 0.39 as a function of angle of attack at trailing pivot (left) lift coefficient (right) drag coefficient.

represent unsteady flow data in *Re* = 8.9k and 4.3k, respectively. The steady flow data based on rectangular wing is also given as circle symbols; the estimation by lifting-line theory is given as green curve. The shaded area presents data standard deviation.

Unlike lower reduced pitch rate *K* = 0.065, the variation of force curves is much pronounced for leading edge and trailing edge pivot axes; for mid-chord pivot axis the force curves are still in a good agreement below 12 degree angles of attack. The variation at lower angle of attack is caused by non-circulatory effect, which is associated with motion acceleration; the resultant vortical structure is the starting vortex. Recall the conditions used to generate wing kinematics from Table 2.2, the kinematics with *Re* = 8.9k has both maximum acceleration and acceleration duration (less than one convective time) twice larger than one with *Re* = 4.3k. As a result, the strength of starting vortex in *Re* = 8.9k would enhance the rotation rate effect during constant pitch-rate phase. As pivot axis location is at leading edge pivot the lift coefficient not only follows the theoretical estimation but also shift upward; for trailing edge pivot the slope of lift curve is in agreement with theoretical estimation. This enhanced vortical structure has less impact on drag coefficient.

5.2.6 Similarity Analysis

In the preceding section, we have discovered that the effect of rotation rate is independent of effect of non-circulatory apparent mass. The former is associated with the first derivative of the wing motion and the latter is relevant with the second derivative of the wing motion. In the next chapter, we will show the effect of non-circulatory apparent mass only promotes the formation of typical starting vortex and its dependence on pivot axis location. The independence between non-circulatory and rotation rate effects suggests the superposition principle to be practicable for the present study, especially at lower angle of attack. Therefore, the non-circulatory force data obtained in the still water condition would be subtracted from force data in the running water condition, leaving only circulatory force data. The insight of rotational rate effect is characterized with effetcs of reduced pivot rate, wing geometry, and pivot axis location, as shown in the following.

5.2.6.1 Effect of reduced pitch rate on pivot axis location

Figure 5.40 shows circulatory lift-coefficient of a rectangular wing as a function of angle of attack to emphasize the effects of reduced pitch rate and pivot axis location; the solid, dashed, and dotted lines represent the pivot axis location at leading edge, mid-chord, and trailing edge. Recall from Equation (3.42), the reduced pitch rate effect is unimportant as pivot axis location is at three-quarter chord, where the change of angle of attack would contribute only to the strength of circulation. Consider lift coefficient for a given pivot axis is shifted to the three-quarter chord using Equation (5.2), the impact of circulatory effect in the flow field with respect to pivot axis is obtained and shown in Figure 5.40. It is noted that the effects of pivot axis and non-circulatory apparent mass are not significant in the steady flow; the rectangular wing at mid-chord pivot is also provided as baseline.

$$\Delta\alpha = (3/4 - \bar{x}_p)\alpha'_m t_c = (3/4 - \bar{x}_p)\alpha'_m t_p / \tau \qquad (5.2)$$

where $\bar{x}_p$ is pivot axis location normalized with wing chord, τ is the ratio of pitch time to convective time. The shifted angle is positive as the pivot axis location is ahead of three-quarter chord and negative as the pivot axis location is after three-quarter chord.

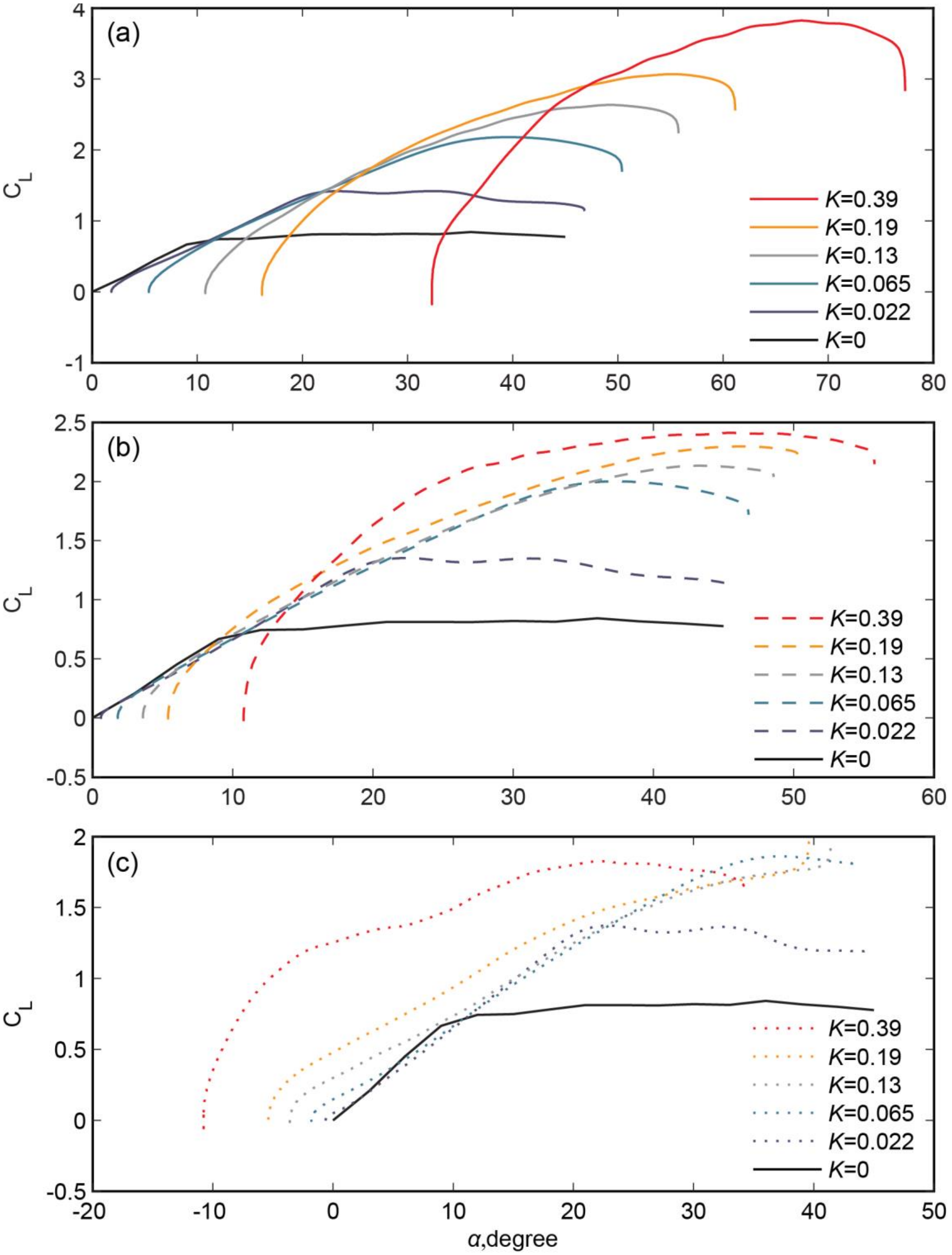

Figure 5.40 Similarities of reduced pitch rate in terms of circulatory lift-coefficients as a function of angle of attack for (a) leading edge pivot, (b) mid-chord pivot, and (c) trailing edge pivot.

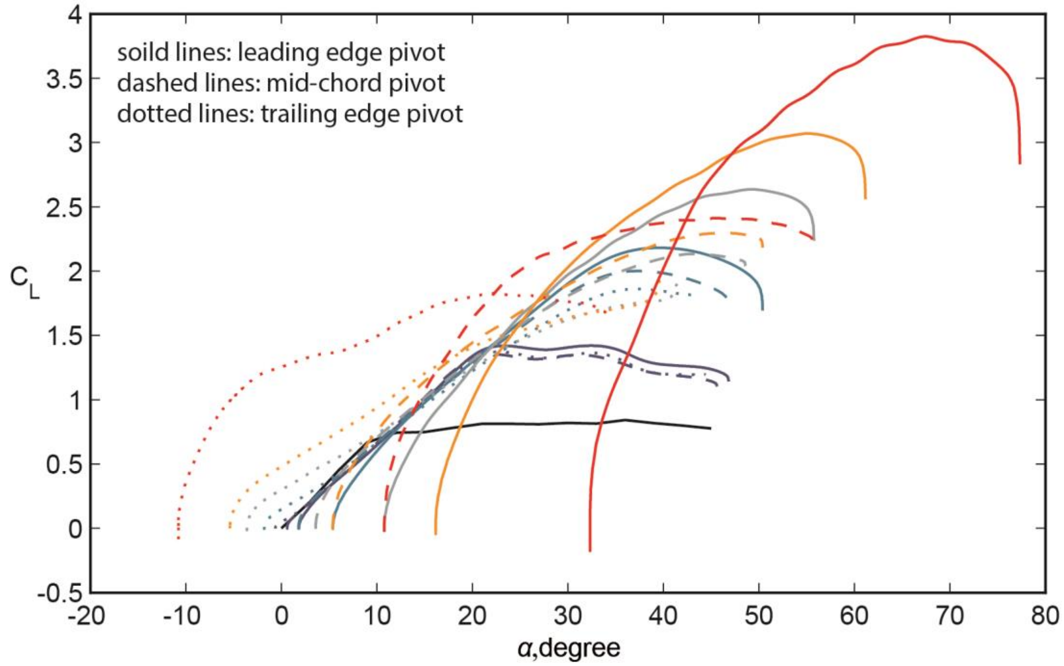

Figure 5.41 Similarities of pivot axis location in terms of circulatory lift-coefficients as a function of angle of attack.

As shown in Figure 5.40, the lift-curve becomes nonlinear as reduced pitch rate increases and pivot axis location is away from the leading edge. The variation of zero-lift angle of attack is in accordance with the incorporation of reduced pitch rate and pivot axis location, as well as the variation of vortical structure. For leading edge pivot, the zero-lift angle of attack increases because of effect of reduced pitch rate. The lift-curves before the saturation extend linearly with increasing reduced pitch rate up to angle of attack of 60 degrees, showing an upper limit of lift coefficient. For mid-chord pivot, the extension of the lift-curve is also observed but becomes nonlinear as reduced pitch rate is increased. The variation of zero-lift angle of attack in terms of reduced pitch rate is less pronounced. For trailing edge pivot, the zero-lift angle of attack is shifted to the opposite side due to effect of pivot axis location. The extension of lift-curve is no longer observed as reduced pitch rate is increased; however, the lift-curve shifts upward. From the flow visualization data, the starting vortex at leading edge is the vortical structure formed at lower angle of attack for the cases at trailing edge pivot axis, which may contribute to this nonlinearity of lift-curve.

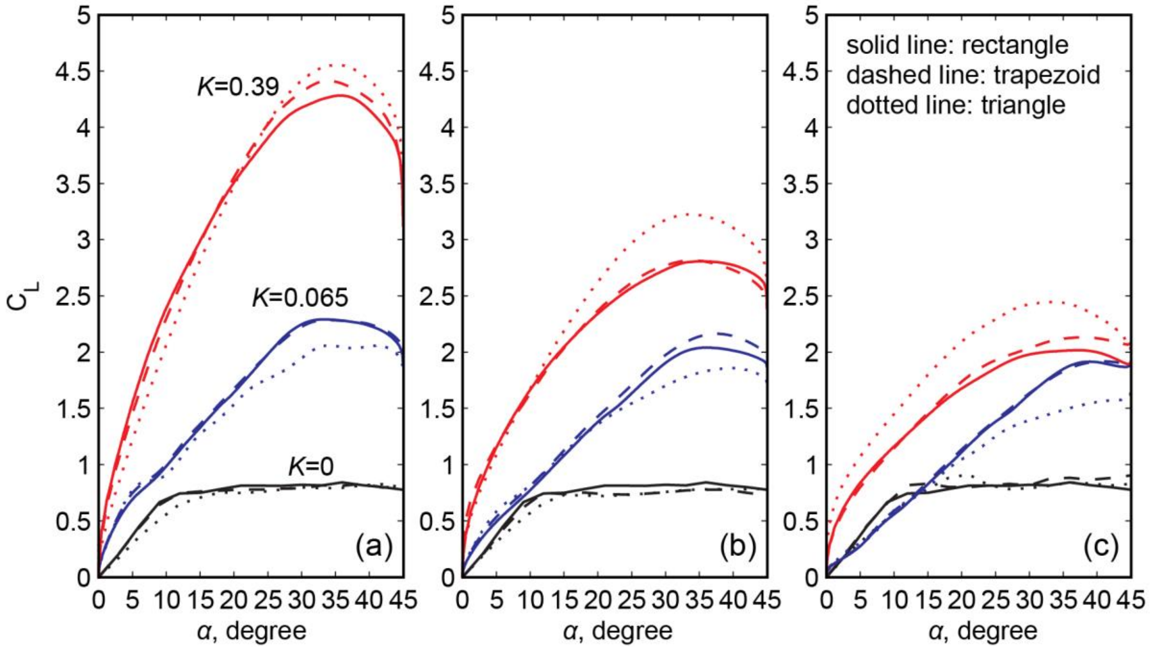

Figure 5.42 Similarities of wing planform in terms of circulatory lift-coefficient as a function of angle of attack for (a) leading edge pivot, (b) mid-chord pivot, and (c) trailing edge pivot.

Figure 5.41 shows the complete series of force data of pivot axis location with respect to reduced pitch rate. For a given reduced pitch rate, the lift-curve at different pivot axis location can be connected. This connection of the lift-curve seems to increase linearly with angle of attack and shifts upward as reduced pitch rate is increased with decreasing slope.

5.2.6.2 Effect of wing planform on pivot axis location

Figure 5.42 and Figure 5.43 show circulatory lift- and drag- coefficients as a function of angle of attack, respectively; the effect of wing planform is shown for a given reduced pitch rate and pivot axis location. The solid, dashed, and dotted lines represent rectangular, trapezoidal, and triangular wings, respectively. The black, blue, and red lines represent the reduced pitch rate K = 0, 0.065, and 0.39, respectively. Effect of wing planform is more pronounced for pivot axis location other than the leading edge and higher reduced pitch rate. The influence of wing planform is less pronounced as taper ratio higher than 0.5.

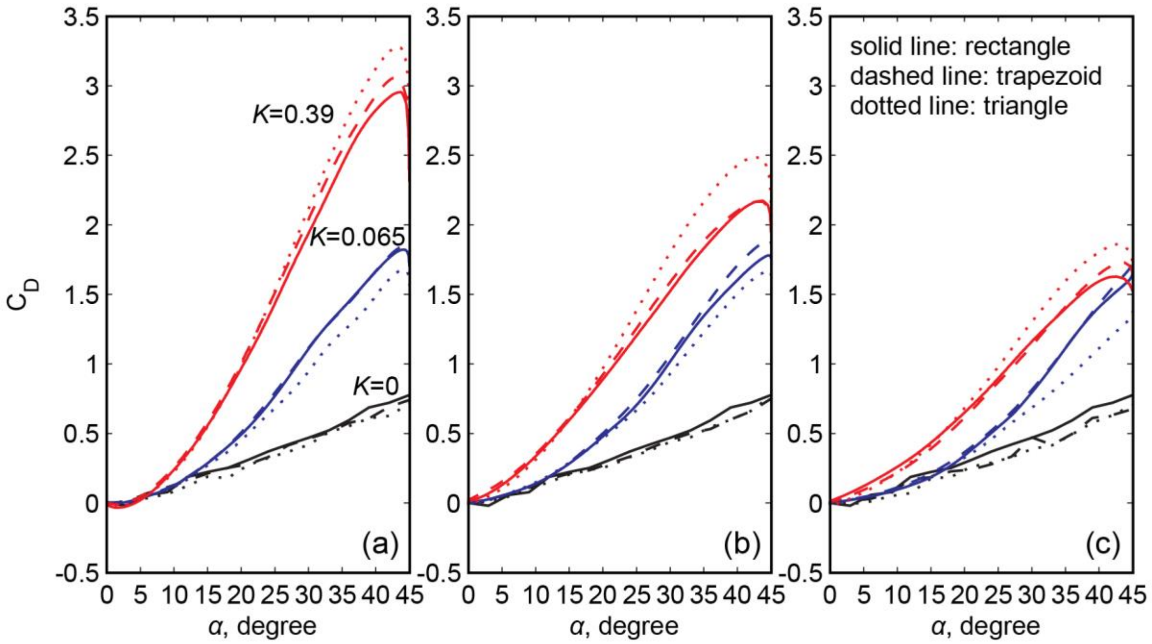

Figure 5.43 Similarities of wing planform in terms of circulatory drag-coefficient as a function of angle of attack for (a) leading edge pivot, (b) mid-chord pivot, and (c) trailing edge pivot.

CHAPTER 6

PIV FLOW FIELD MEASUREMENTS

The PIV data at several span locations of a pitching rectangular wing are presented; the pivot locations were at leading edge, mid-chord, and trailing edge. The test cases are highlighted in Figure 6.1. The parameters used to find particle displacements are given in Table 6.1; they were found from PIV data in calibration. With camera sensor frame of 4008 by 2672 pixels, the field of view for Camera 1 and Camera 2 was 242 by 161 mm and 243 by 162 mm, respectively. The PIV system and calibration procedure are given in Section2.6.

6.1 MEASUREMENT UNCERTAINTY

The major measurement uncertainty was contributed from alignment of two

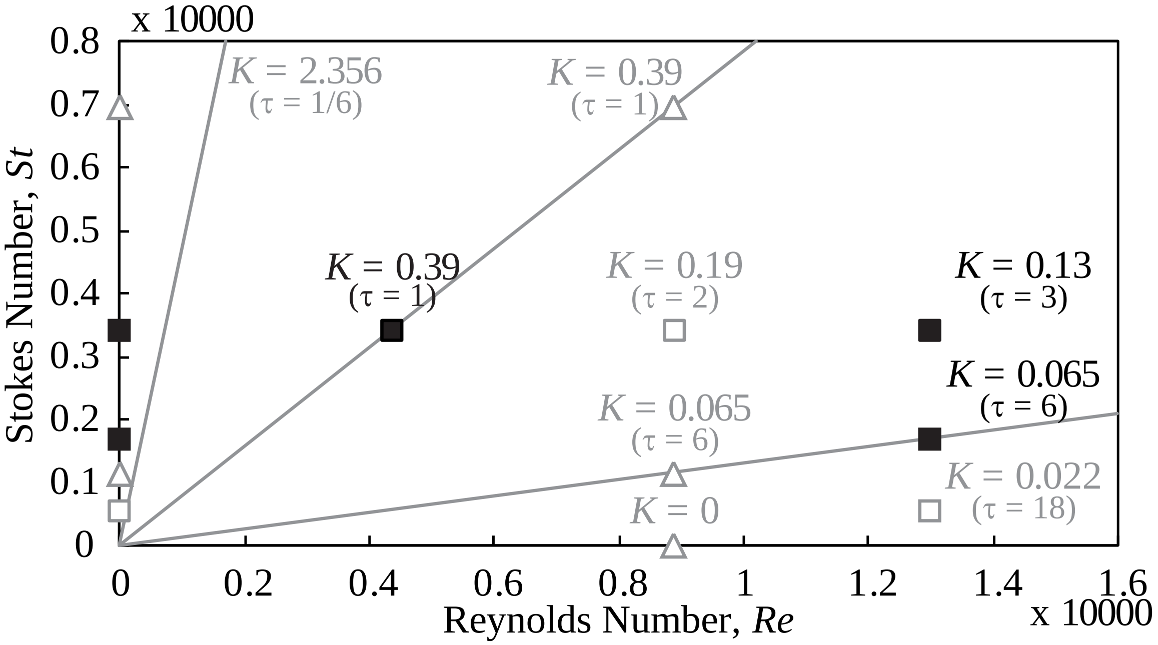

Figure 6.1 Test cases using 2D PIV in *St* - *Re* space.

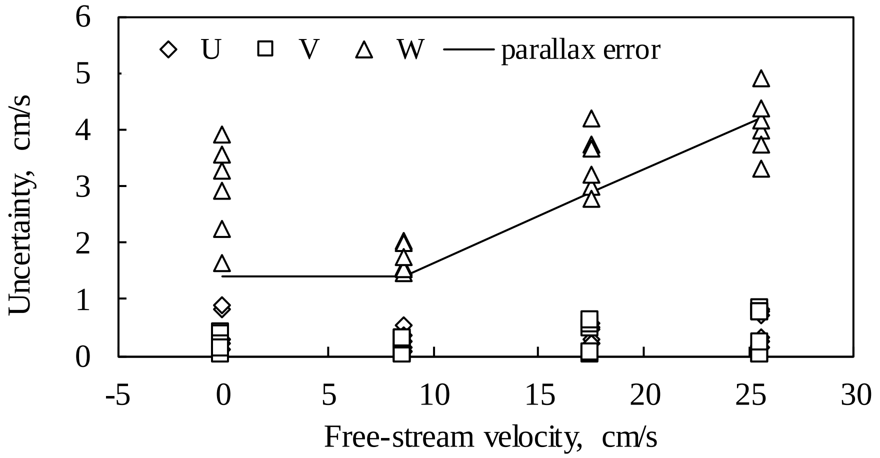

Figure 6.2 Measurement uncertainty for each velocity component.

cameras. The maximum spatial difference from camera field of view was found to be 0.06 pixels; this is parallax error. The uncertainty of displacement in Z-component due to parallax error was 0.03 mm. This uncertainty in terms of speed would be changed in regard to exposure time. The exposure time was determined in order to maintain validation data points over field of view; it was selected to have three-pixel-particle displacement between two interrogation windows according to wing chord-edge speed in still water and free-stream velocity. The exposure times in use are variable and given in Figure 6.2. As a result, the uncertainty of flow velocity in Z-component due to parallax error was 4.22 cm/s for U_∞ = 25.6 cm/s and 0.27 cm/s for α_m' = 37.5°/s at mid-chord pivot. In addition, the laser-sheet thickness of 1.8 mm was determined by a laser-sheet illumination on a ruler, where all particle displacements were measured. The maximum particle displacement had to be less than laser-sheet thickness. Hence, the possible maximum speed is W_{max} = 253.44 cm/s for test case in U_∞ = 25.6 cm/s, and W_{max} = 16.4 cm/s for test cases at mid-chord pivot using α_m' = 37.5°/s in still water.

Table 6.1 Parameters for present PIV data using lens-shifted configuration.

Parameter	Magnification, px/mm		Object distance, mm		Lens displacement, mm	
	M	w_M	p	w_p	ΔX	$w_{\Delta X}$
Camera 1	16.510	0.115	837.258	0.109	60.117	0.183
Camera 2	16.456	0.098	879.793	0.146	-44.601	0.137

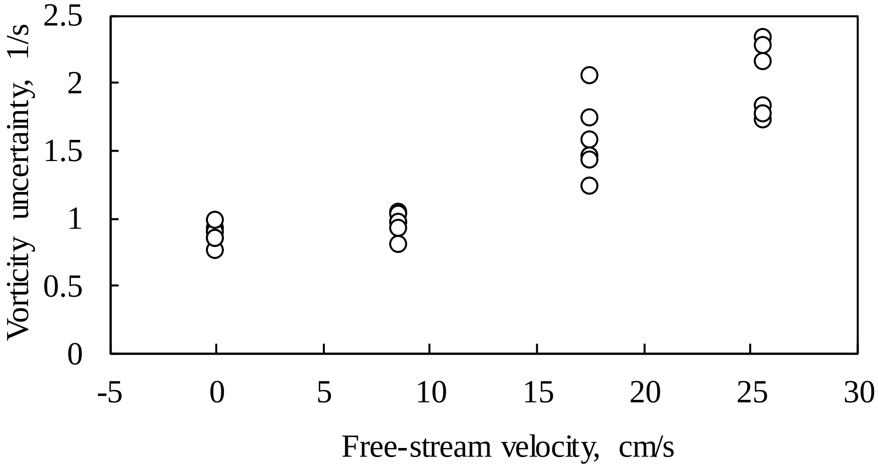

Figure 6.3 Measurement uncertainty for vorticity.

Moreover, measurement uncertainties of flow quantities were measured in uniform flow without wing model at several water depths. For all flow conditions, sixty PIV images were taken with an interval of one second and averaged using the strategy discussed in Section0. The exposure time was adjusted according to free-stream velocity; however, the exposure time for still water measurement was specified as the ones used for U_∞ = 8.4 cm/s. The data in still water would reveal the limitation of cross-correlation of two interrogation windows; the velocity in Z- and Y- components would show the fluctuation of particles due to motor and propeller. The results are shown in Figure 6.2 and Figure 6.3, and are employed to arrange contour colorbar.

Figure 6.2 shows measurement uncertainty of particle velocity U, V, and W at several specified free-stream velocities. Extreme averaged data in the image field of view are presented; the parallax error is given as baseline uncertainty for W velocity. The

Table 6.2 Exposure time for present PIV data.

$U_\propto$	0 cm/s		8.6 cm/s	25.6 cm/s
α_m'	LE/TE	MC	LE/MC/TE	LE/MC/TE
37.5°/s	0.005468457	0.010936918	0.002114165	0.000710227
76.4°/s	0.002684126	0.005368252	0.002114165	0.000710227

All units are in seconds; LE, leading edge pivot; MC, mid-chord pivot; TE, trailing edge pivot;

variations of U and V components are significant less than W component and their uncertainties are less than 1 cm/s. The variations of W component increase with increasing free-stream velocity; they are reasonable as compared with data in still water. The uncertainities of W component follow the parallax error but have higher values; the maximum value is less than 5 cm/s for U_∞ = 8.4 cm/s. Figure 6.3 shows vorticity measurement uncertainty versus free-stream velocity; the extreme averaged data from field of view were present. The uncertainty and variation increase as free-stream velocity is increased; the maximum vorticity uncertainty is less than 2.5 per second.

6.2 VORTICITY AND OUT-OF-PLANE VELOCITY FIELD

Figure 6.4 - Figure 6.7 show vorticity flow field of a rectangular wing pitching at leading edge for reduced pitch rates $K = \infty$, 0.39, 0.13, and 0.065, sequentially; the corresponding out-of-plane velocity fields are given in Figure 6.8 - Figure 6.11. The vorticity fields at three span locations are considered in attempt to character the perspective of vortical flow during the pitch-up phase, which are 50% span, 75% span, and 100% span. The out-of-plane velocity field would indicate the evolution of three-dimensional flow; the dramatic out-of-plane velocities shown at right upper corner in the figures are parallax errors, which were deteriorated by axial flow. The PIV data are also correlated to the force data shown in Figure 5.12 and Figure 5.15.

For $K = \infty$ at 50% span, the force data showed the first normal force spike occurs within motion acceleration where angle of attack is less than 7°; this normal force spike is associated with a starting vortex shown in the PIV data at 7.5° in Figure 6.4, which rotates counterclockwise. The core of this starting vortex is accompanied with a pair of out-of-plane velocity; the positive value indicates the flow moves out of paper and the negative value indicates the flow moves into the paper. The magnitude of the starting vortex increases slightly in next few phases and then starts to dissipate as increasing angle of attack to 45°. Meanwhile, more negative vorticity accumulate at leading edge due to pitch rate; during this process, the force data did not show significant force generated. The strength of the starting vortex decreases as the span location moves to the wing tip but does not vanish. At the wingtip, negative vorticity formed on the leeward surface at higher angle of attack while the starting vortex is stretching due to negative out-of-plane velocity. As angle of attack is increased, the positive out-of-plane velocity on the leeward surface is observed and the negative out-of-plane velocity is at the outside, which indicates a circulation flow around the wing tip. The starting vortex turns into positive vorticity as detached from the trailing edge; more negative vorticity is formed on the leeward surface during the formation of the tip vortex. These vortical structures dissipate quickly after the wing is at maximum angle of attack.

For K = 0.39 at 50% span, there is a starting vortex formed at trailing edge; the deflection of the streamlines toward the starting vortex indicates its presence at an angle of attack 7.5° in Figure 6.5. Similar deflected streaklines were introduced to identify the occurrence of starting vortex for flow visualization data. The force data showed that the normal force was increased rapidly within this phase angle. As the angle of attack is increased to 22.5°, the starting vortex is washed downward and convects downstream; the negative vorticity at leading edge becomes much thicker with positive out-of-plane velocity around the vortex core. The force data showed an increase of normal force with a slope similar to those with lower reduced pitch rates in the same free-stream flow, this angle of attack is well beyond the steady stall angle of attack (i.e., about 12°). As the angle of attack is increased to 37.5°, the negative vorticity at leading edge forms a well-known leading-edge vortex, which is identified according to the presence of streamline circulation core. This leading-edge vortex circulates on the leeward surface and forms positive vorticity in a cavity underneath the neck of the leading-edge vortex; this positive vorticity forms a well-known secondary vortex. As the angle of attack is increased to about 45°, the starting vortex is about one chord downstream from the trailing edge; the leading-edge vortex grows in size at frontal portion of the chord on the leeward surface. The positive vorticity on the leeward surface is also fed by negative out-of-plane velocity. At this phase, the force data decreased in accordance with the wing deceleration. The span variation of the flow evolution is small, except the flow evolution at the wing tip. At higher angle of attack, the starting vortex formed at earlier stage does not move downstream but interacts with out-of-plane velocity field at trailing edge. The starting vortex becomes a portion of positive vorticity above the negative vorticity on the leeward surface. The out-of-plane velocity field shows an increase of wingtip circulation with increasing angle of attack; this wingtip circulation stays close to the wing, introducing significant drag on the wing.

For K = 0.13 at 50% span, the starting vortex appears in the near wake at an angle of attack 7.5°, as shown in Figure 6.6, instead of occurring at the trailing edge like other cases with higher reduced pitch rate. The force data showed a significant increase of normal force while comparing with the case with K = 0.39. As the angle of attack is increased to 22.5°, the negative vorticity (with positive out-of-plane velocity about the core) at leading edge grows much thicker than the case with higher reduced pitch rate; more trailing edge vortices are observed in the wake. As the angle of attack is increased to 30°, a leading-edge vortex is in the vicinity, which is much earlier than the case with K = 0.39. This leading-edge vortex covers most of the wing chord and also introduces a secondary vortex (with negative out-of-plane velocity) on the leeward surface close to the leading edge. The force data showed the normal force increases with increasing angle of attack in a slope similar to the case with K = 0.39. The spanwise variation is more significant than the cases with higher reduced pitch rate, which is evidenced from both vorticity and out-of-plane velocity field. At the wingtip, the starting vortex formed at earlier stage is stretched into positive vorticity in the near wake by the wingtip circulation. This wingtip circulation convects downstream with increasing angle of attack.

For K = 0.065 at 50% span, the starting vortex is indiscernible at the lower angle of attack 7.5°; there are few trailing-edge vortices in the near wake. From the force data, there is not normal force spike within this angle of attack, which indicates the importance of the starting vortex to the normal force spike. The negative vorticity thickness becomes much thicker as the angle of attack is increased to 15° with more trailing edge vortices in the wake. This is the common feature before leading-edge vortex is present. The leading-edge vortex is discernible at an angle of attack 22.5°, which is much earlier than the other cases with higher reduced pitch rate. This leading-edge vortex covers entire wing chord and grows in size as increasing angle of attack; the secondary vortex is introduced during the growth of the leading-edge vortex as well. Moreover, the spanwise variation is more pronounced than the other higher reduced pitch rates in both vorticity and out-of-plane velocity field. At the wingtip, the onset of wingtip circulation begins from the negative out-of-plane velocity about trailing edge and positive out-of-plane velocity on the leeward surface, similar to the other cases with higher reduced pitch rates; however, the wingtip circulation convects downstream much quicker for a given angle of attack due to larger time ratio t_p/t_c.

6.3 EFFERCT OF REDUCED PITCH RATE

We have shown the development of vorticity and out-of-plane velocity during pitch-up phase for each reduced pitch rate; it is still ambiguous how the reduced pitch rate impacts the flow. In this section, the effect of reduced pitch rate is discussed in two aspects. The first aspect is to compare PIV data at a phase t_2, as shown in Figure 6.12, which is the second sharp corner of the motion. The second aspect is to compare PIV data in a sequence of convective times with an interval of one convective time; the onset of the series PIV data starting from t_1, as shown in Figure 6.13. All PIV data considered here are from the wing pitched at leading edge.

As shown in Figure 6.12, increasing the reduced pitch rate increases the size of leading-edge vortex and transports the starting vortex further downstream, which is consistent with a reduced pitch rate for a given maximum angle of attack. Recall from Figure 6.1, the reduced pitch rate $K = \infty$, 0.39, 0.13, and 0.065 indicates the ratio of pitch time to convective time from 0, 1, 3, to 6, respectively. Also, the wingtip circulation is elongated downstream in accordance with the time ratio, as expected.

As shown in Figure 6.13, both starting vortex at trailing edge and leading-edge vortex are critical vortical structures for rapid increase of lift and drag forces, and are features of higher reduced pitch rate $K = 0.39$. For lower reduced pitch rate, the formation of leading-edge vortex is delayed partially due to wing angle of attack, which increases lift force being predicted by the potential flow theory. The decrease of forces is associated with the dissipation of the leading-edge vortex and the formation of an in-transition trailing-edge vortex. This in-transition vortex at trailing edge has same counterclockwise rotation as the trailing-edge vortex during pitching motion, but its presence impairs the force generation. This process initiates the oscillatory behavior observed from the force data and may generates arch vortex as reported by Visbal (2011), and Yilmaz and Rockwell (2012).

6.4 EFFECT OF PIVOT AXIS LOCATION

From the flow visualization data for $K = 0.39$, we have found there is a starting vortex at leading edge on the windward surface as pivot axis location is at trailing edge pivot and as for leading edge pivot there is a starting vortex at trailing edge. It is unclear the formation of the starting vortex at mid-chord pivot and effect of pivot axis location on reduced pitch rates. In this section, the inspection of pivot axis effect on reduced pitch rates is given; only vorticity field by the wing at t_2 is considered.

As shown in Figure 6.14, for $K = \infty$, a starting vortex is formed at trailing edge as the pivot axis location is at leading edge; as the pivot axis location is at trailing edge a starting vortex is formed at leading-edge. This is consistent with flow visualization data. As the pivot axis location is at mid-chord, there are two starting vortices; one is at leading edge and the other is at trailing edge; both are weak in strength compared to those where the pivot axis location is the end of wing chord. The presence of the starting vortex toward the leading edge on the windward surface delays the formation of leading edge vortex on the leeward surface, as shown for cases with finite reduced pitch rate. The trailing-edge vortices in the wake follow the starting vortex. An increase of numbers of trailing-edge vortex is in consistent with an increase of the negative vorticity at the frontal portion of the leeward surface in forming a leading-edge vortex, which would satisfy Kelvin’s circulation theorem. At any given pivot axis location, the leading-edge vortex grows in size with increasing reduced pitch rate.

Consider the delayed formation of leading-edge vortex is due to the presence of the starting vortex and the dissipation of the starting vortex is associated with the pivot axis location with respect to free-stream velocity. It would be intriguing to discover the similarity of the PIV data by shifting a phase between leading edge and pivot axis location. As shown in Figure 6.15, the PIV data at the first row are at phase t_2 for leading edge pivot. The second row and third row are PIV data at phase delay of 0.5 t_c for mid-chord pivot and 1 t_c for trailing edge pivot, respectively. The vortical structures are similar after shifting phases with respect to pivot-axis location; the force data also show the same similarity.

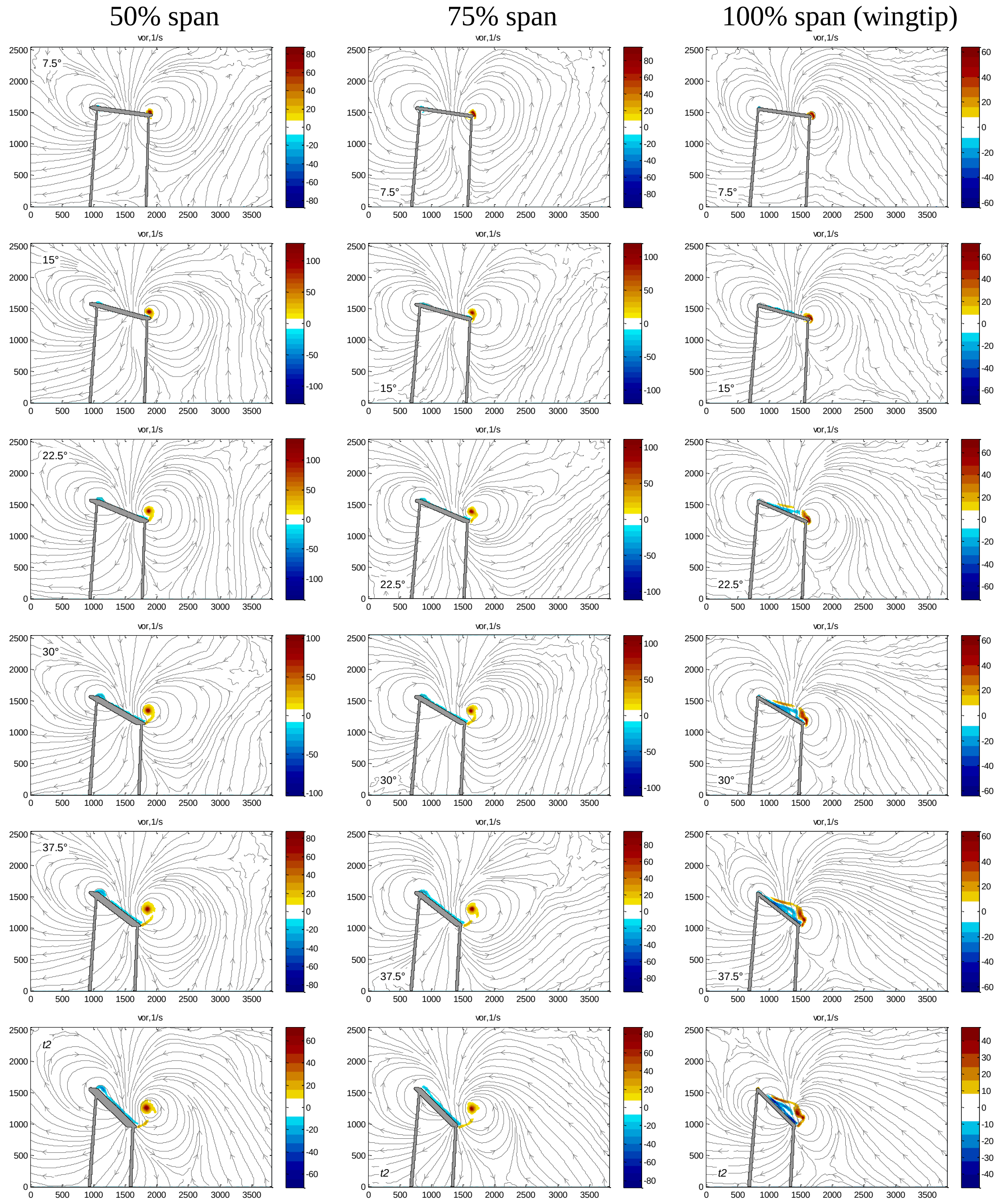

Figure 6.4 PIV instantaneous vorticity field and streamline for $K = \infty$ at leading edge pivot.

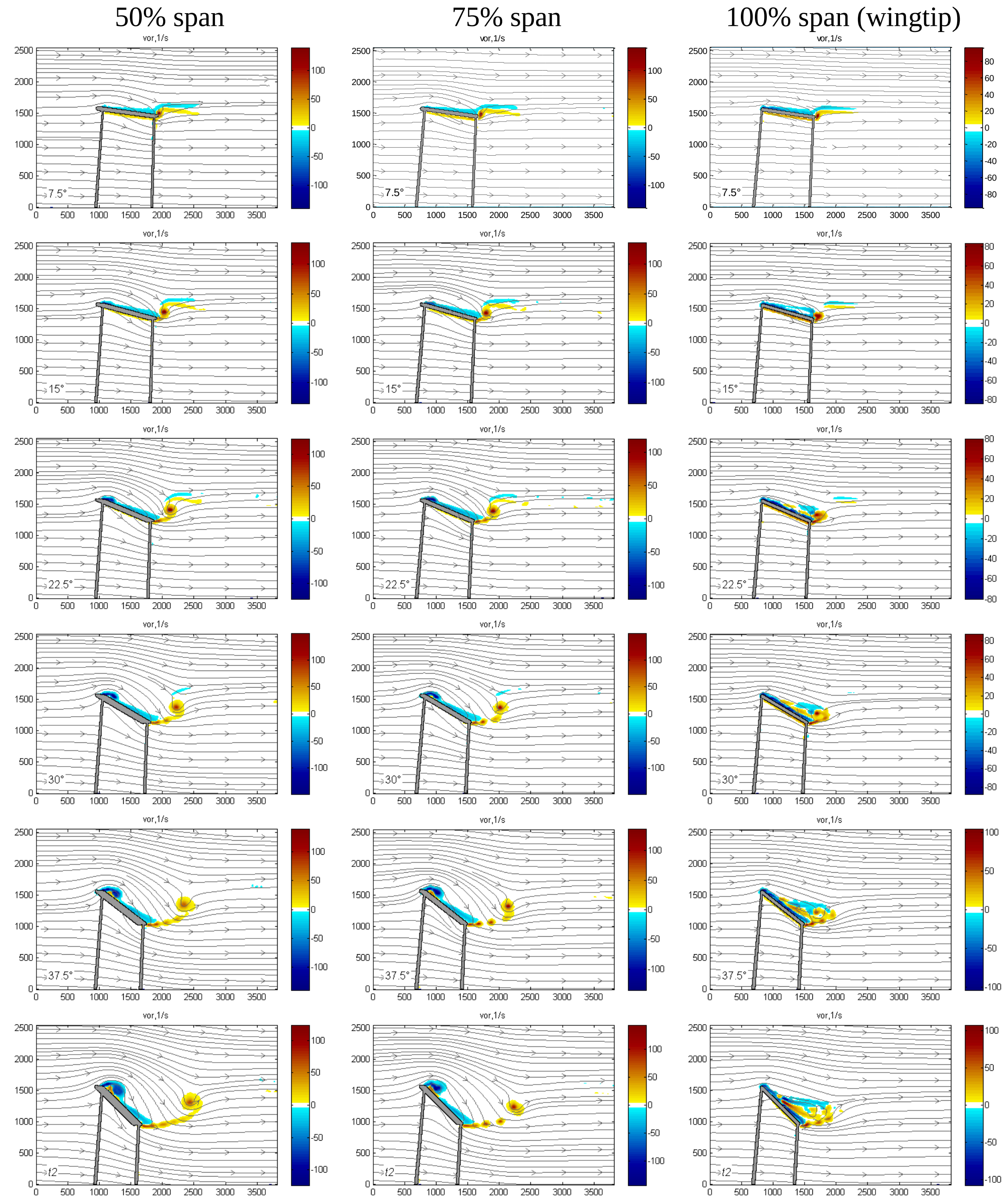

50% span

75% span

100% span (wingtip)

Figure 6.5 PIV instantaneous vorticity field and streamline for K = 0.39 at leading edge pivot.

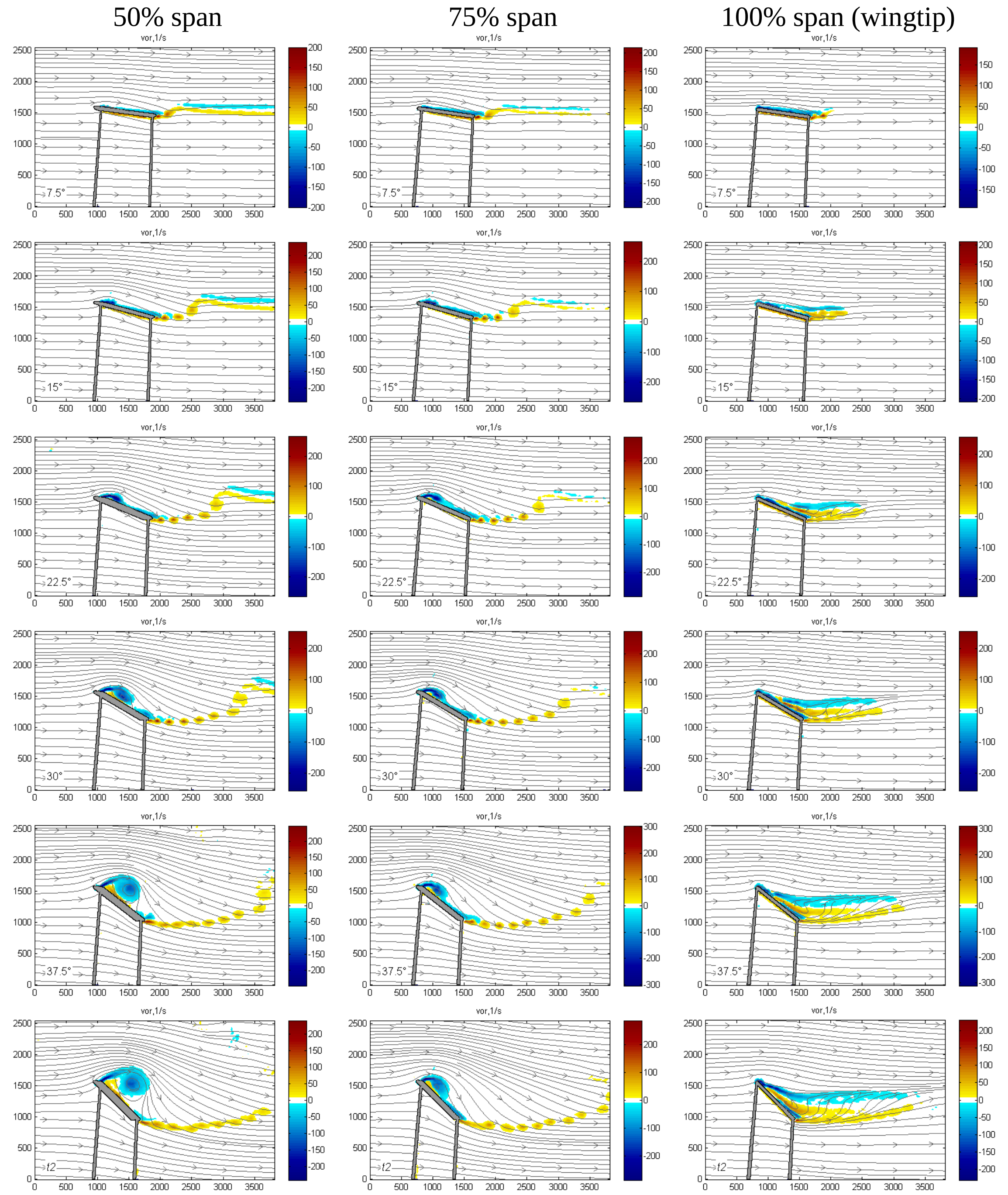
50% span

75% span

100% span (wingtip)

Figure 6.6 PIV instantaneous vorticity field and streamline for K = 0.13 at leading edge pivot.

50% span 75% span 100% span (wingtip)

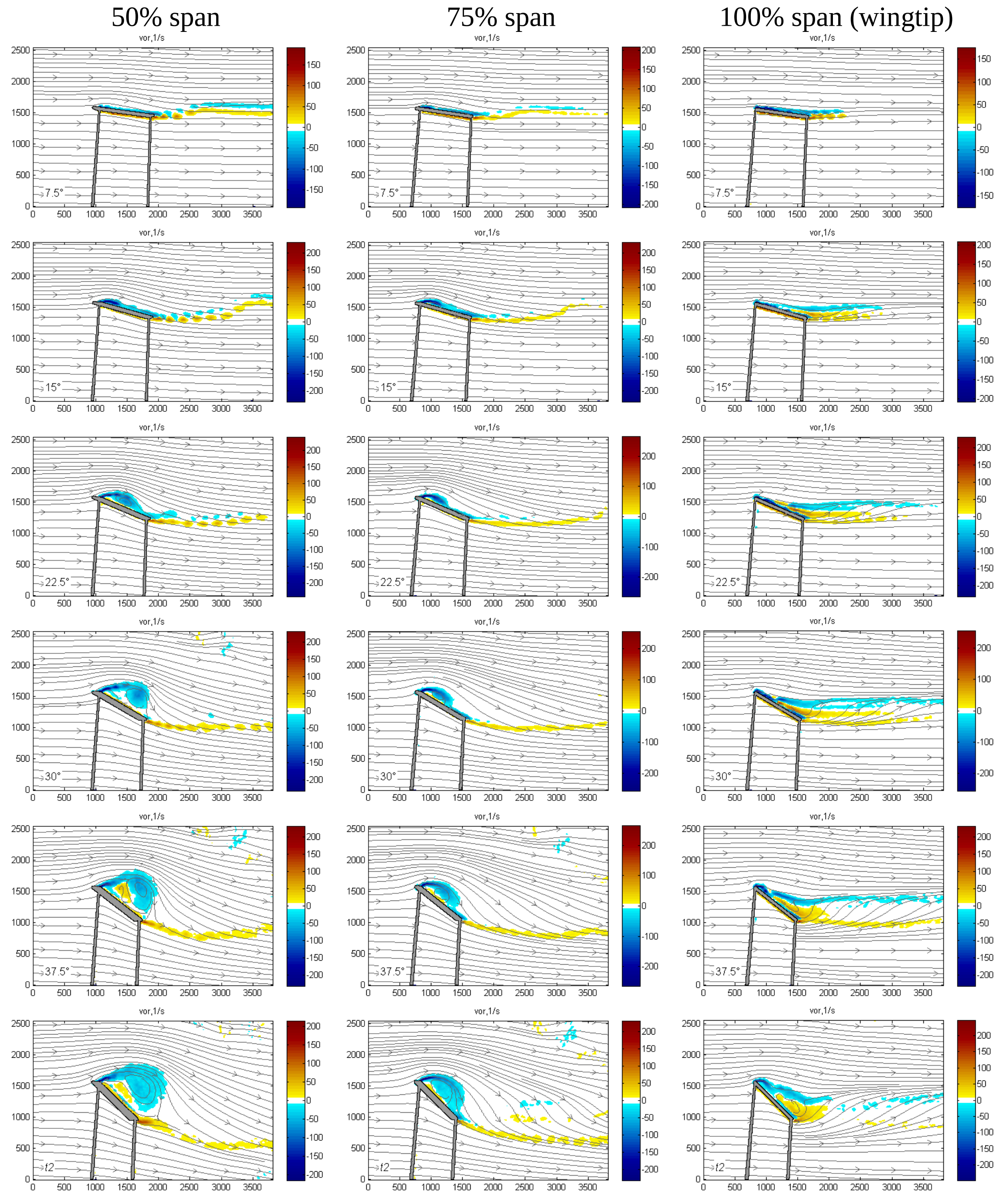

Figure 6.7 PIV instantaneous vorticity field and streamline for K = 0.065 at leading edge pivot.

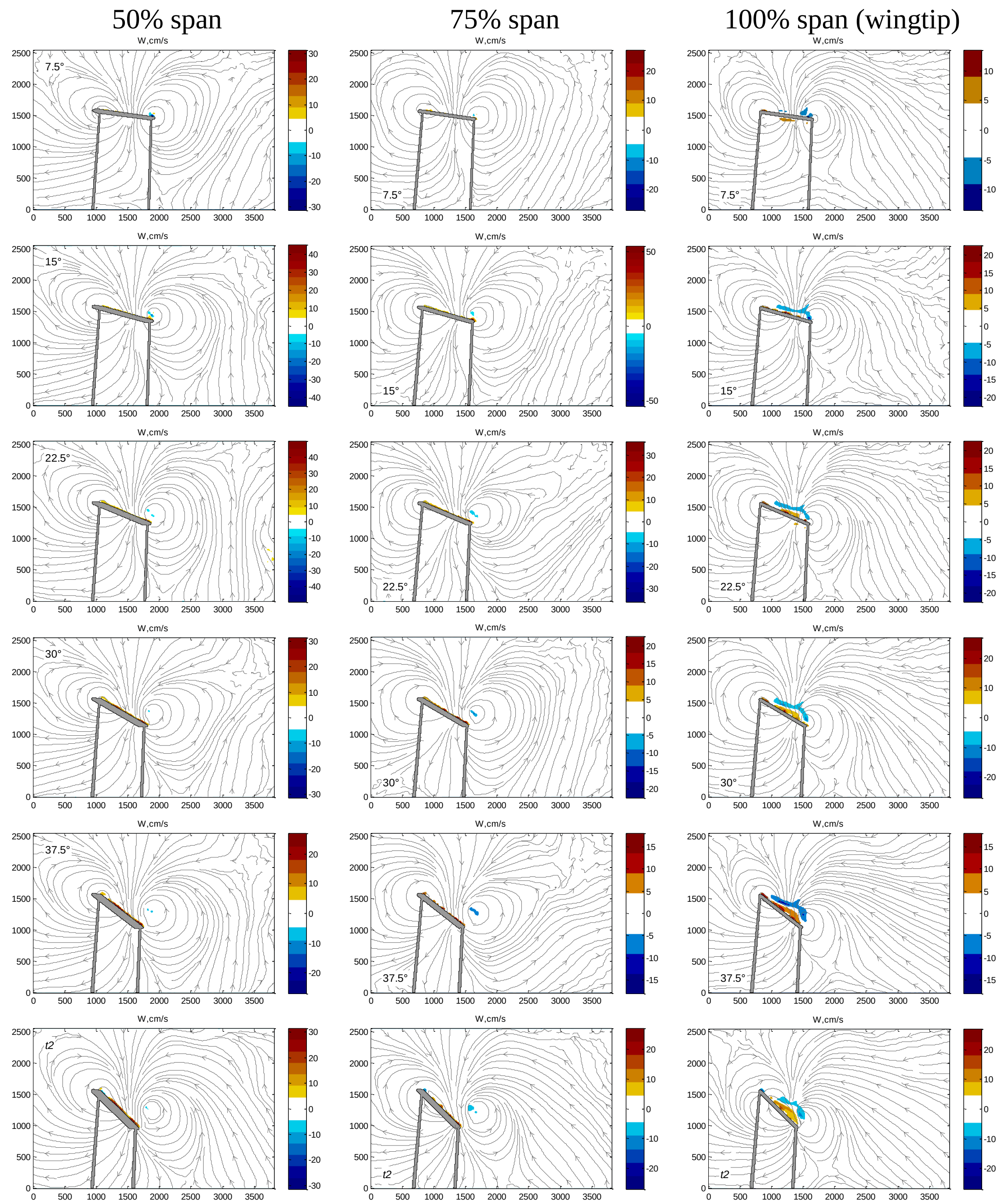

Figure 6.8 PIV instantaneous out-of-plane velocity field and streamline for $K = \infty$ at leading edge pivot.

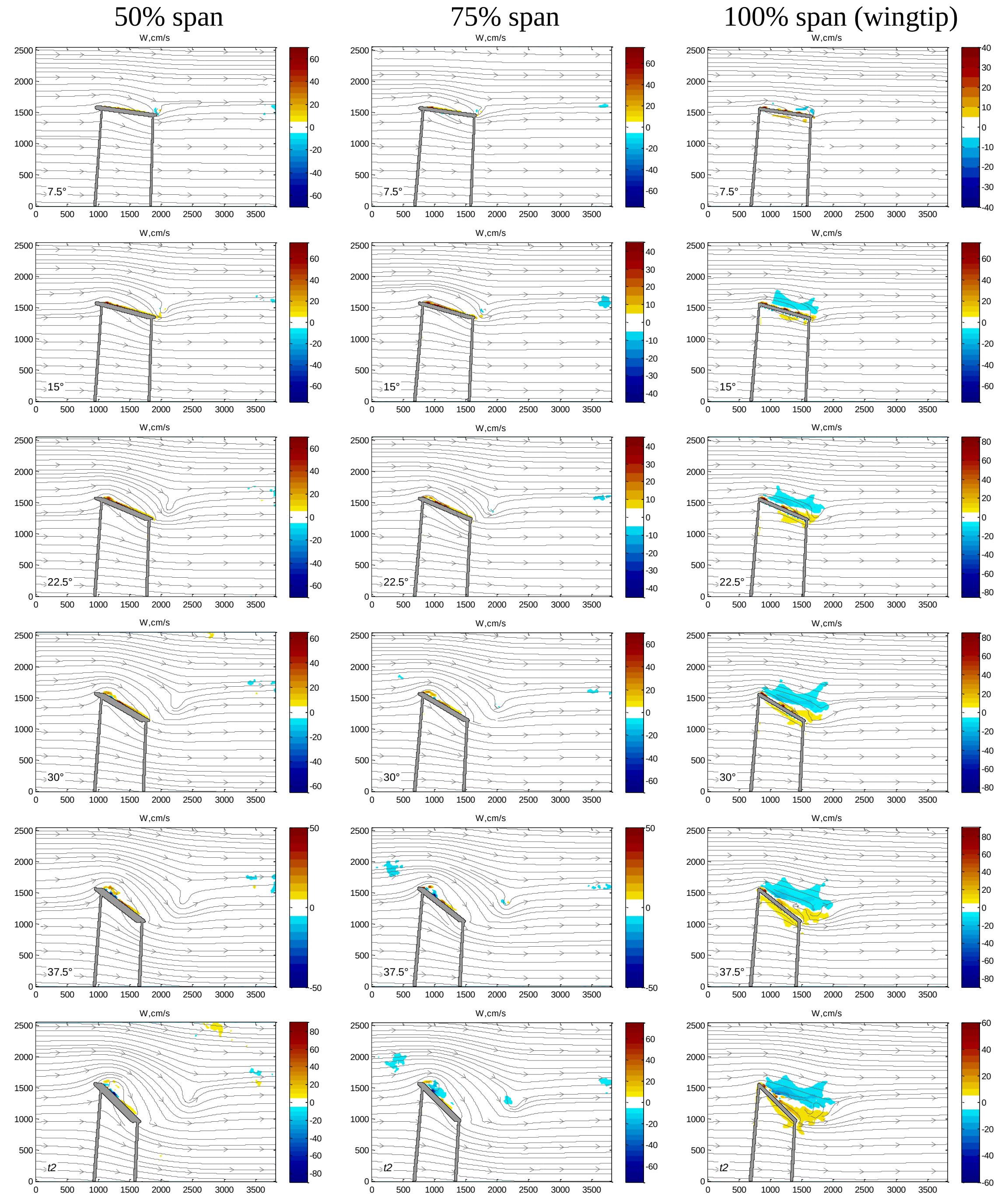

Figure 6.9 PIV instantaneous out-of-plane velocity field and streamline for K = 0.39 at leading edge pivot.

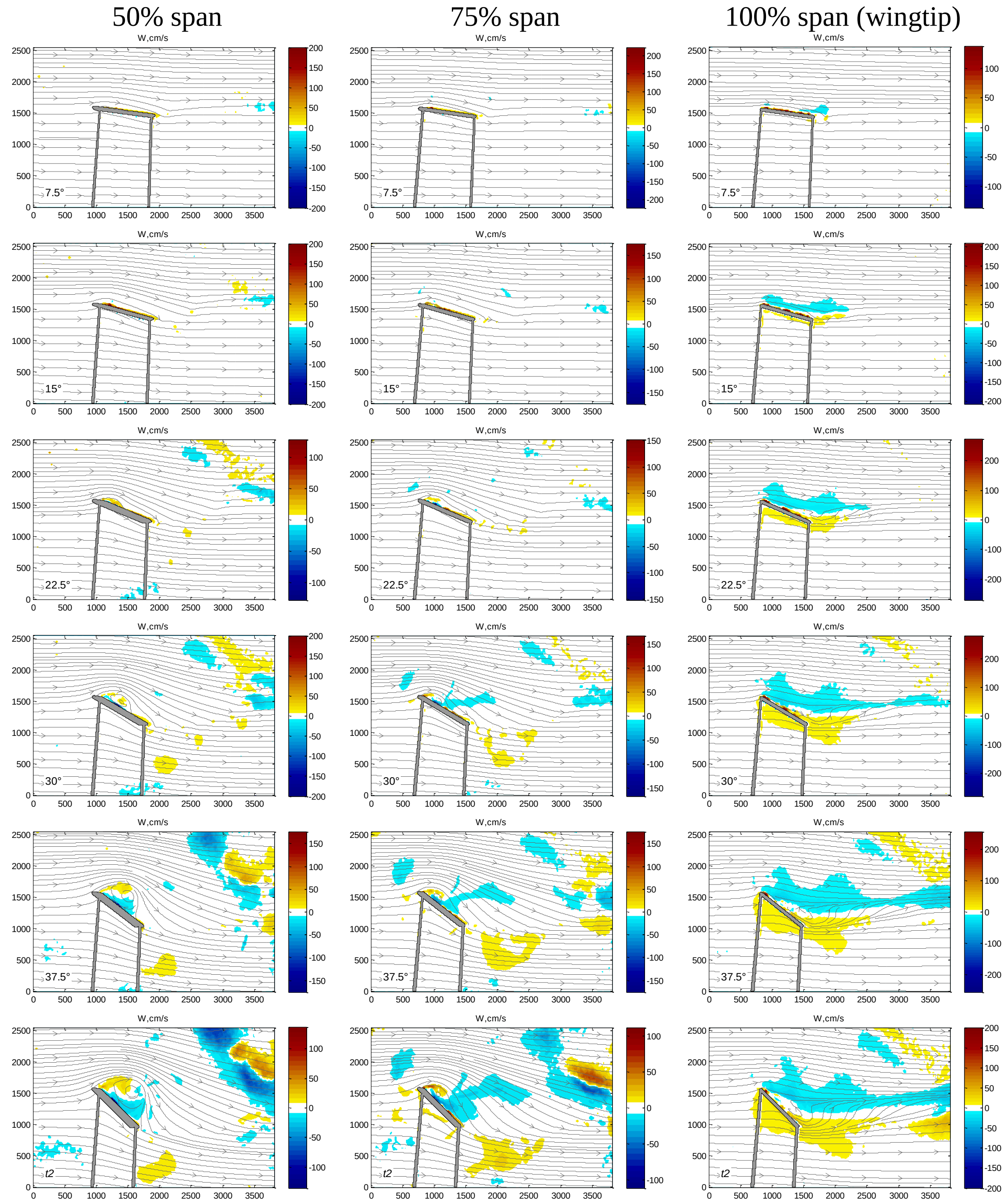

Figure 6.10 PIV instantaneous out-of-plane velocity field and streamline for $K = 0.13$ at leading edge pivot.

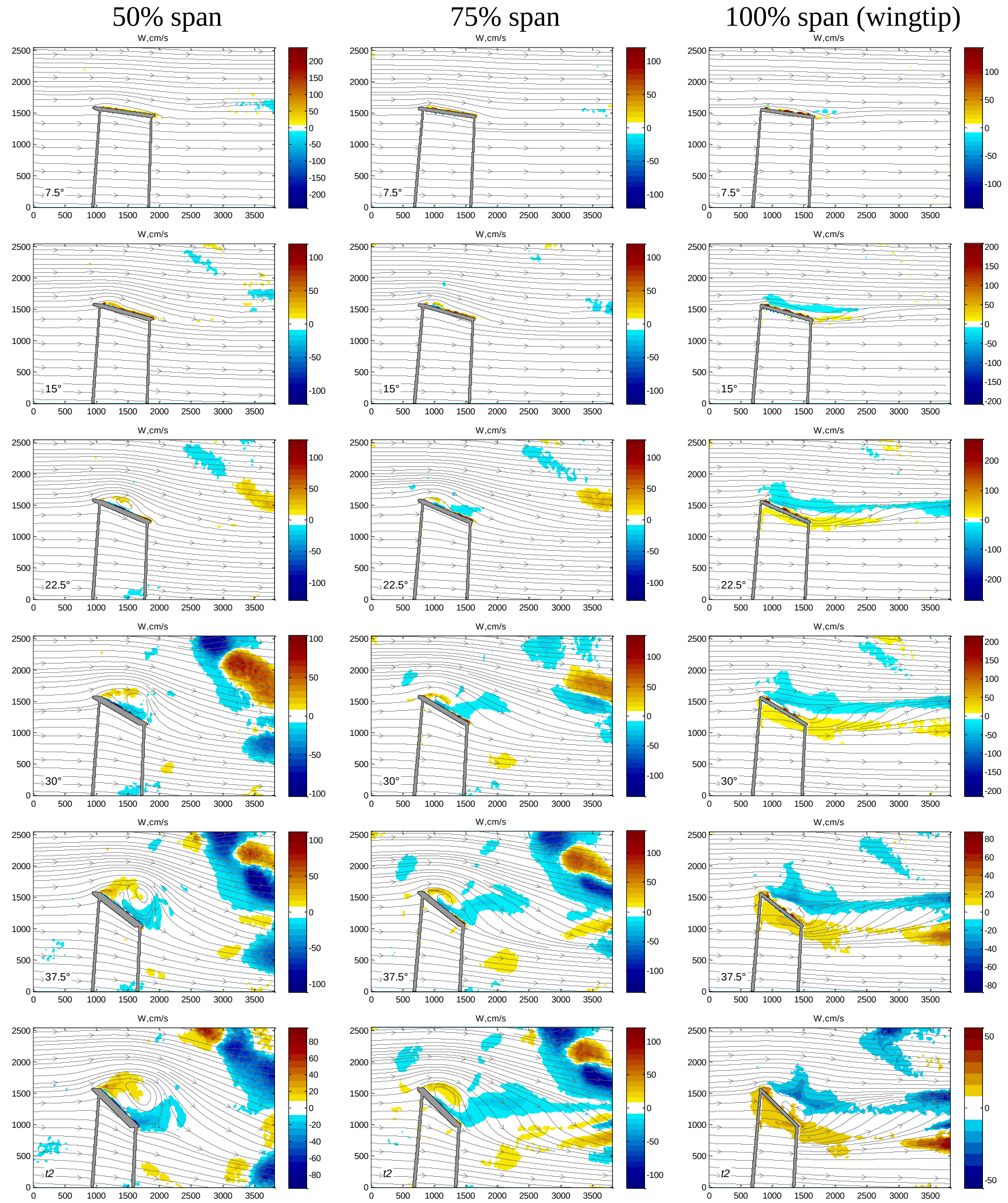

Figure 6.11 PIV instantaneous out-of-plane velocity field and streamline for *K* = 0.065 at leading edge pivot.

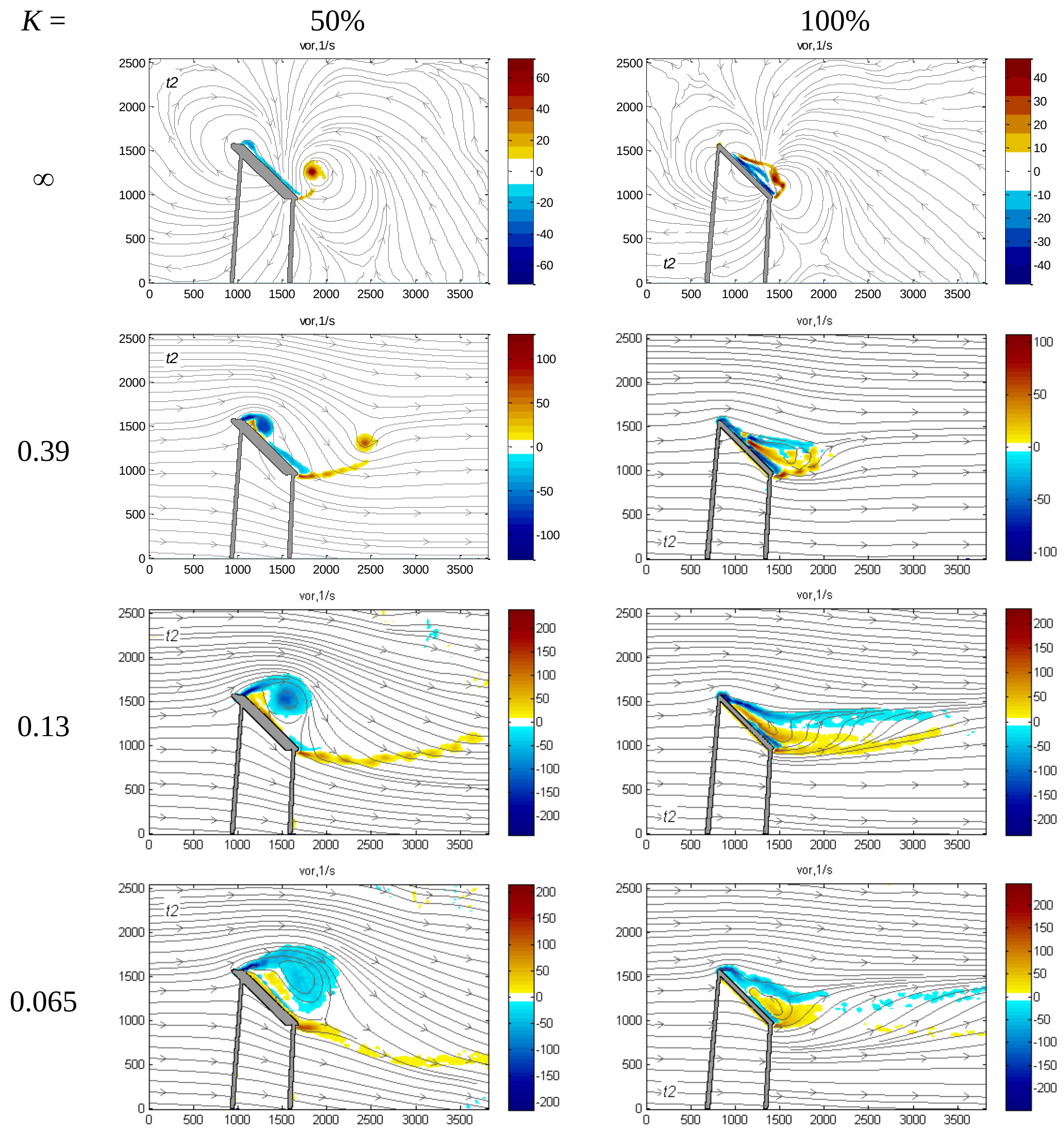

Figure 6.12 Effect of reduced pitch rate for a given phase from PIV instantaneous data.

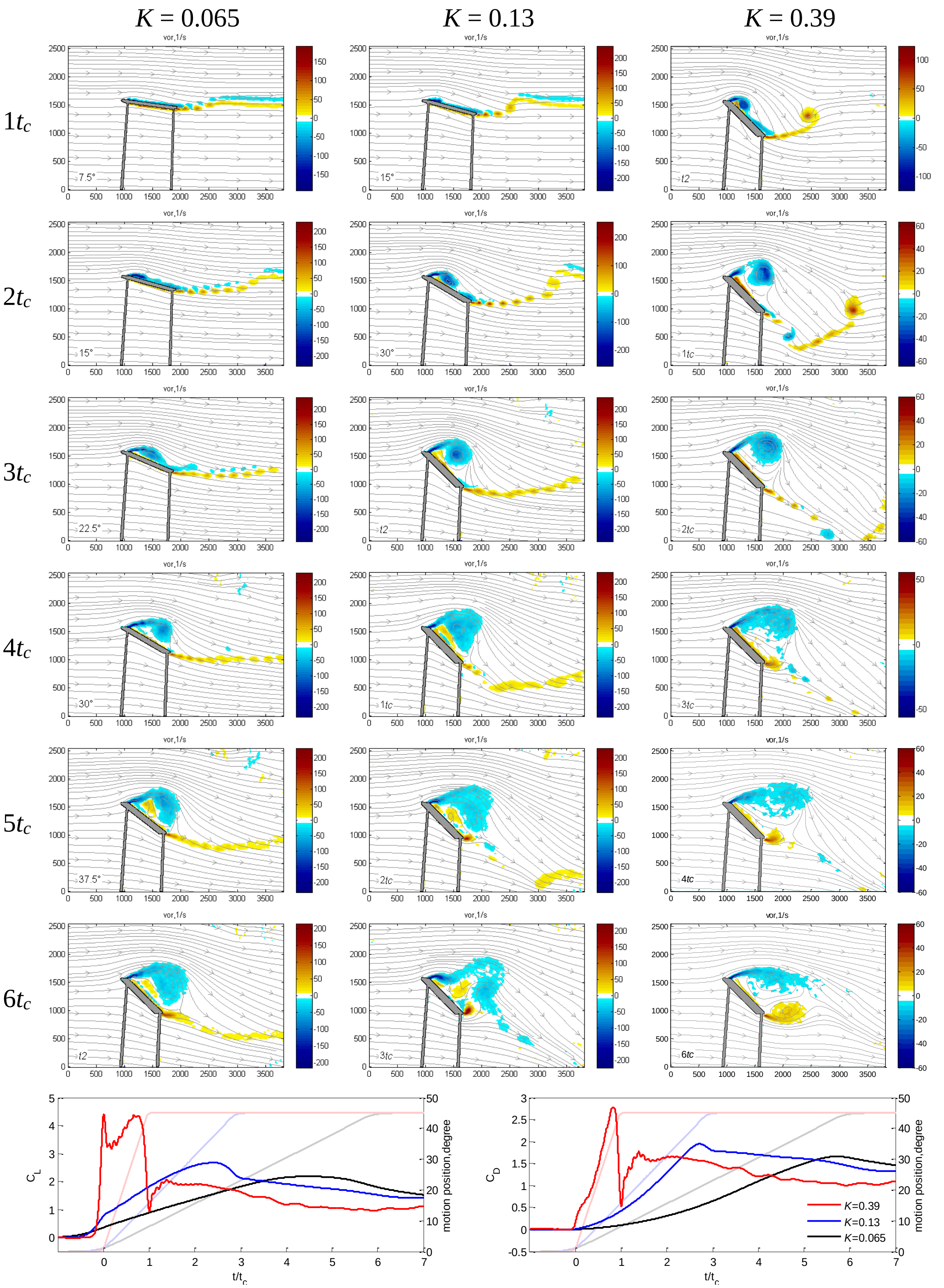

Figure 6.13 PIV instantaneous vorticity field and streamline at leading edge pivot. t_c *is convective time* c/U_∞.

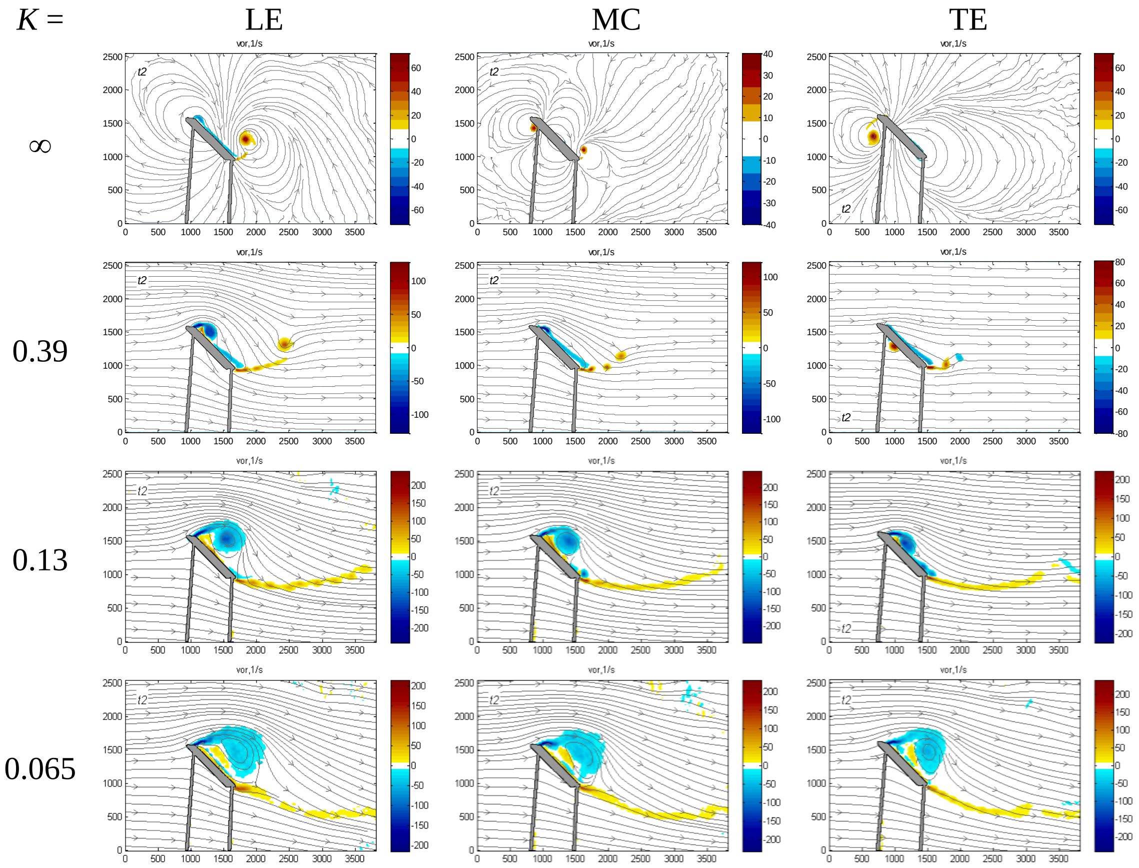

Figure 6.14 Effect of pivot axis location for a given phase from PIV instantaneous data.

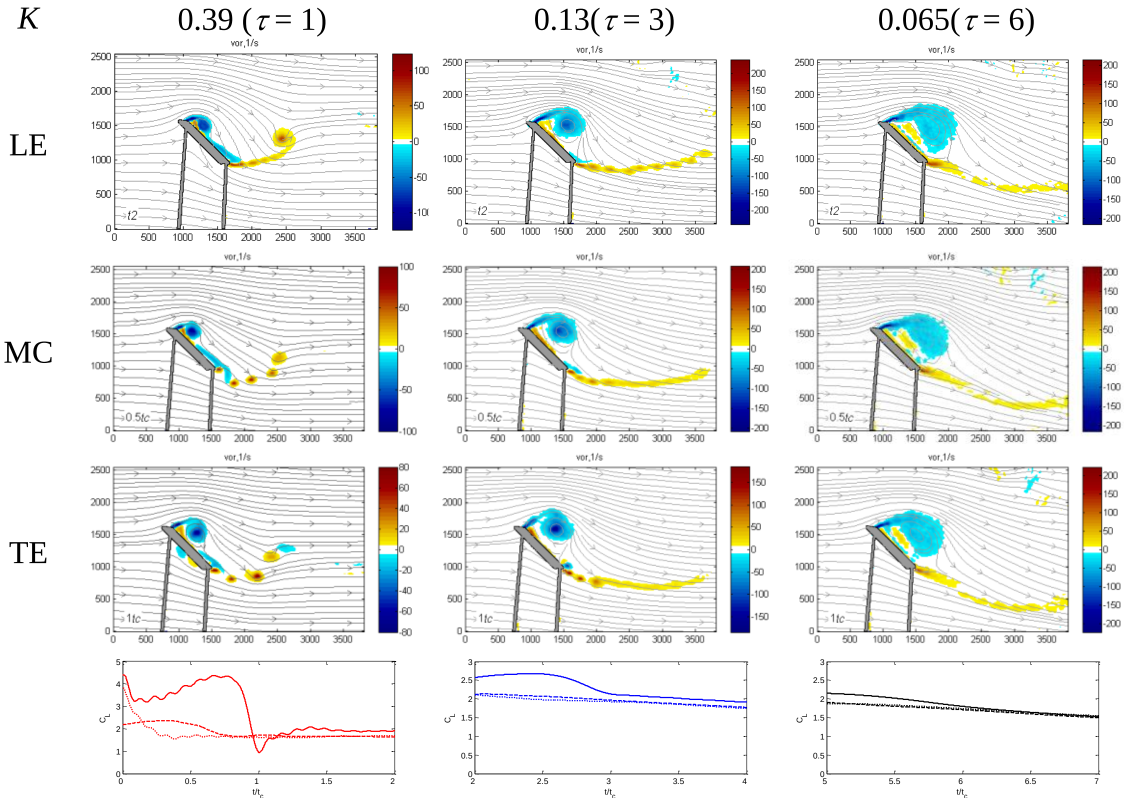

Figure 6.15 Similarity of vortical flow and lift coefficient for pivot-axis location effect. *LE is for leading-edge pivot axis; MC is for mid-chord pivot axis; TE is for trailing-edge pivot axis. The baseline images are at a phase* t_2 *for LE; the images for MC are at a delayed phase* $t_2+0.5t_c$*; the images for TE are at a delayed phase* t_2+1t_c*.* t_c *is convective time* c/U_∞*.*

CHAPTER 7

CONCLUSIONS AND RECOMMENDATIONS

Flow visualization, unsteady aerodynamic force, and PIV flow measurements are reported for pitching flat-plate wings with constant pitch rates to a maximum angle of attack of 45 degrees. The wings had an aspect ratio equal to 4; three wing geometries were considered: rectangular, trapezoidal, and triangular wings. Changing either wing pitch rate or free stream flow results in a change of reduced pitch rate within an interval of $0.022 \leq K \leq 0.39$ in a parameter space of Stokes number (*St*) and Reynolds number (*Re*). Also the case of $Re = 0$ (i.e., $K = \infty$) and $K = 0$ in $Re = 8.9$k are documented to gain additional insight on the nature of non-circulatory effect and unsteady effect.

7.1 CONCLUSIONS

In this study, the maneuvering kinematics was presented and the results suggest the leading-edge pivot axis gives great benefit to aircrafts, such as fixed-wing system or flapping-wing system. However, the wing geometry does not show significant impact on force generation. The conclusions of the study are summarized as follows.

From flow visualization data,

1. The flow is substantially two-dimensional at early stage of rotation and high reduced pitch rate.
2. The starting vortex is more pronounced at high reduced pitch rate, associated with rapid increase of force generation. High taper-ratio wing produces starting vortex on the plane of sideview, low taper-ratio wing produces starting vortex on the plane of topview.

3. For leading-edge pivot, a typical starting vortex forms in the wake near the trailing edge at pitch angle 11° with counterclockwise rotation. The formation of leading-edge vortex is independent of taper ratio.
4. For trailing-edge pivot axis, a reverse starting vortex forms in the wake near the trailing edge at pitch angle 21° with clockwise rotation. A starting vortex forms at leading edge on the windward surface as documented by PIV measurements in Yu and Bernal (2013).
5. The evolution of the starting vortex at the trailing edge differs depending on taper ratio.
6. The flow visualization data suggest trailing-edge vortex is linked to the tip vortex for the rectangular wing. For other wing planforms the development of streamwise swirling is more pronounced.
7. Flow visualization data also suggests three-dimensional flow is enhanced by triangular wing.

From steady force measurements ($K = 0$),

1. For taper ratio higher than 0.5, the lift coefficient follows the lifting-line theory up to 9°. Lower taper ratio yields lower lift coefficient at a given angle of attack.
2. For trailing-edge pivot, taper ratio higher than 0.5 gives stall angle higher than 15°.
3. Drag coefficients are independent of leading-edge-sweep angle and taper ratio, and increase linearly with angle of attack, which are inconsistent with theoretical prediction.
4. Pitching-moment coefficient about pivot axis is negative for leading-edge pivot, and positive for mid-chord and trailing-edge pivot. Effects of taper ratio are small at low angle of attack.

From unsteady force measurements ($K > 0$),

1. Effects of reduced pitch rate and pivot axis location for rectangular wing

1) In all cases the force coefficients increase during the pitch-up portion of the motion and decrease until they reach the steady-state condition.

2) Force oscillations are observed during the transient in the hold phase, consistent with incipient vortex shedding; but oscillatory behaviors disappear after approximately 30 convective times before the steady state condition is reached.

3) Non-circulatory apparent mass effects are found for reduced pitch rate greater than 0.066 and for leading-edge and trailing-edge pivot axes. These effects are confined within the non-zero acceleration region at the start and the end of the wing rotation, where the formation of starting vortex is associated.

4) Non-circulatory apparent mass effects are small at lower reduced pitch rate K = 0.065 and for mid-chord pivot axis.

5) Rotation rate effects are observed in the constant rotation-rate region for reduced pitch rate $K > 0.022$.

6) For leading-edge pivot, both non-circulatory effect and rotation-rate effect incorporate to produce very large force coefficients, well above estimates based on the lifting line theory.

7) For trailing-edge pivot, non-circulatory effect and rotation-rate effect oppose each other resulting in lower force coefficients below the lifting-line theoretical estimates.

8) For reduced pitch rate below $K = 0.022$ the flow is quasi-steady and the lifting line theoretical results provide good estimates of the lift coefficients for angles of attack below the steady stall angle, approximately 20 degrees.

9) For reduced pitch rate below $K = 0.022$, the drag coefficient based on the lifting line theory for induced drag are a factor of 2 below measured results. This is attributed to the failure of accounting for the low leading edge suction force on the thin rectangular flat plate.

2. Effects of wing geometry and pivot axis location at $K = 0.065$

   1) Triangular wing produce slightly larger non-circulatory inertial effect at the beginning of the rotation.
   2) Rectangular and trapezoid wings give very similar force curves at low angle of attack during constant rotation-rate region, which is higher than triangular wing. This wing geometry effect is similar to the steady flow results.
3. Effects of wing geometry and pivot axis location at $K = 0.39$
   1) Potential flow theory including rotation rate effect is in reasonable agreement with measurement results.
   2) Triangular wing produce larger forces compared to other wing geometries.
   3) This wing geometry effect for $K = 0.39$ is different from that for steady flow and $K = 0.065$.

From the PIV images,

1. PIV data show formation of LEV and TEV vortices at the end of the rotation, but the rate of development depends on pivot axis location and reduced pitch rate.
2. PIV measurements also show important differences in flow topology for different pivot axis due to the formation of starting vortex. For leading edge pivot axis the starting vortex is formed at the trailing edge. For mid-chord pivot axis starting vortices are formed at the leading edge and the trailing edge. For trailing edge pivot axis the starting vortex forms at the leading edge.
3. Formation of a starting vortex at the leading edge delays the development of the LEV.
4. Significant spanwise variation of the LEV size is found for low reduced pitch rate.

7.2 FUTURE WORK

Many researchers have shown a significant leading-edge vortex over semi-elliptical wing or Zimmerman wing; this leading-edge vortex covered the entire wing leading-edge axis toward the wingtip while higher degree-of-freedom wing motion was in use. Most of them considered the leading-edge vortex is important for high lift generation. The PIV data presented in this study showed the leading-edge vortex is diminishing toward the wingtip where wingtip vortex or wingtip circulation forms; the rapid increase of lift is associated with both reduced pitch rate and starting vortex. In addition, contrary to the shedding of leading-edge vortex and trailing-edge vortex in the literature, the present data showed the leading-edge vortex is not shed but dissipates during the rotation. At earlier time of holding at 45-degree angle of attack, there is trailing-edge vortex developing. The discrepancies suggest the future work as follows:

1. To implement higher degree-of-freedom wing kinematics to obtain the insight of vortical structure formation and its correlation with aerodynamics.
2. To obtain better understanding of vortex dynamics by implementing vortex detection algorithms Γ_1 and Γ_2 (Graftieaux et al., 2001).
3. To improve uncertainty of the lens-shifted stereoscopic PIV system by increasing laser sheet thickness and time between camera exposures

APPENDIX A

MATLAB PROGRAM FOR MOTION COMMAND

Input Parameter.m

```
%   The file is to generate motion command to control VMX Rotary Table
%
%   Code: Huai-Te Yu
%   Date: 04/10/2011
%   Version: 1
%   Version history:
%       v1: using smoothing equation in a form of convective time

clear
clc
%% part1: input parameters
a = 11; % free parameter
U = 34.346; % prescribed freesream velocity for motion generation,
[cm/s]
k = 0.2; % reduced frequency
s = 1; % start parameter, number of convective time in design
h = 1; % hold parameter, number of convective time in design
e = 1; % relaxation parameter, number of convective time in design
deg = 45; % maximum angle of attack, [degree]
stepdeg = 20; % rotary stepper resolution, [steps/degree]
chord = 2; % wing chord length, [inch]
rho = 998; % water density [kg/m^3]
nu = 0.001; % water dynamic viscosity, [kg/m.s]

L = 20; % # of kinematics repeated
Fs = 10000; % sample rate in design

% evaluate parmeters
Re = U*0.01*chord*2.54*0.01*rho/nu; % Reynolds number in design
tp = (deg*pi/180)*chord*2.54/(2*U*k); % pitch time in design
tc = chord*2.54/U; % convective time in design
A = a/(2*k);
B = a*(deg*pi/180)/(2*k);

% assign part of filename using input parameters
[yyyy mm dd] = datevec(date);
dateK = sprintf('%04d%02d%02d',yyyy,mm,dd);
temp1 =
sprintf('C%02dk%02dh%02ddeg%02dsd%02d',chord,round(k*10),h,deg,stepdeg);
temp2 = sprintf('Re%02dk',round(Re/1000));
tempname = strcat(temp1,'K',dateK,temp2);
```

```
%% Part2: discrete smoothing function
[MotionInFunction,tiInFunction] =
getSmoothingFunctionV1(k,deg,a,s,h,e,stepdeg,Fs,tp,tc,tempname);

% Note:
% 1) MotionInFunction contains time, position, speed, acceleration in
[degree]
% 2) plots are shown in [deg]
% 3) text filename ended with "MotionInSmoothingFunction"

%% Part3: get smoothing regions
[MotionInSmoothing,gamma,DivisorInAngleAttack,DivisorInTiming,beta] =
getSmoothingRegionV4(MotionInFunction,Fs,k,a,h,stepdeg,tc,tiInFunction,
tempname,B);

% Note:
% 1) MotionInSmoothing contains time, alpha, d_alpha, dd_alpha in [step]
% 2) plots are shown in [deg]
% 3) text filename ended with "MotionInSmoothingPoints"

%% Part4: generate VMX motion commands and verification
[MotionInCommand,MotionInDesignFunction,MotionInDesignSmoothing,tsInCom
mand,tsInDesign,tiInDesignFunction] =
getVelmexV3(MotionInFunction,MotionInSmoothing,stepdeg,k,a,h,L,deg,tiIn
Function,tc,tempname,Fs);
% Note:
% 1) outputs are in steps
% 2) the holding time in commands and smoothing function is calibrated
with
%    pause resolution in VMX controller, the comparison can be made by
%    inspecting outputs
% 3) plots are shown in [deg]
% 4) The Velmex command has filename ended with VMXCommand

%% Part5: save important parameters
% save important parameters for kinematic reconstruction
filename = strcat(tempname,'MotionInformation.mat');
save(filename,'U','k','chord','Fs','a','A','B','gamma','beta','DivisorI
nAngleAttack','DivisorInTiming','stepdeg','deg',...
    'tiInFunction','tiInDesignFunction','tsInCommand','tsInDesign',...

'MotionInFunction','MotionInSmoothing','MotionInDesignFunction','Motion
InDesignSmoothing','MotionInCommand');
```

getSmoothingFunctionV1.m

```
function [MotionInFunction,tiInFunction] =
getSmoothingFunctionV1(k,deg,a,s,h,e,stepdeg,Fs,tp,tc,tempname)
%   This is smoothing function defined by Eldredge, used to miminize
the vibration
%   induced by rotating airfoil. The data is also written with a name
%   k_h_a_1.txt.
%   Schematics of pitchup-hold-pitchdown motion and notions of time
%   definition
%   |   |    |.......|    |      |
%   |   |   .|       | .  |      |
%   |   |  . |       |  . |      |
%   |   | .  |       |   .|      |
%   |---|----|-------|----|------|---
%   |dTs| dTp|  dTh  | dTp|  dTe |
%       t1   t2      t3   t4     t5
%
%   Input:
%       k       = reduced frequency
%       chord   = chord length
%       deg     = maximum angle of attack
%       a       = free paramenter
%       s       = start parameter
%       h       = hold parameter
%       e       = relaxation parameter
%       stepdeg = rotary stepper resolution, [steps/deg]
%       Re      = Reynolds number in design
%       tp      = pitch time in design
%       tc      = convective time in design
%   Output:
%       tiInFunction.t1      = time that wings start to pitch-up in an
unsmoothing trace
%       tiInFunction.t2      = time that wings start to hold in an
unsmoothing trace
%       tiInFunction.t3      = time that wings start to pitch-down in
an unsmoothing trace
%       tiInFunction.t4      = time that wings stop at the origin in an
unsmoothing trace
%       tiInFunction.t5      = time that the motion is complete
%       MotionInFunction     = contains time, alpha, d_alpah, dd_alpha
%           (The data is also written with a name k_h_a_1.txt.)
%       alpha_maxd = maximum alpah obtained, used to make sure maximum
%                    alpha is achieved
%   Code: Huai-Te Yu
%   Date: 04/10/2011
%   Version: 1
%   Version history:
%       v1: using smoothing equation in a form of convective time

dTp = tp; % pitch ramp duration
dTs = s*tc; % start duration
dTh = h*tc; % hold duration
dTe = e*tc; % relaxation duration

tiInFunction.t1 = dTs; % time from reference 0 to the unsmoothed ramp
starts
```

```
tiInFunction.t2 = tiInFunction.t1+dTp; % tiInFunction.t1 + duration of
the pitch upstoke to position of hold
tiInFunction.t3 = tiInFunction.t2+dTh; % tiInFunction.t2 + unsmoothed
hold time
tiInFunction.t4 = tiInFunction.t3+dTp; % tiInFunction.t3 + unsmoothed
pitchdownstroke duration
tiInFunction.t5 = tiInFunction.t4+dTe; % tiInFunction.t4 + duration of
ending
MotionInFunction.t = 0:1/Fs:tiInFunction.t5; % duration of a cycle
MotionInFunction.t(end+1) = tiInFunction.t5;

[MotionInFunction.position, MotionInFunction.speed,
MotionInFunction.acceleration] =
SmoothingFunctionV1(k,a,MotionInFunction.t,tc,tiInFunction.t1,tiInFunct
ion.t2,tiInFunction.t3,tiInFunction.t4);

display('*************************************************************
***');
display(['maximum incidence in smoothing function: '
num2str(max(MotionInFunction.position),7) ' deg']);
if max(MotionInFunction.position) < deg
    display('!!! NEED TO BE ROUNDED OFF AND CONVERT TO STEPS!!!');
elseif max(MotionInFunction.position) > deg
    display('WRONG!!! CHECK smoothing function inputs!!!');
    return
end

%% plot
figure;
ax1fig1 = subplot(3,1,1); % angular position time history
y1max = ceil(max(MotionInFunction.position)/10)*10+5;
y1min = -(ceil(abs(min(MotionInFunction.position))/10)*10+5);
dy1 = round((y1max - y1min)/6/10)*10;
h1(1) =
line(MotionInFunction.t,MotionInFunction.position,'color','k','LineWidt
h',1); axis tight
sub_pos1 = get(ax1fig1,'position');
set(ax1fig1,'position',sub_pos1.*[1 0.9 1 1.1]) % stretch its width and
height
set(ax1fig1,'xcolor','k','ycolor','k');
set(ax1fig1,'Xlim',[0
tiInFunction.t5],'XTick',0:1:tiInFunction.t5,'XTickLabel',[],...
    'Ylim',[y1min y1max],'YTick',y1min:dy1:y1max);
% xlabel('$t [sec]$','Interpreter','Latex','FontSize',12);
ylabel('$\alpha [deg]$ ','Interpreter','Latex','FontSize',12);
% plot position versus convective time
ax2fig1 = axes('Position',get(ax1fig1,'Position'),...
           'XAxisLocation','top',...
           'YAxisLocation','right',...
           'Color','none',...
           'XColor','k','YColor','k');
h1(2) =
line(MotionInFunction.t,MotionInFunction.position,'color',[0,0,0],...
    'LineStyle','-','parent',ax2fig1); axis tight
sub_pos1 = get(ax2fig1,'position');
```

```
set(ax2fig1,'position',sub_pos1.*[1 1 1 1]) % stretch its width and
height
xlabel('t_c');
set(ax2fig1,'Xlim',[0
tiInFunction.t5],'XTick',tiInFunction.t1:tc:tiInFunction.t5,'XTickLabel
',0:1:tiInFunction.t5/tc,...
    'Ylim',[y1min y1max],'YTick',y1min:dy1:y1max,...
    'Ycolor','k');
linkaxes([ax1fig1 ax2fig1],'xy');

ax1fig2 = subplot(3,1,2); % angular velocity time history
y2max = ceil(max(MotionInFunction.speed)/10)*10+5;
y2min = -(ceil(abs(min(MotionInFunction.speed))/10)*10+5);
dy2 = round((y2max - y2min)/6);
h2(1) =
line(MotionInFunction.t,MotionInFunction.speed,'color','k','LineWidth',
1); axis tight
sub_pos2 = get(ax1fig2,'position');
set(ax1fig2,'position',sub_pos2.*[1 0.9 1 1.1]) % stretch its width and
height
set(ax1fig2,'xcolor','k','ycolor','k');
% set(ax1fig2,'xtick',[]); % turn off xlabel (t [sec])
set(ax1fig2,'Xlim',[0
tiInFunction.t5],'XTick',0:1:tiInFunction.t5,'XTickLabel',[],...
    'Ylim',[y2min y2max],'YTick',y2min:dy2:y2max);
% xlabel('$t [sec]$','Interpreter','Latex','FontSize',12);
ylabel('$\dot \alpha [\frac{deg}{s}]
$','Interpreter','Latex','FontSize',12);
ax2fig2 = axes('Position',get(ax1fig2,'Position'),...
           'XAxisLocation','top',...
           'YAxisLocation','right',...
           'Color','none',...
           'XColor','k','YColor','k');
h2(2) =
line(MotionInFunction.t,MotionInFunction.speed,'color',[0,0,0],...
    'LineStyle','-','parent',ax2fig2); axis tight
sub_pos2 = get(ax2fig2,'position');
set(ax2fig2,'position',sub_pos2.*[1 1 1 1]) % stretch its width and
height
set(ax2fig2,'Xlim',[0
tiInFunction.t5],'XTick',tiInFunction.t1:tc:tiInFunction.t5,'XTickLabel
',[],...
    'Ylim',[y2min y2max],'YTick',y2min:dy2:y2max,...
    'Ycolor','k');
linkaxes([ax1fig2 ax2fig2],'xy');

ax1fig3 = subplot(3,1,3); % angular acceleration time history
y3max = ceil(max(MotionInFunction.acceleration)/10)*10+5;
y3min = -(ceil(abs(min(MotionInFunction.acceleration))/10)*10+5);
dy3 = round((y3max - y3min)/6);
h3(1) =
line(MotionInFunction.t,MotionInFunction.acceleration,'color','k','Line
Width',1); axis tight
sub_pos3 = get(ax1fig3,'position');
set(ax1fig3,'position',sub_pos3.*[1 0.9 1 1.1]) % stretch its width and
height
```

```
set(ax1fig3,'xcolor','k','ycolor','k');
set(ax1fig3,'Xlim',[0
tiInFunction.t5],'XTick',0:1:tiInFunction.t5,'XTickLabel',0:1:tiInFunct
ion.t5,...
    'Ylim',[y3min y3max],'YTick',y3min:dy3:y3max);
xlabel('$t [sec]$','Interpreter','Latex','FontSize',12);
ylabel('$\ddot \alpha
[\frac{deg}{s^2}]$','Interpreter','Latex','FontSize',12);
% plot position versus convective time
ax2fig3 = axes('Position',get(ax1fig3,'Position'),...
           'XAxisLocation','top',...
           'YAxisLocation','right',...
           'Color','none',...
           'XColor','k','YColor','k');
h3(2) =
line(MotionInFunction.t,MotionInFunction.acceleration,'color',[0,0,0],.
..
    'LineStyle','-','parent',ax2fig3); axis tight
sub_pos3 = get(ax2fig3,'position');
set(ax2fig3,'position',sub_pos3.*[1 1 1 1]) % stretch its width and
height
set(ax2fig3,'Xlim',[0
tiInFunction.t5],'XTick',tiInFunction.t1:tc:tiInFunction.t5,'XTickLabel
',[],...
    'Ylim',[y3min y3max],'YTick',y3min:dy3:y3max,...
    'Ycolor','k');
linkaxes([ax1fig3 ax2fig3],'xy');

%% write to file
filename = strcat(tempname,'MotionInFunction.txt');
fid = fopen(filename,'wt');
fprintf(fid,'This data is generated from smoothing function for
interpolation in next step\n');
fprintf(fid,'Stepping motor %g [step/deg], k=%g, h=%g,
a=%g\n',stepdeg,k,h,a);
fprintf(fid,' t[s]   alpha[deg] d_alpha[deg/s] dd_alpha[deg/s^2]\n');
fprintf(fid,'%-8.5f %10.5f %10.5f
%12.5f\n',[MotionInFunction.t;MotionInFunction.position;MotionInFunctio
n.speed;MotionInFunction.acceleration]);
fclose(fid);
```

getSmoothingRegionV4.m

```
function
[MotionInSmoothing,gamma,DivisorInAngleAttack,DivisorInTiming,beta] =
getSmoothingRegionV4(MotionInFunction,Fs,k,a,h,stepdeg,tc,tiInFunction,
tempname,B)
%
%   This file gives the points of interest for VMX controller
%
%   Input:
%       DivisorInAngleAttack       = # of points during smoothing
regions
%       MotionInFunction    = MotionInFunction, containing time,
position, speed, acceleration
%       k       = reduced frequency
%       a       = free paramenter
%       stepdeg = rotary stepper resolution, [steps/deg]
%       tc      = convective time in design
%
tiInFunction.t1,tiInFunction.t2,tiInFunction.t3,tiInFunction.t4,tiInFun
ction.t5 = timepoints at corners
%       Fs = sample rate
%   Output:
%       data1   = containing points of interest, [step]
%
%   Code: Huai-Te Yu
%   Data: 2013/03/12
%   Version: 1
%   Version history:
%       v1: using filter concept
%       v2: defining gamma
%       v3: include more timing points at beginning and end of rotation

%% define acceleration regions
prompt = {'Enter the ratio of acceleration change to maximum
acceleration',...
    '# of divident in angle of attack in the acceleration regions',...
    '# of divident in timing at the beginnning/end of pitching'};
dlgtitle = 'DEFINE ACCELERATION REGIONS';
numlines = 1;
if exist('gamma','var') && exist('DivisorInAngleAttack','var')
    defaultanswer = {num2str(gamma),num2str(DivisorInAngleAttack)};
else
    defaultanswer = {'0.01','11','6'};
end
answer = inputdlg(prompt,dlgtitle,numlines,defaultanswer,'on');
if isempty(answer)
    return,
end
gamma = sscanf(char(answer(1)),'%f');
DivisorInAngleAttack = sscanf(char(answer(2)),'%f');
DivisorInTiming = sscanf(char(answer(3)),'%f');

beta = acosh(sqrt(1/gamma))/B;

%% find accelertion regions and corresponding position, speed, and
% acceleration
```

```
Dt = tc*acosh(sqrt(1/gamma))/a; % the corresponding time change during
smoothing regions

%% evaluate smoothing regions
ts11 = tiInFunction.t1-Dt;
ts12 = tiInFunction.t1+Dt;
ts21 = tiInFunction.t2-Dt;
ts22 = tiInFunction.t2+Dt;
ts31 = tiInFunction.t3-Dt;
ts32 = tiInFunction.t3+Dt;
ts41 = tiInFunction.t4-Dt;
ts42 = tiInFunction.t4+Dt;
[tspositionInDegree,tsspeedInDegree,tsaccelerationInDegree] =
SmoothingFunctionV1(k,a,[ts11,ts12,ts21,ts22,ts31,ts32,ts41,ts42],tc,ti
InFunction.t1,tiInFunction.t2,tiInFunction.t3,tiInFunction.t4);
% make sure maximum angle is 45 degrees and the angle changes are the
same
% for each smoothing regions
tspositionInDegreeRound = roundn(tspositionInDegree,-2); % in radian
display('***---------------------------------------------***');
fprintf('Incidences during smoothing regions, [deg]:\n')
display(num2str(tspositionInDegreeRound));
fprintf('The corresponding timepoints, [s]:\n')
display(num2str([ts11 ts12 ts21 ts22 ts31 ts32 ts41 ts42]));

%% convert degrees to steps
tspositionInStep = tspositionInDegreeRound*stepdeg; % in step
tspositionInStepRound = round(tspositionInStep); % in step
% convert steps back to degrees
tspositionInDegreeRoundNew = tspositionInStepRound/stepdeg;
% find new timing for rounded angle of attack
ts11New = ts11;

[Positiont1t2NewTemp,indext1t2] =
sort(MotionInFunction.position(1:floor((tiInFunction.t2+tiInFunction.t3
)*Fs/2)));
Timet1t2Temp = MotionInFunction.t(indext1t2);
uniq1 = [true, diff(Positiont1t2NewTemp) ~= 0];
ts12New =
interp1(Positiont1t2NewTemp(uniq1),Timet1t2Temp(uniq1),tspositionInDegr
eeRoundNew(2));
ts21New =
interp1(Positiont1t2NewTemp(uniq1),Timet1t2Temp(uniq1),tspositionInDegr
eeRoundNew(3));

ts22New = ts22;
ts31New = ts31;

[Positiont3t4NewTemp,indext3t4] =
sort(MotionInFunction.position(floor((tiInFunction.t2+tiInFunction.t3)*
Fs/2)+1:end));
Timet3t4Temp =
MotionInFunction.t(floor((tiInFunction.t2+tiInFunction.t3)*Fs/2)+1:end);
Timet3t4Temp1 = Timet3t4Temp(indext3t4);
uniq2 = [true, diff(Positiont3t4NewTemp) ~= 0];
```

```
ts32New =
interp1(Positiont3t4NewTemp(uniq2),Timet3t4Temp1(uniq2),tspositionInDeg
reeRoundNew(6));
ts41New =
interp1(Positiont3t4NewTemp(uniq2),Timet3t4Temp1(uniq2),tspositionInDeg
reeRoundNew(7));
ts42New = ts42;
fprintf('New incidences during smoothing regions, [deg]:\n')
display(num2str(tspositionInDegreeRoundNew));
fprintf('The corresponding new timepoints, [s]:\n')
display(num2str([ts11New ts12New ts21New ts22New ts31New ts32New
ts41New ts42New]));

%% define incremental incidence during acceleration phase
% region 1: ts1-ts2 (acceleration)
ts1ts2positionInDegree =
linspace(tspositionInDegreeRoundNew(1),tspositionInDegreeRoundNew(2),Di
visorInAngleAttack);
ts1ts2positionInStep = ts1ts2positionInDegree*stepdeg;
ts1ts2positionInStepRound = round(ts1ts2positionInStep);
% difts1ts2positionInstepRound = diff(ts1ts2positionInstepRound);
ts1ts2time =
interp1(Positiont1t2NewTemp(uniq1),Timet1t2Temp(uniq1),ts1ts2positionIn
Degree);
ts1ts2time(1) = ts11New; % Due to NAN evaluated using interp1

% region 2: ts3-ts4 (decceleration)
ts3ts4positionInDegree =
linspace(tspositionInDegreeRoundNew(3),tspositionInDegreeRoundNew(4),Di
visorInAngleAttack);
ts3ts4positionInStep = ts3ts4positionInDegree*stepdeg;
ts3ts4positionInStepRound = round(ts3ts4positionInStep);
% difts3ts4positionInstepRound = diff(ts3ts4positionInstepRound);
ts3ts4time =
interp1(Positiont1t2NewTemp(uniq1),Timet1t2Temp(uniq1),ts3ts4positionIn
Degree);
ts3ts4time(end) = ts22New; % Due to NAN evaluated using interp1

% region 3: ts5-ts6 (decceleration)
ts5ts6positionInDegree =
linspace(tspositionInDegreeRoundNew(5),tspositionInDegreeRoundNew(6),Di
visorInAngleAttack);
ts5ts6positionInStep = ts5ts6positionInDegree*stepdeg;
ts5ts6positionInStepRound = round(ts5ts6positionInStep);
% difts5ts6positionInstepRound = diff(ts5ts6positionInstepRound);
ts5ts6time =
interp1(Positiont3t4NewTemp(uniq2),Timet3t4Temp1(uniq2),ts5ts6positionI
nDegree);
ts5ts6time(1) = ts31New; % Due to NAN evaluated using interp1

% region 4: ts7-ts8 (acceleration)
ts7ts8positionInDegree =
linspace(tspositionInDegreeRoundNew(7),tspositionInDegreeRoundNew(8),Di
visorInAngleAttack);
ts7ts8positionInStep = ts7ts8positionInDegree*stepdeg;
ts7ts8positionInStepRound = round(ts7ts8positionInStep);
```

```
% difts7ts8positionInstepRound = diff(ts7ts8positionInstepRound);
ts7ts8time =
interp1(Positiont3t4NewTemp(uniq2),Timet3t4Temp1(uniq2),ts7ts8positionI
nDegree);
ts7ts8time(end) = ts42New;

%% refine segments at the beginning and the end of rotation
% pitch-up phase
ts1ts2Addtime = linspace(ts1ts2time(1),ts1ts2time(2),DivisorInTiming);
[ts1ts2AddpositionInDegree,ts1ts2AddspeedInDegree,ts1ts2Addacceleration
InDegree] =
SmoothingFunctionV1(k,a,ts1ts2Addtime,tc,tiInFunction.t1,tiInFunction.t
2,tiInFunction.t3,tiInFunction.t4);
ts1ts2AddpositionInStep = ts1ts2AddpositionInDegree*stepdeg;
ts1ts2AddpositionInStepRound = round(ts1ts2AddpositionInStep);

ts3ts4Addtime = linspace(ts3ts4time(end-
1),ts3ts4time(end),DivisorInTiming);
[ts3ts4AddpositionInDegree,ts3ts4AddspeedInDegree,ts3ts4Addacceleration
InDegree] =
SmoothingFunctionV1(k,a,ts3ts4Addtime,tc,tiInFunction.t1,tiInFunction.t
2,tiInFunction.t3,tiInFunction.t4);
ts3ts4AddpositionInStep = ts3ts4AddpositionInDegree*stepdeg;
ts3ts4AddpositionInStepRound = round(ts3ts4AddpositionInStep);

% pitch-return phase
ts5ts6Addtime = linspace(ts5ts6time(1),ts5ts6time(2),DivisorInTiming);
[ts5ts6AddpositionInDegree,ts5ts6AddspeedInDegree,ts5ts6Addacceleration
InDegree] =
SmoothingFunctionV1(k,a,ts5ts6Addtime,tc,tiInFunction.t1,tiInFunction.t
2,tiInFunction.t3,tiInFunction.t4);
ts5ts6AddpositionInStep = ts5ts6AddpositionInDegree*stepdeg;
ts5ts6AddpositionInStepRound = round(ts5ts6AddpositionInStep);

ts7ts8Addtime = linspace(ts7ts8time(end-
1),ts7ts8time(end),DivisorInTiming);
[ts7ts8AddpositionInDegree,ts7ts8AddspeedInDegree,ts7ts8Addacceleration
InDegree] =
SmoothingFunctionV1(k,a,ts7ts8Addtime,tc,tiInFunction.t1,tiInFunction.t
2,tiInFunction.t3,tiInFunction.t4);
ts7ts8AddpositionInStep = ts7ts8AddpositionInDegree*stepdeg;
ts7ts8AddpositionInStepRound = round(ts7ts8AddpositionInStep);

%% rename points of interest
MotionInSmoothing.t = [0 ts1ts2Addtime ts1ts2time(3:end)
ts3ts4time(1:end-2) ts3ts4Addtime ts5ts6Addtime ts5ts6time(3:end)
ts7ts8time(1:end-2) ts7ts8Addtime tiInFunction.t5];
MotionInSmoothing.position = [0 ts1ts2AddpositionInStepRound
ts1ts2positionInStepRound(3:end) ts3ts4positionInStepRound(1:end-2)
ts3ts4AddpositionInStepRound ts5ts6AddpositionInStepRound
ts5ts6positionInStepRound(3:end) ts7ts8positionInStepRound(1:end-2)
ts7ts8AddpositionInStepRound 0];
[position, speed, acceleration] =
SmoothingFunctionV1(k,a,MotionInSmoothing.t,tc,tiInFunction.t1,tiInFunc
tion.t2,tiInFunction.t3,tiInFunction.t4); % in degrees
MotionInSmoothing.speed = round(speed*stepdeg);
```

```
MotionInSmoothing.acceleration = round(acceleration*stepdeg);

display('***--------------------------------------------***');
fprintf('Incidences directly from smoothing function, [steps]:\n');
display(num2str(MotionInSmoothing.position));
fprintf('Incidences from smoothing function using interpolated
timepoints, [steps]:\n');
display(num2str(round(position*stepdeg)));

%% write to file
filename = strcat(tempname,'MotionInSmoothingPoints.txt');
fid = fopen(filename,'wt');
fprintf(fid,'This data gives points of interest for VMX \n');
fprintf(fid,'Stepping motor %g [step/deg], k=%g, h=%g,
a=%g\n',stepdeg,k,h,a);
fprintf(fid,' t[s]   alpha[steps] d_alpha[steps]
dd_alpha[steps/s^2]\n');
fprintf(fid,'%-8.5f %10.0f %10.0f
%12.0f\n',[MotionInSmoothing.t;MotionInSmoothing.position;MotionInSmoot
hing.speed;MotionInSmoothing.acceleration]);
fclose(fid);

%% plot
figure;
plot(MotionInSmoothing.t,MotionInSmoothing.position/stepdeg,'o',MotionI
nFunction.t,MotionInFunction.position), axis tight
legend('VMX','smoothing function');
```

getVelmexV3.m

```
function
[MotionInCommand,MotionInDesignFunction,MotionInDesignSmoothing,tsInCom
mand,tsInDesign,tiInDesignFunction] =
getVelmexV3(MotionInFunction,MotionInSmoothing,stepdeg,k,a,h,L,deg,tiIn
Function,tc,tempname,Fs)
%   This function produces VMX commands using MotionInSmoothing
%
%   Input:
%       MotionInSmoothing = t, position, speed, acceleration in [step]
%       stepdeg = pitch motion [step/deg]
%       k = reduced frequency
%       a = free parameter
%       h = holding parameter
%       L = # of loop of testing
%   Note:
%        1)The data is also written to disk with the name of k_h_a_3.txt.
%       2)The command is written to disk with the name of
k_h_a_Velmex.txt, before
%         the use, make sure put "U4" before holding starts to get
signal for
%         verification purpose.
%
%   Code: Huai-Te Yu
%   Date: 04/10/2011
%   Version: 1
%   Version history:
%       v1: generate pulse pattern I
%       v2: generate pulse pattern II
%       v3: generate pulse pattern III

%% process1: delete extra data to get VMX code
N = length(MotionInSmoothing.t);
% increments in time and angle
VMX0 = zeros(N-1,3);
for i = 1:1:N-1
    VMX0(i,1) = MotionInSmoothing.t(i+1)-MotionInSmoothing.t(i); % dt
    VMX0(i,2) = MotionInSmoothing.position(i+1)-
MotionInSmoothing.position(i); % steps in dt
end
VMX0(:,3) = round(VMX0(:,2)./VMX0(:,1)); % speed
d0 = length(MotionInSmoothing.position)-length(VMX0(:,1));
display('***---------------------------------------------***');
display(['process 1: ' num2str(d0) ' points of interest deleted']);

%% process2: accumulate timescale same speed
VMX1(1,:) = VMX0(1,:);
for i = 2:N-1
    if VMX0(i,3)-VMX0(i-1,3)==0;
        VMX1(i,1)=VMX1(i-1,1)+VMX0(i,1);
        VMX1(i,2)=VMX1(i-1,2)+VMX0(i,2);
    else
        VMX1(i,1)=VMX0(i,1);
        VMX1(i,2)=VMX0(i,2);
    end
end
```

```matlab
VMX1(:,3)=VMX0(:,3);
d1 = length(VMX0(:,1))-length(VMX1(:,1));
display(['process 2: ' num2str(d1) ' points of interest deleted']);

%% process3: delete extra-rows with same speed
[r, col] = size(VMX1);
r1 = 1;
VMX2(1,:) = VMX1(1,:);
for i = 2:r
    if VMX1(i,3)-VMX1(i-1,3) == 0;
        VMX2(r1,:) = VMX1(i,:);
    else
        VMX2(r1+1,:) = VMX1(i,:);
        r1 = r1+1;
    end
end
d2 = length(VMX1(:,1))-length(VMX2(:,1));
display(['process 3: ' num2str(d2) ' points of interest deleted']);

%% round off timing due to resolution of "P" command
% "Px" gives tenth second, "P-x" gives tenth milisecond
VMX3 = VMX2;
HoldResolution = 0.0001;
indicator = find(VMX3(:,2)==0);
VMX3(indicator,1) =
round(VMX3(indicator,1)/HoldResolution)*HoldResolution;
dtInCommandtemp = VMX2(indicator,1)-VMX3(indicator,1);
% for i = 1:length(VMX3)
%     if VMX3(i,3)==0
%         VMX3(i,1) = round(VMX3(i,1)/HoldResolution)*HoldResolution; %
resolution of pause command is tenth milisecond
%     end
% end

%% write VMX Commands
% define pulses every n-steps
prompt = {'Enter # of steps every pulse'};
dlgtitle = 'DEFINE PULSE EVERY STEPS';
numlines = 1;
if exist('Npulse','var')
    defaultanswer = {num2str(Npulse)};
else
    defaultanswer = {'0'};
end
answer = inputdlg(prompt,dlgtitle,numlines,defaultanswer,'on');
if isempty(answer)
    return,
end
Npulse = sscanf(char(answer(1)),'%f');

if Npulse~=0 && round(stepdeg*deg/Npulse)~=stepdeg*deg/Npulse
    fprintf(['Change number of pulses during the ramp-up/return
phase\n','It needs to be interger\n'])
    return
end
filename1 = strcat(tempname,'VMXCommand.txt');
```

```
fid = fopen(filename1,'wt');
fprintf(fid,'E, ;Enable On-Line mode with echo "on"\n');
fprintf(fid,'PM-1,  ;Select and clear program\n');
fprintf(fid,'A1M127,    ;Set base acceleration/speed\n');
P = 1; % number of program capable for VMX controller
for i = 1:length(VMX3)
    while i == 25*P
        P = P+1; % # of program
        fprintf(fid,'J%1.0f,    ;Jump to program\n',P);
        fprintf(fid,'PM-%.0f,   ;Select and clear program\n',P); % new
program
    end
    if VMX3(i,3) == 0
        if i ~= 1
            fprintf(fid,'U99,   ;End of continuous index with no
deceleration\n');
        end
        fprintf(fid,'U5,    ;Output1 pulse high\n');
        fprintf(fid,'P-%.0f,    ;Pause %.4f
seconds\n',VMX3(i,1)/HoldResolution,VMX3(i,1));
        fprintf(fid,'U4,    ;Output1 pulse low\n');
        flag1 = i;
    else
        if i == flag1+1
            fprintf(fid,'U77,   ;Start continuous index with no
output\n');
            if Npulse == 0
                fprintf(fid,'setP1M0, ;Disable pulse every steps on
output2\n');
                fprintf(fid,'setPA1,  ;Disable pulse width\n');
            else
                fprintf(fid,'setP1M%.0f, ;Pulse every %.0f steps on
output2\n',stepdeg*deg/Npulse,stepdeg*deg/Npulse/10);
                fprintf(fid,'setPA200,  ;Set pulse width, 2ms\n');
            end
        end
        if abs(VMX3(i,2)) == max(VMX3(:,2))
            fprintf(fid,'U5,    ;Output1 pulse high\n');
        end
        fprintf(fid,'SA1M%4.0f,I1M%4.0f,\n',abs(VMX3(i,3)),VMX3(i,2));
        if abs(VMX3(i,2)) == max(VMX3(:,2))
            fprintf(fid,'U4,    ;Output1 pulse low\n');
        end
    end
end
fprintf(fid,'\n');
fprintf(fid,'PM-0,  ;Select and clear program\n');
fprintf(fid,'JM1,   ;Jump to program and come back for more\n');
fprintf(fid,'L%3.0f,    ;%2.0f loops\n',L+1, L); % # of loop
fprintf(fid,'U5,    ;Output1 pulse high\n');
fprintf(fid,'P5,    ;Pause 0.5 seconds to indicate the end of
motion\n');
fprintf(fid,'U4,    ;Output1 pulse low\n');
fclose(fid);

%% predict VMX motion from motion commands
%(without considering resolution of "P" command, which is tenth seconds)
```

```
for i = 1:length(VMX3)
    if VMX3(i,2)==0
        dt(i) = abs(VMX3(i,1));
    else
        dt(i) = abs(VMX3(i,2)/VMX3(i,3));
    end
end

% preallocate memory
MotionInCommand.t = zeros(1,length(VMX3)+1);
MotionInCommand.position = zeros(1,length(VMX3)+1);
MotionInCommand.speed = zeros(1,length(VMX3)+1);

% evaluate motion from VMX controller
for i = 2:length(VMX3)+1
    MotionInCommand.t(i) = MotionInCommand.t(i-1)+dt(i-1); % time
    MotionInCommand.position(i) = MotionInCommand.position(i-1)+VMX3(i-
1,2); % position, [steps]
    MotionInCommand.speed(i-1) = VMX3(i-1,3); % speed, [steps/s]
end

% display VMX motion prediction
display('***--------------------------------------------***');
fprintf('Motion predicted from commands:\n')
display(['time:     ' num2str(MotionInCommand.t,7)]);
display(['position:' num2str(MotionInCommand.position,7)]);
display(['speed:    ' num2str(MotionInCommand.speed,7)]);

% write to file
filename2 = strcat(tempname,'MotionInCommand.txt');
fid = fopen(filename2,'wt');
fprintf(fid,'This is the motion pridiction for stepping motor\n');
fprintf(fid,'Stepping motor %g [step/deg], k=%g, h=%g,
a=%g\n',stepdeg,k,h,a);
fprintf(fid,' t[s]   position[step] speed[step/s]\n');
fprintf(fid,'%-8.5f %10.0f %10.0f
\n',[MotionInCommand.t;MotionInCommand.position;MotionInCommand.speed]);
fclose(fid);

% get acceleration region from commands
tempVMX = MotionInCommand.t(2:end) - MotionInCommand.t(1:end-1);
tempVMXts = sort(tempVMX,'descend');
indextsInCommand =
find(tempVMX==tempVMXts(1)|tempVMX==tempVMXts(2)|tempVMX==tempVMXts(3)|
tempVMX==tempVMXts(4)|tempVMX==tempVMXts(5));
tsInCommand.ts1 = MotionInCommand.t(indextsInCommand(1)+1);
tsInCommand.ts2 = MotionInCommand.t(indextsInCommand(2));
tsInCommand.ts3 = MotionInCommand.t(indextsInCommand(2)+1);
tsInCommand.ts4 = MotionInCommand.t(indextsInCommand(3));
tsInCommand.ts5 = MotionInCommand.t(indextsInCommand(3)+1);
tsInCommand.ts6 = MotionInCommand.t(indextsInCommand(4));
tsInCommand.ts7 = MotionInCommand.t(indextsInCommand(4)+1);
tsInCommand.ts8 = MotionInCommand.t(indextsInCommand(5));
display('***--------------------------------------------***');
display('smoothing points in commands:');
```

```
display(num2str([tsInCommand.ts1,tsInCommand.ts2,tsInCommand.ts3,tsInCo
mmand.ts4,tsInCommand.ts5,tsInCommand.ts6,tsInCommand.ts7,tsInCommand.t
s8],7));

%% adjust hold-timing from smoothing points
% (to be consistent with resolution of "P-x" command, which is tenth
second)
% preallocate memory
MotionInDesignSmoothing.t = zeros(1,length(MotionInSmoothing.t));
MotionInDesignSmoothing.position  =  zeros(1,length(MotionInSmoothing.t));
MotionInDesignSmoothing.speed = zeros(1,length(MotionInSmoothing.t));

% assign motion from smoothing points
MotionInDesignSmoothing.position = MotionInSmoothing.position;
MotionInDesignSmoothing.speed = MotionInSmoothing.speed;
MotionInDesignSmoothing.acceleration = MotionInSmoothing.acceleration;

% using VMX controller timing resolution
dtInDesignSmoothing = diff(MotionInSmoothing.t);
dxInDesignSmoothing = diff(MotionInSmoothing.position);
indexInDesignSmoothing = find(dxInDesignSmoothing==0);
dtInDesignSmoothing(indexInDesignSmoothing) =
round(dtInDesignSmoothing(indexInDesignSmoothing)/HoldResolution)*HoldR
esolution; % resolution of pause command is tenth second

for i = 2:length(VMX0)+1
    MotionInDesignSmoothing.t(i) = MotionInDesignSmoothing.t(i-
1)+dtInDesignSmoothing(i-1);
end

% display motion from smoothing function with calibration in pause
display('***--------------------------------------------***');
fprintf('Motion from smoothing function:(calibrated with pause
command)\n')
display(['time:    ' num2str(MotionInDesignSmoothing.t,7)]);
display(['position:' num2str(MotionInDesignSmoothing.position,7)]);
display(['speed:   ' num2str(MotionInDesignSmoothing.speed,7)]);

% save to file
filename3 = strcat(tempname,'MotionInDesignSmoothing.txt');
fid = fopen(filename3,'wt');
fprintf(fid,'This is the motion pridiction for stepping motor\n');
fprintf(fid,'Stepping motor %g [step/deg], k=%g, h=%g,
a=%g\n',stepdeg,k,h,a);
fprintf(fid,' t[s]   position[step] speed[step/s]\n');
fprintf(fid,'%-8.5f %10.0f %10.0f
\n',[MotionInDesignSmoothing.t;MotionInDesignSmoothing.position;MotionI
nDesignSmoothing.speed]);
fclose(fid);

% get acceleration region from smoothing points
%(using timing resolution during the pause from VMX controller)
tempSmoothing = MotionInDesignSmoothing.t(2:end)-
MotionInDesignSmoothing.t(1:end-1);
tempSmoothingts = sort(tempSmoothing,'descend');
```

```
indextsInDesignSmoothing =
find(tempSmoothing==tempSmoothingts(1)|tempSmoothing==tempSmoothingts(2
)|tempSmoothing==tempSmoothingts(3)|tempSmoothing==tempSmoothingts(4)|t
empSmoothing==tempSmoothingts(5));
tsInDesign.ts1 =
MotionInDesignSmoothing.t(indextsInDesignSmoothing(1)+1);
tsInDesign.ts2  =  MotionInDesignSmoothing.t(indextsInDesignSmoothing(2));
tsInDesign.ts3 =
MotionInDesignSmoothing.t(indextsInDesignSmoothing(2)+1);
tsInDesign.ts4  =  MotionInDesignSmoothing.t(indextsInDesignSmoothing(3));
tsInDesign.ts5 =
MotionInDesignSmoothing.t(indextsInDesignSmoothing(3)+1);
tsInDesign.ts6  =  MotionInDesignSmoothing.t(indextsInDesignSmoothing(4));
tsInDesign.ts7 =
MotionInDesignSmoothing.t(indextsInDesignSmoothing(4)+1);
tsInDesign.ts8  =  MotionInDesignSmoothing.t(indextsInDesignSmoothing(5));

display('smoothing points in design:(calibrated with pause command)');
display(num2str([tsInDesign.ts1,tsInDesign.ts2,tsInDesign.ts3,...

tsInDesign.ts4,tsInDesign.ts5,tsInDesign.ts6,tsInDesign.ts7,tsInDesign.
ts8],7));

%% adjust hold-timing for function
% (to be consistent with resolution of "P-x" command, which is tenth
second)
% preallocate memory
MotionInDesignFunction.t = zeros(1,length(MotionInFunction.t));
MotionInDesignFunction.position = zeros(1,length(MotionInFunction.t));
MotionInDesignFunction.speed = zeros(1,length(MotionInFunction.t));
MotionInDesignFunction.acceleration =
zeros(1,length(MotionInFunction.t));

% re-assign motion from function
MotionInDesignFunction.position = MotionInFunction.position;
MotionInDesignFunction.speed = MotionInFunction.speed;
MotionInDesignFunction.acceleration = MotionInFunction.acceleration;

% using VMX controller timing resolution
indexInDesignFunctionInStart = round(tiInFunction.t1*Fs/4);
indexInDesignFunctionInHold =
round((tiInFunction.t2+tiInFunction.t3)*Fs/2);
indexInDesignFunctionInRelaxation =
round((tiInFunction.t4+tiInFunction.t5)*Fs/2);

MotionInDesignFunctiontime1 =
MotionInFunction.t(1:indexInDesignFunctionInStart);
MotionInDesignFunctiontime2 =
MotionInFunction.t(indexInDesignFunctionInStart+1:indexInDesignFunction
InHold)-dtInCommandtemp(1);
MotionInDesignFunctiontime3 =
MotionInFunction.t(indexInDesignFunctionInHold+1:indexInDesignFunctionI
nRelaxation)-dtInCommandtemp(1)-dtInCommandtemp(2);
MotionInDesignFunctiontime4 =
MotionInFunction.t(indexInDesignFunctionInRelaxation+1:end)-
dtInCommandtemp(1)-dtInCommandtemp(2)-dtInCommandtemp(3);
```

```
MotionInDesignFunction.t =
[MotionInDesignFunctiontime1,MotionInDesignFunctiontime2,MotionInDesign
Functiontime3,MotionInDesignFunctiontime4];

tiInDesignFunction.t1 = tiInFunction.t1 - dtInCommandtemp(1);
tiInDesignFunction.t2 = tiInFunction.t2 - dtInCommandtemp(1);
tiInDesignFunction.t3 = tiInFunction.t3 - dtInCommandtemp(1)-
dtInCommandtemp(2);
tiInDesignFunction.t4 = tiInFunction.t4 - dtInCommandtemp(1)-
dtInCommandtemp(2);
tiInDesignFunction.t5 = tiInFunction.t5 - dtInCommandtemp(1)-
dtInCommandtemp(2)-dtInCommandtemp(3);

%% plot VMX motion vs smoothing function
%(may not correctly represent the timing by "P" command, which can be
% adjusted manually)
figure;
ax1fig1 = subplot(2,1,1);
sub1_pos1 = get(ax1fig1,'position'); % get subplot axis position
set(ax1fig1,'position',sub1_pos1.*[1 1 1 1.3]) % stretch its width and
height
sub1h1 =
line(MotionInDesignFunction.t,MotionInDesignFunction.position,'LineStyl
e','-',...
    'color','k');
sub1h2 =
line(MotionInCommand.t,MotionInCommand.position/stepdeg,'LineStyle','no
ne',...
    'Marker','o','color','b');
% xlabel('t, s','FontName','Times New Roman','FontAngle','normal');
ylabel('angle of attack, deg','FontName','Times New
Roman','FontAngle','normal');
sublegend1 = legend('smoothing function','VMX');
set(sublegend1,'FontName','Times New Roman','FontAngle','normal');
ax2fig1 = axes('Position',get(ax1fig1,'Position'),...
           'XAxisLocation','top',...
           'YAxisLocation','right',...
           'Color','none',...
           'XColor','k','YColor','k');
set(ax1fig1,'Xlim',[0
tiInFunction.t5],'XTick',0:1:tiInFunction.t5,'XTickLabel',[]);
set(ax2fig1,'Xlim',[0
tiInFunction.t5],'XTick',tiInFunction.t1:tc:tiInFunction.t5,'XTickLabel
',0:1:tiInFunction.t5/tc);
linkaxes([ax1fig1 ax2fig1],'xy');

ax1fig2 = subplot(2,1,2);
sub2_pos1 = get(ax1fig2,'position'); % get subplot axis position
set(ax1fig2,'position',sub2_pos1.*[1 1 1 1.3]) % stretch its width and
height
sub2h1 =
line(MotionInDesignFunction.t,MotionInDesignFunction.speed,'LineStyle',
'-',...
    'color','k'); hold on
sub2h2 = stairs(MotionInCommand.t,MotionInCommand.speed/stepdeg,'b');
xlabel('t, s','FontName','Times New Roman','FontAngle','normal');
```

```
ylabel('angular speed, deg/s','FontName','Times New
Roman','FontAngle','normal');
% ylabel('$\prime \alpha \frac{deg}{s}
$','Interpreter','Latex','FontSize',12);
sublegend2 = legend('smoothing function','VMX');
set(sublegend2,'FontName','Times New Roman','FontAngle','normal');
ax2fig2 = axes('Position',get(ax1fig2,'Position'),...
           'XAxisLocation','top',...
           'YAxisLocation','right',...
           'Color','none',...
           'XColor','k','YColor','k');
set(ax1fig2,'Xlim',[0
tiInFunction.t5],'XTick',0:1:tiInFunction.t5,'XTickLabel',0:1:tiInFunct
ion.t5);
set(ax2fig2,'Xlim',[0
tiInFunction.t5],'XTick',tiInFunction.t1:tc:tiInFunction.t5,'XTickLabel
',[]);
linkaxes([ax1fig2 ax2fig2],'xy');
s = suptitle(['k=',num2str(k),' ,a=',num2str(a),' ,h=',num2str(h)]);
set(s,'fontsize',12);
```

APPENDIX B

MOTION COMMAND FOR KINEMATICS OF INTEREST

B.1 PITCH RATE 155 °/S (ROTARY TABLE B4818TS)

```
E,;Enable On-Line mode with echo "on"
PM-1,;Select and clear program
A1M127,    ;Set base acceleration/speed
U5,    ;Output1 pulse high
P-2266,    ;Pause 0.2266 seconds
U4,    ;Output1 pulse low
U77,;Start continuous index with no output
setP1M0, ;Disable pulse every steps on output2
setPA1,  ;Disable pulse width
SA1M  65,I1M   1,
SA1M 131,I1M   2,
SA1M 393,I1M   6,
SA1M 982,I1M  15,
SA1M1827,I1M  25,
SA1M2439,I1M  25,
SA1M2657,I1M  24,
SA1M2946,I1M  25,
SA1M2923,I1M  24,
SA1M3098,I1M  25,
SA1M3003,I1M  24,
SA1M3144,I1M  25,
SA1M3027,I1M  24,
U5,    ;Output1 pulse high
SA1M3099,I1M 410,
U4,    ;Output1 pulse low
SA1M3153,I1M  25,
SA1M3018,I1M  24,
SA1M3128,I1M  25,
SA1M2974,I1M  24,
SA1M3044,I1M  25,
SA1M2828,I1M  24,
SA1M2767,I1M  25,
SA1M2341,I1M  24,
SA1M1827,I1M  25,
J2,    ;Jump to program
PM-2,;Select and clear program
SA1M 982,I1M  15,
SA1M 393,I1M   6,
SA1M 131,I1M   2,
SA1M  65,I1M   1,
U99,   ;End of continuous index with no deceleration
U5,    ;Output1 pulse high
P-1629,;Pause 0.1629 seconds
P400,;Pause 40 seconds
U4,    ;Output1 pulse low
U77,;Start continuous index with no output
setP1M0, ;Disable pulse every steps on output2
setPA1,  ;Disable pulse width
SA1M  65,I1M  -1,
SA1M 131,I1M  -2,
SA1M 393,I1M  -6,
SA1M 982,I1M -15,
SA1M1827,I1M -25,
SA1M2341,I1M -24,
SA1M2767,I1M -25,
SA1M2828,I1M -24,
SA1M3044,I1M -25,
SA1M2974,I1M -24,
SA1M3128,I1M -25,
SA1M3018,I1M -24,
SA1M3153,I1M -25,
U5,    ;Output1 pulse high
SA1M3099,I1M-410,
U4,    ;Output1 pulse low
SA1M3027,I1M -24,
SA1M3144,I1M -25,
SA1M3003,I1M -24,
SA1M3098,I1M -25,
SA1M2923,I1M -24,
SA1M2946,I1M -25,
J3,    ;Jump to program
PM-3,;Select and clear program
SA1M2657,I1M -24,
SA1M2439,I1M -25,
SA1M1827,I1M -25,
SA1M 982,I1M -15,
SA1M 393,I1M  -6,
SA1M 131,I1M  -2,
SA1M  65,I1M  -1,
U99,   ;End of continuous index with no deceleration
U5,    ;Output1 pulse high
P-2266, ;Pause 0.2266 seconds
U4,    ;Output1 pulse low
P90,;Pause 9 seconds

PM-0,  ;Select and clear program
JM1,   ;Jump to program and come back for more
L 21,    ;20 loops
U5,    ;Output1 pulse high
P5,    ;Pause 0.5 seconds to indicate the end of motion
U4,    ;Output1 pulse low
```

B.2 PITCH RATE 76.4 °/S (ROTARY TABLE B4836TS)

```
E,;Enable On-Line mode with echo "on"
PM-1,;Select and clear program
A1M127,    ;Set base acceleration/speed
U5,    ;Output1 pulse high
P-2340,    ;Pause 0.2340 seconds
U4,    ;Output1 pulse low
U77,;Start continuous index with no output
setP1M0, ;Disable pulse every steps on output2
setPA1,  ;Disable pulse width
SA1M  63,I1M   1,
SA1M 127,I1M   2,
SA1M 444,I1M   7,
SA1M 950,I1M  15,
SA1M1768,I1M  25,
SA1M2359,I1M  25,
SA1M2676,I1M  25,
SA1M2849,I1M  25,
SA1M2943,I1M  25,
SA1M2995,I1M  25,
SA1M3023,I1M  25,
SA1M3039,I1M  25,
SA1M3047,I1M  25,
U5,    ;Output1 pulse high
SA1M3057,I1M1300,
U4,    ;Output1 pulse low
SA1M3047,I1M  25,
SA1M3039,I1M  25,
SA1M3023,I1M  25,
SA1M2995,I1M  25,
SA1M2943,I1M  25,
SA1M2849,I1M  25,
SA1M2676,I1M  25,
SA1M2359,I1M  25,
SA1M1768,I1M  25,
J2,    ;Jump to program
PM-2,;Select and clear program
SA1M 950,I1M  15,
SA1M 444,I1M   7,
SA1M 127,I1M   2,
SA1M  63,I1M   1,
U99,   ;End of continuous index with no deceleration
U5,    ;Output1 pulse high
P-1682,    ;Pause 0.1682 seconds
P400,;Pause 40 seconds
U4,    ;Output1 pulse low
U77,;Start continuous index with no output
setP1M0, ;Disable pulse every steps on output2
setPA1,  ;Disable pulse width
SA1M  63,I1M  -1,
SA1M 127,I1M  -2,
SA1M 444,I1M  -7,
SA1M 950,I1M -15,
SA1M1768,I1M -25,
SA1M2359,I1M -25,
SA1M2676,I1M -25,
SA1M2849,I1M -25,
SA1M2943,I1M -25,
SA1M2995,I1M -25,
SA1M3023,I1M -25,
SA1M3039,I1M -25,
SA1M3047,I1M -25,
U5,    ;Output1 pulse high
SA1M3057,I1M-1300,
U4,    ;Output1 pulse low
SA1M3047,I1M -25,
SA1M3039,I1M -25,
SA1M3023,I1M -25,
SA1M2995,I1M -25,
SA1M2943,I1M -25,
SA1M2849,I1M -25,
J3,    ;Jump to program
PM-3,;Select and clear program
SA1M2676,I1M -25,
SA1M2359,I1M -25,
SA1M1768,I1M -25,
SA1M 950,I1M -15,
SA1M 444,I1M  -7,
SA1M 127,I1M  -2,
SA1M  63,I1M  -1,
U99,   ;End of continuous index with no deceleration
U5,    ;Output1 pulse high
P-2340,    ;Pause 0.2340 seconds
U4,    ;Output1 pulse low
P60,;Pause 6 seconds

PM-0,  ;Select and clear program
JM1,   ;Jump to program and come back for more
L 21,    ;20 loops
U5,    ;Output1 pulse high
P5,    ;Pause 0.5 seconds to indicate the end of motion
U4,    ;Output1 pulse low
```

B.3 PITCH RATE 37.5 °/S (ROTARY TABLE B4836TS)

```
E,;Enable On-Line mode with echo "on"
PM-1,;Select and clear program
A1M127,    ;Set base acceleration/speed
U5,    ;Output1 pulse high
P-4769,    ;Pause 0.4769 seconds
U4,    ;Output1 pulse low
U77,;Start continuous index with no output
setP1M0, ;Disable pulse every steps on output2
setPA1,  ;Disable pulse width
SA1M  31,I1M   1,
SA1M  62,I1M   2,
SA1M 218,I1M   7,
SA1M 466,I1M  15,
SA1M 868,I1M  25,
SA1M1157,I1M  25,
SA1M1313,I1M  25,
SA1M1398,I1M  25,
SA1M1444,I1M  25,
SA1M1469,I1M  25,
SA1M1483,I1M  25,
SA1M1491,I1M  25,
SA1M1495,I1M  25,
U5,    ;Output1 pulse high
SA1M1500,I1M1300,
U4,    ;Output1 pulse low
SA1M1495,I1M  25,
SA1M1491,I1M  25,
SA1M1483,I1M  25,
SA1M1469,I1M  25,
SA1M1444,I1M  25,
SA1M1398,I1M  25,
SA1M1313,I1M  25,
SA1M1157,I1M  25,
SA1M 868,I1M  25,
J2,    ;Jump to program
PM-2,;Select and clear program
SA1M 466,I1M  15,
SA1M 218,I1M   7,
SA1M  62,I1M   2,
SA1M  31,I1M   1,
U99,   ;End of continuous index with no deceleration
U5,    ;Output1 pulse high
P-3428,    ;Pause 0.3428 seconds
P400,   ;Pause 40 seconds
U4,    ;Output1 pulse low
U77,;Start continuous index with no output
setP1M0, ;Disable pulse every steps on output2
setPA1,  ;Disable pulse width
SA1M  31,I1M  -1,
SA1M  62,I1M  -2,
SA1M 218,I1M  -7,
SA1M 466,I1M -15,
SA1M 868,I1M -25,
SA1M1157,I1M -25,
SA1M1313,I1M -25,
SA1M1398,I1M -25,
SA1M1444,I1M -25,
SA1M1469,I1M -25,
SA1M1483,I1M -25,
SA1M1491,I1M -25,
SA1M1495,I1M -25,
U5,    ;Output1 pulse high
SA1M1500,I1M-1300,
U4,    ;Output1 pulse low
SA1M1495,I1M -25,
SA1M1491,I1M -25,
SA1M1483,I1M -25,
SA1M1469,I1M -25,
SA1M1444,I1M -25,
SA1M1398,I1M -25,
J3,    ;Jump to program
PM-3,;Select and clear program
SA1M1313,I1M -25,
SA1M1157,I1M -25,
SA1M 868,I1M -25,
SA1M 466,I1M -15,
SA1M 218,I1M  -7,
SA1M  62,I1M  -2,
SA1M  31,I1M  -1,
U99,   ;End of continuous index with no deceleration
U5,    ;Output1 pulse high
P-4769,    ;Pause 0.4769 seconds
U4,    ;Output1 pulse low
P60,;Pause 6 seconds

PM-0,  ;Select and clear program
JM1,   ;Jump to program and come back for more
L 21,    ;20 loops
U5,    ;Output1 pulse high
P5,    ;Pause 0.5 seconds to indicate the end of motion
U4,    ;Output1 pulse low
```

B.4 PITCH RATE 25.7 °/S (ROTARY TABLE B4836TS)

```
E,;Enable On-Line mode with echo "on"
PM-1,;Select and clear program
A1M127,    ;Set base acceleration/speed
U5,    ;Output1 pulse high
P-3483,    ;Pause 0.3483 seconds
U4,    ;Output1 pulse low
U77,;Start continuous index with no output
setP1M0, ;Disable pulse every steps on output2
setPA1,  ;Disable pulse width
SA1M  91,I1M   4,
SA1M 364,I1M   8,
SA1M 558,I1M  11,
SA1M 812,I1M  12,
SA1M 921,I1M  12,
SA1M 981,I1M  12,
SA1M 929,I1M  11,
SA1M1031,I1M  12,
SA1M1041,I1M  12,
SA1M 959,I1M  11,
SA1M1049,I1M  12,
U5,    ;Output1 pulse high
SA1M1026,I1M1566,
U4,    ;Output1 pulse low
SA1M1049,I1M  12,
SA1M 959,I1M  11,
SA1M1041,I1M  12,
SA1M1031,I1M  12,
SA1M1013,I1M  12,
SA1M 899,I1M  11,
SA1M 921,I1M  12,
SA1M 812,I1M  12,
SA1M 558,I1M  11,
SA1M 364,I1M   8,
SA1M  91,I1M   4,
J2,    ;Jump to program
PM-2,;Select and clear program
U99,   ;End of continuous index with no deceleration
U5,    ;Output1 pulse high
P-2785,    ;Pause 0.2785 seconds
P400,;Pause 40 seconds
U4,    ;Output1 pulse low
U77,;Start continuous index with no output
setP1M0, ;Disable pulse every steps on output2
setPA1,  ;Disable pulse width
SA1M  91,I1M  -4,
SA1M 364,I1M  -8,
SA1M 558,I1M -11,
SA1M 812,I1M -12,
SA1M 921,I1M -12,
SA1M 899,I1M -11,
SA1M1013,I1M -12,
SA1M1031,I1M -12,
SA1M1041,I1M -12,
SA1M 959,I1M -11,
SA1M1049,I1M -12,
U5,    ;Output1 pulse high
SA1M1026,I1M-1566,
U4,    ;Output1 pulse low
SA1M1049,I1M -12,
SA1M 959,I1M -11,
SA1M1041,I1M -12,
SA1M1031,I1M -12,
SA1M 929,I1M -11,
SA1M 981,I1M -12,
SA1M 921,I1M -12,
SA1M 812,I1M -12,
SA1M 558,I1M -11,
SA1M 364,I1M  -8,
SA1M  91,I1M  -4,
U99,   ;End of continuous index with no deceleration
U5,    ;Output1 pulse high
P-3483,    ;Pause 0.3483 seconds
U4,    ;Output1 pulse low
P90,;Pause 9 seconds

PM-0,  ;Select and clear program
JM1,   ;Jump to program and come back for more
L 21,    ;20 loops
U5,    ;Output1 pulse high
P5,    ;Pause 0.5 seconds to indicate the end of motion
U4,    ;Output1 pulse low
```

B.5 PITCH RATE 12.6 °/S

```
E,;Enable On-Line mode with echo "on"
PM-1,;Select and clear program
A1M127,    ;Set base acceleration/speed
U5,    ;Output1 pulse high
P-5091,    ;Pause 0.5091 seconds
U4,    ;Output1 pulse low
U77,;Start continuous index with no output
setP1M0, ;Disable pulse every steps on output2
setPA1,  ;Disable pulse width
SA1M  31,I1M   1,
SA1M  62,I1M   2,
SA1M 155,I1M   5,
SA1M 312,I1M   9,
SA1M 370,I1M   8,
SA1M 472,I1M   9,
SA1M 446,I1M   8,
SA1M 461,I1M   8,
SA1M 528,I1M   9,
SA1M 473,I1M   8,
SA1M 535,I1M   9,
SA1M 477,I1M   8,
U5,    ;Output1 pulse high
SA1M 503,I1M1632,
U4,    ;Output1 pulse low
SA1M 477,I1M   8,
SA1M 535,I1M   9,
SA1M 473,I1M   8,
SA1M 528,I1M   9,
SA1M 461,I1M   8,
SA1M 446,I1M   8,
SA1M 472,I1M   9,
SA1M 370,I1M   8,
SA1M 312,I1M   9,
SA1M 155,I1M   5,
J2,    ;Jump to program
PM-2,;Select and clear program
SA1M  62,I1M   2,
SA1M  31,I1M   1,
U99,   ;End of continuous index with no deceleration
U5,    ;Output1 pulse high
P-4072,    ;Pause 0.4072 seconds
P400,   ;Pause 40 seconds
U4,    ;Output1 pulse low
U77,;Start continuous index with no output
setP1M0, ;Disable pulse every steps on output2
setPA1,  ;Disable pulse width
SA1M  31,I1M  -1,
SA1M  62,I1M  -2,
SA1M 155,I1M  -5,
SA1M 312,I1M  -9,
SA1M 370,I1M  -8,
SA1M 472,I1M  -9,
SA1M 446,I1M  -8,
SA1M 461,I1M  -8,
SA1M 528,I1M  -9,
SA1M 473,I1M  -8,
SA1M 535,I1M  -9,
SA1M 477,I1M  -8,
U5,    ;Output1 pulse high
SA1M 503,I1M-1632,
U4,    ;Output1 pulse low
SA1M 477,I1M  -8,
SA1M 535,I1M  -9,
SA1M 473,I1M  -8,
SA1M 528,I1M  -9,
SA1M 461,I1M  -8,
SA1M 446,I1M  -8,
SA1M 472,I1M  -9,
SA1M 370,I1M  -8,
SA1M 312,I1M  -9,
J3,    ;Jump to program
PM-3,;Select and clear program
SA1M 155,I1M  -5,
SA1M  62,I1M  -2,
SA1M  31,I1M  -1,
U99,   ;End of continuous index with no deceleration
U5,    ;Output1 pulse high
P-5091,    ;Pause 0.5091 seconds
U4,    ;Output1 pulse low
P60,;Pause 6 seconds

PM-0,  ;Select and clear program
JM1,   ;Jump to program and come back for more
L 21,    ;20 loops
U5,    ;Output1 pulse high
P5,    ;Pause 0.5 seconds to indicate the end of motion
U4,    ;Output1 pulse low
```

APPENDIX C

VERIFICATION OF KINEMATICS OF INTEREST

Two approaches can be used to verify wing kinematics indexed by stepper motor. The first approach involves checking wing position by inspecting scales on Rotary Table using the naked eye or reading the feedback from VMX controller through COSMOS software, which was implemented during the operation.

The second approach, which is presented here, is to verify wing angular speed by inspecting the timing when the wing travels to specific wing position. Shown in the Tables B.1-B.5 are the representative timings at start and stop of the smoothing maneuver, and period for a complete pitch up-hold-return motion for all kinematics of interest.

To determine whether Rotary Table or stepper motor correctly implements wing kinematics of interest, we look at pulses generated at selected phases/angles from VMX controller and compare the corresponding timing with VMX input commands as desired, which are shown in the second and third rows in the table. Firstly, looking at the first part of the smoothing maneuver (i.e., $t_1 \pm \Delta t$ and $t_4 \pm \Delta t$), we found that the Rotary Table was operated as expected, the differences are within a few milliseconds. For the second part of the smoothing maneuver (i.e., $t_2 \pm \Delta t$ and $t_3 \pm \Delta t$), the VMX pulses give shorter timing than the estimation from VMX input commands, and result in much shorter timing in the period (denoted by T). For pitch rate from high to low, the difference in period is 32.5 ms, 34.2 ms, 65.2 ms, 23.0 ms, and 64.7 ms. This is because the inertia of the Rotary Table still drives the stepper motor after operating at constant pitch rate, and moves the stepper motor to next index, and eventually results in the Rotary Table completes the smoothing maneuver earlier than the estimation. Also noted is that this inertia effect is significantly impacted by the duration of the smoothing maneuver. For instance, pitch rates .37.5 °/s or 12.6 °/s have a smoothing duration of 300.8 ms or 269.2 ms, respectively, and yields much shorter duration for the second part of smoothing maneuver. Other kinematics of interest such as 155°/s, 76.4°/s, and 25.7°/s have shorter smoothing duration 142.8 ms, 147.6 ms, and 183.6 ms, respectively; their durations in the second smoothing maneuver are in the same order.

In addition, the comparison of smoothing regions from the theoretical function and actual selections for VMX input commands is also provided by inspecting the first and second rows in tables. The VMX input commands have shorter duration of smoothing regions because of the resolution of Rotary Table. For Rotary Table B4836TS one step represents 0.025°, any rounded step less than one is regarded as zero, which makes smoothing maneuver in practice different from theoretical function. For B4818TS one step is for 0.05°.

Table C.1 Timing comparison between smoothing function, VMX commands, and measurement during selected phases for pitch rate 155 °/s and *B* = 11.

time Sources	Pitch-up phase				Pitch return phase				T
	t_1-Δt	t_1+Δt	t_2-Δt	t_2+Δt	t_4-Δt	t_4+Δt	t_3-Δt	t_3+Δt	
Function	0.2113	0.3693	0.5016	0.6596	0.7919	0.9499	1.0822	1.2402	1.4515
VMX Commands	0.2266	0.3694	0.5017	0.6445	0.8074	0.9502	1.0825	1.2253	1.4519
VMX Pulses	0.2268	0.3694	0.5018	0.6288	0.7912	0.9338	1.0660	1.1932	1.4194

Table C.2 Timing comparison between smoothing function, VMX commands, and measurement during selected phases for pitch rate 76.4 °/s and *B* = 21.60.

time Sources	Pitch-up phase				Pitch return phase				T
	t_1-Δt	t_1+Δt	t_2-Δt	t_2+Δt	T_4-Δt	t_4+Δt	t_3-Δt	t_3+Δt	
Function	0.2182	0.3815	0.8068	0.9701	1.1067	1.2700	1.6952	1.8586	2.0765
VMX Commands	0.2340	0.3816	0.8068	0.9544	1.1226	1.2702	1.6954	1.8430	2.0770
VMX Pulses	0.2342	0.3816	0.8064	0.9376	1.1054	1.2528	1.6778	1.8092	2.0428

Table C.3 Timing comparison between smoothing function, VMX commands, and measurement during selected phases for pitch rate 37.5 °/s and *B* = 21.60.

time Sources	Pitch-up phase				Pitch return phase				T
	t_1-Δt	t_1+Δt	t_2-Δt	t_2+Δt	T_4-Δt	t_4+Δt	t_3-Δt	t_3+Δt	
Function	0.4448	0.7777	1.6443	1.9771	2.2556	2.5885	3.4551	3.7880	4.2328
VMX Commands	0.4769	0.7777	1.6444	1.9452	2.2880	2.5888	3.4555	3.7563	4.2332
VMX Pulses	0.4772	0.7774	1.6438	1.9130	2.2552	2.5556	3.4222	3.6914	4.1680

Table C.4 Timing comparison between smoothing function, VMX commands, and measurement during selected phases for pitch rate 25.7 °/s and *B* = 46.15.

time	Pitch-up phase				Pitch return phase				T
Sources	t_1-Δt	t_1+Δt	t_2-Δt	t_2+Δt	T_4-Δt	t_4+Δt	t_3-Δt	t_3+Δt	
Function	0.3043	0.5320	2.0578	2.2855	2.4760	2.7037	4.2295	4.4572	4.7615
VMX Commands	0.3483	0.5319	2.0582	2.2418	2.5203	2.7039	4.2303	4.4139	4.7622
VMX Pulses	0.3486	0.5312	2.0574	2.2308	2.5090	2.6916	4.2176	4.3912	4.7392

Table C.5 Timing comparison between smoothing function, VMX commands, and measurement during selected phases for pitch rate 12.6 °/s and *B* = 64.47.

time	Pitch-up phase				Pitch return phase				T
Sources	t_1-Δt	t_1+Δt	t_2-Δt	t_2+Δt	t_4-Δt	t_4+Δt	t_3-Δt	t_3+Δt	
Function	0.4448	0.7782	4.0253	4.3587	4.6372	4.9705	8.2177	8.5510	8.9958
VMX Commands	0.5091	0.7783	4.0228	4.2919	4.6991	4.9683	8.2128	8.4820	8.9911
VMX Pulses	0.5094	0.7766	4.0214	4.2602	4.6670	4.9342	8.1788	8.4176	8.9264

APPENDIX D

SPECTRUM ANALYSIS

Power spectral density analysis is the analysis using Fourier Transform to look at information in the frequency domain. In our experiment, the output signals are discrete-time signals, which are obtained by sampling the continue-time signals in voltages; therefore, the method Discrete Fourier Transform (DFT) is preferred. Due to different scenarios the DFT are further classified into two types, which are real DFT and complex DFT. In order to have highly efficient computing speed, we adapt the Fast Fourier Transform (FFT), a type of complex DFT.

In principle, the transform from time-domain signals x_j to frequency-domain signals X_k is a forward process; this process is represented by Equation (D.1), also called the analysis equation. Equation (D.2) shows the transform from frequency domain to time domain, which is an inverse process, and the equation is called the synthesis equation. On the other hand, the time-domain signals are decomposed into cosine and sine waves, the cosine waves are the real parts of the frequency-domain signals, the sine waves are the imaginary parts of the frequency–domain signals. The amplitude or magnitude spectrum $\left|X_k\right|$ and phase spectrum ϕ_k of the frequency-domain signals can then be evaluated in complex coordinates. The spectrum here is defined as the distribution of amounts of quantity over a range of frequency of influence. The signals are finite data set, not infinite; therefore, the method to estimate power spectral density is required.

$$X_k = \sum_{j=1}^{N} x_j e^{-i2\pi(j-1)(k-1)/N}\ ,\ k = 1, 2, ..., N \tag{D.1}$$

$$x_k = \frac{1}{N}\sum_{j=1}^{N} X_j e^{i2\pi(j-1)(k-1)/N}\ ,\ k = 1, 2, ..., N \tag{D.2}$$

where N is the length of FFT and recommended to be powers of 2 for efficient computation, *k* is an index of the spectrum and ranging from 1 to N.

Equation (D.3) illustrates the frequency resolution, which has to be small enough to identify two close intrinsic frequencies (i.e., f_1 and f_2) in measurements.

$$df = f_s / N < f_2 - f_1, \tag{D.3}$$

The power spectrum, shown in Equation (D.4), is the square of the amplitude, its unit is voltage squared. Since X_k is complex the power spectrum can be also evaluated by multiplying its conjugate.

$$P_{k+1} = \left|X_{k+1}\right|^2 = X_{k+1} \cdot conj\left(X_{k+1}\right) \tag{D.4}$$

Considering the magnitude spectrum and power spectrum in decibel (*dB*), they can be evaluated using Equation (D.5).

$$dB = 20\log_{10}\left(\left|X_{k+1}\right|\right) = 10\log_{10}\left(P_{k+1}\right) \tag{D.5}$$

D.1 PERIODOGRAM METHOD

Periodogram is generally used for sequence data with high Signal-to-Noise Ratio (SNR) and long data length. It estimates the power spectral density (PSD) using Equation (D.6), and can be interpreted as how much power is present at unit frequency (Smith, 1997) or the Fourier transform of the sample autocorrelation function. In the current study, it has the unit of voltage squared per hertz.

$$PSD_k = \left|X_k\right|^2 / N = \sum_{j=1}^{N} R_{xx,\,j-1} e^{-i2\pi(k-1)(j-1)/N}, \; k = 1, 2, ..., N \tag{D.6}$$

To compensate the spectral leakage due to discrete frequency, the Periodogram is modified as shown in Equation (D.7).

$$PSD_k = \frac{1}{NU}\left|\sum_{j=1}^{N} x_k e^{-i2\pi(k-1)(j-1)/N}\right|^2 \tag{D.7}$$

where

$$U = \frac{1}{N}\sum_{n=1}^{N}\left|w_n\right|^2$$

The U is the window normalization constant to ensure the average power is independent of window chooses. The window w_n can be either rectangular or nonrectangular. For rectangular window, the amplitude of side-lobes is reduced due to the spurious frequencies introduced when the window abruptly truncates the signals at the edges; for the nonrectangular window, the spurious frequencies are less.

A MATLAB code used to estimate PSD using Periodogram, which was implemented mostly to identify noise sources in the study.

```
% PSD using Periodogram
ChannelNumber = 1; % channel number from force transducer
DataNew = Data(:,ChannelNumber)-mean(Data(:,ChannelNumber)); % sequence
input in voltage
Fs = ActualRate; % sampling rate
nfft = length(DataNew); % number of total points in frequency domain,
yielding frequency resolution
[SGPSD,f] = periodogram(DataNew(:,1),[],'onesided',nfft,Fs); % estimate
PSD of DataNew
Figure; plot(f,SGPSD); axis tight;
```

D.2 WELCH METHOD

Welch’s method is used for data sets with lower SNR. The data set is divided into several segments, and then identically overlaps these segments to generate the overlapping segments. Applying the modified periodogram to each overlapping segment estimates the PSD. Averaging estimated PSD yields the final expression of the estimation, which results in lower variance of the estimation than Periodogram. Equation (D.8) shows the compact form of Welch’s method.

$$PSD_{k+1} = \frac{1}{NF_s U} \int_{-F_s/2}^{F_s/2} \left| W\left(f - f'\right)\right|^2 PSD\left(f'\right) df' \tag{D.8}$$

A MATLAB code used to estimate PSD using Welch’s method is given below.

```
% PSD using Welch’s method
ChannelNumber = 1; % channel number from force transducer
DataNew = Data(:,ChannelNumber)-mean(Data(:,ChannelNumber)); % sequence
input in voltage
window = ???; % window size
noverlap = 0.5; % percentage of samples common to two adjacent segments
nfft = length(DataNew); % number of total points in frequency domain,
yielding frequency resolution
Fs = ActualRate; % sampling rate
[SGPSD,f] = pwelch(DataNew(:,1),window,noverlap,nfft,Fs,'onesided'); %
estimate PSD of DataNew
Figure; plot(f,SGPSD); axis tight;
```

APPENDIX E

DETERMINATION OF FILTER CUTOFF FREQUENCY AND ITS EFFECTS

Since wing motion acceleration gives considerable frequency regions, comparable with motion position and velocity, we are interested in its response in frequency domain and inspect the spectrum by power spectrum density (PSD). Estimation of PSD is accomplished using periodogram. The objective is to determine proper cutoff frequency to process data from direct force measurement using digital filter.

E.1 CUTOFF FREQUENCY

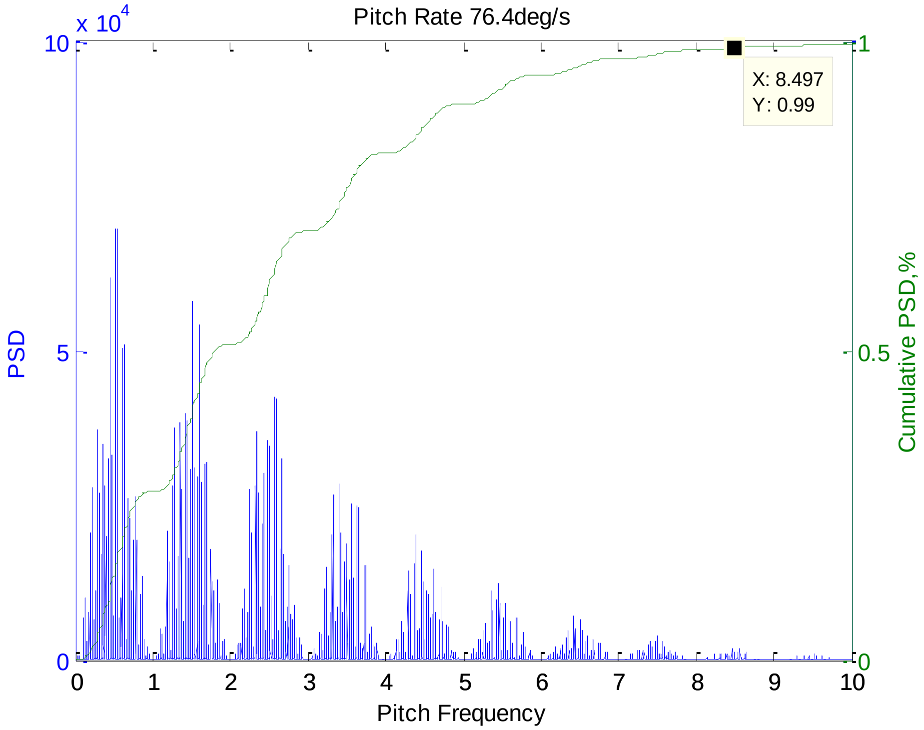

Figure E.1 An example of spectrum and energy content of acceleration kinematics for pitch rate 76.4 deg/s.

Input signal for periodogrm is motion acceleration in time; the signal structure is similar to experimental work. Pre-triggered and indication pulse duration were set to 5 seconds and 0.5 seconds, respectively. And holding and relaxation durations were at least 130 and 30 convective times, respectively, to ensure the flow approaching the steady state and to return the flow to undisturbed initial condition. In these durations, samples were padded with zero-acceleration using sampling rate of 5000Hz. Final input signal contains 20 repeated motion acceleration to enhance signal strength in frequency domain.

An example of spectrum distribution with respect to pitch frequency is shown in Figure E.1; it is estimated using kinematics with pitch rate of 76.4 °/s. In the figure, we find frequency envelopes are enclosed within pitch frequency and their magnitudes decay with increasing pitch frequency. Several spikes are observed within each frequency envelope due to discrete samples, which indicates rational frequency resolution in use. This phenomenon is called leakage and is one of of the periodogram features.

Moreover, integrating PSD from zero to a specific frequency determines the amount of energy/information within the frequency, as shown as a green curve in the figure. This observation suggests selection of cutoff frequency for direct force measurement is the capability of retaining energy/information of kinematics. Data cursor shown in the figure reveals 99-percent energy/information of kinematics is contained within frequency of 14.4Hz. A simple MATLAB script shown below is used to interpolate frequency at energy content of interest.

```
Percentage = 0.99; % specify percentage of energy contents
x = CPSD/max(CPSD); % normalize PSD
[temp1,i,j] = unique(x); % make sure x being distinct
interp1(temp1,f(i),Percentage,'cubic') % interpolate corresponding
frequency
```

E.2 EFFECTS OF FILTERING

We would like to maintain all information from wing kinematics after filtering force data; however, there may be many noises interfering with force sensor, which makes the task difficult. The compensation is to retain as much energy and information as possible; hence, effects of filtering and cutoff frequency become important. For all cases considered in the study, we employed low-pass zero-phase first-order Butterworth filter, the detailed discussion in selection of this filter is provided in Section 2.5.2.

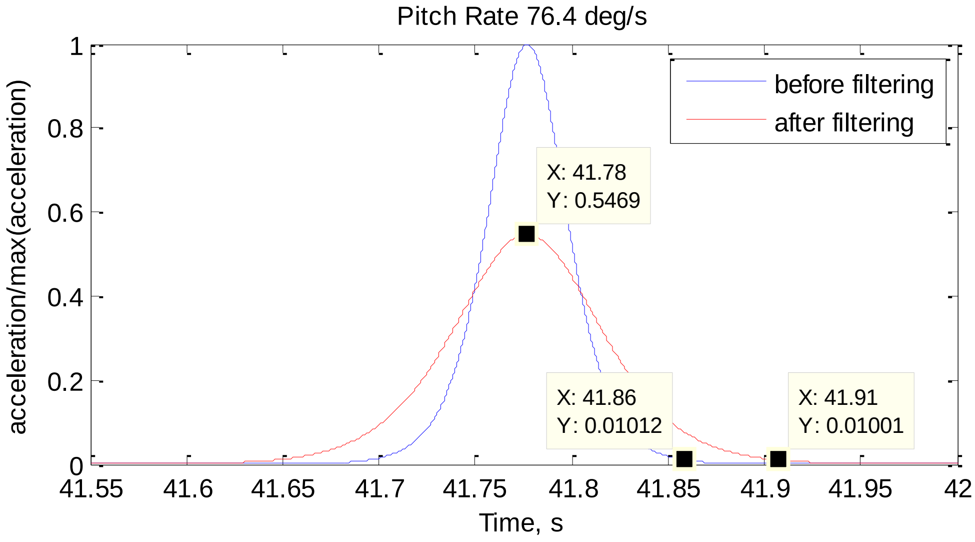

Figure E.2 Behavior of acceleration kinematics before and after low-pass zero-phase first-order two-path Butterworth filter.

Figure E.2 shows the effects of filtering to maintain 90% information of kinematics from pitch rate of 76.4 °/s. The profile of motion acceleration is provided due to association with non-circulatory apparent mass effects. It is observed that motion acceleration becomes shorter and wider. Similar change is expected on effects relative to motion acceleration in the measurement. The attenuation of motion acceleration is evaluated using Equation (E.1).

$$dB = 20\log 10\left(A_2 / A_1\right) \tag{E.1}$$

where A_1 is peak amplitude before filtering and A_2 is peak amplitude after filtering.

Change of acceleration width is evaluated using Equation (E.2) according to times on the marginal distribution where 1% of maximum acceleration is exists.

$$W = \left|t_{i+1\%} - t_i\right|_{after} / \left|t_{i+1\%} - t_i\right|_{before} \tag{E.2}$$

For all kinematics of interest, using cutoff frequency to retain 90% energy of kinematics gives 53% of attenuation of acceleration and 1.6 times of acceleration width. Effects of filtering for kinematics of interest were tabulated in Table E.1-Table E.5.

Table E.1 Effects of filtering for pitch rate 155°/s and β = 27.2%. *According to additional holding and relaxation durations being 40 and 9 seconds, respectively; frequency resolution is 0.9857 mHz.*

α'_m, °/s		Variance	99%	95%	90%	85%	80%	75%	70%	65%	60%	55%	50%
155	f ,Hz		15.242	11.277	8.7602	8.0665	6.1245	5.6283	5.3112	5.0144	4.7170	4.3995	2.9921
	Path	Effects											
	1	*dB*	-1.6388	-2.4399	-3.2945	-3.6108	-4.7985	-5.2028	-5.491	-5.785	-6.107	-6.486	-8.812
		W	1.125	1.232	1.373	1.431	1.672	1.762	1.829	1.898	1.976	2.070	2.697
	2	*dB*	-2.8633	-4.1146	-5.3892	-5.8481	-7.5221	-8.0774	-8.4698	-8.868	-9.302	-9.809	-12.939
		W	1.233	1.407	1.621	1.705	2.046	2.169	2.260	2.354	2.459	2.586	3.419
	3	*dB*	-3.831	-5.3610	-6.8679	-7.4003	-9.3085	-9.9341	-10.375	-10.824	-11.312	-11.887	-15.511
		W	1.329	1.555	1.820	1.923	2.334	2.482	2.589	2.701	2.826	2.976	3.944
	4	*dB*	-4.6276	-6.3441	-7.9943	-8.57	-10.617	-11.288	-11.763	-12.248	-12.780	-13.409	-17.441
		W	1.417	1.684	1.991	2.110	2.577	2.744	2.866	2.992	3.133	3.301	4.297

Table E.2 Effects of filtering for pitch rate 76.4°/s and β = 13.9%. *According to additional holding and relaxation durations being 40 and 6 seconds, respectively; frequency resolution is 1.034 mHz.*

α'_m, °/s		Variance	99%	95%	90%	85%	80%	75%	70%	65%	60%	55%	50%
76.4	f ,Hz		14.435	10.669	8.7145	7.5283	6.2394	5.8861	5.4491	4.4920	4.2221	3.9723	3.0633
	Path	Effects											
	1	*dB*	-1.690	-2.511	-3.195	-3.758	-4.564	-4.833	-5.202	-6.193	-6.529	-6.869	-8.408
		W	1.131	1.243	1.355	1.458	1.621	1.679	1.762	1.997	2.081	2.168	2.571
	2	*dB*	-2.945	-4.223	-5.243	-6.059	-7.195	-7.567	-8.073	-9.397	-9.839	-10.281	-12.235
		W	1.243	1.424	1.594	1.745	1.975	2.055	2.168	2.482	2.590	2.696	3.073
	3	*dB*	-3.933	-5.491	-6.697	-7.643	-8.935	-9.352	-9.915	-11.372	-11.852	-12.330	-14.420
		W	1.342	1.576	1.787	1.971	2.249	2.345	2.478	2.824	2.927	3.018	3.259
	4	*dB*	-4.744	-6.488	-7.809	-8.829	-10.206	-10.647	-11.24	-12.761	-13.259	-13.753	-15.910
		W	1.433	1.709	1.954	2.165	2.479	2.585	2.729	3.053	3.131	3.192	3.332

Table E.3 Effects of filtering for pitch rate 37.5°/s and β = 13.9%. *According to additional holding and relaxation durations being 40 and 6 seconds, respectively, frequency resolution is 0.9899 mHz.*

α'_m, °/s		Variance	99%	95%	90%	85%	80%	75%	70%	65%	60%	55%	50%
37.5	f		7.0864	5.2551	4.2994	3.7020	3.0458	2.8867	2.6672	2.1893	2.0699	1.9506	1.4925
	Path	Effects											
	1	*dB*	-1.689	-2.499	-3.1745	-3.749	-4.587	-4.835	-5.214	-6.229	-6.534	-6.865	-8.452
		W	1.131	1.241	1.351	1.456	1.626	1.680	1.764	2.006	2.082	2.167	2.582
	2	*dB*	-2.943	-4.205	-5.214	-6.046	-7.228	-7.571	-8.089	-9.445	-9.845	-10.275	-12.290
		W	1.243	1.421	1.589	1.742	1.982	2.056	2.172	2.494	2.591	2.694	3.080
	3	*dB*	-3.931	-5.470	-6.663	-7.628	-8.971	-9.356	-9.933	-11.424	-11.859	-12.324	-14.479
		W	1.342	1.572	1.781	1.968	2.257	2.345	2.482	2.836	2.929	3.017	3.263
	4	*dB*	-4.741	-6.464	-7.772	-8.813	-10.245	-10.651	-11.259	-12.815	-13.266	-13.747	-15.970
		W	1.432	1.704	1.947	2.161	2.488	2.586	2.733	3.062	3.132	3.192	3.333

Table E.4 Effects of filtering for pitch rate 25.7°/s and β = 6.49%. *According to additional holding and relaxation durations being 40 and 9 seconds, respectively, frequency resolution is 0.9253 mHz.*

Variance α'_m, °/s			99%	95%	90%	85%	80%	75%	70%	65%	60%	55%	50%
25.7	f		10.453	7.5518	6.0639	5.3560	4.7605	4.2032	3.7204	3.2367	3.0686	2.6226	2.4556
	Path	Effects											
	1	*dB*	-1.668	-2.553	-3.307	-3.791	-4.288	-4.854	-5.446	-6.168	-6.457	-7.344	-7.732
		W	1.128	1.249	1.375	1.464	1.564	1.684	1.818	1.991	2.063	2.296	2.403
	2	*dB*	-2.910	-4.286	-5.407	-6.106	-6.811	-7.596	-8.403	-9.365	-9.744	-10.891	-11.385
		W	1.238	1.434	1.623	1.754	1.894	2.062	2.245	2.480	2.577	2.888	3.031
	3	*dB*	-3.889	-5.566	-6.888	-7.697	-8.500	-9.384	-10.281	-11.336	-11.749	-12.986	-13.513
		W	1.336	1.588	1.823	1.982	2.152	2.353	2.572	2.851	2.966	3.334	3.502
	4	*dB*	-4.693	-6.571	-8.016	-8.887	-9.745	-10.681	-11.623	-12.724	-13.151	-14.428	-14.97
		W	1.426	1.723	1.995	2.178	2.371	2.599	2.846	3.161	3.290	3.705	3.893

Table E.5 Effects of filtering for pitch rate 12.56°/s and β = 4.64%. *According to additional holding and relaxation durations being 40 and 6 seconds, respectively, frequency resolution is 0.9046 mHz.*

Variance α'_m, °/s			99%	95%	90%	85%	80%	75%	70%	65%	60%	55%	50%
12.56	f		7.0910	5.1446	4.1461	3.5649	3.1998	2.8909	2.5995	2.3451	2.0725	1.8179	1.5998
	Path	Effects											
	1	*dB*	-1.687	-2.566	-3.309	-3.903	-4.366	-4.828	-5.341	-5.865	-6.527	-7.268	-8.026
		W	1.130	1.251	1.375	1.486	1.580	1.678	1.793	1.917	2.081	2.276	2.486
	2	*dB*	-2.941	-4.306	-5.410	-6.267	-6.920	-7.561	-8.260	-8.963	-9.836	-10.794	-11.755
		W	1.242	1.437	1.624	1.785	1.917	2.054	2.212	2.380	2.601	2.861	3.141
	3	*dB*	-3.928	-5.590	-6.892	-7.881	-8.623	-9.345	-10.123	-10.897	-11.849	-12.881	-13.907
		W	1.342	1.592	1.824	2.020	2.179	2.344	2.532	2.732	2.994	3.301	3.632
	4	*dB*	-4.737	-6.597	-8.020	-9.084	-9.876	-10.640	-11.458	-12.267	-13.255	-14.32	-15.374
		W	1.432	1.728	1.996	2.221	2.402	2.589	2.802	3.027	3.322	3.668	4.039

APPENDIX F

UNCERTAINTY ANALYSIS FOR DIRECT FORCE MEASUREMENT

F.1 UNCERTAINTY FOR LIFT/DRAG

The parameters commonly used for aerodynamics are lift force and drag force; both are evaluated by three independent variables from our direct force measurement: axial force (F_A), normal force (F_N), and angle of attack (α), and given in Equations (F.1) and (F.2), respectively.

$$L = -F_A \sin\alpha + F_N \cos\alpha \tag{F.1}$$

$$D = F_A \cos\alpha + F_N \sin\alpha \tag{F.2}$$

Defining the uncertainty for each independent variable as their corresponding standard deviation in the measurement and denoted by w_{F_A}, w_{F_N}, and w_α, the uncertainty for lift and drag can be formulated using Equations (F.3) and (F.4), respectively.

$$w_L = \left[\left(w_{F_A} \frac{\partial L}{\partial F_A} \right)^2 + \left(w_{F_N} \frac{\partial L}{\partial F_N} \right)^2 + \left(w_\alpha \frac{\partial L}{\partial \alpha} \right)^2 \right]^{1/2} \tag{F.3}$$

$$w_D = \left[\left(w_{F_A} \frac{\partial D}{\partial F_A} \right)^2 + \left(w_{F_N} \frac{\partial D}{\partial F_N} \right)^2 + \left(w_\alpha \frac{\partial D}{\partial \alpha} \right)^2 \right]^{1/2} \tag{F.4}$$

where the derivatives of lift and drag with respect to each independent variable are called sensitivity coefficients, they are derived and given as follows.

$$\frac{\partial L}{\partial F_A} = -\sin\alpha$$

$$\frac{\partial L}{\partial F_N} = \cos\alpha$$

$$\frac{\partial L}{\partial \alpha} = -F_A \cos\alpha - F_N \sin\alpha$$

$$\frac{\partial D}{\partial F_A} = \cos\alpha$$

$$\frac{\partial D}{\partial F_N} = \sin\alpha$$

$$\frac{\partial D}{\partial \alpha} = -F_A \sin\alpha + F_N \cos\alpha$$

Substituting sensitivity coefficients into Equations (F.3) and (F.4), we could find the uncertainties for lift and drag forces, as shown in Equations (F.5) and (F.6), respectively. They have the same unit as their representatives.

$$w_L = \left\{ \left(-w_{F_A} \sin\alpha\right)^2 + \left(w_{F_N} \cos\alpha\right)^2 + \left[w_\alpha \left(-F_A \cos\alpha - F_N \sin\alpha\right)\right]^2 \right\}^{1/2} \tag{F.5}$$

$$w_D = \left\{ \left(w_{F_A} \cos\alpha\right)^2 + \left(w_{F_N} \sin\alpha\right)^2 + \left[w_\alpha \left(-F_A \sin\alpha + F_N \cos\alpha\right)\right]^2 \right\}^{1/2} \tag{F.6}$$

In present study, we say the angle of attack α is well positioned by Rotary Table; the last terms in Equations (F.5) and (F.6) are dropped off and the equations are reduced to Equations (F.7) and (F.8).

$$w_L = \left\{ \left(-w_{F_A} \sin\alpha\right)^2 + \left(w_{F_N} \cos\alpha\right)^2 \right\}^{1/2} \tag{F.7}$$

$$w_D = \left\{ \left(w_{F_A} \cos\alpha\right)^2 + \left(w_{F_N} \sin\alpha\right)^2 \right\}^{1/2} \tag{F.8}$$

F.2 UNCERTAINTY FOR LIFT/DRAG COEFFICIENT

Lift and drag coefficients are popularly employed to compare data between experimental and computational approaches in different test flow condition. Non-dimensionalizing lift and drag forces with dynamic pressure ($\rho U_\infty^2/2$) and wing area (S=bc), the lift and drag coefficients are obtained and given in Equations (F.9) and (F.10), respectively.

$$C_L = 2L / \rho U_\infty^2 S = C_L \left\{L, c, b, U_\infty\right\} \tag{F.9}$$

$$C_D = 2D / \rho U_\infty^2 S = C_D \left\{D, c, b, U_\infty\right\} \tag{F.10}$$

Using the same procedure demonstrated in the preceding section, the uncertainties for lift and drag coefficients are obtained and expended in Equations (F.11) and (F.12), respectively.

$$
\begin{aligned}
w_{c_L} &= \left\{ \left(w_L \frac{\partial C_L}{\partial L} \right)^2 + \left(w_c \frac{\partial C_L}{\partial c} \right)^2 + \left(w_b \frac{\partial C_L}{\partial b} \right)^2 + \left(w_{U_\infty} \frac{\partial C_L}{\partial U_\infty} \right)^2 \right\}^{1/2} \\
&= \left\{ \left(w_L \frac{C_L}{L} \right)^2 + \left(w_c \frac{C_L}{c} \right)^2 + \left(w_b \frac{C_L}{b} \right)^2 + \left(w_{U_\infty} \frac{2C_L}{U_\infty} \right)^2 \right\}^{1/2}
\end{aligned}
\tag{F.11}
$$

$$
\begin{aligned}
w_{c_D} &= \left\{ \left(w_D \frac{\partial C_D}{\partial D} \right)^2 + \left(w_c \frac{\partial C_D}{\partial c} \right)^2 + \left(w_b \frac{\partial C_D}{\partial b} \right)^2 + \left(w_{U_\infty} \frac{\partial C_D}{\partial U_\infty} \right)^2 \right\}^{1/2} \\
&= \left\{ \left(w_D \frac{C_D}{D} \right)^2 + \left(w_c \frac{C_D}{c} \right)^2 + \left(w_b \frac{C_D}{b} \right)^2 + \left(w_{U_\infty} \frac{2C_D}{U_\infty} \right)^2 \right\}^{1/2}
\end{aligned}
\tag{F.12}
$$

where the uncertainty for wing geometry is w_b=w_c=0.5mm from the ruler resolution, and the uncertainty for free-stream velocity ($w_{U\infty}$) is measured using 2D PIV configuration.

APPENDIX G

WING DESIGN AND INERTIA

In design phase, wing planform geometry was generated using SolidWorks. Three wing planforms with the same geometry aspect ratio 2 were considered, including those with rectangular, trapezoidal, and triangular wings. All wings have mean chord length of 2”, full span length of 5.25”, and rounded edges. During the test, 4” span was immersed in the water, and water surface regards as symmetrical plane, resulting in effective aspect ratio of 4. Pivot axis locations were arranged by hole-patterns at three locations, including leading edge, mid-chord, and trailing edge, and being coincident with sensor axis.

The moment of inertia contributed to the sensor, including wing itself and a sensor adapter, is found using Equation (G.1), which can be evaluated directly by SolidWorks in the directory *Tools\Mass Properties*. It is noted that the estimation gives ideal values assuming the test condition in vacuum. If surrounding fluid is water, the estimation may not be in a good agreement. In addition, the wing was made of acrylic and the sensor adaptor was made of aluminum, their corresponding material properties are given in Table G.1 for estimation moment of inertia.

$$I = \begin{bmatrix} I_{xx} & I_{xy} & I_{xz} \\ I_{yx} & I_{yy} & I_{yz} \\ I_{zx} & I_{zy} & I_{zz} \end{bmatrix} \tag{G.1}$$

Table G.1 Material property of wing and sensor adaptor.

Properties / Material	Density, kg/m^3	Poisson ratio	Young’s Modulus, GPa	Shear Modulus, GPa
Aluminum	2700	0.35	70	26
Acrylic	1200	0.35	3	0.89

where

$$
\begin{aligned}
I_{xx} &= \int \left(y^2 + z^2 \right) dm \\
I_{yy} &= \int \left(x^2 + z^2 \right) dm \\
I_{zz} &= \int \left(x^2 + y^2 \right) dm \\
I_{xy} = I_{yx} &= -\int \left(xy \right) dm \\
I_{xz} = I_{zx} &= -\int \left(xz \right) dm \\
I_{yz} = I_{zy} &= -\int \left(yz \right) dm
\end{aligned}
$$

To ensure safety of force sensor in use, we estimate torques contributing to force sensor using Equation (G.2).

$$\tau = \begin{Bmatrix} \tau_x \\ \tau_y \\ \tau_z \end{Bmatrix} = \begin{bmatrix} I_{xx} & I_{xy} & I_{xz} \\ I_{yx} & I_{yy} & I_{yz} \\ I_{zx} & I_{zy} & I_{zz} \end{bmatrix} \begin{Bmatrix} \alpha''_x \\ \alpha''_y \\ \alpha''_z \end{Bmatrix} = \left[I \right] \left\{ \alpha'' \right\} \tag{G.2}$$

where [*I*] is momentum of inertia from Equation (G.1), and α''_m is the maximum acceleration from wing kinematics in radian from our cases considered, which is 51.26 rad/s^2 for kinematics with pitch rate 155°/s.

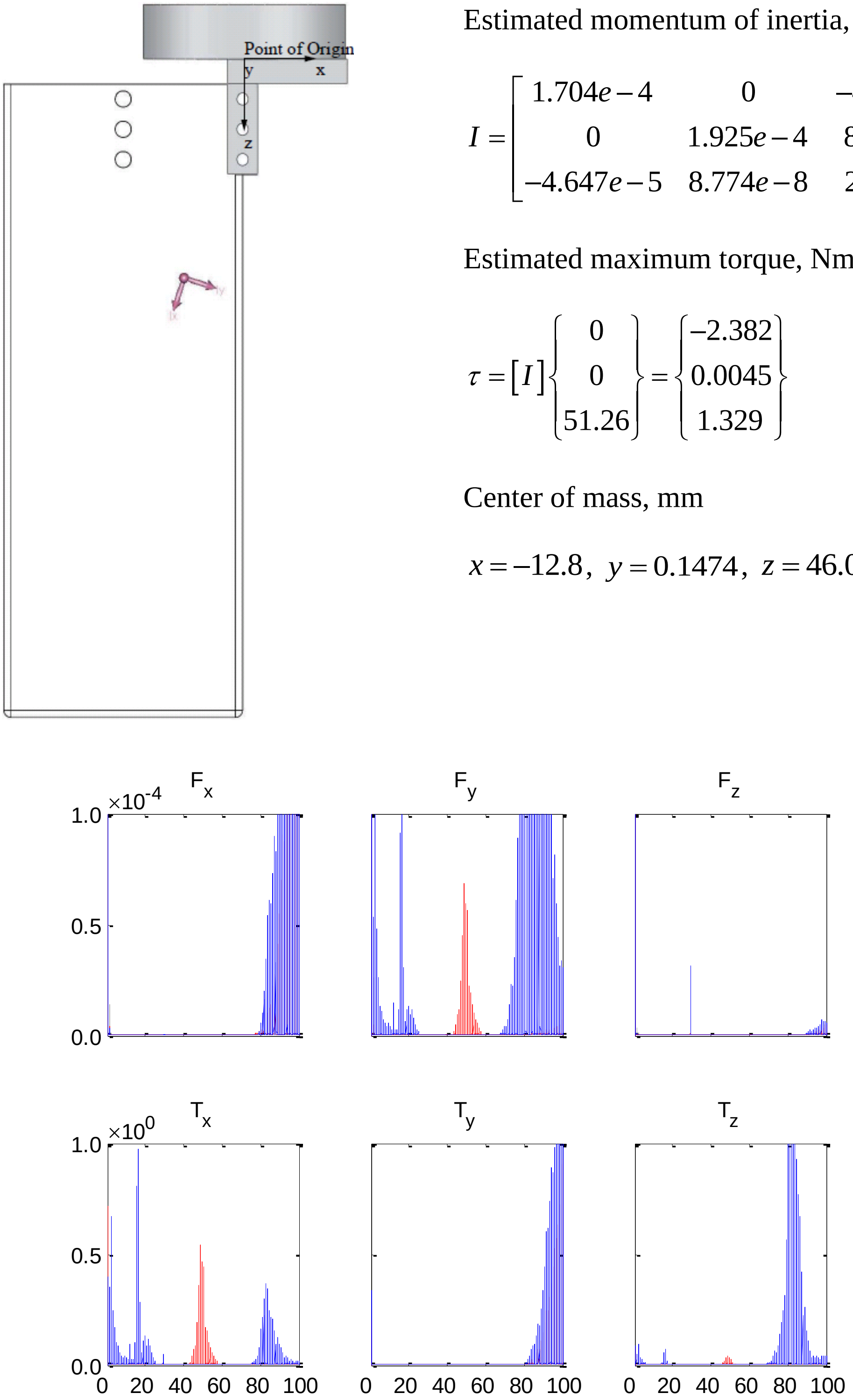

Estimated momentum of inertia, kgm^2

$$I = \begin{bmatrix} 1.704e-4 & 0 & -4.647e-5 \\ 0 & 1.925e-4 & 8.774e-8 \\ -4.647e-5 & 8.774e-8 & 2.593e-5 \end{bmatrix}$$

Estimated maximum torque, Nmm

$$\tau = [I]\begin{Bmatrix} 0 \\ 0 \\ 51.26 \end{Bmatrix} = \begin{Bmatrix} -2.382 \\ 0.0045 \\ 1.329 \end{Bmatrix}$$

Center of mass, mm

$$x = -12.8,\ y = 0.1474,\ z = 46.03$$

Figure G.1 Rectangular wing at leading/trailing edge pivot and spectrum distribution from the sensor Nano43 (SN: FT12311) subject to kinematics with pitch rate 155°/s.

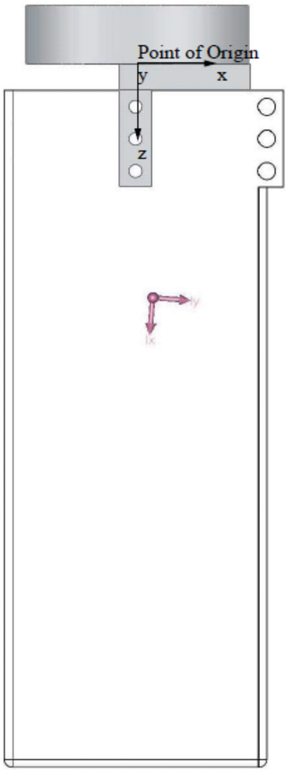

Momentum of inertia, kgm^2

$$I = \begin{bmatrix} 1.704e-4 & 0 & -1.98e-7 \\ 0 & 1.759e-4 & 8.774e-8 \\ -1.98e-7 & 8.774e-8 & 9.315e-6 \end{bmatrix}$$

Torque, Nmm

$$\tau = [I]\begin{Bmatrix} 0 \\ 0 \\ 51.26 \end{Bmatrix} = \begin{Bmatrix} -0.0101 \\ 0.0045 \\ 0.4775 \end{Bmatrix}$$

Center of mass, mm

$$x = 3.032,\ y = 0.1474,\ z = 46.03$$

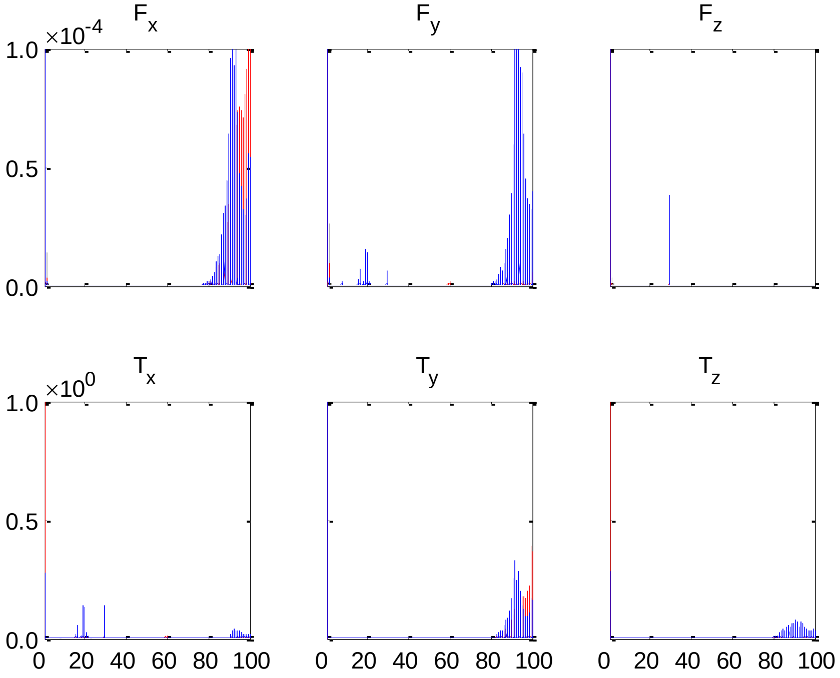

Figure G.2 Rectangular wing at mid-chord edge pivot and spectrum distribution from the sensor Nano43 (SN: FT12311) subject to kinematics with pitch rate 155°/s.

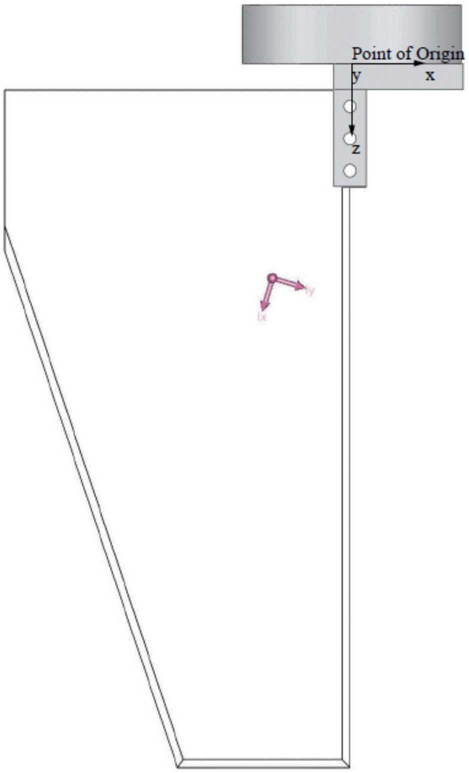

Momentum of inertia, kgm^2

$$I=\begin{bmatrix} 1.525e-4 & 0 & -4.522e-5 \\ 0 & 1.84e-4 & 8.772e-8 \\ -4.522e-5 & 8.772e-8 & 3.532e-5 \end{bmatrix}$$

Torque, Nmm

$$\tau=[I]\begin{Bmatrix} 0 \\ 0 \\ 51.26 \end{Bmatrix}=\begin{Bmatrix} -2.3180 \\ 0.0045 \\ 1.8105 \end{Bmatrix}$$

Center of mass, mm

$$x=-15.54,\ y=0.1398,\ z=42.21$$

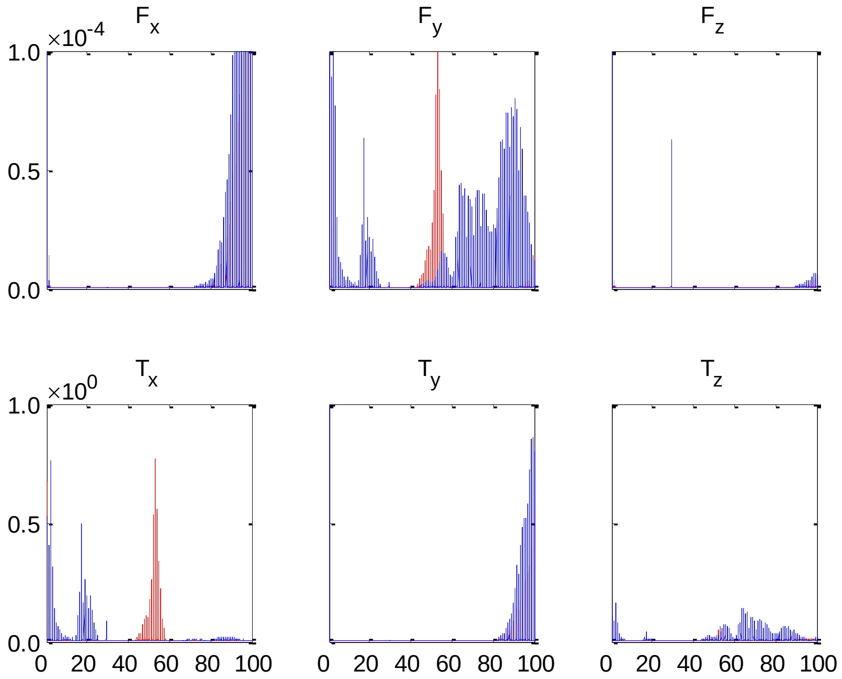

Figure G.3 Trapezoidal wing at leading/trailing edge pivot and spectrum distribution from the sensor Nano43 (SN: FT12311) subject to kinematics with pitch rate 155°/s.

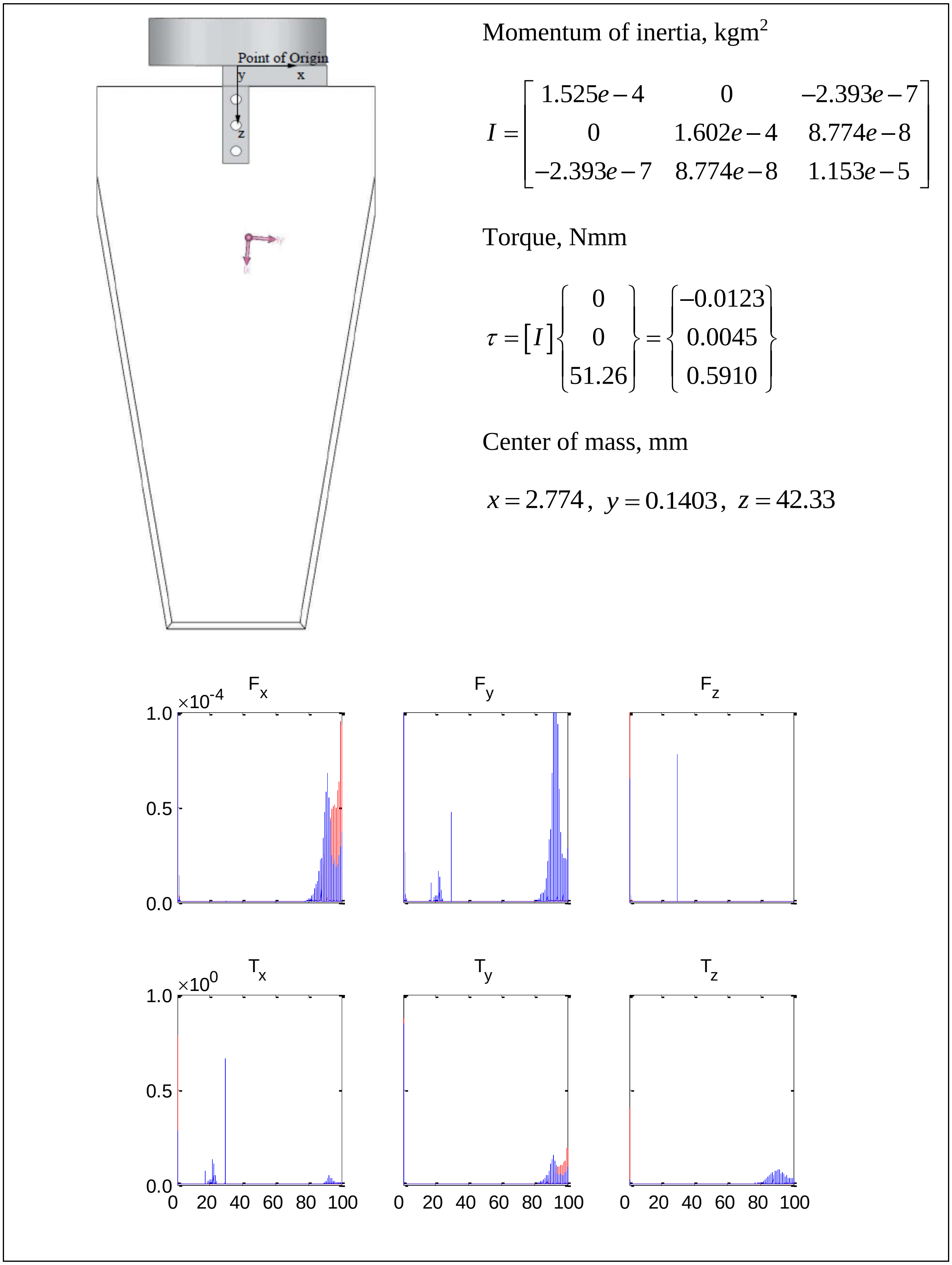

Momentum of inertia, kgm^2

$$I = \begin{bmatrix} 1.525e-4 & 0 & -2.393e-7 \\ 0 & 1.602e-4 & 8.774e-8 \\ -2.393e-7 & 8.774e-8 & 1.153e-5 \end{bmatrix}$$

Torque, Nmm

$$\tau = [I]\begin{Bmatrix} 0 \\ 0 \\ 51.26 \end{Bmatrix} = \begin{Bmatrix} -0.0123 \\ 0.0045 \\ 0.5910 \end{Bmatrix}$$

Center of mass, mm

$$x = 2.774,\ y = 0.1403,\ z = 42.33$$

Figure G.4 Trapezoidal wing at mid-chord pivot and spectrum distribution from the sensor Nano43 (SN: FT12311) subject to kinematics with pitch rate 155°/s.

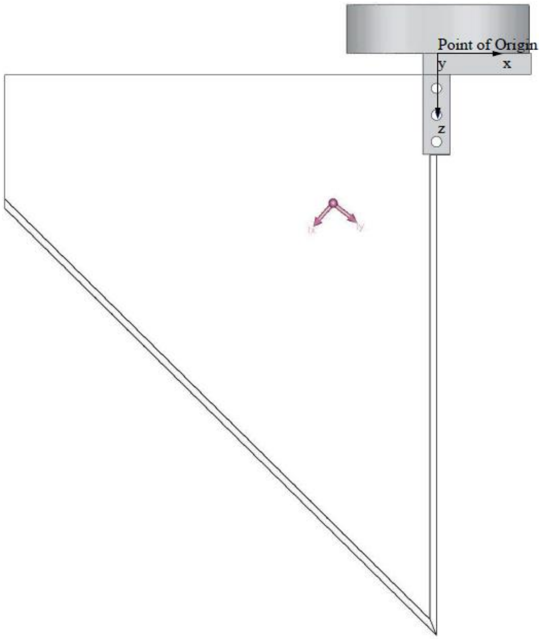

Momentum of inertia, kgm^2

$$I=\begin{bmatrix} 1.162e-4 & 0 & -5.421e-5 \\ 0 & 1.925e-4 & 8.774e-8 \\ -5.421e-5 & 8.774e-8 & 8.018e-5 \end{bmatrix}$$

Torque, Nmm

$$\tau=[I]\begin{Bmatrix} 0 \\ 0 \\ 51.26 \end{Bmatrix}=\begin{Bmatrix} -2.7788 \\ 0.0045 \\ 4.1100 \end{Bmatrix}$$

Center of mass, mm

$$x=-24.66,\ y=0.1275,\ z=35.68$$

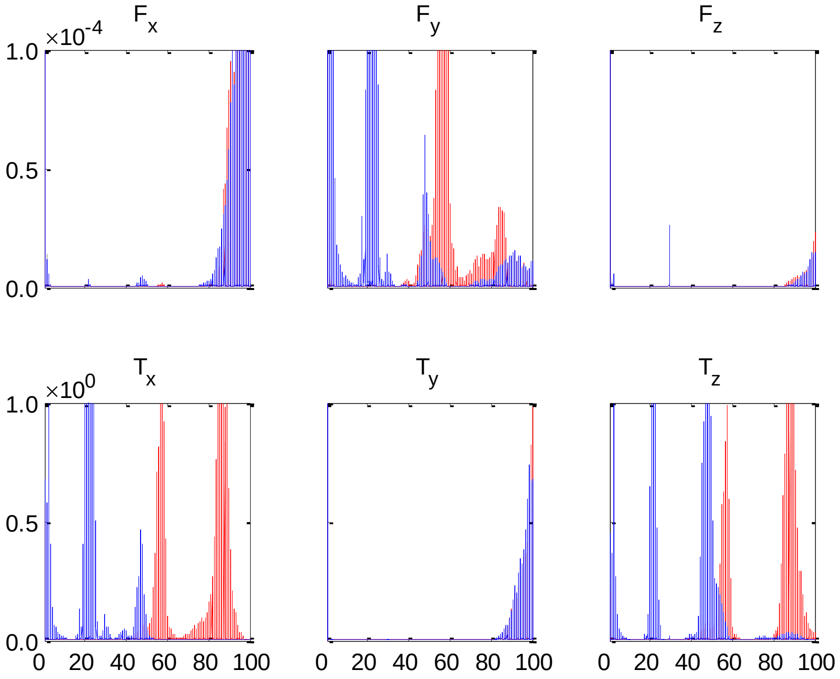

Figure G.5 Triangular wing at leading/trailing edge pivot and spectrum distribution from the sensor Nano43 (SN: FT12311) subject to kinematics with pitch rate 155°/s.

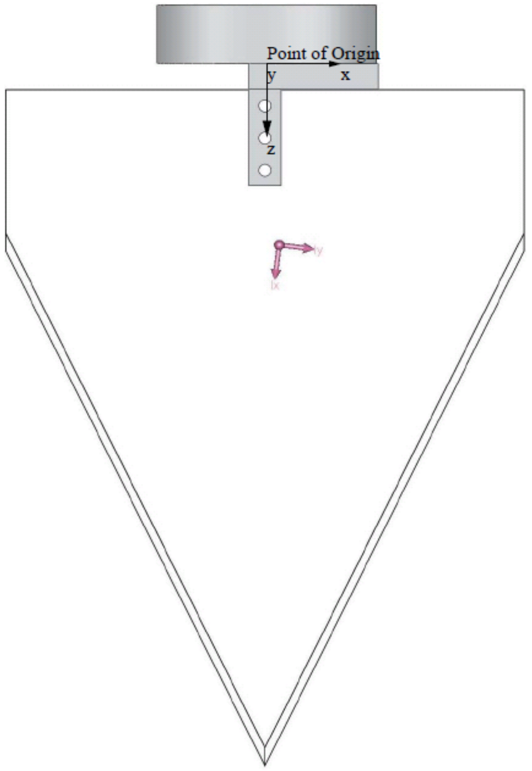

Momentum of inertia, kgm^2

$$I=\begin{bmatrix} 1.163e-4 & 0 & -1.976e-7 \\ 0 & 1.351e-4 & 8.774e-8 \\ -1.976e-7 & 8.774e-8 & 2.267e-5 \end{bmatrix}$$

Torque, Nmm

$$\tau=[I]\begin{Bmatrix} 0 \\ 0 \\ 51.26 \end{Bmatrix}=\begin{Bmatrix} -0.0101 \\ 0.0045 \\ 1.1620 \end{Bmatrix}$$

Center of mass, mm

$$x=2.503,\ y=0.128,\ z=35.81$$

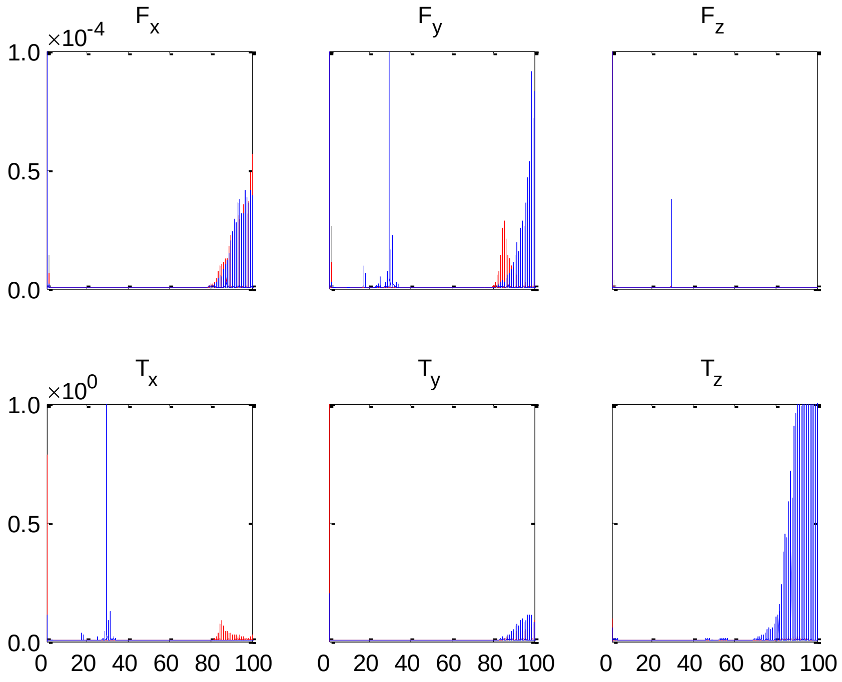

Figure G.6 Triangular wing at mid-chord pivot and spectrum distribution from the sensor Nano43 (SN: FT12311) subject to kinematics with pitch rate 155°/s.

APPENDIX H

LENS-SHIFTED STEREOSCOPIC PIV CALIBRATION

Stereo PIV provides the capability to resolve the instantaneous out-of-plane velocity in addition to the in-plane component. In a common configuration, the image, lens, and object planes are not parallel, resulting in different magnification over the field of view of the image which causes perspective distortion of the image. This configuration is called Scheimpflug condition or angular displacement system. In this report, we examine a different setup, a lens translation (shift) system, providing the same magnification over the field of view of the image. The image, lens, and object planes are parallel, two cameras are placed parallel to each other and a distance apart, the lens of the cameras are shifted transversely to image the same region on the object plane.

To measure the out of plane velocity, several tests have to be conducted to ensure that the following requirements are satisfied:

1.Could we capture the field of view of the interest?

2.The magnification factor has to be in the range 10 to 15 px/mm

3.For magnification in the range of interest, how far away from the object must the cameras be located? Does the flow facility have enough space for the lens-shift stereo PIV setup?

4.Are images recorded by the two cameras of the same flow region different from each other?

H.1 APPARATUS

Two cameras are employed; both are pco.4000 CCD camera with a resolution up to 4008 x 2672 pixels; the pixel spacing is 9 · m. Both cameras are equipped with standard Nikon F-mount adaptors. A perspective control lens, PC-E Micro NIKKOR, is used in each camera. They have a focal length of 85mm and could provide shift and tilt movements of ・ 11.5mm and ・ 8.5^0, respectively. In the tests, the two cameras are placed side by side in front of a blackboard, a ruler (60 cm long) or calibration grid is attached on the blackboard. As shown in Figure H.1, the camera on right is denoted by PIV1, the camera on the left is denoted by PIV2.

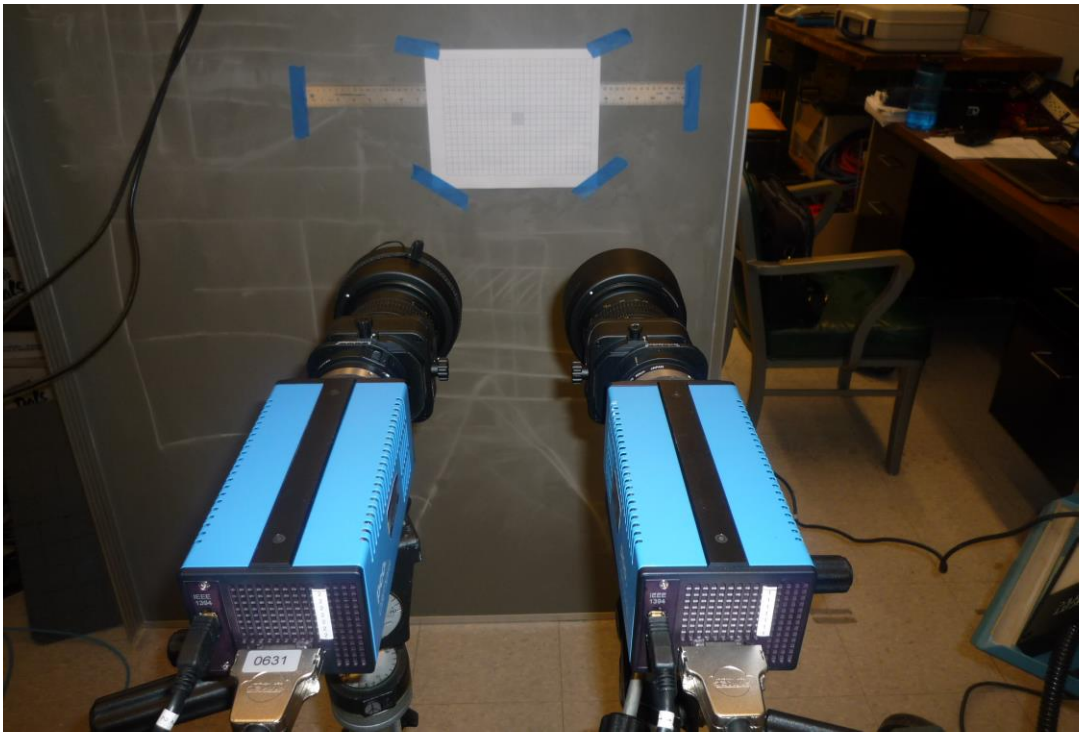

Figure H.1 Configuration of translation stereo PIV pre-test

H.2 MAGNIFICATION AND FIELD OF VIEW OF THE CAMERAS

In the experiment, a wing with 2” chord will be used. We would like to have a field of view in the stream-wise direction 6 times the wing chord, which is approximately 300mm. To satisfy this requirement, both cameras are placed in front of the blackboard at a distance of 0.75m. The images and field of view of both cameras are shown in Figure H.2 and Figure H.3 for PIV1 and PIV2, respectively. In this part of test, the lens is not shifted and the axis of each camera is also the center of image.

The images are analyzed using MATLAB. Several measurement tips are placed on the ruler which is calibrated in SI units to determine the magnification factor. Reading the x location in pixels of neighboring measurement tips, which are 1cm apart in the object plane, the magnification factor is calculated. Three locations are of interest, at the left, center, and right sides of the field of view. Following this procedure, the magnification of camera PIV1, shown inFigure H.2, is 13.3pixel/mm, 13.3pixel/mm, and 13.2pixel/mm, respectively. For camera PIV2 (shown inFigure H.3), the magnification is 13.2pixel/mm, 13.2pixel/mm, and 13.4pixel/mm. The magnification factors in both cameras are likely homogenous within the entire field of view, which indicates that the camera sensor, lens and objected planes are normal to each other within measurement uncertainty and the magnification is within specifications.

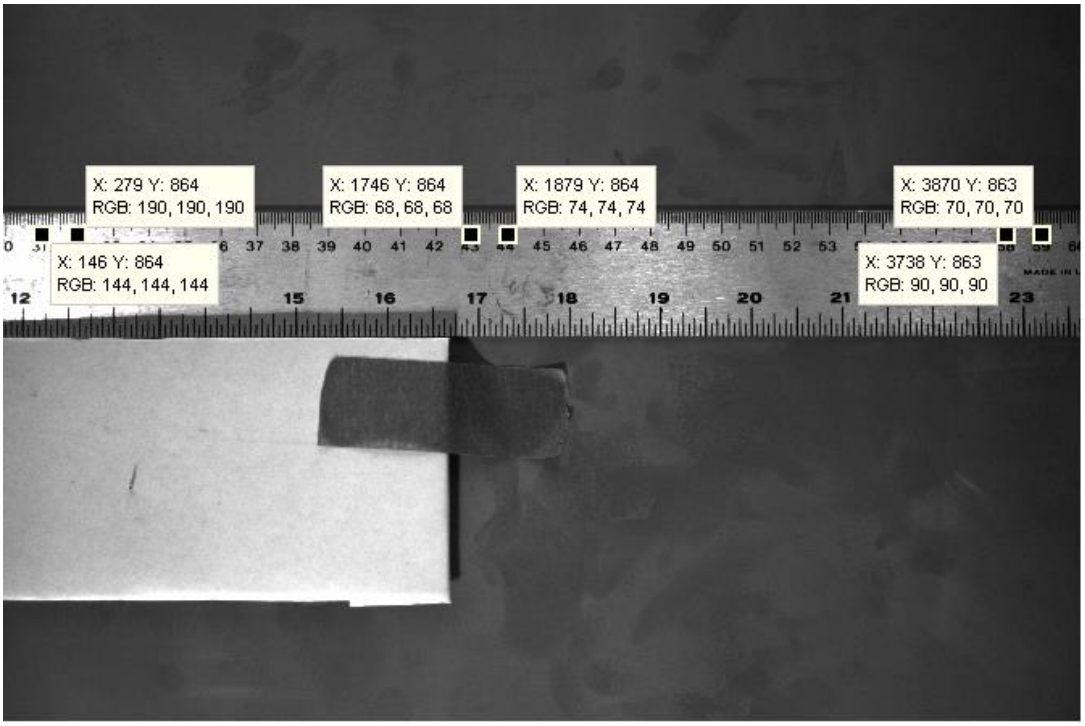

Figure H.2 Field of view from PIV1.

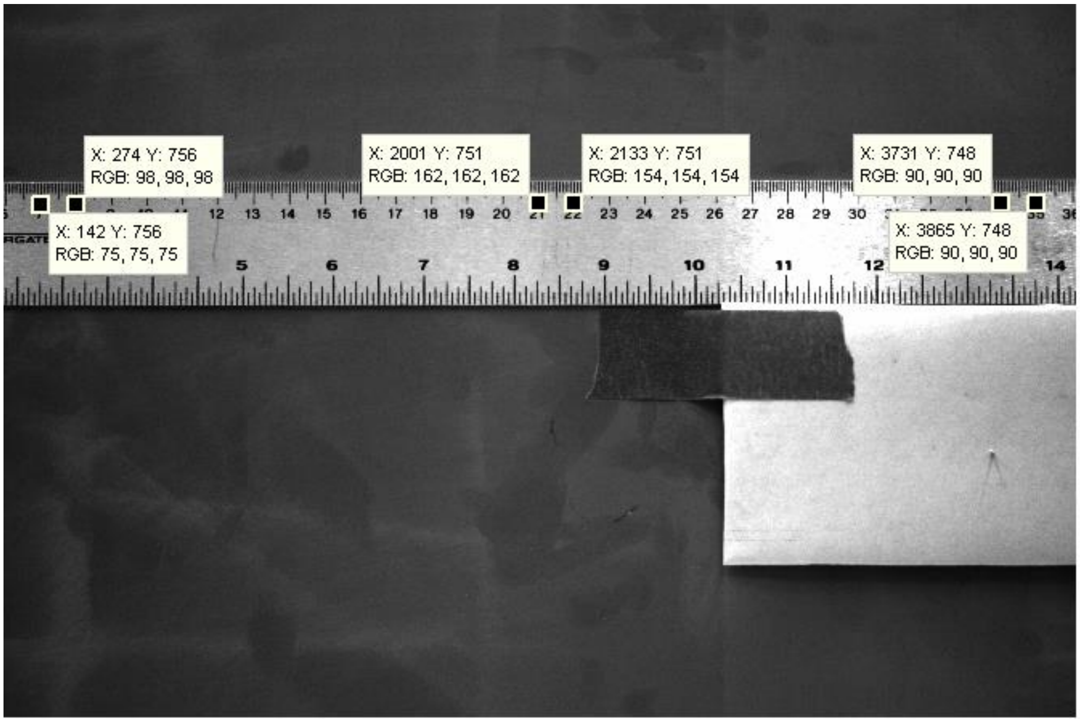

Figure H.3 Field of view from PIV2.

H.3 FIELD OF VIEW OF CAMERAS AFTER LENS SHIFT

Next, we measure the magnification of the cameras when the lens on camera PIV1 is shifted 11.5mm towards camera PIV2, and the lens on camera PIV2 is shifted 11.5mm towards camera PIV1.

Figure H.4 and Figure H.5 show the images after the shifting for PIV1 and PIV2, respectively. For PIV1, the field of view moves to the left side of the ruler, it is shifted from a range of 30 cm-60 cm to 19 cm-49 cm, which is about 11cm total displacement. For PIV2, the field of view changes from a range of 6cm-36 cm to 17 cm-47 cm, which is about 11cm total displacement to the right. The magnification is determined by the measurement tips pairs 1cm apart at the left, center, and right sides of the field of view. Magnification for camera PIV1 is 13.3 pixel/mm, 13.3 pixel/mm, and 13.3 pixel/mm, respectively. For camera PIV2, the magnification is read as 13.3 pixel/mm, 13.3 pixel/mm, and 13.3 pixel/mm, respectively. The magnifications in the field of view are the same within measurement uncertainty compared to the results before the lenses were shifted, and uniform throughout the field of view.

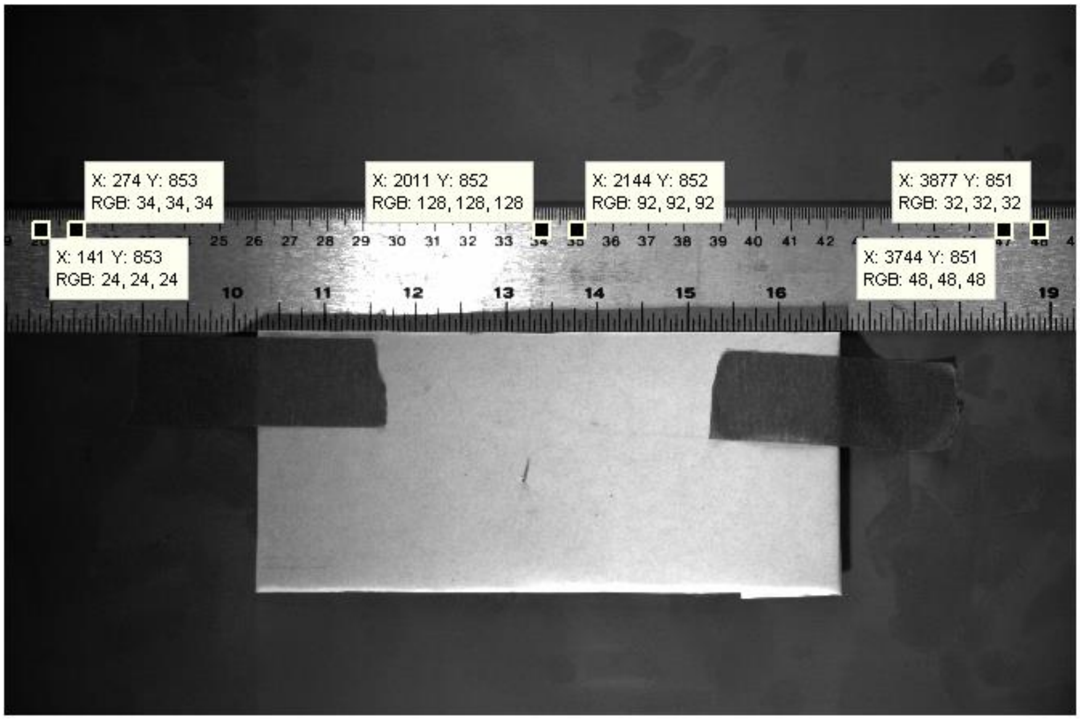

Figure H.4 Field of view from PIV1 after lens shifted 11.5mm.

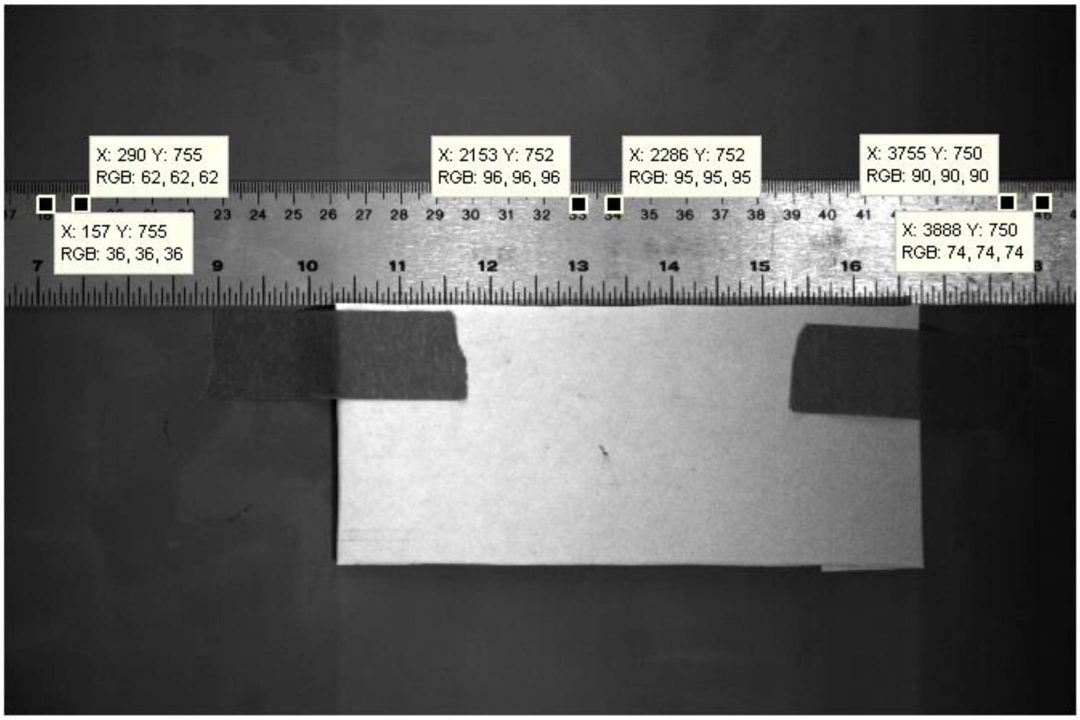

Figure H.5 Field of view of PIV2 after lens shifted 11.5mm.

H.4 ALIGNMENT OF CAMERAS PIV1 AND PIV2

In the previous test, it was observed that the field of view of the two cameras is not the same. To ensure that the two cameras image the same field of view, a calibration plate was used. It consists of a rectangular grid with grid size uniformly spaced 1 cm apart as shown in Figure H.6 and Figure H.7. The center of the calibration plate is located at the center of the grey area, which has to be positioned at the center of the field of view of both cameras.

Figure H.6 and Figure H.7show typical results after centering the field of view of cameras PIV1 and PIV2, respectively. The error is about 2-4 pixels, which is approximately 0.15-0.3 mm. It should be noted the slightly lower image intensity on the left of the camera PIV1 image and on the right of camera PIV2 image. These are believed to be effect of the steep light incidence angle on those parts of the images.

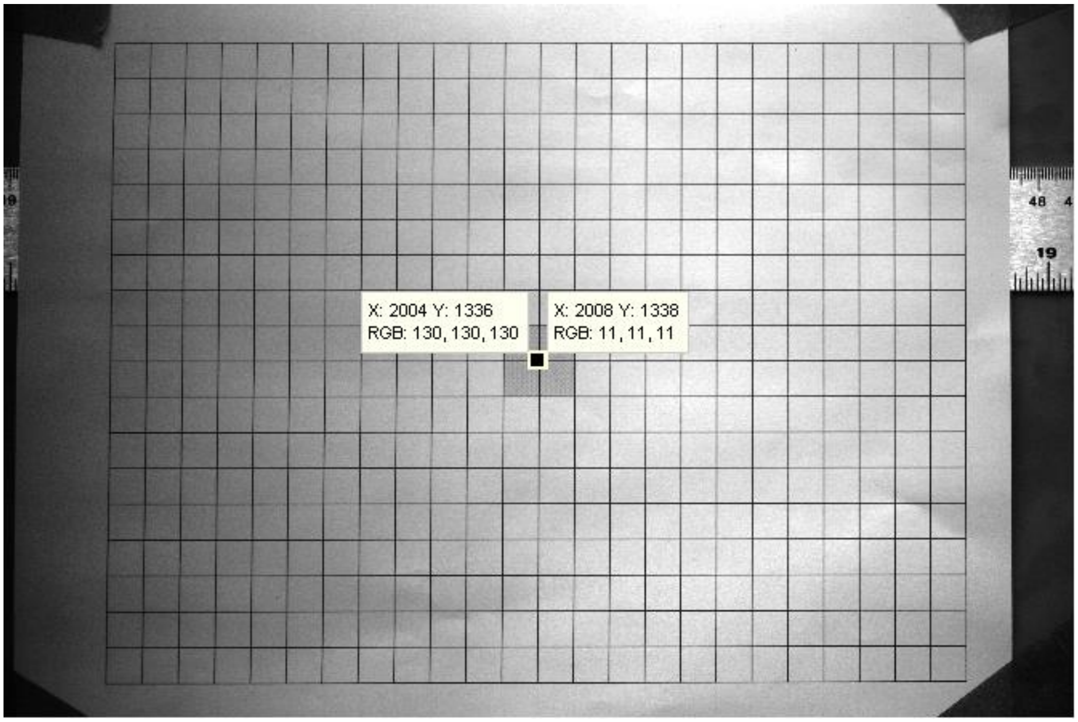

Figure H.6 Field of view of PIV1 with translation of 11.5mm and calibration board.

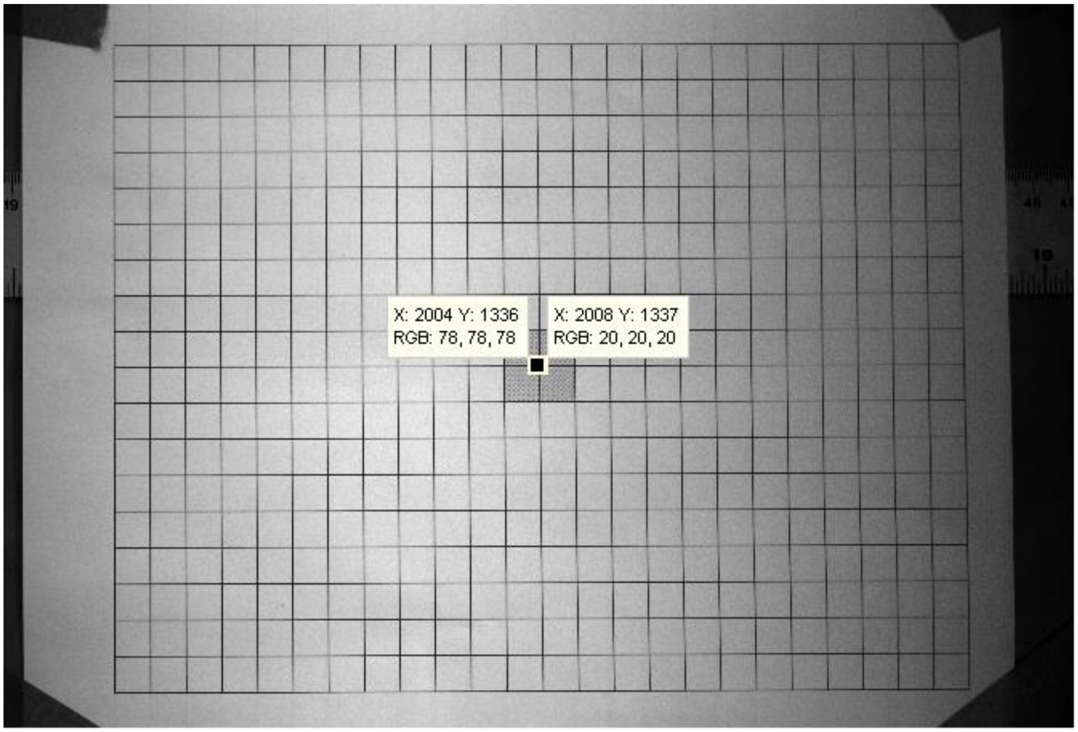

Figure H.7 Field of view of PIV2 with translation of 11.5mm and calibration board.

H.5 DETERMINATION OF THE OBJECT PLANE (P) AND PLANE (Q) DISTANCES

In addition, the distance between the object plane and the lens (denoted by *p*) and the distance between the image plane and the lens (denoted by *q*) are important to characterize the experimental setup. The last part of this report describes the measurement of these distances.

The distances of interest could be found by the definition of magnification factor and the thin lens equation, as given in Eq. (H.1) and Eq. (H.2) respectively.

$$m = -q / p < 0 \tag{H.1}$$

$$1/f = 1/q + 1/p \tag{H.2}$$

There are four variables and two equations. However, in the current setup, the focal length (*f*) and the magnification factor (*m*) are known, and are equal to 85mm and 13.3 pixel/mm (or m = -0.1197), respectively. The distance from the object plane (*p*) and the distance from the image plane (*q*) could be obtained using Eq. (H.3) and Eq. (H.4).

$$p = f\left(1 - 1/m\right) \tag{H.3}$$

$$q = f\left(1 - m\right) \tag{H.4}$$

Therefore, the distance from the object plane (p) is 795.1mm and the distance from the image plane (q) is 95.2mm.

BIBLIOGRAPHY

1. Acharya, M. and Metwally, M. H., "Unsteady Pressure Field and Vorticity Production over a Pitching Airfoil," AIAA Journal, Vol. 30, No. 2, 1992, pp. 403-411.
2. Albertson, J. A., Troutt, T. R., and Kedzie, C. R., "Unsteady Aerodynamic Forces at Low Airfoil Pitching Rates," AIAA Paper 88-2579-CP, June 1988.
3. Anderson, J. D., Fundamentals of Aerodynamics, 5th ed., McGraw-Hill, New York, 2011, Chaps. 4-5.
4. Aono, H. and Liu, H., "Vortical Structure and Aerodynamics of Hawkmoth Hovering," *Journal of Biomechanical Science and Engineering*, Vol. 1, No. 1, 2006, pp. 234-245.
5. Aono, H., Liang, F., and Liu, H., "Near- and Far-Field Aerodynamics in Insect Hovering Flight: an Integrated Computational Study," *The Journal of Experimental Biology*, Vol. 211, 2008, pp. 239-257.
6. Aono, H., Shyy, W., and Liu, H., "Near Wake Vortex Dynamics of a Hovering Hawkmoth," *Acta Mech Sin*, Vol. 25, 2009, pp. 23-36.
7. Baik, Y. S., Aono, H., Rausch, J. M., Bernal, L. P., Shyy, W., and Ol, M. L., "Experimental Study of a Rapidly Pitched Flat Plate at Low Reynolds Number," AIAA Paper 2010-4462, June, 2010.
8. Baik, Y. B., Bernal, L. P., Granlund, K., and Ol, M. V., "Unsteady Force Generation and Vortex Dynamics of Pitching and Plunging Aerofoils," *Journal of Fluid Mechanics*, Vol. 709, 2012, pp. 37-68.
9. Bartholomew, G. A. and Casey, T. M., "Oxygen Consumption of Moths during Rest, Preflight Warm-up, and Flight in Relation to Body Size and Wing Morphology," *The Journal of Experimental Biology*, Vol. 76, 1978, pp. 11-25.

10. Bertin, J. J. and Cummings, R. M., *Aerodynamics for Engineering*, 5th ed., Pearson Prentice-Hall, New Jersey, 2009, Chaps. 6-7.
11. Bishop, N., *The Secrets of Animal Flight*, Houghton Mifflin Company, Boston, 1997.
12. Bullen, R. D. and McKenzie, N. L., "Bat Airframe Design: Flight Performance, Stability and Control in Relation to Foraging Ecology," *Australian Journal of Zoology*, Vol. 49, 2001, pp. 235-261.
13. Bullen, R. D. and McKenzie, N. L., "Scaling bat wingfrequency and amplitude," *The Journal of Experimental Biology*, Vol. 205, 2002, pp. 2615-2626.
14. Casey, T. M., "Energetics and Thermoregulation of Malacosoma Amerocanum (Lepidoptera: Lepidocampidae) during Hovering Flight," *Physiological Zoology*, Vol. 54, No. 3, 1981, pp. 362-371.
15. Casey, T. M., "Flight Energetics and Heat Exchange of Gypsy Moths in Relation to Air Temperature," *The Journal of Experimental Biology*, Vol. 88, 1980, pp. 133-145.
16. Casey, T. M., May, M. L., and Morgan, K. R., "Flight Energetics of Euglossine Bees in Relation to Morphology and Wing Stroke Frequency," *The Journal of Experimental Biology*, Vol. 116, 1985, pp. 271-289.
17. Conger, R. N. and Ramapriant, B. R., "Pressure Measurements on a Pitching Airfoil in a Water Channel," *AIAA Journal*, Vol. 32, No. 1, 1993, pp. 108-115.
18. Currier, J. M., and Fung, K. -Y., "Analysis of the Onset of Dynamic Stall," *AIAA Journal*, Vol. 30, No 10. 1992, pp. 2469-2477.
19. Daely, D. C. and Jumper, E. J., "Experimental Investigation of Dynamic Stall for a Pitching Airfoil," *Journal of Aircraft*, Vol. 21, No. 10, 1984, pp. 831-832.
20. Danthanarayana, W., *Insect Flight: Dispersal and Migration*, Springer-Verlag, New York, 1986.
21. Dudley, R., The Biomechanics of Insect Flight: Form, Function, Evolution, Princeton Press, New Jersey, 2000.
22. Eldredge, J. D. and Wang, C., "High-Fidelity Simulations and Low-Order Modeling of a Rapidly Pitching Plate," AIAA Paper 2010-4281, June 2010.

23. Eldredge, J. D., Wang, C., and Ol, M. V. “A Computational Study of a Canonical Pitch-up, Pitch-down Wing Maneuver,” AIAA Paper 2009-3687, June 2009.
24. Ellington, C. P, “The aerodynamics of Hovering Insect Flight. II. Morphological Paratemers,” Philosophical *Transactions of the Royal Society of London. Series B, Biological,* Vol. 305, No. 1122, 1984b, pp. 17-40.
25. Ellington, C. P, “The aerodynamics of Hovering Insect Flight. III. Kinematics,” Philosophical *Transactions of the Royal Society of London. Series B, Biological*, Vol. 305, No. 1122, 1984c, pp. 41-78.
26. Ellington, C. P., “The aerodynamics of Hovering Insect Flight. I. The Quasi-Steady Analysis,” Philosophical *Transactions of the Royal Society of London. Series B, Biological*, Vol. 305, No. 1122, 1984a, pp. 1-15.
27. Feduccia, A., *The Origin and Evolution of Birds*, Yale University, New York, 1997.
28. Francis, M. S. and Keesee, J.E., “Airfoil Dynamic Stall Performance with Large-Amplitude Motions”, *AIAA Journal*, Vol. 23, No. 11, 1985, pp. 1653-1659.
29. Freymuth, P., “Thrust Generation by An Airfoil in Hover Modes,” Experiments in Fluids, Vol. 9, 1990, pp. 17-24.
30. Fry, S. N., Sayaman, R., and Dickinson, M. H., “The aerodynamics of hovering flight in Drosophila,” *The Journal of Experimental Biology*, Vol. 208, 2005, pp. 2303-2318.
31. Garrick, I. E., “Propulsion of a Flapping and Oscillating Airfoil,” NACA Rept. 567, 1937.
32. Glauert, H., The Elements of Aerofoil and Airscrew Theory, Cambridge University Press, London, 1926.
33. Graftieaux L, Michard, M., and Grosjean, N., “Combing PIV, POD and Vortex Identification Algorithms for the Study Unsteady Turbulent Swirling Flows,” Measurement Science and Technology, Vol. 12, 2001, pp. 1422-1429.
34. Graham, G. M., “An Experimental Investigation on an Airfoil Pitching at Moderate to High Rates to Large Angles of Attack,” Ph.D. Dissertation, Mechanical Engineering Dept., Lubbock, Texas Tech University, TX, 1985.

35. Graham, G. M. and Strickland, J. H., “An Experimental Investigation of an Airfoil Pitching at Moderate to High Rates to Large Angles of Attack,” AIAA Paper 86-0008, Jan. 1986b.
36. Grandlund, K. O., Ol, M. V., Garmann, D., Visbal, M., and Bernal, L. P., “Experiments and Computations on Abstraction of Perching,” AIAA Paper 2010-4943, June 2010.
37. Granlund, K. O., Ol, M. V., and Bernal, L. P., “Experiments on Pitching Plates: Force and Flowfield Measurements at Low Reynolds Numbers,” AIAA Paper 2011-872, Jan. 2011a.
38. Granlund, K. O., Ol, M. V., and Bernal, L. P., “Flowfield Evolution vs. Lift Coefficient History for Rapidly-Pitching Low Aspect Ratio Plates,” AIAA Paper 2011-3118, June 2011b.
39. Granlund, K. O., Ol, M. V., and Bernal, L. P., “Unsteady Pitching Flat Plates,” Journal of Fluid Mechanics, Vol. 733, 2013, R5.
40. Grimaldi, D. and Engel, M. S., *Evolution of the Insects*, Cambridge, New York, 2005.
41. Grodnitsky, D. L., *Form of Insect Wings: The Evolution of Biological Structures*, The John Hopkins University Press, Baltimore and London, 1999.
42. Helin, H. E. and Walker, J. M., “Interrelated Effects of Pitch Rate and Pivot Point on Airfoil Dynamic Stall,” AIAA Paper 85-0130, Jan 1985.
43. Herbst, W. B. and Krogull, B., “Design for Air Combat,” *Journal of Aircraft*, Vol. 10, No. 4, 1973, pp. 247-253.
44. Herbst, W. B., “Dynamics of Air combat,” *Journal of Aircraft*, Vol. 20, No. 7, 1983, pp. 594-598.
45. Herbst, W. B., “Future Fighter Technologies”, *Journal of Aircraft*, Vol. 17, No. 8, 1980, pp. 561-566.
46. Ho, S., Nassef, H., Pornsinsirirak, N., Tai, Y. C., and Ho, C. M., “Unsteady and Flow Control for Flapping wing flyers,” *Progress in Aerospace Sciences*, Vol. 39, No. 8, 2003, pp. 635-681.

47. Jumper, E. J., Dimmick, R. L, and Allaire, A. J. S., "The effect of Pitch Location on Dynamic Stall," *Journal of Fluids Engineering*, Vol. 111, 1989, pp. 256-262.
48. Jumper, E. J., Schreck, S. J., and Dimmick, R. L., " Lift-Curve Characteristics for an Airfoil Pitching at Constant Rate," *Journal of aircraft*, Vol. 24, 1987, pp. 680-687.
49. Kerlinger, P., *How Birds Migrate*, 1st ed., Stackpole Books, Pennsylvania, 1995.
50. Kim, Y. J., Choi, H. C., Him, K. H., "A Study on Rotational Effect on Flapping Wing Motion," AIAA Paper 2005-6337, Aug. 2005.
51. Kuethe, A. M. and Chow, C. Y., Foundations of Aerodynamics: Bases of Aerodynamic Design, 3rd ed., John Wiley & Sons, New York, 1976.
52. Lian, Y. and OL, M. V., "Computation and Experiments on a Low Aspect Ratio Pitching Flat Plate", AIAA paper 2010-0385, Jan. 2010.
53. Leishman, J. G., *Principles of Helicopter Aerodynamics*, Cambridge, New York, 2006.
54. Liu, H., Ellington, C. P., Kawachi, K., Berg, C. V. D., and Willmott, A. P., "A Computational Fluid Dynamic Study of Hawkmoth Hovering," *The Journal of Experimental Biology*, Vol. 201, 1998, pp. 461-477.
55. Lorber, P. F. and Carta, F. O., "Airfoil Dynamic Stall at Constant Pitch Rate and High Reynolds Number," *Journal of Aircraft*, Vol. 25, No. 6, 1988, pp. 548-556.
56. Ma, K. Y., Chirarattananon, P., Fuller, S.B., and Wood, R.J., "Controlled Flight of a Biologically Inspired, Insect-Scale Robot," *Science*, Vol. 340, 2013, pp. 603-607.
57. May, M. L., "Wingstroke Frequency of Dragonflies (Odonata: Anisoptera) in Relation of Temperature and Body Size," *Journal of Comparative Physiology B*, Vol. 144, 1981, pp. 229-240.
58. McAlister, K. W. and Carr, L. W., "Water Tunnel Visualizations of Dynamic Stall," Journal of Fluids Engineering, Vol. 101, 1979, pp. 376-380.
59. McCroskey, W. J. and Philippe, J. J., "Unsteady Viscous Flow on Oscillating Airfoils," *AIAA Journal*, Vol. 13, No. 1, 1975, pp. 71-79.
60. McCroskey, W. J., "Unsteady Airfoils," *Annual Review of Fluid Mechanics*, Vol. 14, 1982, pp. 285-311.

61. Mueller, T. J., “Aerodynamic Measurements at Low Reynolds Numbers for Fixed Wing Micro-Air Vehicles,” RTO AVT/VKI Special Course, Belgium, Sep. 13-17, 1999, Lecture Note. Retrieved from www.personal.psu.edu/lnl/097/belgium.pdf.
62. Nagai, H., Isogai, K., Fujimoto, T., and Hayase, T., “Experimental and Numerical Study of Forward Flight Aerodynamics of Insect Flapping Wing,” *AIAA Journal*, Vol. 47, No. 3, 2009, pp. 730-742.
63. Ol, M. V., Altman, A., Eldredge, J. D., Garmann, D. J., and Lian, Y., “Resume of the AIAA FDTC Low Reynolds Number Discussion Group’s Canonical Cases,” AIAA Paper 2010-1085, Jan. 2010.
64. Ol, M. V., Bernal, L. P., Kang, C. K., and Shyy, W., “Shallow and Deep Dynamic Stall for Flapping Low Reynolds Number Airfoils,” *Experiments in Fluids*, Vol. 46, 2009, pp. 883-901.
65. Ol, M. V., Eldredge, J. D, and Wang, C., “High-Amplitude Pitch of a Flat Plate: an Abstraction of Perching and Flapping,” *Internal Journal of Micro Air Vehicles*, Vol.1, No. 3, 2009, pp. 203-216.
66. Ol, M. V., “The High-Frequency, Hight-Amplitude Pitch Problem: Airfoils, Plates and Wings,” AIAA Paper 2009-3686, June 2009.
67. Oshima, H. and Ramaprian, B. R., “Velocity Measurements over a Pitching Airfoil”, *AIAA Journal*, Vol. 35, No. 1, 1997, pp. 119-126.
68. Oshima, H. and Ramapriant, B. R., “Measurements of the Velocity and Vorticity Fields Around a Pitching Airfoil,” AIAA Paper 92-2626-CP, June 1992.
69. Pennycuick, C. J., “Predicting Wingbeat Frequency and Wavelength of Birds,” *The Journal of Experimental Biology*, Vol. 150, 1990, pp.171-185.
70. Pennycuick, C. J., “Speeds and Wingbeat Frequencies of Migrating Birds Compared with Calculated Benchmarks,” *The journal of Experimental Biology*, Vol. 204, pp. 3283-3294, 2001.
71. Pennycuick, C. J., “Thermal Soaring Compared in Three Dissimilar Tropical Bird Species, Fregata Magnificents, Pelecanus Occidentalis and Coragyps Atratus,” *The Journal of Experimental Biology*, Vol. 102, 1983, pp. 307-325.

72. Pennycuick, C. J., “Wingbeat Frequency of Birds in Steady Cruising Flight: New Data and Improved Predictions,” *The Journal of Experimental Biology*, Vol. 199, 1996, pp. 1613-1618.
73. Pines, D. J. and Bohorquez, F., “Challenges Facing Future Micro-Air-Vehicle Development,” *Journal of Aircraft*, Vol. 43, No. 2, 2006, pp. 290-305.
74. Platzer, M. F., Jones, K. D., Young, J., and Lai, J. C., “Flapping Wing Aerodynamics – Progress and Challenges,” AIAA Journal, Vol. 46, No. 9, 2008, pp. 2136-2149.
75. Prasad, A. K. and Adrian, R. J., “Stereoscopic particle image velocimetry applied to liquid flows”, *Experiments in Fluids*, Vol. 15, Issue 1, 1993, pp. 49-60.
76. Prasad, A.K.,”Stereoscopic particle image velocimetry”, *Experiments in Fluids*, Vol.29, Issue 2, 2000, pp. 103-116.
77. Pullin, D. I., “The large-Scale Structure of Unsteady Self-Similar Rolled-Up Vortex Sheets,” Journal of Fluid Mechanics, Vol. 88, 1978, pp. 401-430.
78. Ramesh, K., Gopalarathnam, A., Edwards, J.R., Ol, M. V., and Granlund, K., “Theoretical, Computational and Experimental Studies of a Flat Plate Undergoing High-Amplitude Pitching Motion,” AIAA Paper 2011-217, Jan. 2011.
79. Reich, G. W., Wojnar, M. O., and Albertani, R., “Aerodynamic Performance of a Notional Perching MAV Design,” AIAA Paper 2009-63, Jan. 2009.
80. Rival, D., and Tropea, C., “Characteristics of Pitching and Plunging Airfoils Under Dynamic-Stall Conditions,” *Journal of Aircraft*, Vol. 47, No. 1, 2010, pp. 80-86.
81. Ruppell, G., “Kinematic Analysis of Symmetrical Flight Maneuvers of Odonata,” *The Journal of Experimental Biology*, Vol. 144, 1989, pp. 13-42.
82. Sakakibara, J., Nakagawa, M., and Yoshiha, M., “Stereo-PIV study of flow around a maneuvering fish”, *Experiments in Fluids*, Vol. 36, Issue 2, 2004, pp. 282-293.
83. Sane, S. P. and Dickinson, M. H., “The Control of Flight Force by a Flapping Wing: Lift and Drag Production,” *The Journal of Experimental Biology*, Vol. 204, 2001, pp. 2607-2626.
84. Sane, S. P., “Steady or Unsteady? Uncovering the Aerodynamic Mechanisms of Insect Flight,” *The Journal of Experimental Biology*, Vol. 214, 2011, pp. 349-351.

85. Sane, S. P., “The aerodynamics of Insect Flight”, *The Journal of Experimental Biology*, Vol. 206, 2003, pp. 4191-4208.

86. Savile, D. B. O., “Adaptive evolution in the Avian Wing”, *Evolution*, Vol. 11, No. 2, 1957, pp. 212-224.

87. Schreck, S. J., Faller, W. E., and Robinson, M. C., “Unsteady Separation Processes and Leading Edge Vortex Precursors: Pitch Rate and Reynolds Number Influences,” *Journal of Aircraft*, Vol. 39, No. 5, 2002, pp. 868-875.

88. Sears, W. R. and Telionis, D. P., “Boundary-Layer Separation in Unsteady Flow,” *SIAM Journal on Applied Mathematics*, Vol. 28, No. 1, 1975, pp. 215-235.

89. Shen, S. F., “Unsteady Separation According to the Boundary-Layer Euqation,” Advances in Applied Mechanics, Vol. 18, 1978, pp. 177-220.

90. Shih, C., Lourenco, L., Dommelen, L. V., and KrotHapalli, A., “Unsteady Flow Past an Airfoil Pitching at a Constant Rate,” *AIAA Journal*, Vol. 30, N0. 5, 1992, pp. 1153-1161.

91. Shyy, W., Lian, Y., Tang, J., Viieru, D., and Liu, H., *Aerodynamics of Low Reynolds Number Flyers*, Cambridge, New York, 2008.

92. Smith, S. W., The Scientist and Engineer’s Guide to Digital Signal Processing, 1997.

93. Soloff, S. M., Adrian, R. J., and Liu, Z. C., “Distortion compensation for generalized stereoscopic particle image velocimetry”, *Measurement Science and Technology*, Vol. 8, No. 12, 1997, pp. 1441-1454.

94. Strickland, J. H. and Graham, G. M., “Dynamic Stall Inception Correlation for Airfoils Undergoing Constant Pitch Rate Motions,” *AIAA Journal*, Vol. 24, No. 4, 1986a, pp. 678-680.

95. Strickland, J. H. and Graham, G. M., “Force Coefficients for a NACA-0015 Airfoil Undergoing Constant Pitch Rate Motions,” *AIAA Journal*, Vol. 25, No. 4, 1987, pp. 622-624.

96. Sun, M. and Tang, J., “Unsteady Aerodynamic Force Generation by a Model Fruit Fly Wing in Flapping Motion,” *The Journal of Experimental Biology*, Vol. 205, 2002, pp. 55-70.

97. Sunada, S., Kawachi, K., Matsumoto, A., and Sakaguchi, A., "Unsteady Forces on a Two-Dimensional Wing in Plunging and Pitching Motions," *AIAA Journal*, Vol.39, No. 7, 2001, pp. 1230-1239.

98. Suryadi, A. and Obi, S., "The Estimation of Pressure on the Surface of a Flapping Rigid Plate by Stereo PIV", *Experiments in Fluids*, Vol. 51, Issue 5, 2011, pp. 1403-1416.

99. Suryadi, A., Ishii, T., and Obi, S., "Stereo PIV Measurement of a Finite, Flapping, Rigid Plate in Hovering Condition", *Experiments in Fluids*, 2010, Vol. 49, Issue 2, pp. 447-460.

100. Tang, J., Viieru, D., and Shyy, W., "Effects of Reynolds Number and Flapping Kinematics on Hovering Aerodynamics," *AIAA Journal*, Vol. 46, No. 4, 2008, pp. 967-976.

101. Taylor, G. K., Nudds, R. L., and Thomas, A. L. R., "Flying and Swimming Animals Cruise at a Strouhal Number Tuned for High Power Efficiency," *Nature*, Vol. 425, 2003, pp. 707–711.

102. Tennekes, H., The Simple Science of Flight From Insects to Jumbo Jets, MIT Press, London, England, 2009.

103. Triantafyllou, M. S., Triantafyllou, G. S., and Yue, D. K. P., "Hydrodynamics of fishlike swimming," *Annual Review of Fluid Mechanics*, Vol. 32, 2000, pp. 33–53.

104. Trizila, P., Kang, C. K., Aono, H., Shyy, W., and Visbal, M., "Low Reynolds-Number Aerodynamics of a Flapping Rigid Flat Plate," AIAA Journal, Vol. 49, No. 4, 2001, pp. 806-823.

105. Tuncer, I. H., Walz, R., and Platzer, M. F., "A Computational Study of the Dynamic Stall of a Flapping Airfoil," AIAA Paper 98-2519, June 1998.

106. Vandenheede, R., Bernal, L. P., Morrison, C. L., Gogulapati, A., Friedmann, P. P., Kang, C. P., Shyy, W., "Experimental and Computational Study on Flapping Wings with Bio-Inspired Hover Kinematics", *AIAA Journal*, 2014,

107. Visbal, M. R. and Shang, J.S., "Investigation of the Flow Structure around a Rapidly Pitching Airfoil," *AIAA Journal*, Vol. 27, 1989, pp. 1044-1051.

108. Visbal, M. R. and Shang, J.S., "Numerical Investigation of the Flow Structure around a Rapidly Pitching Airfoil," AIAA Paper 87-1424, June 1987.

109. Visbal, M. R., "Dynamic Stall of a Constant-Rate Pitching Airfoil," *Journal of Aircraft*, Vol. 27, 1990, pp. 400-407.

110. Visbal, M. R., "Evaluation of an Implicit Navier-Stokes Solver for Some Unsteady Separated Flows," AIAA Paper 86-1053, May 1986.

111. Visbal, M. R., "On the Formation and Control of the Dynamic Stall Vortex on a Pitching Airfoil," AIAA Paper 91-0006, Jan. 1991.

112. Visbal, M. R., "Three-Dimensional Flow Structure on a Heaving Low-Aspect-Ratio Wing", AIAA Paper 2011-219, Jan. 2011.

113. Vogel, S., "Flight in Drosophila I. Flight Performance of Tethered Flies," *The Journal of Experimental Biology*, Vol. 44, 1966, pp. 567-578.

114. Walker, J. M. and Chou, D. C., "Forced Unsteady Vortex Flows Driven by Pitching Airfoils," AIAA Paper 87-1331, June 1987.

115. Walker, J. M., Helin, H. E., and Strickland, J. H., "An Experimental Investigation of an Airfoil Undergoing Large-Amplitude Pitching Motions," *AIAA Journal*, Vol. 23, No. 8, 1985a, pp. 1141-1142.

116. Walker, J. M., Helin, H. E., and Chou, D. C., "Unsteady Surface Pressure Measurements on a Pitching Airfoil", AIAA Paper 85-0532, March 1985b.

117. Wang, Z. J., Birch, J. M., and Dickinson, M. H., "Unsteady Forces and Flows in Low Reynolds Number Hovering Flight: Two-Dimensional Computations vs Robotic Wing Experiments", *The Journal of Experimental Biology*, Vol. 207, 2004, pp. 449-460.

118. Weis-Fogh, Torkel, "Quick Estimates of Flight Fitness in Hovering animals, including Novel Mechanisms for Lift Production," *The Journal of Experimental biology*, Vol. 59, 1973, pp. 169-230.

119. Weis-Foght, Torkel, "Energetics of Hovering Flight in Humming Birds and in Drosophila," *The Journal of Experimental Biology*, Vol. 56, 1972, pp. 79-104.

120. Willmott, A. P., and Ellington, C. P., “The Mechanics of Flight in the Hawkmoth Manduca Sexta: I. Kinematics of Hovering and Forward Flight,” *The Journal of Experimental Biology*, Vol. 200, 1997, pp. 2705-2722.
121. Wootton, R., “From Insects to Microvehicles,” *Nature*, Vol. 403, 2000, pp. 144-145.
122. Yilmaz, T. O. and Rockwell, D., “Flow Structure on Finite-Span Wings due to Pitch-Up Motion”, *Journal of Fluid Mechanics*, Vol. 691, 2012, pp518-545.
123. Yilmaz, T., Ol, M., and Rockwell, D., “ Scaling of Flow Separation on a Pitching Low Aspect Ratio plate,” *Journal of Fluids and Structures*, Vol. 26, Issue 6, August 2010, pp. 1034-1041.
124. Young, J., and Lai, J. C. S., “Mechanism Influencing the Efficiency of Oscillating Airfoil Propulsion,” *AIAA Journal*, Vol. 45, No. 7, 2007, pp. 1695–1702.
125. Young, J., and Lai, J. C. S., “Oscillation Frequency and Amplitude Effects on the Wake of a Plunging Airfoil,” *AIAA Journal*, Vol. 42, No. 10, 2004, pp. 2042–2052.
126. Yu, H. T., Bernal, L.P., and Morrison, C., “Experimental Investigation of Pitch Ramp-Hold-Return Motion of Flat Plates at Low Reynolds Number,” AIAA Paper 2012-51, Jan. 2012.
127. Yu, H. T. and Bernal, L.P., “Effect of Pivot Point on Aerodynamic Force and Vortical Structure of Pitching Flat Plate Wings,” AIAA Paper 2013-0792, Jan. 2013.
128. Yu, H. T., Bernal, L. P., and Ol, M. V., “Effects of Planform Geometry and Pivot Axis Location on the Aerodynamics of Pitching Low Aspect Ratio Wings,” AIAA Paper 2013-2992, June 2013.
129. Zanker, J. M., “The wing beat of Drosophila melanogaster. I. Kinematics,” Philosophical *Transactions of the Royal Society of London. Series B, Biological*, Vol. 327, No. 1238, 1990, pp. 1-18.
130. Zufferey, J. C., Bio-inspired Flying Robots: Experimental Synthesis of Autonomous Indoor Flyers, EPFL Press, Boca Raton, 2008.